

Electron Cyclotron Heating and Suprathermal Electron Dynamics in the TCV Tokamak

THÈSE N° 5181 (2011)

PRÉSENTÉE LE 28 OCTOBRE 2011
À LA FACULTÉ SCIENCES DE BASE
CRPP - PHYSIQUE DU TOKAMAK TCV
PROGRAMME DOCTORAL EN PHYSIQUE

ÉCOLE POLYTECHNIQUE FÉDÉRALE DE LAUSANNE

POUR L'OBTENTION DU GRADE DE DOCTEUR ÈS SCIENCES

PAR

Silvano GNESIN

acceptée sur proposition du jury:

Prof. V. Savona, président du jury
Dr S. Coda, directeur de thèse
Dr D. Mazon, rapporteur
Dr R. Prater, rapporteur
Dr O. Sauter, rapporteur



ÉCOLE POLYTECHNIQUE
FÉDÉRALE DE LAUSANNE

Suisse
2011

To my parents

Abstract

This thesis is concerned with the physics of suprathermal electrons in thermonuclear, magnetically confined plasmas. Under a variety of conditions, in laboratory as well as space plasmas, the electron velocity distribution function is not in thermodynamic equilibrium owing to internal or external drives. Accordingly, the distribution function departs from the equilibrium Maxwellian, and in particular generally develops a high-energy tail. In tokamak plasmas, this occurs especially as a result of injection of high-power electromagnetic waves, used for heating and current drive, as well as a result of internal magnetohydrodynamic (MHD) instabilities. The physics of these phenomena is intimately tied to the properties and dynamics of this suprathermal electron population. This motivates the development of instrumental apparatus to measure its properties as well as of numerical codes to simulate their dynamics. Both aspects are reflected in this thesis work, which features advanced instrumental development and experimental measurements as well as numerical modeling.

The instrumental development consisted of the complete design of a spectroscopic and tomographic system of four multi-detector hard X-ray (HXR) cameras for the TCV tokamak. The goal is to measure bremsstrahlung emission from suprathermal electrons with energies in the 10-300 keV range, with the ultimate aim of providing the first full tomographic reconstruction at these energies in a noncircular plasma. In particular, suprathermal electrons are generated in TCV by a high-power electron cyclotron heating (ECH) system and are also observed in the presence of MHD events, such as sawtooth oscillations and disruptive instabilities. This diagnostic employs state-of-the-art solid-state detectors and is optimized for the tight space requirements of the TCV ports. It features a novel collimator concept that combines compactness and flexibility as well as full digital acquisition of the photon pulses, greatly enhancing its potential for full spectral analysis in high-fluency scenarios. Additional flexibility is afforded by the possibility to rotate the orientation of two of the cameras, permitting the crucial comparison of radiation emitted perpendicular and parallel to the primary magnetic field. The design of the HXR system was optimized through an extensive iterative simulation process with the aid of tomographic reconstruction codes as well as quasilinear Fokker-Planck modeling of ECH-driven TCV plasmas. In parallel, the selection of the detectors for this system was performed through comprehensive laboratory testing of several candidate detectors available on the market. While the design was completed in the course of the thesis work, commissioning of the system has only commenced recently with one of the four cameras installed on TCV. The first preliminary results, discussed in the last part of this thesis, include basic parameter scans of ECH wave-plasma interaction and the investigation of the dynamic response of suprathermal electrons to modulated ECH. In addition, the cameras possess the novel ability to discriminate against very high-energy γ -ray radiation that cannot be collimated and must thus be excluded from spatial distribution analysis. A basic study of the conditions for γ -ray suppression was conducted in preparation for future experiments.

The Fokker-Planck modeling tool used in this diagnostic development was acquired through a collaboration with CEA-Cadarache, initially with the primary motivation of studying the simultaneous plasma heating by 2nd and 3rd harmonic electron cyclotron waves that is uniquely possible on TCV. This motivated a dedicated study, both

theoretical and experimental, of one particular instance of this combined heating, which became a second primary subject of this thesis work. The particular scenario studied here is one in which a single ECH frequency is resonant at both harmonics in the same plasma. The primary objective of this study was to determine whether a synergy effect existed, permitting an enhancement of the intrinsically weak 3rd harmonic absorption by the suprathermal electrons generated at the 2nd harmonic resonance. An associated question was whether this effect, if it existed, was experimentally measurable or was in fact observed in TCV. The simulations performed in the course of this study indeed predict the existence of such a synergy, although the answer to the second question was ultimately negative, at least within the current technical limitations. This study has proven nevertheless highly valuable in providing new insight into the complex velocity-space dynamics that govern ECH wave-particle interaction and suprathermal electron dynamics.

Keywords: heating, current drive, plasma, TCV tokamak, synergy, suprathermal electrons, fast electrons, runaway electrons, ECH, ECCD, tomography, HXRS, hard X-ray, detector, CdTe, EGS, Monte Carlo, Fokker-Planck, LUKE, nuclear fusion, bremsstrahlung emission, ECE, electron cyclotron emission, spectroscopy, Soller collimator, shielding, digital signal acquisition, pileup, coherent averaging, charge sensitive amplifier.

Version abrégée

Cette thèse porte sur la physique des électrons suprathermiques dans des plasmas thermonucléaires à confinement magnétique. Dans différentes conditions, à la fois dans le laboratoire et dans l'espace, la fonction de distribution en vitesse des électrons n'est pas en équilibre thermodynamique à cause d'agents internes ou externes. Pour cette raison la fonction de distribution s'éloigne de la fonction Maxwellienne d'équilibre, et en particulier peut développer une queue à haute énergie. Dans les tokamaks, ceci est généralement dû à l'injection d'ondes électromagnétiques à haute puissance, utilisées pour le chauffage et l'entraînement de courant, et peut également être dû à des instabilités magnétohydrodynamiques (MHD) internes. La physique de ces phénomènes est étroitement liée aux propriétés et à la dynamique de cette population d'électrons suprathermiques. Ceci motive le développement de dispositifs instrumentaux pour mesurer ses propriétés ainsi que de codes numériques pour simuler leur dynamique. Les deux aspects apparaissent dans ce travail de thèse, qui contient un développement instrumental avancé et mesures expérimentales ainsi que la modélisation numérique.

Le développement instrumental a consisté en la conception et design complet d'un système spectroscopique et tomographique de quatre caméras à rayons X durs (HXR) multi-détecteur pour le tokamak TCV. Le but est de mesurer l'émission de freinage des électrons suprathermiques avec énergies entre 10 et 300 keV, avec l'objectif final d'obtenir la première reconstruction tomographique à ces énergies dans un plasma non-circulaire. En particulier, des électrons suprathermiques sont générés dans TCV par un système de chauffage par ondes cyclotroniques électroniques (ECH) et sont également observés en présence d'événements MHD, tels les oscillations à dent-de-scie et les instabilités disruptives. Ce diagnostic utilise des détecteurs modernes à état solide et est optimisée pour l'espace limité des queusots du tokamak TCV. Il comprend un nouveau concept de collimateur à la fois compact et flexible, ainsi qu'une acquisition digitale de la séquence complète des impulsions photoniques, avec un grand potentiel d'analyse spectrale complète dans des situations de flux intense. Une flexibilité ultérieure dérive de la possibilité de tourner l'orientation de deux des caméras, permettant ainsi une comparaison cruciale entre la radiation émise perpendiculairement et celle émise parallèlement au champ magnétique primaire.

Le design du système HXR a été optimisé au moyen d'un processus de simulation itérative étendu, à l'aide de codes de reconstruction tomographique ainsi que d'une modélisation quasi-linéaire Fokker-Planck des plasmas de TCV chauffés par ECH. En parallèle, le choix des détecteurs pour ce système a été accompli par un processus exhaustif de plusieurs candidats disponibles sur le marché. Le design a été complété pendant ce travail de thèse mais la mise en oeuvre du système a commencé seulement récemment avec l'installation de la première des quatre caméras sur TCV. Les premiers résultats préliminaires, présentés dans la dernière partie de cette thèse, comprennent des explorations paramétriques de base de l'interaction onde ECH-particule et une investigation de la réponse dynamique des électrons suprathermiques à la modulation ECH. Les caméras possèdent aussi la nouvelle capacité de distinguer la radiation γ à très haute énergie qui ne peut pas être collimatée et doit donc être exclue d'une analyse de

distribution spatiale. Une étude initiale des conditions de suppression de la radiation γ a été effectuée en préparation d'expériences futures.

L'outil de modélisation Fokker-Planck utilisé dans ce développement de diagnostic a été acquis à travers une collaboration avec CEA-Cadarache, avec la motivation initiale d'étudier le chauffage simultané par l'ECH à la 2^{ème} et 3^{ème} harmonique qui est possible uniquement sur TCV. Ceci a motivé une étude focalisée, théorique ainsi qu'expérimentale, d'un type particulier de ce chauffage combiné, qui est devenue un deuxième sujet primaire de ce travail de thèse. Dans ce scénario particulier la même fréquence ECH est résonante aux deux harmoniques dans le même plasma. L'objectif principal de cette étude était de déterminer s'il existe un effet de synergie qui permettrait une augmentation de l'absorption (intrinsèquement faible) à la 3^{ème} harmonique par les électrons suprathermiques générés à la résonance à la 2^{ème} harmonique. Une question ancillaire était si cet effet – pourvu qu'il existe – était expérimentalement mesurable ou avait été en fait observé sur TCV. Les simulations effectuées durant cette étude en effet prévoient l'existence d'une telle synergie. Toutefois, la réponse à la deuxième question était finalement négative, du moins en tenant compte des limites techniques actuelles. Cette étude s'est montrée néanmoins très utile dans la mesure où elle a permis une compréhension plus profonde de la dynamique complexe dans l'espace des vitesses qui régie l'interaction onde ECH-particule et la dynamique des électrons suprathermiques.

Mots clefs : chauffage, génération de courant, plasma, TCV tokamak, synergie, électrons suprathermiques, électrons rapides, électrons runaway, tomographie, rayons X-durs, capteur, CdTe, EGS, code Monte Carlo, Fokker-Planck, LUKE, fusion nucléaire, émission de freinage, émission d'onde cyclotronique, spectroscopie, collimateur, acquisition digital du signal, amplificateur de charge.

Contents

Abstract	i
Version abrégée	iii
I. Introduction	
1. Introduction and scientific motivation	1
1.1 The energy problem.....	1
1.2 Nuclear fusion.....	2
1.3 Magnetic confinement.....	5
1.4 The tokamak principle.....	5
1.5 Scientific motivations.....	8
2. The TCV experiment	11
2.1 TCV vessel and plasma configurations.....	11
2.2 First wall.....	12
2.3 Plasma heating.....	12
3. Plasma current drive in tokamaks by wave-particle interaction	17
3.1 Introduction	17
3.2 The resonance condition.....	17
3.3 Electron cyclotron current drive.....	19

4. The Fokker-Planck modeling of the electron distribution function	25
4.1 The Fokker-Planck approach to the problem.....	25
4.2 TCV Fokker-Planck modeling tools	33
4.3 Conclusion.....	38
5. Suprathermal electron diagnostics	39
5.1 X-ray plasma bremsstrahlung emission.....	40
5.2 Electron cyclotron emission	46

II. Research achievements

6. 3rd harmonic ECRH absorption enhancement by 2nd harmonic heating at the same frequency in TCV	49
6.1 Introduction.....	49
6.2 Experimental setup.....	50
6.3 Experimental results	52
6.4 Numerical modeling of the experiment	54
6.5 Interpretation of the numerical results: phase space analysis.....	56
6.6 Modeling vs experiment: non-thermal bremsstrahlung analysis	59
6.7 Conclusions.....	67
7. The HXRS tomographic spectroscopic diagnostic	69

7.1	Introduction	69
7.2	Tomography in plasmas	70
7.3	Semiconductor detectors for hard X-ray detection	74
7.4	Detector tests and choice	84
7.5	Collimator design.....	93
7.6	Vacuum windows and filters	111
7.7	Modeling of detector responsivity in the presence of collimators and shields...	114
7.8	System responsivity simulation with the EGSnrc Monte Carlo code.....	119
7.9	Shielding: requirements	130
7.10	Optimization of HXRS diagnostic design by simulation of tomographic reconstruction.....	135
7.11	Signal acquisition and processing.....	145
7.12	Implementation of the equatorial HXRS camera.....	153
7.13	Conclusion.....	155
8.	HXRS camera commissioning and first results	159
8.1	Introduction.....	159
8.2	Observation of runaways during low density plasma discharges and with stabilized sawteeth.....	160
8.3	Suprathermal emission in ECCD plasmas	165
8.4	Parallel asymmetry on non thermal bremsstrahlung emission	169
8.5	Coherent averaging on modulated ECCD experiments.....	172
8.6	Conclusion.....	177

9. Conclusions and Outlook	179
Bibliography	181
Acknowledgements	185
Curriculum Vitae	187

1. Introduction and scientific motivations

1.1 The energy problem

Energy needs are constantly increasing due to the enhancement of the standard of living of people and the increase in the world population itself.

In particular, the economies of highly populated countries such as China and India are developing rapidly so that their need to gain access to energy sources has become a top priority. Figure 1.1 depicts the time evolution of the global world energy consumption projected to 2035 [1].

The increase in worldwide energy demand together with the limited stocks of traditional non-renewable energy sources such as oil, coal or gas drives up the cost of energy and is causing unsustainable increases in greenhouse gas emission (Fig.1.2).

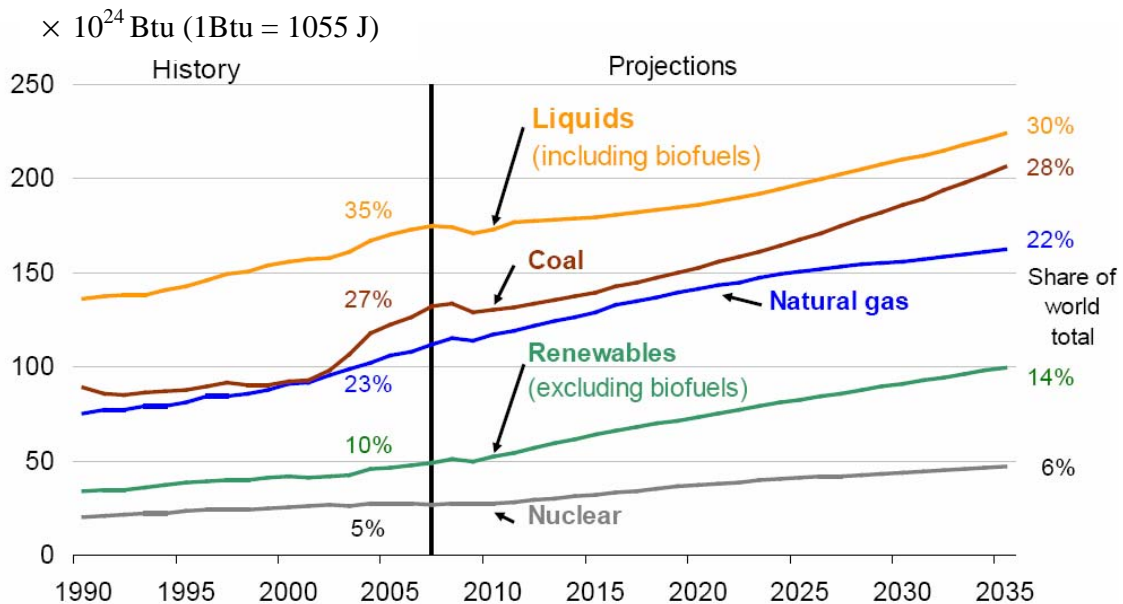


Figure 1. 1 World primary energy consumption by fuel type, EIA projection to 2035 (source: EIA, International Energy Outlook 2010 [1]. <http://www.eia.doe.gov/oiaf/ieo/>)

Even though the scientific community is still divided concerning the details of the greenhouse gas effects on the global environment, there is agreement on the benefits of a prevention policy aimed at limiting waste emissions, in parallel with a push to develop alternative energy sources. Natural renewable sources are especially attractive; these include hydroelectric, geothermic, and sun powered energy forms such as wind and photoelectric.

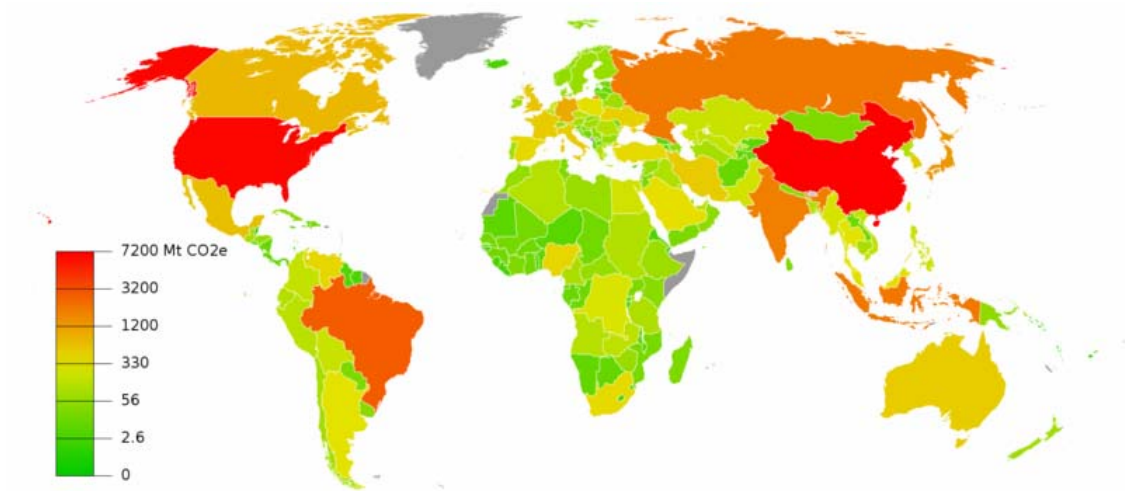


Figure 1.2 Green house emission (Mt CO₂), source : http://en.wikipedia.org/wiki/Global_warming.

Another option already in use in many countries around the world is nuclear fission. This source however still depends on the finite availability of uranium, and has additional drawbacks such as long lifetime radioactive waste production and the danger of nuclear weapon proliferation. Furthermore, a loss of control of the intrinsically unstable fission reaction can occur as a consequence of unpredictable events such as earthquakes or tsunamis, resulting in danger to the population and to the natural environment, an issue brought dramatically to the forefront by the recent Fukushima accident.

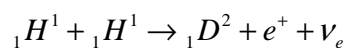
The opposite process to fission is fusion of a light nucleus (such as hydrogen isotopes). This form of energy, after decades of studies, is still in the research phase, in spite of considerable progress. This kind of energy source has several advantageous features: higher safety level for a power plant (explosive events are excluded because of the low fuel quantities involved and the impossibility of a chain reaction effect), short-lived radioactive waste, no link to weapon proliferation and practically unlimited availability of fuel, which can be obtained directly from ocean water.

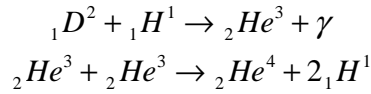
To sustain the future world energy requirements we will likely need to employ a mix of these energy sources, motivating all of them to be pursued as research avenues. Hereafter we will focus our discussion on nuclear fusion.

1.2 Nuclear fusion

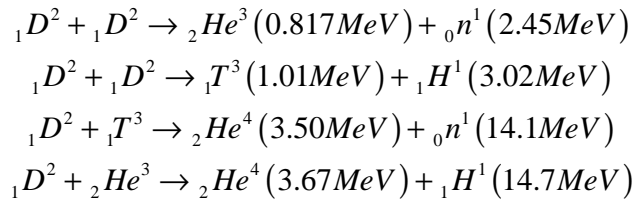
Most of the energy supplied by conventional fuels such as coal, oil and gas also has its origin in the energy radiated by the sun, so it can be considered in a sense a form of solar energy.

Fusion is the basic process governing solar energy production. The dominant fusion reactions occurring in the sun are the following:





In all these reactions the final total mass loss is converted to energy radiated toward the external layers of the sun through successive absorption and re-emission processes. In order to obtain a commercial source of energy on earth different possible fusion reactions have been considered and analyzed, such as



Among them the D-T reaction is the one currently envisioned for the first commercial power plants, since it displays the largest cross section at the lowest energy of the reacting nuclei (Fig. 1.3) and is therefore the most efficient reaction.

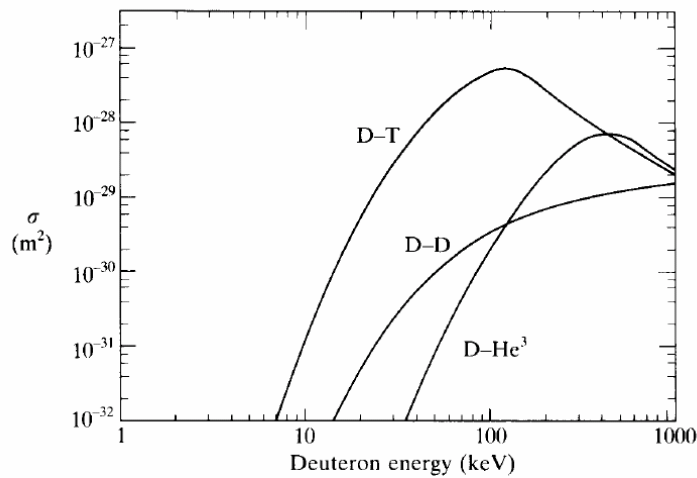
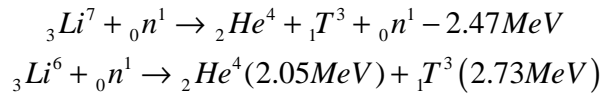


Figure 1.3 $D-T$, $D-D$ and $D-He^3$ fusion reaction cross sections.

Deuterium is available in bulk quantities from ordinary water, whereas tritium is not present in nature because of its short radioactive half-life (12.3 years). An attractive scheme for generating the necessary tritium is to surround a fusion reactor with a lithium blanket (breeder blanket layer): fission reactions induced by the fusion-generated neutrons result in the generation of tritium. This scheme has been employed in US light water nuclear fission power plants (e.g., Tennessee Valley Authority's Watts Bar and

Sequoyah Nuclear Plants, Units 1 and 2, in Tennessee; see also: <http://www.nrc.gov/reading-rm/doc-collections/fact-sheets/tritium.html>). The relevant reactions are



The relative abundances of the two lithium isotopes ${}_3\text{Li}^6$ and ${}_3\text{Li}^7$ are 7.4% and 92.6% respectively.

Natural resources of deuterium and lithium isotopes dissolved in the sea water are estimated to meet the global energy requirements for several million years at today's annual global electricity consumption rates. Thus, nuclear fusion promises to be a practically inexhaustible source of energy.

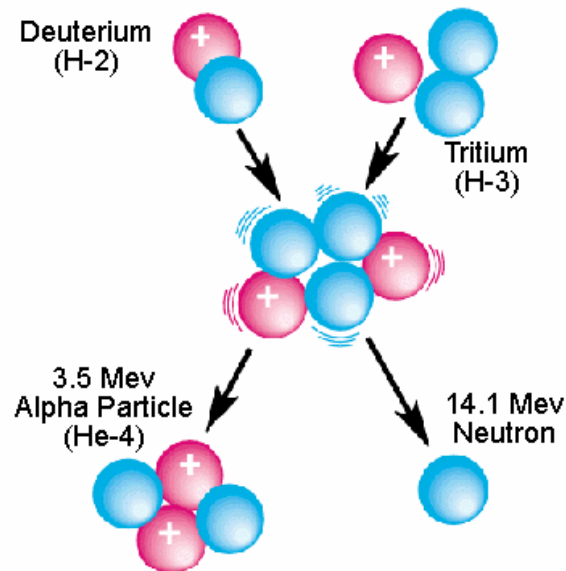


Figure 1. 4 Deuterium – Tritium fusion reaction (picture from: <http://www.seas.columbia.edu/>)

Each D-T nuclear fusion reaction (Fig. 1.4) delivers an amount of energy $\Delta E = E_\alpha + E_n = 17.6\text{MeV}$ shared between the helium nucleus (alpha particle) and the neutron. In order to produce enough energy for commercial interest we need to satisfy three conditions. The first condition is to attain a high temperature T (several tens of millions of degrees Celsius): at such temperature the gas is completely ionized, i.e. it is in the plasma state. The second condition is that the density (n_e) be sufficiently high. Finally, it is necessary that the plasma can keep its energy for a time (τ_E) sufficient for the reaction rate to generate more power than is supplied to it. This is summarized in the Lawson criterion for fusion plasmas (also named triple product condition):

$$n_e T \tau_E \geq 10^{21} \text{ keV s/m}^3$$

Different methods of external power injection are used to increase the triple product beyond the threshold, as will be discussed in chapter 3 with special emphasis on electron heating methods by radio frequency wave injection.

1.3 Magnetic confinement

Plasmas are composed of free charged particles; the most commonly used way to confine such charged particles is to constrain them to orbit around the magnetic field lines of an externally applied magnetic field B (Fig. 1.5) In such a configuration electrons and ions perform a cyclotron motion characterized by the gyro radius $\rho_j = \frac{m_j v_{\perp}}{q_j B}$ and the Larmor

or cyclotron angular frequency $\Omega_c = \frac{q_j B}{m_j}$, where j is the species index ($j = i, e$), m and q are the particle's mass and charge, respectively, and v_{\perp} is the velocity component perpendicular to B . Particles are then trapped in the perpendicular direction but can move freely in the parallel direction as shown in Fig. 1.5.

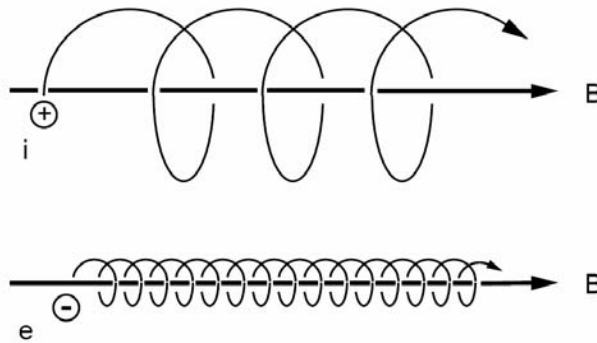


Figure 1. 5 Trajectories of charged particles in a homogeneous magnetic field B

1.4 The Tokamak principle

Straight field line magnetic field configurations as described in the previous paragraph prevent the charged particles from escaping in the orthogonal directions but permit losses at the two extremities. The next step in confining a plasma in a finite enclosure consists of closing the magnetic field lines in a toroidal configuration. Unfortunately this arrangement causes the field to be non-homogeneous.

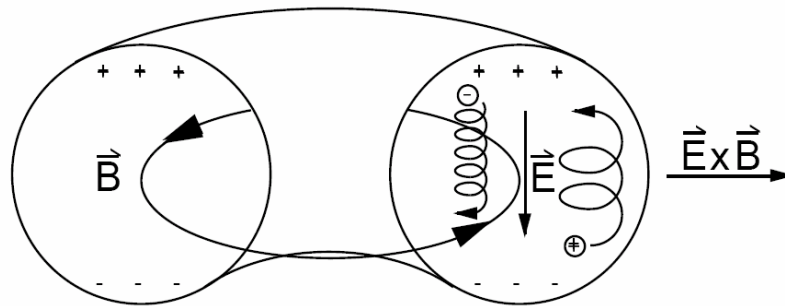


Figure 1. 6 Particle drift motion in a toroidal magnetic field

The gradient of the field amplitude and the curvature of the field lines lead to drift motions of ions and electrons in opposite vertical directions; this results in a charge separation that creates an electric field perpendicular to the magnetic field: the plasma consequently experiences an outward $\vec{E} \times \vec{B}$ drift motion (Fig. 1.6). This effect can be prevented by twisting the magnetic field lines, so that each field line samples the upper and lower parts of the torus. In this case, when the drifts are averaged along the particle orbits, which follow the magnetic field line, the net vertical drift vanishes and no electric field is generated on average.

The twisting of the magnetic lines is obtained by adding to the toroidal field B_{tor} an extra poloidal component B_{pol} generated by a toroidal plasma current, obtained by means of a transformer induction, in which the plasma plays the role of secondary circuit. As this toroidal confinement configuration was proposed first by Russian scientists (Igor Tamm and Andrei Sacharov in 1951), it has become known by the Russian acronym Tokamak, which stands for “Toroidalnaja Kamera a Magnitnymi Katuskami” or “Toroidal chamber with magnetic coils”. The toroidal geometry and the plasma pressure lead to a force trying to expand the plasma ring. This force is balanced by applying a vertical magnetic field B_v , which interacts with the plasma current to impart an inward force to the plasma. We have a visual summary of the situation in Fig 1.7.

The induction of the plasma current allows only for pulsed operation. Further efforts have been devoted to developing alternative ways to drive the plasma current, such as with electromagnetic waves or particle beams, which would in principle allow continuous tokamak operation.

In modern tokamaks additional poloidal field coils carrying a toroidal current are used for shaping the poloidal cross section of the plasma. It has been found that the plasma shape also influences the stability and transport properties of the plasma. Elongated and triangular plasma shapes, for example, exhibit superior properties compared to circular plasmas [2-6]. The elongation κ is defined as the ratio of the vertical to the horizontal semi-axis of the plasma, while the triangularity δ is a parameter describing the deformation of the plasma cross section into a D. Negative values of δ correspond to a plasma whose D-shaped cross-section is left to right inverted.

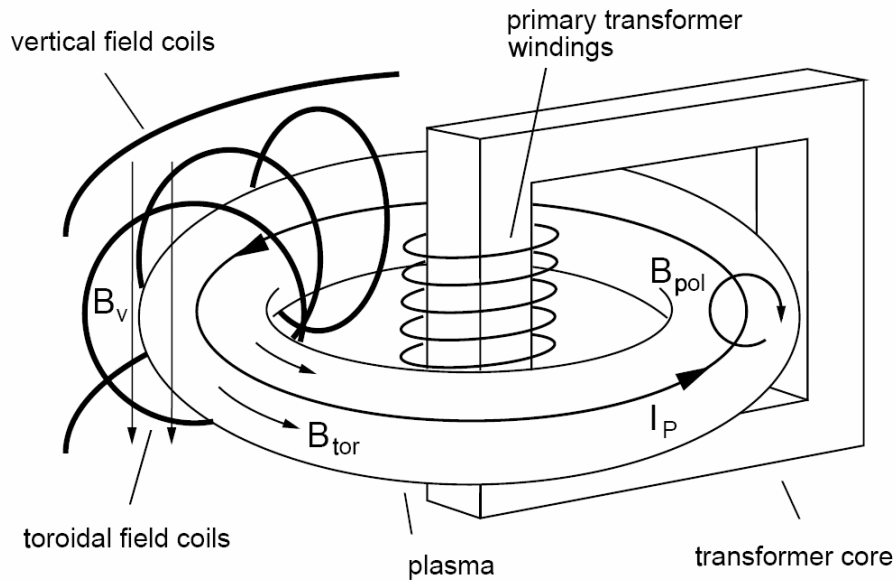


Figure 1.7 Schematic of the coil configuration of a tokamak

Another important task for a plasma confining device is to control the interaction of the plasma with the first wall. There are two main configurations used to separate the plasma from the vacuum vessel wall. In the first configuration the outer boundary of the plasma is defined using a material limiter. In the second configuration the magnetic field structure is modified to induce separation between the inner closed flux surfaces and the outer region with open field lines that can intercept the vessel walls; the separatrix surface is designed to transport heat and particles away from the main plasma region to an especially designed wall interaction region known as a divertor. The two boundary configurations are illustrated in Fig. 1.8.

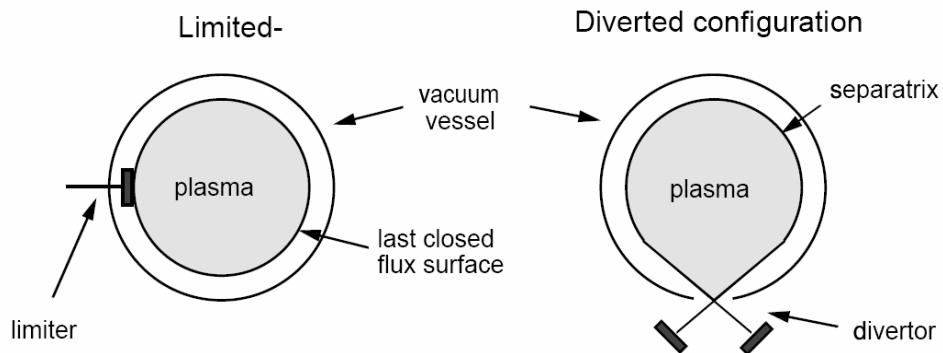


Figure 1.8 Poloidal cross section of the plasma boundary and vessel wall in a limiter and in a diverted configuration.

The present thesis work has been carried out on the “Tokamak à Configuration Variable” (TCV) at the “Centre de Recherches en Physique des Plasmas” (CRPP) in Lausanne (Switzerland). The experimental facility is described in detail in chapter 2.

1.5 Scientific motivations

The ultimate goal of fusion research is to attain the ignition condition. In this case the energy ceded to the plasma by the fusion generated α particles is sufficient to sustain the required plasma temperature without external heating, and the fusion reaction can become self-sustained for steady state operation. True steady-state operation would also require sustaining the plasma current fully non-inductively. Tokamak reactors are at present the most promising technology for achieving steady-state thermonuclear fusion operations. The majority of the current in such a scenario would have to be driven by the internal “bootstrap” effect, which arises from the presence of density and temperature gradients [7]. In particular, tokamak discharges featuring RF heating and current drive can in appropriate conditions develop internal transport barriers (ITBs) that result in improved confinement and are characterized by a large bootstrap current fraction [8], suggesting a potential route to the steady-state mode of operation desirable for a fusion power plant. (An overview of these advanced operational scenarios can be found in [9]). Even when the current is mostly driven by the bootstrap effect, external power sources will likely be necessary, even in an ignited plasma, both for heating and for current drive (CD) for the purposes of tailoring the pressure and current profiles for optimal plasma performance [10] and for MHD instability control [11,12]. Therefore the issue of current-drive efficiency and deposition is of crucial interest for next step fusion devices.

With intense current drive, particularly in the case of the high-power electron cyclotron current drive (ECCD) employed in TCV, a significant fast electron population is generated with energies up to $E \approx 100$ keV or more (to be compared with bulk plasma temperatures of a few to several keV). The physics of heating and current drive is intimately tied to the dynamics of this suprathermal population, and the study of suprathermal electron dynamics can accordingly provide valuable insight into the properties of CD, particularly its deposition location and efficiency. The issue of suprathermal electron transport is a particularly crucial one, as it strongly influences both the total driven current and the current density profile.

The goal of this thesis work is to advance the fundamental understanding of the physics of EC wave-particle interaction and ECCD, both through experimental measurements and through numerical modeling. A basic introduction to these concepts and to the main diagnostic and numerical tools available is provided in chapters 3, 4 and 5.

From a diagnostic point of view, an especially valuable means of probing the suprathermal electron population is the study of the non thermal part of the bremsstrahlung plasma emission, due to collisions of suprathermal electrons with background ions and falling in the so called hard X-ray (HXR) region of the electromagnetic spectrum. A large fraction of this thesis work has been devoted to the design and development of a novel spectroscopic multi-camera system (Hard X-Ray tomographic Spectrometer, or HXRS) to provide the first 2D tomographic reconstruction

of HXR emission from a noncircular plasma with high space resolution. Section 7 of this manuscript reports on the diagnostic development of the HXRS system for TCV, including the construction and commissioning of the first camera in the system. In section 8 the initial experimental results obtained are reviewed and discussed.

In parallel with this experimental work, extensive modeling was conducted for this thesis. Firstly, modeling was performed to aid in the diagnostic design, to assist the planning of the exploitation of the new diagnostic and then for direct comparison with the initial experimental data. Additionally, a specific and especially representative problem was selected for investigation and for comparison with experiments carried out in the TCV tokamak, with measurements provided by a previous single-view HXR camera.

The modeling tools used in this work are the recently developed Fokker-Planck (FP) code LUKE [13], coupled with the C3PO ray-tracing module [14] and the R5-X2 bremsstrahlung calculator [15], described in section 4.2. The modeling allows for electrostatic- and electromagnetic-driven anomalous transport. The code suite has been integrated in the TCV environment and benchmarked with pre-existing simulation tools such as the TORAY-GA ray-tracing code [16] with the Cohen module for current drive [17] and the CQL3D FP code [18]. The specific problem investigated with this modeling suite is the analysis of a series of TCV experiments devised to study the synergistic absorption of electron cyclotron X-mode waves at two different harmonics (2nd and 3rd), particularly through the dynamics and transport properties of the suprathermal electron population generated primarily by 2nd harmonic absorption and its influence on the 3rd harmonic wave absorption. The primary experimental tool employed in this study, providing data that could be directly compared with theoretical predictions, is a single hard X-ray camera. This work is discussed in section 6.

2 The TCV experiment

2.1 TCV vessel and plasma configurations

The Tokamak à Configuration Variable (TCV) [19] is a medium size, highly elongated tokamak. It started operation in 1992 with the main aim to investigate the effect of plasma shape on confinement and stability. TCV was designed to produce a large variety of plasma shapes without requiring hardware modifications. The main machine parameters are summarized in Table 2. 1.

Parameter	Symbol	Value
Major radius	R_0	0.88 m
Minor radius	a	0.25 m
Aspect ratio	$\epsilon = R_0/a$	≈ 3.5
Vacuum vessel elongation	κ_{TCV}	2.9
Toroidal field on axis	B_0	< 1.54 T
Plasma current	I_p	< 1 MA
Loop voltage	V_{loop}	≤ 10 V
Additional heating power (ECH)	$P_{ECH,X2}$	2.8 MW
	$P_{ECH,X3}$	1.4 MW
Discharge duration		< 4 s

Table 2. 1: Main TCV machine parameters

The control coil set, comprising the poloidal coils and the fast internal coils (D and F coils in Figure 2.1), all independently powered, enable flexible shaping including very high elongation. The internal coils are necessary to reach the highest elongations as these result in a fast-growing vertical instability that must be suppressed by feedback control of the coil currents. The resistive vessel penetration time is too long for external coils to control this instability.

TCV has produced a wide range of limited, single null diverted (SND) and double null diverted (DND) discharges as shown in Fig. 2.2(a-d). Plasma currents up to 1MA have been attained, Fig. 2.2(e), and purely wave driven currents up to 210 kA have been achieved, Fig. 2.2(f). The plasma shapes span a wide parameter range with exotic configurations such as the “pear” and doublet shapes, elongations (κ) from 1 to 2.8, triangularity (δ) from -0.8 to 0.9, Figure 2. 2(g – l).

TCV remains an important test bed for new magnetic configurations. Recently a new magnetic topology, the so-called snowflake divertor configuration, has been experimentally obtained for the first time in the magnetic confinement community (Figure 2. 3) [20]. The main feature of this magnetic topology is the presence of a four-

leg divertor that promises to optimize the exhaust and plasma–wall interaction at a level that can be handled safely by first wall materials.

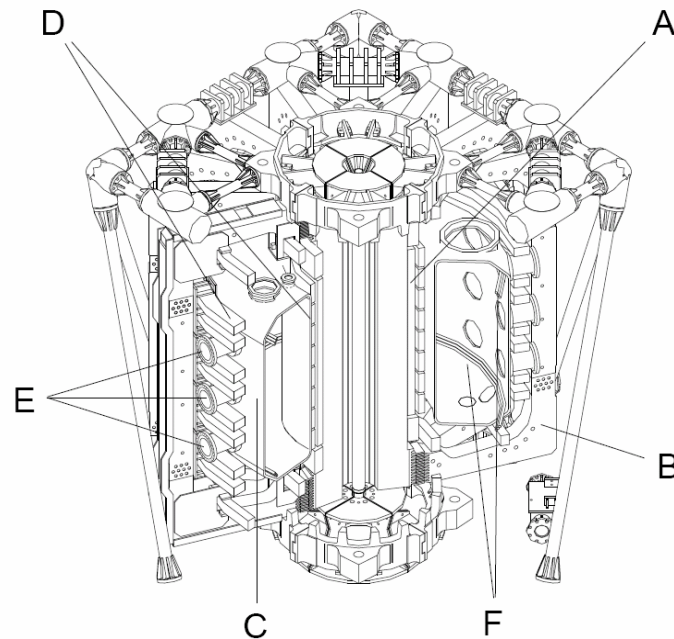


Figure 2.1 Schematic view of TCV showing the Ohmic transformer primary solenoid (A), the toroidal field coils (B), the vacuum vessel (C), the poloidal field coils (D), a selection of diagnostic ports (E) and the internal control coils (F).

2.2 First wall

The internal surface of the stainless steel vacuum vessel has to meet the demands of the variety of possible configurations, with wall components required to play the role of both limiter and divertor surfaces. Therefore, 90% of the internal surface is covered with 24 mm thick graphite tiles, designed to withstand the large power fluxes during EC heating and minimize plasma contamination by metallic impurities. Standard vessel conditioning techniques consist of baking out the vessel up to a temperature of 250°C and boronising the wall 2-3 times a year. During operation the typical base vacuum pressure is less than 10^{-8} mbar. Helium glow discharge cleaning is regularly used between tokamak discharges as a means of controlling the short-term evolution of surface properties.

2.3 Plasma heating

Owing to the resistivity of the plasma the toroidal plasma current also heats the plasma, the Ohmic heating power density being $P_{O-H} = \eta j^2$. However, the plasma resistivity η decreases with increasing temperature as $T^{-3/2}$, and purely Ohmic heating has proved to be insufficient for reaching the necessary temperature for a fusion reactor. Supplementary heating methods are therefore required.

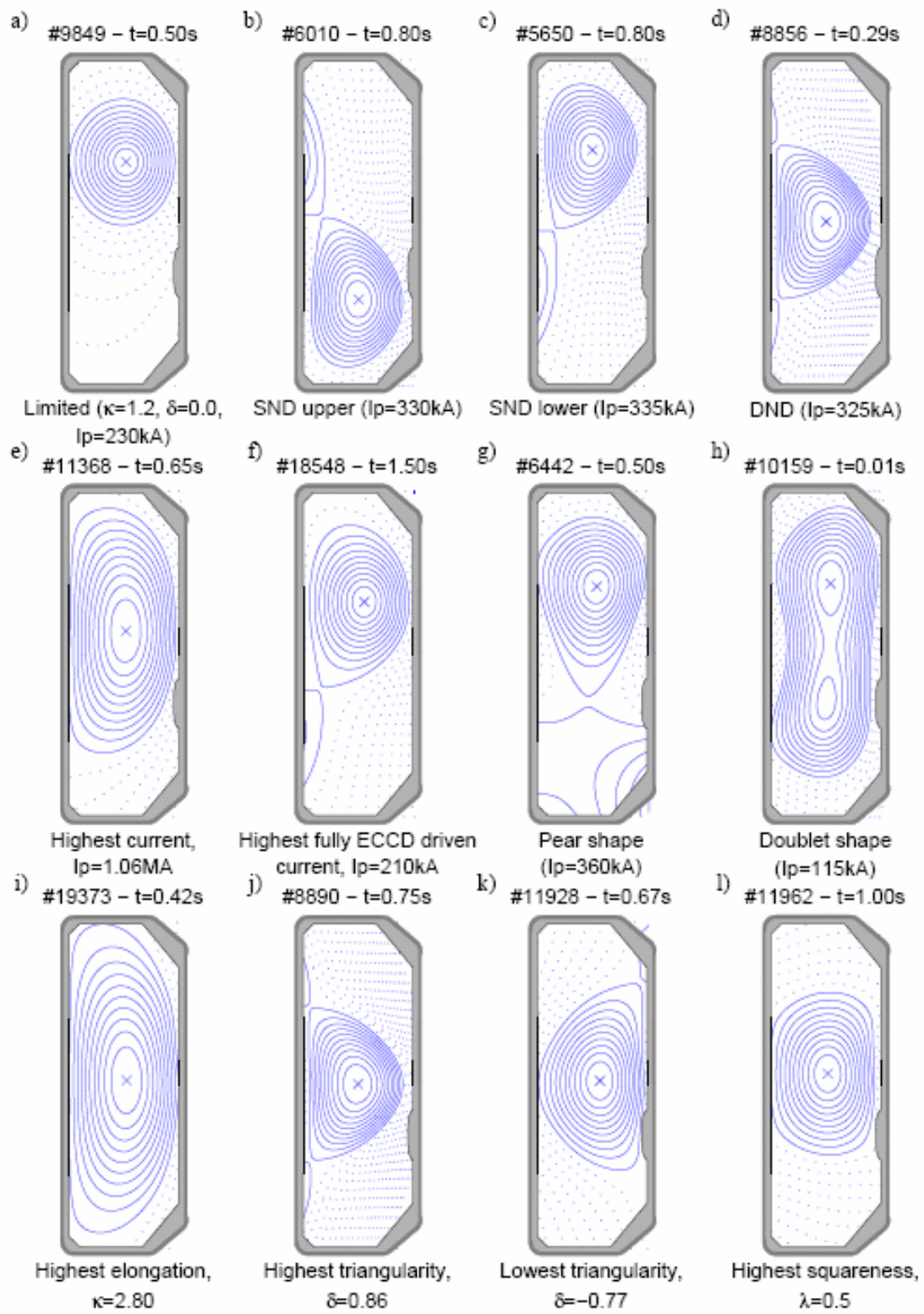


Figure 2. 2 Various plasma configurations and shapes achieved in TCV

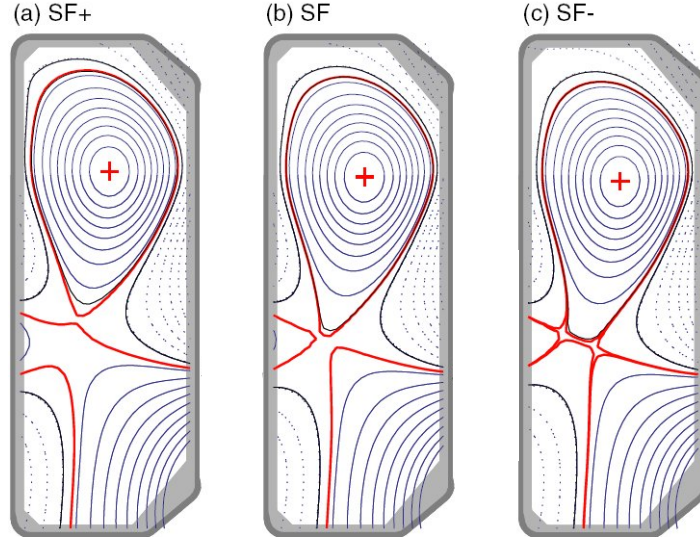


Figure 2.3 (b) Snowflake and (a, c) snowflake-like configurations in TCV. The red lines denote the separatrix.

One such heating method consists of injecting energetic particle beams of neutral hydrogen or deuterium into the plasma. The neutral particles travel unaffected by the magnetic field until they interact by collisions and ionize inside the plasma, where they remain confined by the magnetic field and transfer their energy collisionally to the plasma. No heating beams are installed at present on the TCV tokamak.

An alternative heating method consists of launching electromagnetic waves into the plasma. A variety of electromagnetic waves can propagate in magnetized plasmas and can be absorbed when particular resonance conditions are met. The waves can thus transfer energy to the plasma. Among the absorption schemes adopted successfully in tokamak devices are ion and electron cyclotron resonance heating (ICRH and ECRH). The respective fundamental resonance angular frequencies are:

$$\omega_{ci} = \frac{q_i B}{m_i} \quad , \quad \omega_{ce} = \frac{eB}{m_e}$$

The small electron-ion mass ratio implies that $\omega_{ci} \ll \omega_{ce}$. Resonant absorption can occur also at harmonics of the cyclotron frequencies. Another resonant wave particle interaction can occur at an intermediate frequency $\omega_{LH} \approx (\omega_{ci} \cdot \omega_{ce})^{1/2}$, the so called lower-hybrid (LH) frequency. Ion cyclotron frequencies in tokamaks are typically in the MHz range, from 20 MHz upwards, while the electron cyclotron frequencies are approximately three orders of magnitude higher ranging up to 200 GHz. Lower hybrid frequencies are in the order of a few GHz. The magnetic field dependence of these resonances generally allows for fairly localized heating thanks to the spatial variation of the magnetic field in a

toroidal device. The physics of resonant wave-particle interaction will be discussed in more detail in the next chapter.

In particular, TCV is equipped with a very flexible electron cyclotron heating (ECH) and electron cyclotron current drive (ECCD) system (see Figure 2. 4), which was designed to be compatible with a wide range of plasma shapes [21]. The system consists of six X2 gyrotrons for heating at the second harmonic of the electron cyclotron resonance ($f_{2ce} = 82.7$ GHz), and three X3 gyrotrons for heating at the third harmonic ($f_{3ce} = 118$ GHz). These frequencies correspond to near central heating for a toroidal field of 1.45 T. The nominal power delivered to the plasma is 465 kW for each of the X2 gyrotrons and 480 kW for each of the X3 gyrotrons, resulting in a total power of 4.2 MW for a maximum pulse length of 2s.

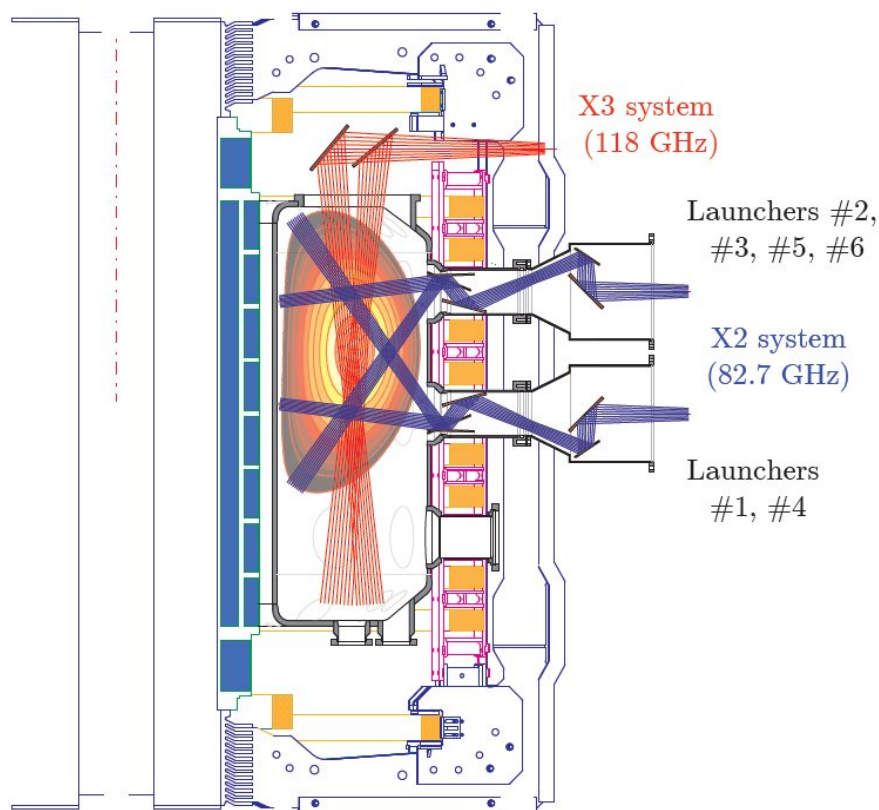


Figure 2. 4 Schematic view of the X2 and X3 launching systems on TCV

Each gyrotron is coupled through a matching optics unit (MOU) to an evacuated transmission line, through which the beam propagates to a quasi-optical launching antenna installed on the tokamak. The polarization of each beam can be modified through manipulation of the optics in the MOU and is usually set for propagation as an extraordinary wave (in case of propagation perpendicularly to the magnetic field B , this corresponds to the wave's electric field being also perpendicular to B), because of its better absorption properties. Each X2 launcher allows for a poloidal or toroidal variation

of the launching angle. The EC injection angle can be varied by the real-time feedback control system providing an extremely powerful tool for control of crucial plasma parameters such as the plasma current and shape, opening the possibility for MHD instability control and/or suppression [22].

3 Plasma current drive in tokamaks by wave-particle interaction

3.1 Introduction

Different methods of non inductive current drive have been implemented in tokamak machines acting both on electrons and ions. Such methods are based mainly on neutral beam injection and wave-particle interactions.

In this section we introduce the basic concepts of the plasma current drive by wave-particle interactions. The focus is on the electron cyclotron (EC) method, which is used in the TCV tokamak to sustain a non-inductive current [23].

TCV experiments have shown that a considerable fraction of the total plasma current can be carried by the bootstrap mechanism in ITB scenarios [24], indeed up to 100% [25].

3.2 The resonance condition

One possible mechanism for wave-driven current generation is the development of an asymmetry in the ion or electron distribution functions in the toroidal direction, imparting net toroidal momentum to the plasma current carriers (electrons and/or ions): this occurs in the case of the Alfvén and lower-hybrid methods. Another mechanism for inducing a net toroidal current, which generally occurs concomitantly with the former, is the generation of an imbalance in the electron distribution function without direct injection of toroidal momentum: this is the only mechanism at play in the case of electron cyclotron current drive (ECCD) [26].

Lower-hybrid current drive (LHCD) is a commonly applied technique because of its high efficiency. The particular resonance used is named “hybrid” as it involves both electron and ion dynamics; indeed, the LH frequency (ω_{LH}) is linked to the ion plasma frequency (ω_{pi}) and both the electron and ion cyclotron frequencies through the relation

$$\frac{1}{\omega_{LH}^2} = \frac{1}{\omega_{pi}^2} + \frac{1}{\omega_{ci}\omega_{ce}}$$

The asymmetry in the electron distribution function resulting from an increase in the parallel momentum of the resonant fast electrons is exemplified in Figure 3.1.

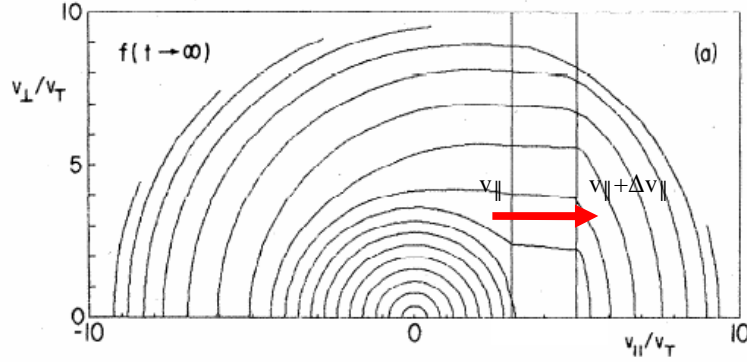


Figure 3.1 Lower hybrid current drive: the electric field induced by the LH wave increases the parallel velocity of the resonant electrons from v_{\parallel} to $v_{\parallel} + \Delta v_{\parallel}$ thus inducing a net current $j_{\text{LH}} = n_e e \Delta v_{\parallel}$. Fokker-Planck numerical calculation from Karney and Fisch (1979) [27].

The wave-particle resonant interaction in an unmagnetized plasma is based on the Landau resonance condition:

$$\omega - \mathbf{k} \cdot \mathbf{v} = 0 \quad (3.1)$$

here ω and \mathbf{k} are the wave angular frequency and the wave vector, respectively, and \mathbf{v} is the resonant particle velocity.

If the particle is subject to an external magnetic field \mathbf{B} , cyclotron resonances occur at all harmonics of the electron cyclotron frequency. The particle velocity can be decomposed into a parallel (v_{\parallel}) and a perpendicular (v_{\perp}) component relative to \mathbf{B} . The electron cyclotron resonance condition is:

$$\omega - k_{\parallel} v_{\parallel} - \frac{\ell \Omega_0}{\gamma} = 0 \quad (3.2)$$

where $\Omega_0 = q_e B / m$ is the particle's cyclotron angular frequency, ℓ is an integer defining the harmonic number and γ is the Lorentz relativistic factor.

Effective ECCD is predicated on preferential heating of electrons whose parallel velocity is finite and oriented in a given direction. The optimization of current drive results from complex velocity-space dynamics. The collisional cross section decreases as the relative speed of the colliding particles increases ($\sigma_c \propto 1 / v_{ei}^3$); therefore suprathermal electrons ($v_{st} \gg v_T$) are less collisional than thermal electrons and can carry current for longer times. Additionally, electrons with high parallel velocities are less likely to be trapped in so called "banana" orbits and to become unable to carry current. The advantage in preferentially heating these high parallel-velocity electrons is counterbalanced, however, by the rapid decrease in their numbers as energy increases.

It is worth noting that in a tokamak magnetic configuration, according to Eq. 3.2, for a given frequency, particles with higher perpendicular energy resonate at inner radial

positions (smaller R), i.e. on the high-field side (HFS) of the cold resonance. This is known as the “relativistic downshift” of the frequency.

3.3 Electron cyclotron current drive

Electron cyclotron wave injection has proven to be a very efficient way to induce current in tokamaks; in particular the highly localized deposition of the electron cyclotron power in the plasma makes this method well suited for current profile tailoring and for the control and/or suppression of MHD instabilities such as sawtooth crashes [12] and neoclassical tearing modes (NTM) [28].

In order to preferentially excite electrons having a specific sign of the parallel velocity v_{\parallel} , according to Eq. 3.2, the electron cyclotron waves are injected into the plasma with a finite tangential component ($k_{\parallel} \neq 0$). The electron current drive mechanism relies on the Fisch-Boozer effect, which is based on the generation of an asymmetric resistivity in the distribution function without directly imparting parallel momentum [29]. This effect is obtained by increasing the perpendicular velocity of the electrons moving in a given direction relative to the main toroidal magnetic field (left or right in Figure 3.2). The accelerated electrons are less collisional than the “hole” they leave behind, and therefore their slowing-down takes longer than the filling of the hole. In this way a net current is generated. The parallel momentum conservation is guaranteed by the collisional shift of the ion population in the opposite direction relative to the accelerated electrons, thus contributing a very small fraction (equal to the electron-ion mass ratio) of the total induced current.

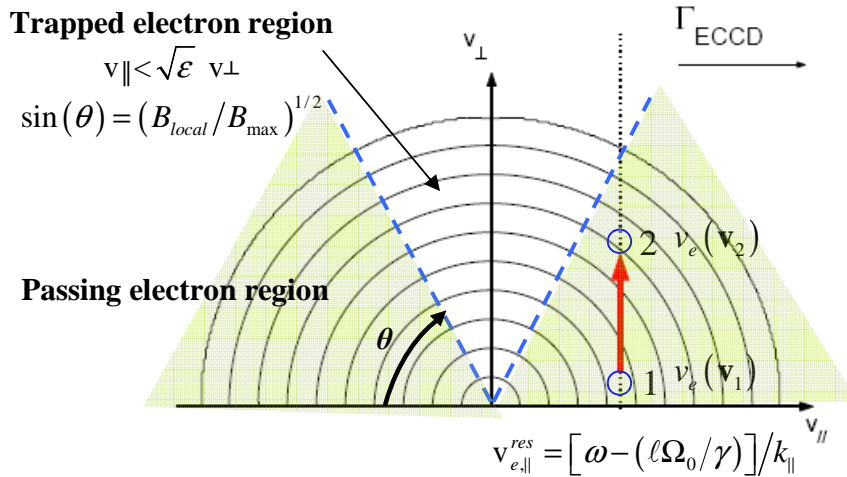


Figure 3.2 Fisch-Boozer current drive mechanism.

Figure 3.2 visually illustrates the Fisch-Boozer current drive mechanism. The cyclotron wave pushes the resonant electrons in the perpendicular direction. The resonant electrons

have a velocity satisfying the resonance condition: $v_{\parallel} = [\omega - (\ell\Omega_0/\gamma)]/k_{\parallel}$. The EC absorption results in a displacement of a certain number of electrons from position 1 (having $v=v_1$) to 2 (having $v=v_2 \cong \sqrt{v_1^2 + \Delta E/2m_e}$) in velocity space. Following the work of Alikaev and Parail [30], the EC induced current can be expressed with the formula: $j = \frac{e\mathbf{v}_1 P_d^{EC}}{\Delta E v_e(\mathbf{v}_2)} \left(1 - \frac{v_e(\mathbf{v}_2)}{v_e(\mathbf{v}_1)} \right)$, where P_d is the EC power density. The current drive arises from the difference in collisionality ν , in this case $j>0$ since $v_e(\mathbf{v}_2) < v_e(\mathbf{v}_1)$.

The Fisch-Boozer electron current drive efficiency η_{ECCD} [29] depends on the electron temperature T_e , density n_e , and on the plasma effective charge Z_{eff}

$$\eta_{ECCD} \equiv \frac{j_{EC}}{P_d^{EC}} \approx \frac{\epsilon_0^2}{\ln \Lambda R n_e e^3} \frac{T_e}{(Z_{eff} + 5)} \quad (3.3)$$

where $\ln \Lambda$ is the Coulomb logarithm ($\ln \Lambda \sim 15$), R is the plasma major radius and ϵ_0 is the vacuum permittivity.

Different factors can influence the ECCD efficiency:

- Toroidal effect

In a tokamak the main toroidal magnetic field increases in magnitude from the LFS to the HFS, thus a region exists in velocity space where electrons having, at the outermost point in their orbit, $v_{\parallel} < \sqrt{\epsilon} v_{\perp}$ ($\epsilon=r/R$ being the inverse aspect ratio of a given flux surface) are trapped, bouncing back and forth along “banana” orbits. Such trapped particles do not contribute to the plasma current; thus any cyclotron absorption occurring in this region results in a loss of current drive efficiency.

Even when the power deposition occurs outside the trapped electron region, it can happen that the EC wave absorption pushes part of the resonant electrons from the passing region into the trapped one. This not only reduces the current drive efficiency but can even result in a current component that runs contrary to the desired one. Indeed, because of the fast bounce motion ($v_{ei} < v_b$), the distribution function is rapidly symmetrized inside the trapped region, and symmetric detrapping occurs on both sides of the trapped region boundaries (positive and negative v_{\parallel}). Asymmetric trapping followed by symmetric detrapping can therefore generate a net current in the opposite direction (as depicted in Fig. 3.3). This is known as the Ohkawa effect [31]. As expected, this effect becomes more important as the power deposition moves further off axis on the LFS. Many experiments both in tokamak and stellarators have documented a degradation of the ECCD efficiency as the EC power deposition moves from the core toward the plasma LFS periphery [32, 33]. The Ohkawa effect may even dominate under some conditions [34]. It should be stressed, however, that an unambiguous demonstration of the Ohkawa effect has not yet been obtained.

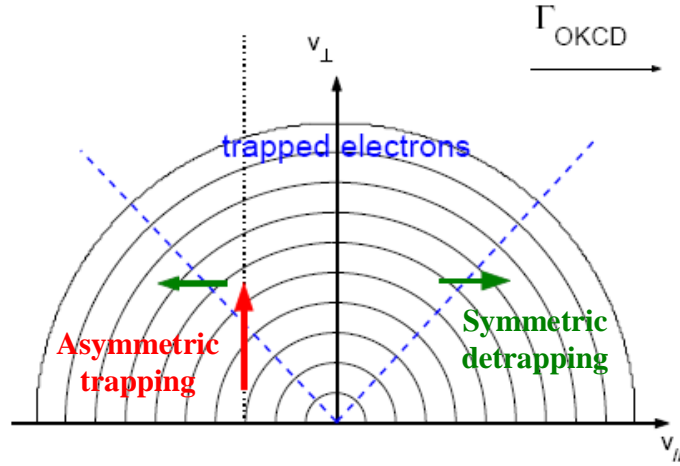


Figure 3.3 Ohkawa current drive mechanism

o Relativistic effects

The wave particle interaction in velocity space has an elliptical shape described by the equation [35]

$$\frac{v_{\perp}^2}{v_{Te}^2} + \left(1 + N_{\parallel}^2 \frac{\omega^2}{\ell^2 \Omega_{ce}^2}\right) \frac{v_{\parallel}^2}{v_{Te}^2} = \left(1 - \frac{\omega^2}{\ell^2 \Omega_{ce}^2}\right) \frac{c^2}{v_{Te}^2} + 2N_{\parallel} \frac{\omega^2}{\ell^2 \Omega_{ce}^2} \frac{c}{v_{Te}} \frac{v_{\parallel}}{v_{Te}} \quad (3.4)$$

where $N_{\parallel} = ck_{\parallel}/\omega$ is the parallel refractive index of the injected wave. In the limit $v/c \rightarrow 0$, the ellipse reduces to a straight vertical line in velocity space (the ellipse's foci are at infinity) with $v_{e,\parallel}^{res} = (\omega - \ell\Omega_0)/k_{\parallel}$. In the limit $N_{\parallel} = 0$, the resonance curve becomes a circle (centered in zero): this is the case of pure ECH (Fig. 3.4a), in which no net current is generated. The general case (for $\ell = 1$ and $\omega/\Omega_{ce} = 1$) is illustrated in Fig. 3.4b. To maximize the current drive efficiency, it is preferable to distance the resonance curve from the trapped region. Fig. 3.4c illustrates this mechanism; electrons satisfying $\omega/\Omega_{ce} < 1$ resonate on the HFS of the cold resonance while the condition $\omega/\Omega_{ce} > 1$ corresponds to wave absorption by resonant electrons on the LFS of the cold resonance. The latter condition is most effective for current drive.

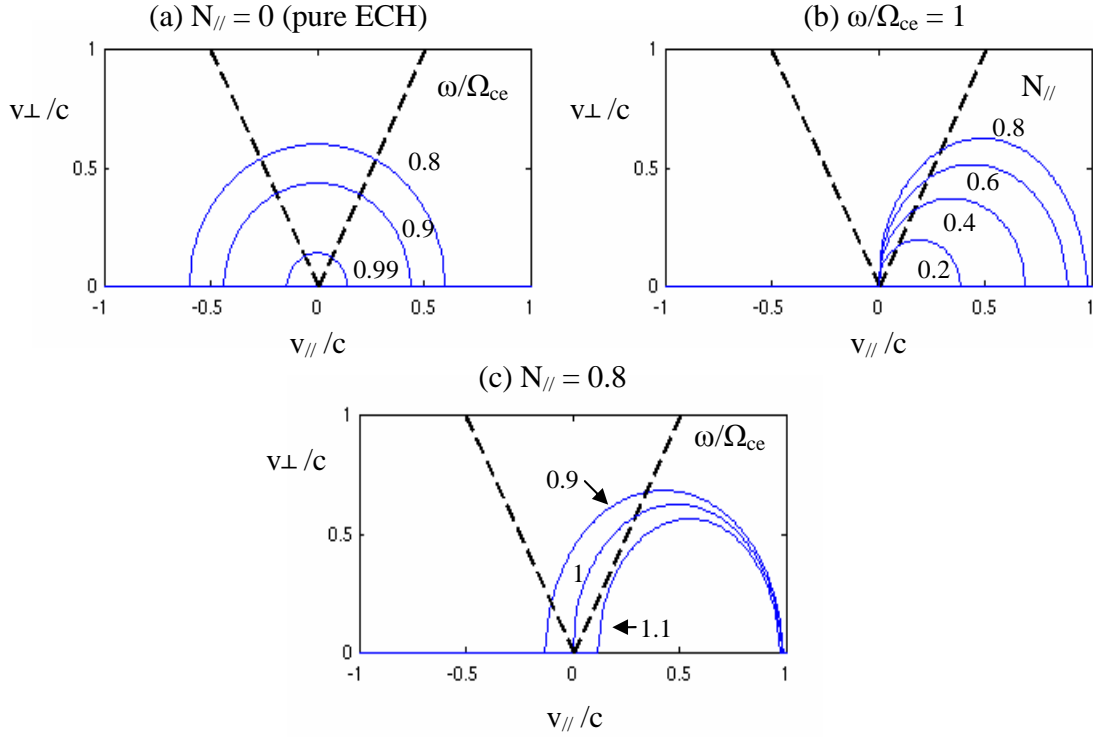


Figure 3. 4 Resonance curves (a) for $N_{\parallel}=0$, pure ECH, (b) for different values of $N_{\parallel}>0$ at a fixed value of $\omega/\Omega_{ce} = 1$ and (c) for different values of ω/Ω_{ce} at fixed value of $N_{\parallel}=0.8$.

When the resonance curves are plotted as functions of the velocity normalized to the thermal velocity v_t , their curvature will increase with temperature, as illustrated by Fig. 3.5. This bending can reduce the interaction with the trapped electron region. Additionally, as either temperature or density increases, more and more particles are resonant farther away from the cold resonance, shifting the absorption region outwards and broadening it at the same time. This results in beneficial current drive properties for increasing beta, especially for off-axis power deposition [32,36]. It must be remembered, however, that while the dependence of the current drive efficiency on temperature is also monotonically increasing, it is inversely proportional to density (Eq. 3.3).

o Toroidal injection angle

The ECCD efficiency depends on the parallel refractive index $N_{\parallel} = ck_{\parallel}/\omega$. This is understood as follows: as N_{\parallel} increases, the EC wave at a given location resonates with higher energy electrons (Fig. 3.4 b), which are more effective in carrying current; however as this effect competes with the decrease in the number of electrons at high energy, this will result in an optimum finite value of N_{\parallel} , i.e. an optimum angle for toroidal EC injection.

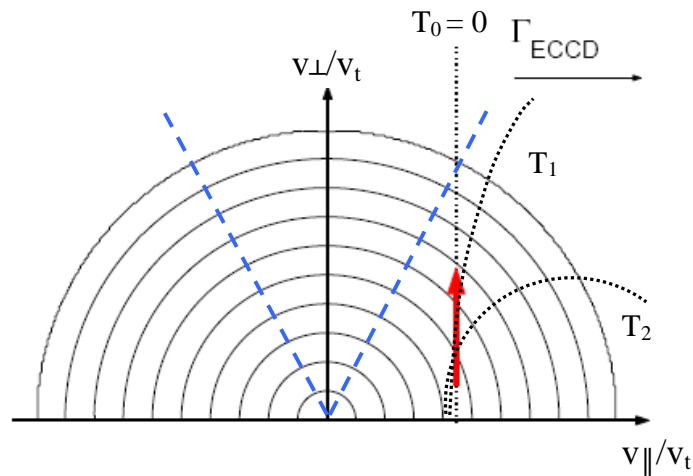


Figure 3.5 Relativistic effect on the resonant region in phase space for different plasma temperatures $T_0 = 0 < T_1 < T_2$.

As a concluding remark on the LH and EC current drive methods, we point out that LHCD displays an overall current drive efficiency typically one order of magnitude higher than ECCD; the latter however has the advantage of being more localized, and thus well suited for current drive tailoring and MHD control. In some cases ECCD and LHCD have been applied simultaneously to a tokamak plasma. In a Tore Supra experiment the results showed an increase of up to a factor four in the ECCD efficiency over the linear value. This effect is predicted by kinetic theory and results from a favorable interplay between the two waves. The electron cyclotron wave in fact accelerates electrons out of the Maxwellian bulk by pumping electrons in the phase space region where the LH wave drives them to higher parallel velocity [37].

The possible coupled synergistic LH-ECCD absorption in ITER has been studied by A. Polevoi et al [38] to explore the possibility of enhancing the CD efficiency in long pulse ITER scenarios. In this study, the predicted synergistic improvement in the current drive efficiency is less than 10%; the role of the synergy is thus only marginal.

4 Fokker-Planck modeling of the electron distribution function

4.1 The Fokker-Planck approach to the problem

Owing to the impracticability of a single particle description of a tokamak plasma, statistical (probabilistic) approaches have been developed, generally solving a time evolution equation for the particle distribution function $f(\mathbf{x}, \mathbf{v}, t)$. The basic concepts of the kinetic treatment, quasilinear theory, drift-kinetic equation, and Fokker-Planck equation are introduced in this section. For a more detailed treatment of these topics the reader is addressed to the appropriate literature references.

4.1.1 The Vlasov and Boltzmann equations

Maxwellian plasmas are adequately treated with fluid equations, describing the evolution of various velocity-space moments of the particle distribution function, which depend only on the configuration space coordinates $\mathbf{x} = (x, y, z)$ and on time.

However, the interaction of high-power electromagnetic waves with the plasma can distort the distribution function significantly from the Maxwellian, which invalidates the fluid approach. The physics of high-power wave-particle interaction in a magnetized plasma is more appropriately described by kinetic theory. The force acting on electrons and ions is due to the self consistent electric (\mathbf{E}) and magnetic (\mathbf{B}) fields that they experience. In the kinetic formalism the total electric and magnetic fields are usually expressed with a first order perturbative expansion:

$$\begin{aligned}\mathbf{E} &= \mathbf{E}_0(\mathbf{x}, t) + \mathbf{E}_1(\mathbf{x}, t) \\ \mathbf{B} &= \mathbf{B}_0(\mathbf{x}, t) + \mathbf{B}_1(\mathbf{x}, t)\end{aligned}\tag{4.1}$$

where \mathbf{E}_0 and \mathbf{B}_0 are the averaged, macroscopic components and $|\mathbf{E}_1(\mathbf{x}, t)| \ll |\mathbf{E}_0(\mathbf{x}, t)|$, $|\mathbf{B}_1(\mathbf{x}, t)| \ll |\mathbf{B}_0(\mathbf{x}, t)|$ are microscopic fluctuating components, due for instance to an externally injected electromagnetic wave. The averaged \mathbf{E}_0 and \mathbf{B}_0 fields obey Maxwell's equations

$$\begin{aligned}\nabla \times \mathbf{B}_0 &= \frac{1}{c} \frac{\partial \mathbf{E}_0}{\partial t} + \frac{4\pi}{c} \mathbf{j} \\ \nabla \times \mathbf{E}_0 &= -\frac{1}{c} \frac{\partial \mathbf{B}_0}{\partial t} \\ \nabla \cdot \mathbf{B}_0 &= 0 \\ \nabla \cdot \mathbf{E}_0 &= 4\pi\rho\end{aligned}\tag{4.2}$$

\mathbf{j} being the current density and ρ the charge density. In the collisionless (hot plasma) limit, the time evolution of the particle distribution function is described by the Vlasov equation

$$\frac{df_\alpha}{dt} = \frac{\partial f_\alpha}{\partial t} + \mathbf{v} \cdot \nabla_{\mathbf{x}} f_\alpha + \frac{q_\alpha}{m} [\mathbf{E} + \mathbf{v} \times \mathbf{B}] \cdot \nabla_{\mathbf{v}} f_\alpha = 0 \quad (4.3)$$

where $\alpha = e, i$ for electrons and ions, respectively. Macroscopic quantities, such as the particle density, the current density and the kinetic energy, for each species, are obtained from the velocity moments of f :

$$\begin{aligned} n_\alpha(\mathbf{x}, t) &= \int f_\alpha(\mathbf{x}, \mathbf{v}, t) d\mathbf{v} \\ \mathbf{j}_\alpha(\mathbf{x}, t) &= eZ_\alpha \int \mathbf{v} f_\alpha(\mathbf{x}, \mathbf{v}, t) d\mathbf{v} \\ E_{kin,\alpha}(\mathbf{x}, t) &= m_\alpha c^2 \int (\gamma_\alpha - 1) f_\alpha(\mathbf{x}, \mathbf{v}, t) d\mathbf{v} \end{aligned} \quad (4.4)$$

The occurrence of Coulomb collisions between charged particles must be taken into account for a more realistic description of the charge particle kinetics in a plasma. By including a term describing the modification of the distribution function as a consequence of collisional effects, the Vlasov equation takes the form of the so-called Boltzmann (also Vlasov-Boltzmann) equation

$$\frac{df_\alpha}{dt} = \frac{\partial f_\alpha}{\partial t} + \mathbf{v} \cdot \nabla_{\mathbf{x}} f_\alpha + \frac{q_\alpha}{m} [\mathbf{E} + \mathbf{v} \times \mathbf{B}] \cdot \nabla_{\mathbf{v}} f_\alpha = \left. \frac{\partial f_\alpha}{\partial t} \right|_c \quad (4.5)$$

the term on the right hand side defining the rate of change of the distribution function f due to collisions.

The quantity $N_p = \int f(\mathbf{x}, \mathbf{v}, t) d\mathbf{x} d\mathbf{v}$ represents the total number of particles in the system at a given time t . The equation for f must respect the conservation of the main physical quantities: number of particles, momentum, and energy. In the limit of a stationary thermal plasma the solution of Eq. 4.5 is the Maxwellian distribution: $f(\mathbf{x}, \mathbf{v}, t) = f_M$. In the present treatment we consider only the electron component of the plasma, hence in the remainder of this thesis work we shall restrict ourselves to the notation $f = f_e$.

4.1.2 The guiding center approximation

In a strongly magnetized plasma, assuming that the scale length of any field inhomogeneity is larger than the Larmor radius of all charged particles (small gyroradius limit: $\rho_L \ll |\mathbf{B}/\nabla\mathbf{B}|$), the usual 7-D problem (3D in configuration space, 3D in velocity space, 1D in time), for the determination of the particle distribution function can be

reduced to a 6D problem by averaging over the fast gyromotion time scale. In this approximation, the position of the particle in physical space is identified by the coordinates of its guiding center \mathbf{x}_{gc} , while its velocity \mathbf{v}_{gc} vector can be decomposed into a parallel and a perpendicular components with respect to the main magnetic field

$$\begin{aligned}\mathbf{b} &= \mathbf{B} / B \\ \mathbf{v}_{\parallel} &= (\mathbf{b} \cdot \mathbf{v}_{gc}) \mathbf{b} \\ \mathbf{v}_{\perp} &= \mathbf{v}_{gc} - \mathbf{v}_{\parallel}\end{aligned}\quad (4.6)$$

where \mathbf{b} is the unit vector in the local magnetic field direction (Fig. 4.1). In the remainder of this chapter we adopt the notation $\mathbf{x} = \mathbf{x}_{gc}$.

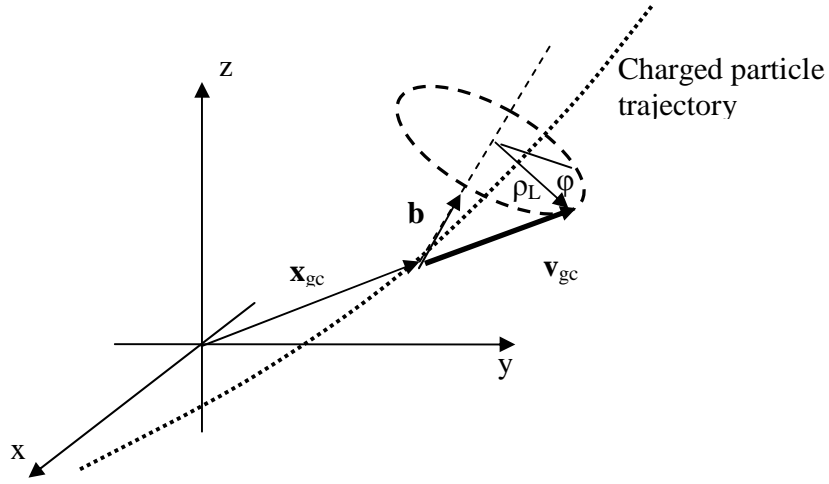


Figure 4.1 Charged particle velocity decomposition in the guiding center reference

The parallel guiding center velocity describes the fast streaming along the magnetic field lines, whereas the perpendicular velocity describes a slow drift motion (\mathbf{v}_D) generated by curvature drift ($\nabla \mathbf{B}$) and by changes in the magnetic field magnitude ($B(R) = B_0/R$) typical of a tokamak configuration. In a constant magnetic equilibrium and in the absence of an external electric field, this drift velocity is given by [39]

$$\mathbf{v}_D = \frac{1}{\Omega_{ce}} \left(\mathbf{v}_{\parallel}^2 + \frac{\mathbf{v}_{\perp}^2}{2} \right) \frac{\mathbf{B} \times \nabla B}{B^2} \quad (4.7)$$

4.1.3 The Drift Kinetic Equation (DKE)

Using the guiding-center approximation in the small gyroradius limit, the kinetic equation (Eq. 4.5) reduces to the drift kinetic equation for the gyro-averaged distribution $\bar{f} = \langle f \rangle_{\varphi}$,

where $\langle \bullet \rangle_\varphi = (2\pi)^{-1} \int_0^{2\pi} d\varphi$ indicates the average on the gyro-angle φ (see Fig. 4.1). The Fokker-Planck form of the drift-kinetic equation is

$$\frac{\partial \bar{f}}{\partial t} + \mathbf{v}_{gc} \cdot \nabla \bar{f} = C(\bar{f}) + Q(\bar{f}) + E(\bar{f}) \quad (4.8)$$

where the terms on the right-hand side account for the physical phenomena affecting the distribution function f , namely, the collisional drag ($C(f) = \left. \frac{\partial f}{\partial t} \right|_c$), the wave-induced quasilinear diffusion in velocity space (Q) and the electric field convection (E). The meaning of these terms will be discussed further in the following sections. To simplify the notation, we adopt henceforth $f = \bar{f}$.

To guide the physical interpretation of the processes involved in the kinetic treatment, we briefly discuss here the main time scales involved in the solution of Eq. 4.8.

i) Parallel motion along the magnetic field lines (τ_b)

The characteristic time scale is the bounce or transit time, for trapped and passing particles respectively, defined by the following integral over the particle (gyro-center) orbit

$$\left\langle \tau_b = \oint \frac{dl_B}{v_{\parallel}} \right\rangle \quad (4.9)$$

where l_B is the arc length along the magnetic field line and the average is taken over the distribution function.

ii) Drift motion across magnetic flux surfaces (τ_d)

The drift time scale is a measure of the gyro-center motion in the radial direction. It is defined as the average time employed by particles to cover a radial distance of the order of the plasma minor radius a_p [40]

$$\tau_d \simeq \frac{2\pi R_p a_p}{v_T \rho_L} \frac{B}{B_\phi} \quad (4.10)$$

where R_p is the plasma major radius, v_T is the thermal velocity, ρ_L the particle Larmor radius and B_ϕ is the magnetic field component along the toroidal direction.

iii) Collision time (τ_c)

The collision time represents the average time scale for the deflection of a particle from its unperturbed trajectory by an angle $\pi/2$, through the accumulation of many small deflections, and is given by the formula [39]

$$\tau_c = v_c^{-1} = \frac{4\pi\epsilon_0 m^2 v_T^3}{q^4 n \ln \Lambda} \quad (4.11)$$

where $\ln \Lambda$ is the Coulomb logarithm, a slowly varying function of the plasma temperature and density (n). The appropriate collision description in the DKE equation will be discussed later in terms of the Fokker-Planck operator (section 4.1.5).

iv) Quasilinear (QL) diffusion time scale

In quasilinear theory (section 4.1.4), the presence of radio frequency (RF) fields affects the distribution function by causing particles (mainly electrons) to diffuse in velocity space; the corresponding time scale is given by [40]

$$\tau_{QL} = \frac{p_{Te}^2}{D_{QL}} \quad (4.12)$$

where p_{Te} is the electron thermal momentum and D_{QL} the quasilinear diffusion coefficient in momentum space that will be discussed in the next section. The typical time scale of the quasilinear diffusion in TCV is of the order of milliseconds..

4.1.4 The quasilinear formalism and the RF diffusion operator

The quasilinear theoretical approach was initially developed to describe non-equilibrium processes in a plasma such as the growth rate of weak wave induced turbulence [41,42]. Other processes resulting in a distortion of the distribution function from the Maxwellian are properly described by this formalism; the wave-particle resonant absorption of the electron cyclotron wave is one such process.

The quasilinear theory is based on a perturbative approach to the solution of the collisionless kinetic equation (Vlasov description). The problem is split into a slow time scale, typical of the global equilibrium τ_{eq} , and a fast time scale, characteristic of the fast oscillation due to the perturbation τ_ω , with $\tau_\omega \ll \tau_{eq}$. Neglecting perturbative orders greater than the first, the global distribution function f can be expanded as follows

$$f(\mathbf{x}, \mathbf{v}, t) = f_0(\mathbf{v}, t) + f_1(\mathbf{x}, \mathbf{v}, t) \quad (4.13)$$

The zero-order component $f_0(\mathbf{v}, t) = \langle f(\mathbf{x}, \mathbf{v}, t) \rangle$ is the slowly varying equilibrium distribution function, where the average is taken over a time scale longer and spatial scale larger than the characteristic fluctuation scales.

The first order terms in Eqs. 4.1 and 4.13 are analyzed in Fourier space:

$$\begin{aligned} f_1(\mathbf{x}, \mathbf{v}, t) &= \frac{1}{(2\pi)^3} \int_{-\infty}^{\infty} \tilde{f}_k(\mathbf{v}, t) e^{i(\mathbf{k}\cdot\mathbf{x} - \omega t)} d\mathbf{k} \\ \mathbf{E}_1(\mathbf{x}, t) &= \frac{1}{(2\pi)^3} \int_{-\infty}^{\infty} \tilde{E}(\mathbf{k}, t) e^{i(\mathbf{k}\cdot\mathbf{x} - \omega t)} d\mathbf{k} \\ \mathbf{B}_1(\mathbf{x}, t) &= \frac{1}{(2\pi)^3} \int_{-\infty}^{\infty} \tilde{B}(\mathbf{k}, t) e^{i(\mathbf{k}\cdot\mathbf{x} - \omega t)} d\mathbf{k} \end{aligned} \quad (4.14)$$

At sufficiently high power, electron cyclotron heating and current drive cause a distortion in the zeroth-order distribution function (f_0). This takes the form of a diffusive process in velocity space, which tends to fill in the velocity gradient and leads to a flattening in the equilibrium distribution function $f_0(\mathbf{v})$ (the so called quasilinear flattening or plateau, see Fig. 4.2).

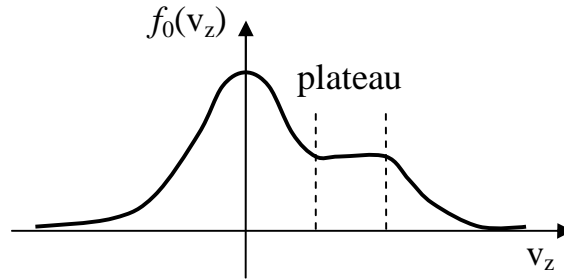


Figure 4.2 One-dimensional representation of the quasilinear plateau in the equilibrium distribution function.

We address now the problem of resonant diffusion in velocity space in the non-collisional limit (Vlasov description) to derive an equation for the quasilinear diffusion operator. We start from the decomposition of the electric and magnetic fields of Eq. 4.1, and the first-order decomposition for the equilibrium electron distribution function (Eq. 4.13). Assuming that no static \mathbf{E} field is present ($\mathbf{E}_0=0$), we can rewrite Eq. 4.3 in the form

$$\frac{\partial f_0}{\partial t} + \frac{q}{m} [\mathbf{v} \times \mathbf{B}_0] \cdot \nabla_{\mathbf{v}} f_0 = \frac{q}{m} \langle [\mathbf{E}_1 + \mathbf{v} \times \mathbf{B}_1] \cdot \nabla_{\mathbf{v}} f_1 \rangle \quad (4.15)$$

In this equation the variation of the zeroth-order f_0 is due to second-order terms appearing on the right-hand side of the equation; the $\langle \cdot \rangle_{\mathbf{v}}$ brackets denote volume averaging. The equation for the first order perturbation is

$$\begin{aligned} \frac{\partial f_1}{\partial t} + \mathbf{v} \cdot \nabla_{\mathbf{x}} f_1 + \frac{q}{m} [\mathbf{v} \times \mathbf{B}_0] \cdot \nabla_{\mathbf{v}} f_1 + \frac{q}{m} [\mathbf{E}_1 + \mathbf{v} \times \mathbf{B}_1] \cdot \nabla_{\mathbf{v}} f_0 = \\ \frac{q}{m} \left[(\mathbf{E}_1 + \mathbf{v} \times \mathbf{B}_1) \cdot \nabla_{\mathbf{v}} f_1 - \langle (\mathbf{E}_1 + \mathbf{v} \times \mathbf{B}_1) \cdot \nabla_{\mathbf{v}} f_1 \rangle \right] \end{aligned} \quad (4.16)$$

Second-order terms are present again on the RHS. Equation 4.16 is in general solved first and the f_1 solution is then inserted into Eq. 4.15 to solve for the slowly varying f_0 . By applying the Fourier decomposition (Eq. 4.14) to f_1 , \mathbf{E}_1 and \mathbf{B}_1 , we can write the diffusion equation in the form [43]

$$\frac{\partial f_0}{\partial t} = \nabla_{\mathbf{v}} \cdot (\mathbf{D}_{QL} \cdot \nabla_{\mathbf{v}} f_0). \quad (4.17)$$

An explicit formulation for the quasilinear diffusion operator, using a Bessel function expansion, can be found in [44]:

$$\mathbf{D}_{QL} = \sum_n \frac{q_e^2}{m_e^2} \int \frac{d\mathbf{k}}{(2\pi)^3} \frac{1}{V_p} \pi \delta[\omega(\mathbf{k}) - k_{\parallel} v_{\parallel} - n\Omega_e] \mathbf{a}_n^* \mathbf{a}_n \quad (4.18)$$

where V_p is the plasma volume, the sum is performed over n Bessel components, the integral is performed over the wave number \mathbf{k} and the delta function $\delta[\omega(\mathbf{k}) - k_{\parallel} v_{\parallel} - n\Omega_e]$ accounts for the resonant wave-particle interaction; for the form of the $\mathbf{a}^* \mathbf{a}$ terms in Eq 4.18 see [44, 45]

This non-collisional, quasilinear term accounts for the diffusion of charged particles in velocity space due to the wave perturbation. An exhaustive treatment of the quasilinear theory can be found in classic textbooks [46, 47].

4.1.5 The Fokker-Planck equation

As discussed in section 4.1.4, the physics of ECH and ECCD is best treated in the context of quasilinear theory. As the slowly varying equilibrium distribution function f_0 is intrinsically averaged over a long time scale (many oscillation periods), the effect of collisions must be taken into account in the kinetic equation. The collisional relaxation of charged particles in a plasma is governed by the long range Coulomb forces acting on them.

The Coulomb collisional operator that appears in the Fokker-Planck (FP) equation, Eq. 4.8, can be written as a sum over the species:

$$C_{\alpha,\beta} = \sum_{\beta} C_{FP}(f_{\alpha}, f_{\beta}) \quad (4.19)$$

describing the collisional drag of species α (in our case electrons) on particles of different species β (background ions and other higher Z impurities) having their respective mass m_β and atomic number Z_β . For economy of notation, in the following, we shall neglect the subscript α .

In the usual form the FP collision terms can be written

$$C_{FP}(f, f_\beta) = -\Gamma \frac{\partial f}{\partial \mathbf{v}} \cdot \left(f \frac{\partial H}{\partial \mathbf{v}} \right) + \frac{\Gamma}{2} \frac{\partial^2}{\partial \mathbf{v} \partial \mathbf{v}} : \left(f \frac{\partial^2 G}{\partial \mathbf{v} \partial \mathbf{v}} \right) \quad (4.20)$$

where $H(\mathbf{v}) = \sum_\beta Z_\beta^2 \left(\frac{m + m_\beta}{m_\beta} \right) \int \frac{f_\beta(\mathbf{v}_\beta)}{|\mathbf{v} - \mathbf{v}_\beta|} d\mathbf{v}_\beta$ and $G(\mathbf{v}) = \sum_\beta Z_\beta^2 \int |\mathbf{v} - \mathbf{v}_\beta| f_\beta(\mathbf{v}_\beta) d\mathbf{v}_\beta$

are the so called Rosenbluth potentials [48] and $\Gamma = -\frac{Z^2 e^4}{4\pi \epsilon_0^2 m^2} \ln \Lambda$.

The first term on the RHS of Eq. 4.20 has negative sign and corresponds to a dynamical friction that decelerates the species α . The second term is diffusive; it describes the collisional spread of particles in velocity space. The Fokker-Planck equation conserves momentum and energy.

In addition to collisions ($C(f)$) and quasilinear diffusion ($Q(f)$), the effect of an externally imposed electric field $E(f)$ has to be included in a more general formulation of the Fokker-Planck equation. Experiments have also proven the existence of a non-negligible fast electron radial transport $T(f)$ affecting the evolution of the suprathermal tail of the distribution [49, 50]. We can thus rewrite Eq. 4.8 in the more complete form:

$$\frac{df}{dt} = C(f) + Q(f) + E(f) + T(f) \quad (4.21)$$

This equation can also be conveniently rewritten in a conservative form [45]

$$\frac{\partial f}{\partial t} + \nabla \cdot \mathbf{S} = (s_+ + s_-) \quad (4.22)$$

where s_+ and s_- are possible source (impurities from walls or injected particles from an external beam) and sink terms (e.g. loss of particles in magnetic ripples). We note that the collisional term has both diffusive (D) and convective (F) parts:

$$\mathbf{S}_c = C(f) = -\mathbf{D}_c \cdot \nabla_{\mathbf{v}} f + \mathbf{F}_c f \quad (4.23)$$

the RF term instead is purely diffusive in velocity space $\mathbf{S}_Q = Q(f) = -\mathbf{D}_{QL} \cdot \nabla_v f_e$ while the electric-field component is expressed by a purely convective term [45]: $\mathbf{S}_E = E(f) = (q_e E / m_e) f_e$.

4.2 TCV Fokker-Planck modeling tools

4.2.1 Introduction

In the TCV tokamak, the main tools used in the past for modeling the effect of auxiliary heating and current drive on the electron and ion distribution functions are the TORAY-GA ray-tracing code [16] and the quasilinear Fokker-Planck code CQL3D [51]. Through the correct inclusion of radial transport CQL3D is capable of reproducing the driven currents measured in TCV. CQL3D also includes a module calculating the HXR emission for any given detector geometry, which is an ideal tool to employ in conjunction with a HXR diagnostic to constrain the interpretation.

However, at the time of initial experiments with combined X2 and X3 heating, CQL3D did not have the capability of simulating the X2/X3 synergy with waves launched at different frequencies and thus could not address the experimentally observed enhanced absorption of X3 in the presence of X2 ECCD [52, 53]. This initially motivated us to employ an alternative quasilinear Fokker-Planck code that offered that capability, namely LUKE [13].

4.2.2 The LUKE Fokker-Planck code: generalities

This thesis work included the joint integration of the LUKE code in the TCV environment, in collaboration with the code developers from the CEA Association (J. Decker and Y. Peysson). This fully relativistic 3D bounce-averaged Fokker-Planck solver is coupled with the C3PO ray tracing code [14] and the R5-X2 bremsstrahlung calculator [15]. LUKE can take as input data any arbitrary numerical equilibrium (in the TCV case this is provided by the LIUQE magnetic equilibrium reconstruction [54] of a given TCV shot) as well as the launching parameters (EC injected power, mirror angles, wave polarization), the electron and ion temperatures, and the effective charge (Z_{eff}) provided by the Thomson scattering, soft X-ray, and charge exchange diagnostics.

The LUKE code accounts for the effect of an applied electric field (inductive loop voltage). Written in a fully conservative form, the code naturally conserves the electron density as well as momentum for the correct treatment of the current drive problem.

The Fokker-Planck equation is solved in a time-scale frame, in which the magnetic field is assumed to be large enough that the electron gyro-motion period Ω^{-1} is much shorter than the collision time τ_c and bounce time τ_b . Also, electrons are assumed to remain on a given flux-surface for a time long compared to the poloidal electron bounce time: this

condition is equivalent to writing: $\tau_b \ll \tau_d \approx \tau_f$, where τ_d (Eq. 4.10) corresponds to the time for an electron to drift radially across the plasma (due to the magnetic field gradient and curvature) and τ_f is the characteristic fast electron radial transport time. Furthermore, trapped electrons are assumed to perform several bounce motions before being scattered off the trapped region by Coulomb collisions. These assumptions can be summarized by the following time ordering:

$$\Omega^{-1} \ll \tau_b \ll \tau_c \ll \tau_d \approx \tau_f \ll \tau_{eq} \quad (4.24)$$

where τ_{eq} is the equilibrium evolution time scale. The bounce-averaged Fokker-Planck equation is evaluated on a 3-D (ψ : radial, p : momentum, ξ_0 : equatorial pitch angle coordinate) space grid and takes the form of a continuity equation for the electron distribution function f (Eq. 4.22).

The collision operator, $C(f)$, is decomposed into a self-collision (e-e) component plus a component describing the collision of electrons with all ion species s :

$$C(f) = C(f, f) + \sum_s C(f, f_{Ms}) \quad (4.25)$$

where f_{Ms} is the Maxwellian ion distribution function for ions of temperature T_s and density n_s . The electron self-collision term is linearized using the assumption that collisions dominate the thermal electrons, such that the distribution function f can be expanded as

$$f \approx f_{Me} + \delta f \quad (4.26)$$

where f_{Me} is the Maxwellian electron distribution, and δf is the perturbative component due to the interaction of the electron population with the RF wave; as usual, δf is supposed to be small compared to f_{Me} . The linearized form for $C(f, f)$ is

$$C(f, f) \approx C(f, f_{Me}) + C(f_{Me}, f) \quad (4.27)$$

The non linear term $C(\delta f, \delta f)$ is neglected while the term $C(f_{Me}, f_{Me}) = 0$. $C(f, f_{Me})$ and the electron-ion collision term $C(f, f_{Ms})$ are differential operators that can be expressed in a conservative form (as in Eq. 4.22). An appropriate form, conserving the kinetic momentum, is obtained for the integral term $C(f_{Me}, f)$ by expanding the gyro-averaged distribution function f as a sum of Legendre polynomials. This approach is of capital relevance in order to obtain a correct calculation for the current.

The linearized electron-electron collision term conserves momentum, whereas energy is not conserved, so that there is no need to introduce a loss term in the kinetic equation to compensate for the RF power deposition in order to converge to a steady-state.

4.2.3 Fast electron transport in LUKE

The LUKE code offers the possibility to incorporate any type of fast electron radial transport (collision, turbulence or wave induced), a key ingredient for the correct calculation of local plasma properties such as the driven current density [52]. Arbitrary radial diffusion ($D_{\psi\psi}$) and convection (F_{ψ}) terms can be introduced and integrated in an expression for the flux

$$S_T = -D_{\psi\psi} \nabla f + F_{\psi} f \quad (4.28)$$

Two types of radial transport diffusion coefficients are currently implemented to model two particular mechanisms believed to be responsible for anomalous radial electron transport:

- (i) Electrostatic-fluctuation induced transport (ES): fast electrons with normalized parallel velocity exceeding a given threshold ($v_{e\parallel}$) diffuse radially with a constant radial diffusion coefficient ($D_{\psi\psi 0}$ [m^2s^{-1}]) that can be set by the user
- (ii) Electromagnetic-fluctuation induced transport (EM): this form of turbulence causes a radial fast electron diffusion coefficient proportional to the parallel electron velocity:
 $D_{EM} \propto v_{e\parallel}$.

The code can also be fed with models of more general radial profiles of diffusion and convection. The particles escaping the radial domain of integration are “artificially” re-injected at rest (cold particles) into the system to conserve the local plasma density.

The LUKE FP code can deal with LH and EC waves at any given harmonic number simultaneously. The Fokker-Planck equation is evaluated in a 3D (r: radial, p: momentum, ξ_0 : pitch angle coordinate) phase-space and takes the form of a continuity equation for the electron distribution function f .

Many output files and plots are generated by LUKE; a non-exhaustive list includes the total current density profile, the ohmic current density contribution, the RF power deposition and absorption efficiency, the driven current density profile, and finally 2D contour plots of the electron distribution function as well as of the RF diffusion tensor, evaluated in (p_{\parallel}, p_{\perp}) space (see chapter 6).

4.2.4 The C3PO ray-tracing code

The C3PO ray-tracing code solves the ray equations in the (ψ, θ, ϕ) coordinate system, where ψ and θ are the radial flux and the poloidal angular coordinate respectively, and ϕ is the toroidal angular coordinate. Typically the beam propagation and linear absorption

are calculated for a 12-ray bundle (3 transverse positions x 4 radial positions) using the experimental magnetic numerical equilibrium $B(\psi, \theta)$ and plasma profiles $(n_e(\psi), T_e(\psi))$. The numerical calculation is performed with a fifth-order Runge-Kutta algorithm.

The code can handle both LH wave propagation and EC wave propagation (O/X modes); the wave polarization along the ray path remains constant provided that no reflection of the ray occurs, whereas a mode conversion (O-X and X-O) is performed if the wave is cut-off by the plasma. By default a cold plasma model for the wave propagation is used, but a kinetic model is also available.

C3PO is written in a highly modular form and uses the most appropriate plasma model for the wave of interest (EC or LH). However, the physical model and the metric are completely separated for maximum generality.

One of the secondary projects within this thesis entailed addressing the problem of multiple beam reflections from the TCV first wall, including a calculation of the mode conversion (O-X and X-O) at each reflection. This aspect can become relevant under conditions of low first-pass absorption typical of far off-axis beam injection.

4.2.5 Non-thermal electron bremsstrahlung: synthetic diagnostic

The R5-X2 bremsstrahlung calculator [15] included in the LUKE environment can be used for comparison with the measured bremsstrahlung emission for a given TCV plasma in any direction of observation (for example: backward parallel, forward parallel, perpendicular to the toroidal magnetic field direction). The integration of any X-ray camera geometry is easy to perform. In particular, the geometry for the new HXR cameras designed in the course of this thesis work, as reported in chapter 7, has been integrated in the code, enabling us to complement the tomographic reconstructions with direct comparison of calculated emission with experimental measurements.

The calculation of line integrated HXR signal, for each line of sight, is provided by the integral

$$N_{E_0} = \int_t^{t+\Delta t} dt \int_{E_0-\Delta E/2}^{E_0+\Delta E/2} \frac{dN_E(t, E)}{dt dE} dE$$

which gives the total number of photons recorded by a given detector in the time interval $[t, t + \Delta t]$ and in the $[E_0 - \Delta E/2, E_0 + \Delta E/2]$ energy range. In this equation, the pulse energy spectrum $dN_E(t, E)/(dt dE)$ is defined by

$$\frac{dN_E(t, E)}{dt dE} = \int_0^\infty \eta_A(k) [1 - \eta_D(k)] G(k, E) \frac{dN_k(t, k)}{dt dk} dk$$

where $dN_k(t, k)/(dt dk)$ is the effective photon energy spectrum (number of photons per unit time and unit energy k) emitted by the plasma volume in the solid angle spanned by a

given detector and $G(k,E)$ is the normalized instrumental response function; $\eta_A(k)$ is the fraction of photons traveling along the line of sight that reach the detector volume, since part of them can be lost by plasma (re-)absorption or other material filtering. The fraction of photons that are effectively stopped inside the active volume of the detector is $[1-\eta_D]$, where $\eta_D(k)$ is the detector transmissivity as a function of the incoming photon energy. A complete treatment of the different terms including the non-thermal bremsstrahlung calculation can be found in [15].

4.2.6 The LUKE user interface

The LUKE code is installed in the CRPP Linux Analysis Cluster (LAC), a high-performance multi-machine system (4 machines with up to 48 GB RAM with 4-4-8-16 cores each) and operates in a Matlab environment. A user interface is available as shown in Fig.4.3.

To generate a LUKE simulation of a given TCV shot, the procedure is as follows:

After specifying the environmental parameters, the user loads the input data (plasma profiles) from a local database (external structure) and the input magnetic equilibrium from LIUQE. A purely synthetic LUKE simulation can also be generated starting from a custom input equilibrium and plasma profiles. In both cases the code generates its own plasma equilibrium defined on its own spatial grid. This grid is configured through an input structure that specifies all the parameters used by the Fokker-Planck calculator, including the number of points in the radial, poloidal and momentum (ρ, θ, p) mesh-grid used by the finite element calculation.

Optional structures can then be added, including the ohmic electric field, the injected RF waves, and the fast electron radial transport.

Extensive use of LUKE Fokker-Planck analysis is made in this thesis work to model the synergistic interaction in simultaneous 2nd and 3rd harmonic absorption experiments as discussed in chapter 6. The use of LUKE for comparison with measurements with the recently installed equatorial HXRS camera, during high power ECH and ECCD experiments is described in chapter 8.

```

----- < LUKE > -----
Machine : TCV
***** STATUS *****
LUKE data          : LUKE_DATA_TCV_43619_0.5400_C3P0_L1_C3P0_L4_C3P0_L5_C3P0_L6_ES_1.mat
Work directory     : /home/gnesin/HXR/hxrs/Mission_1146/
LUKE path          : LOCAL
LUKE parameters    : EC_RT
Equilibrium        : TCV_43619_0.5400
RF waves           : C3P0_L1; C3P0_L4; C3P0_L5; C3P0_L6
Ohmic E-field     : < The 'ohm' structure is optional >
Fast electron transport: ES_1
Magnetic ripple losses : < The 'ripple' structure is optional >

LUKE output        : TCV_43619_0.5400_C3P0_L1_C3P0_L4_C3P0_L5_C3P0_L6_ES_1
External database  : TCV_43619_0.5400_0.52_0.56_L_1_4_5_6

***** MENU *****

Please select one of the following options:

[1]  Load existing data file
[2]  Save current data in file
[3]  Specify work directory
[4]  Load/clear data from external database

[5]  Load/create/modify 'dkepath' structure (LUKE paths)
[6]  Load/create/modify 'dkeparam' structure (LUKE parameters)
[7]  Load/create/modify 'equil' structure (Plasma equilibrium)
[8]  Load/create/modify 'wave' structures (RF waves)
[9]  Load/create/modify 'ohm' structure (Ohmic E-field)
[10] Load/create/modify 'transpfaste' structure (Fast electron transport)
[11] Load/create/modify 'ripple' structure (Magnetic ripple losses)

[12] Display equilibrium data
[13] Display RF wave data
[14] Display LUKE results

[15] Calculate HXR emission
[16] Generate LUKE run script

[17] Go to command line
[18] Close all figures

[0]  Run LUKE or load BATCH LUKE results
[-1] Exit LUKE
[-2] Exit LUKE, close all figures and removes all variables, globals, functions and MEX links

? [-1] :

```

Figure 4.3 The LUKE Matlab user interface.

4.3 Conclusion

The Fokker-Planck formalism adopted to model the physical behavior of electrons in a tokamak plasma device with resonant wave heating has been introduced in this chapter. The basis of the quasilinear wave-particle interaction has been reviewed. In particular, the LUKE Fokker-Planck code has been chosen as a modeling tool especially in view of experiments where simultaneous multiple harmonic resonant interactions are present.

5 Suprathermal electron diagnostics

Through wave-particle interaction, RF heating and current drive result in a deformation of the particle distribution function in both physical and velocity spaces. In particular, in sufficiently high-power-density experiments there is evidence of a distinct suprathermal electron population. The suprathermal electron dynamics related to Lower Hybrid current drive (LHCD) have been a key research topic during the past two decades, with several experiments carried out on major tokamaks: Tore Supra, ASDEX, JET [55] and JT -60 [56]. The suprathermal dynamics induced by ECCD have been explored primarily on the TCV and DIII-D tokamaks [49]. These studies were motivated by the need to assess the ability of the LH and EC waves to be used for steady state operation and for current profile control. In the context of ECCD, results from the TCV tokamak have shown that the presence of a suprathermal electron population strongly affects the magnitude and the spatial location of the driven current [50]. In addition to external electromagnetic wave injection, suprathermal activity is also observed in conjunction with magnetic reconnection, sawtooth activity and disruptive instabilities [57-60].

It is clear that the dynamics of suprathermal electrons and particularly their spatial transport properties are far from being completely understood. Their study retains capital importance for understanding and controlling the spatial deposition of ECRH and ECCD and their effect on current tailoring, on energy and particle confinement, and on MHD instabilities. It should be stressed, however, that the effect of suprathermal electrons is expected to be minor in most tokamak scenarios, where the power density is much lower than in TCV.

An increased understanding of suprathermal electron dynamics can have direct implications for the first experimental fusion reactor currently under construction, ITER. Indeed, ECCD is planned to be used as a tool in ITER for MHD stability control; additionally, sawtooth activity and disruptive instabilities are expected to occur in the ITER baseline regime, with substantial suprathermal electron generation.

In the remainder of this section, the primary diagnostic tools for studying suprathermal electron dynamics will be reviewed, particularly in the context of the TCV tokamak [61, 62].

TCV is a particularly favorable testbed for studying the physics of suprathermal electrons: because of the high EC power density, a significant and measurable distortion from the Maxwellian distribution can be obtained more easily than in bigger tokamak devices. The Harvey criterion [63] gives a quantitative threshold for the appearance of nonlinear effects in the electron distribution function due to EC power absorption. This threshold is given by the formula

$$P_{EC}[\text{Wm}^{-3}]/n_e[10^{19}\text{m}^{-3}] > 0.5 .$$

In TCV ECH and ECCD operations values of $P_{EC}/n_e \sim 10$ are commonly attained. By contrast, in ITER nonlinear effects are expected to be entirely negligible.

Information about the suprathermal electron population in hot plasmas is derived mainly from two distinct physical phenomena: continuum (bremsstrahlung) hard X-ray (HXR) emission and Electron Cyclotron Emission (ECE) [64]. We shall examine them in turn.

5.1 X-ray plasma bremsstrahlung emission

5.1.1 The origin of hard X-ray bremsstrahlung emission

Fast electrons in tokamak devices undergo Coulomb collisions with other electrons and ions, the latter resulting in the emission of continuum bremsstrahlung radiation (Fig. 5.1). Electron-electron collisions are also present but in a non-relativistic approximation collisions between identical particles result in no net electromagnetic emission. Thermal bremsstrahlung produces a characteristic spectrum. Each collision event can be regarded as producing a photon (single-photon emission dominates in the high-energy range), and the energy of the photon corresponds to the energy loss suffered by the electron during the collision. The electrons in a gas have a distribution of energies, with the mean random energy proportional to the temperature. The distribution of the bremsstrahlung photon energies is related to the electron energy distribution, and in the case of a Maxwellian distribution has an average which is also proportional to the temperature. Thus, a measurement of the spectrum can be used to determine the temperature of the gas.

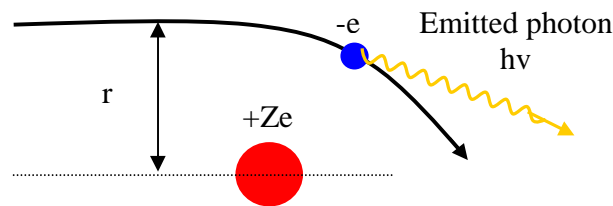


Figure 5.1. Schematic representation of bremsstrahlung emission

Owing to the high energy of the fast electron population, their bremsstrahlung emission lies mostly in the HXR energy range. This is why the detection of HXR emission is a prime method of studying fast electrons.

Using a semi-classical treatment, a Coulomb collision subjects a Ze charged particle to the force $Ze^2/4\pi\epsilon_0 r^2$, where r is the electron-ion distance; the acceleration $a = \frac{Ze^2}{4\pi\epsilon_0 mr^2}$

generates a radiation power $P = \frac{e^2}{6\pi\epsilon_0 c^3} a^2$; the ions' contribution to bremsstrahlung is

then negligible as we can realize considering the mass ratio $m_e \ll m_i$.

Taking $2r/v$ as an estimation of the collision duration, where v is the electron velocity, the energy lost per collision is $\delta E = P2r/v$; thus we have

$$\delta E = \frac{Z^2 e^6}{6(2\pi\epsilon_0 c r)^3 m_e^2 v}$$

Integrating over the impact parameter r , the bremsstrahlung radiation power per unit volume is

$$P_{br} = n_e n_i \int \delta E v 2\pi r dr = \frac{n_e n_i Z^2 e^6}{24\pi^2 \epsilon_0^3 c^3 m_e^2} \int \frac{1}{r^2} dr$$

To prevent the integral from diverging we use the lower quantum mechanical limit for $r_{\text{inf}} = \hbar/m_e v$ using the relation $\frac{1}{2} m_e v^2 = \frac{3}{2} T_e$.

A full calculation gives the bremsstrahlung power from a thermal plasma due to electron encounters with ions of charge Z as

$$P_{br} = g \frac{n_e n_i Z^2 e^6 T_e^{1/2}}{6(3/2)^{1/2} \pi^{3/2} \epsilon_0^3 c^3 \hbar m_e^{3/2}}$$

where g is the Gaunt factor which gives a quantum mechanical correction. In typical tokamak plasmas $g = 2\sqrt{3}/\pi$ and with this assumption

$$P_{br} = 5.35 \times 10^{-37} n_e n_i Z^2 T_e^{1/2} \text{ Wm}^{-3}, \text{ where } T_e \text{ is in keV and densities are in m}^{-3}.$$

The bremsstrahlung emission power per unit volume, solid angle and angular frequency as a function of the photon frequency is [65]

$$\epsilon_\omega(T_e) = \frac{8}{3\sqrt{3}} \frac{Z^2 n_e n_i}{m^2 c^3} \left(\frac{e^2}{4\pi\epsilon_0} \right)^3 \left(\frac{m}{2\pi k T_e} \right)^{1/2} g(\omega, T_e) e^{-\hbar\omega/kT_e}$$

where in general the Gaunt factor depends on ω and on T_e , but is a relatively slowly varying function of $\hbar\omega/kT_e$, so we can consider that the main dependence on frequency and temperature is given by the factor $\epsilon_\omega(T_e) = (m/2\pi k T_e)^{1/2} \exp(-\hbar\omega/kT_e)$.

5.1.2 Deducing the suprathreshold electron temperature from hard X-ray bremsstrahlung emission

If the plasma distribution function is Maxwellian, the bremsstrahlung emission ϵ depends mainly on frequency and temperature through the factor: $\epsilon_\nu(T_e) = (m/2\pi k T_e)^{1/2} \exp(-h\nu/T_e)$; thus the slope of a log-linear plot of the

bremsstrahlung emissivity provides a direct measure of T_e . For the fast electron population we can assume $h\nu \geq T_e$.

This approach is valid if no energy-localized line emission is present in the measured energy spectrum. This is the case for the HXR energy domain of interest (20-300 keV) in the present work. Low (carbon) and medium Z (iron) impurities emit at energies below the threshold of 20 keV (7 keV for Fe K-edge). Elements with higher atomic number, such as the tungsten used for line of sight collimation, can induce a fluorescence contribution at 59.3 (W-K α) and 67.2 (W-K β) keV. As discussed in chapter 7.8, however, the fluorescence emission from the tungsten collimator is negligible and does not influence the calculated photon temperature.

If a substantial non-thermal population exists, such as to distort the distribution function significantly from a Maxwellian, bremsstrahlung will be enhanced at the higher energies and will provide information on the non-thermal tail (Fig. 5.2).

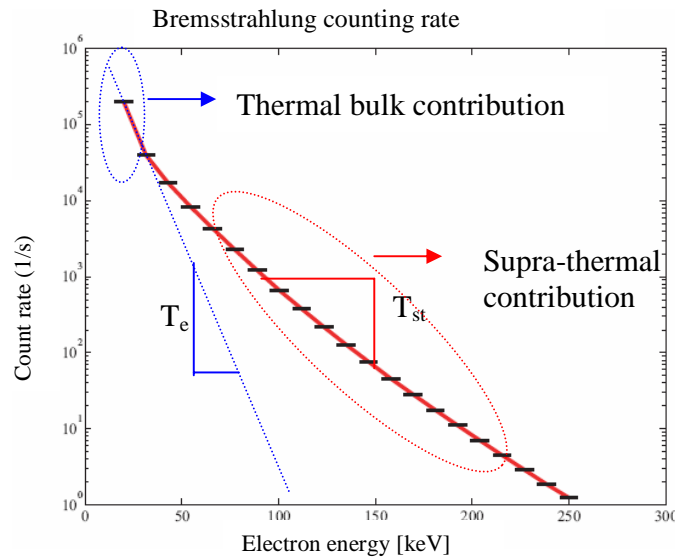


Figure 5.2. Energy spectrum of the bremsstrahlung emission in the presence of a suprathermal electron population

In such a situation we may approximate the total electron distribution function (M_p) as resulting from two different contributions: one corresponding to the thermal bulk (M_b) and one to the non-thermal population in the high energy range (M_{st}). This has motivated simplified modeling of the electron distribution function as a bi-Maxwellian [62] (Fig. 5.3), i.e. a linear superposition of two Maxwellians. In this case the temperatures of the two components can be derived with the slope method in the two regions of the spectrum.

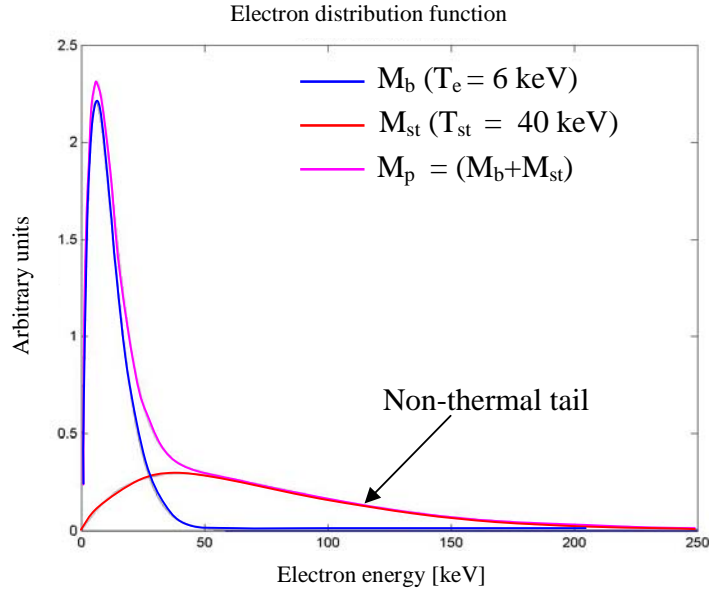


Figure 5.3. Example of the bi-Maxwellian model of the total electron distribution function $M_p = M_b + M_{st}$.

5.1.3 Angular distribution of the bremsstrahlung emission

Another important feature of the bremsstrahlung emission is its distribution as a function of the angle between the incident electron direction and the resulting photon direction. The bremsstrahlung emission from suprathermal electron-ion encounters results in a narrow forward cone along the electron line of flight as depicted in Figure 5.4.

Bremsstrahlung emission from suprathermal electrons in the forward direction is clearly stronger than the backward emission; this effect is larger for higher electron energy. In order to collect the major part of the signal it is thus essential to view the plasma from the direction along which the major part of the radiation is emitted.

It is worth noting that ECRH and ECCD transfer to the electrons momentum perpendicular to the magnetic field; it can therefore be expected that significant emission will occur in the poloidal plane, unlike in the case of Lower Hybrid current drive. For this reason suprathermal electron investigations with ECCD have thus far been performed using diagnostics with poloidal lines of sight. It should be noted however that pitch angle scattering can contribute to re-orient electrons in the toroidal direction. Up to now, no direct measurements have been made to determine whether perpendicular or parallel emission is dominant in the presence of ECCD. Results from quasilinear Fokker-Planck simulations suggest in fact that the two could be comparable.

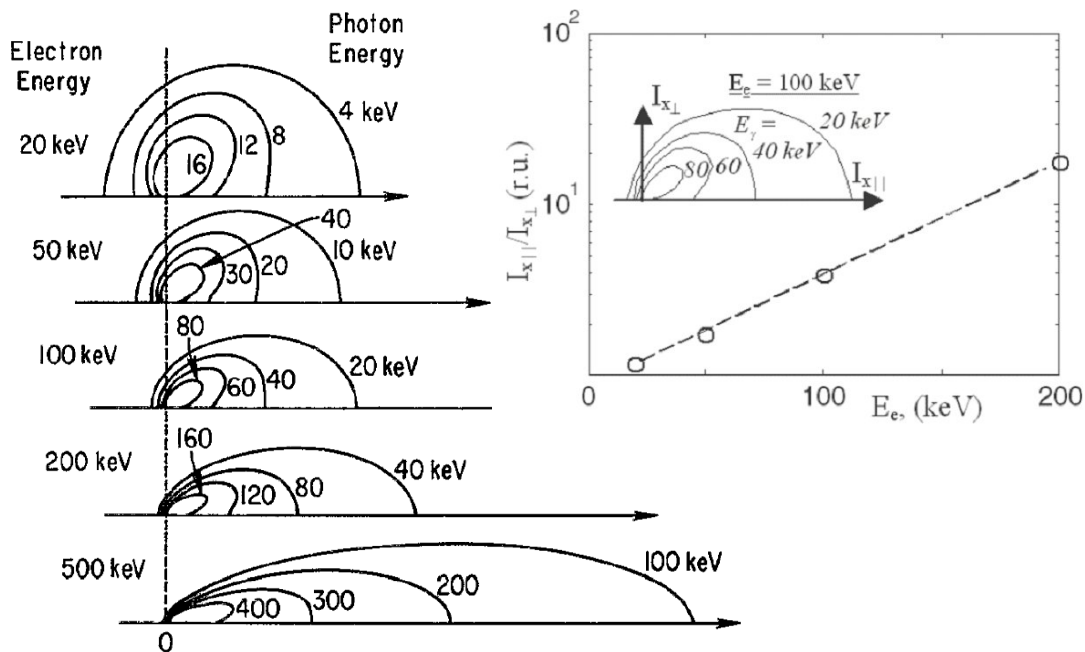


Figure 5.4 Ratio of forward to transverse intensity of the bremsstrahlung radiation for various energies of the incident electrons colliding with protons. The polar plot shows the bremsstrahlung intensity for incident electrons with energy $E_e = 100$ keV. Intensity patterns are plotted for photon energies equal to every 20% of the incident electron energy (for original data see [66]). The length of the vector from the origin to a point on a polar curve is proportional to the bremsstrahlung power emitted in that direction at the energy associated with that particular polar curve.

5.1.4 Past HXR studies in TCV

The development of high Z semiconductor compound materials such as CdTe, CZT, GaAs, InPb and HgI₂ has been opening new possibilities for the implementation of compact HXR detectors [64]. Room temperature operation has become possible and bulky magnetic shielding is no longer necessary.

During different periods between 1998 and 2009, a HXR camera on loan from Tore Supra [68, 69] was employed for suprathreshold studies in TCV (Fig. 5.5). This system included 21 5×5 mm² x 2 mm thick detectors, of which 14 had a view of the plasma in TCV. The plasma was viewed through a 5×5 mm² square pinhole collimator and a 0.25 mm thick beryllium window.

This diagnostic system afforded only a view of the low field side (LFS) of the plasma, albeit covering the whole minor radius, and provided a single viewpoint. Lacking the possibility of tomographic reconstruction, the line-integrated data were inverted by assuming uniform emission over a flux surface. Nevertheless two lines of sight reaching the high field side of the TCV plasma revealed asymmetry in the HXR emission. Therefore as can be expected (the LFS being populated by trapped electrons) the hypothesis of poloidal symmetry in the emission is not fully adequate and a tomographic reconstruction would offer a valuable new opportunity to investigate the full 2D bremsstrahlung distribution.

The detector signal was processed by a charge preamplifier followed by a Gaussian pulse shaping amplifier. Pulse height spectroscopy was performed by splitting each signal 8 ways to feed 8 analog variable-threshold discriminators. The end result was a set of time traces of photon counts for 8 energy bins (the highest of which had no upper bound) for each chord. The energy thresholds could be set before each discharge. Stainless steel absorbers of varying thickness could also be inserted between discharges to reduce the flux and avoid saturation.

Several experiments employing ECCD were performed in order to study the dynamics of suprathermal electrons in TCV. Experimental measurements demonstrated the role of ECCD in the creation and sustainment of the suprathermal population and the dependence of the suprathermal distribution on the toroidal microwave injection angle. In particular the suprathermal dynamics were found to strongly influence the ECCD current drive efficiency [50-53]. The presence of a suprathermal electron population generated by X2 ECCD has also been shown to engender enhanced absorption of X3 waves over that expected for a Maxwellian plasma [52]. Clearly the role of the suprathermal electrons is crucial for understanding ECCD efficiency in TCV and deserves to be investigated further.

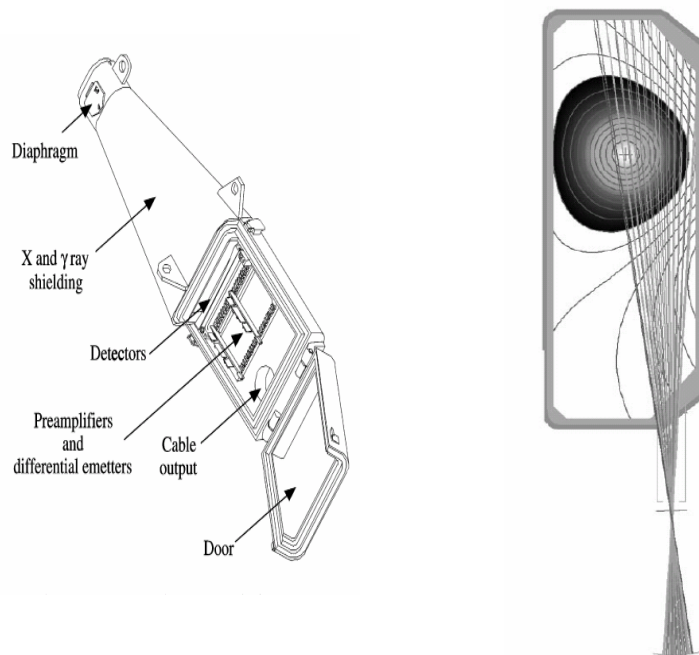


Figure 5.5. The hard X-ray camera employed in TCV (on loan from Tore Supra)

5.2 Electron Cyclotron Emission

5.2.1 Principles of ECE

ECE arises from radiation produced by the gyro-motion of charged particles confined in a magnetic field. In contrast with X-ray bremsstrahlung, where an electron can emit photons of any energy up to its kinetic energy, Electron Cyclotron Emission occurs at a discrete set of frequencies

$$\omega = \frac{nqB}{\gamma m_0 c} \frac{1}{1 - \beta_{\parallel} \cos(\theta)} = \frac{n\omega_0}{\gamma} \frac{1}{1 - \beta_{\parallel} \cos(\theta)}$$

where ω is the emission angular frequency, n is the harmonic number (integer >0), $\gamma = (1 - \beta^2)^{-1/2}$ is the relativistic factor, β_{\parallel} is the normalized electron velocity parallel to the magnetic field, and θ is the angle between the direction of emission and the magnetic field direction. At each harmonic there are three effects which lead to variation in the emission frequency: the magnetic field inhomogeneity affects the local rest-mass cyclotron frequency $\omega_0 = eB/m_0c$, the relativistic mass increase lowers the actual cyclotron frequency $\omega_c = \omega_0/\gamma$ as the energy $\gamma m_0 c^2$ increases, and the Doppler shift caused by the relative motion in the parallel direction between the emitting electron and the observer shifts the frequency by $\beta_{\parallel} \cos(\theta)$ [70]. In the weakly relativistic limit the relative intensity of the harmonics depends on the electron temperature and is a decreasing function of the harmonic number.

Two main contributions to the line width $\Delta\omega$ can be mentioned: the Doppler ($\Delta\omega_D$) and the relativistic broadening ($\Delta\omega_r$) [65]:

$$\Delta\omega_D = n\omega_0 (2kT_e/mc^2)^{1/2} \cos(\theta); \quad \Delta\omega_r = \sqrt{2\pi n} \cdot n\omega_0 (kT_e/mc^2);$$

The relativistic broadening is due to the relativistic mass shift. To minimize the Doppler broadening one must place the ECE receiver direction at an angle $\theta = \pi/2$ to the magnetic field.

ECE provides measurements of the electron temperature profile if the electron distribution function is Maxwellian. In this condition, the plasma behaves like a blackbody. The radiation temperature T_r is defined by the relation

$$I_{\omega} = \frac{\omega^2}{8\pi^3 c^2} kT_r (1 - e^{-\tau_b})$$

where I_ω is the intensity of EC radiation (power per unit area per unit angle per unit angular frequency) at the frequency ω , $\tau_b(\omega) = -\int_L^0 \alpha(\omega) ds$ is the bulk total optical depth, $\alpha(\omega)$ is the absorption coefficient of the plasma traversed by the EC radiation and L is the plasma length traversed (0 indicating the point of detection). For a Maxwellian plasma in thermal equilibrium it is found that $T_r = T_e$, i.e. the radiation temperature corresponds to the electron temperature. Moreover, if the plasma is optically thick ($\tau_b > 3$), I_ω is the blackbody intensity, so we can measure the electron temperature through the simple formula

$$kT_e = I_\omega \frac{8\pi^3 c^2}{\omega^2}.$$

ECE can also provide spatially resolved temperature information. The main component of the magnetic field in a tokamak configuration is B_{tor} . This field varies inversely with the major radius R as

$$B_{tor} = \frac{B_0 R_0}{R},$$

where B_0 and R_0 indicate values on the magnetic axis of the plasma.

For observation at right angles to the magnetic field and along R , a simple relationship therefore exists between the frequency of the emitted radiation and the location of the point of emission: $\omega = n \frac{eB_0 R_0}{m_e R}$,

where n is the harmonic number. Then the measured electron temperature is a function of the major radius along the viewing chord.

5.2.2 High-field-side ECE as a suprathermal electron diagnostic

When ECE is measured through a perpendicularly viewing antenna on the high-field side (HFS) of the torus and the electron distribution function differs significantly from a Maxwellian, i.e. a substantial population of suprathermal electron exists, the emission will be dominated by this population. Because of the relativistic downshift of the cyclotron frequency with energy, for a given frequency the resonant high-energy electrons will be shifted to the HFS with respect to the resonant bulk electrons. In an optically thick plasma, emission will be dominated by the layer closest to the receiving antenna, i.e., in this case the suprathermal population. Thus a HFS ECE radiometer can be used as a fast electron diagnostic.

A vertically viewing geometry can also be employed. Since the ECE frequency for a given electron energy is approximately constant along a vertical line, by tuning the frequency below the bulk cyclotron frequency one can in principle target a population of

specific energy, removing the ambiguity between emission location and energy that occurs in the case of a perpendicular view. However, since the suprathermal population is relatively tenuous and thus generally optically thin, the emission is then line-integrated, and localization is lost. Additionally, refraction effects contribute to broadening the antenna pattern and effectively reduce the energy resolution.

5.2.3 Oblique ECE

Oblique ECE detection is performed when the ECE emission is collected along a cone of view whose axis intercepts the magnetic field at an angle different from the perpendicular. In this case the Doppler up shift in the resonance frequency

$$\omega = n \frac{\omega_0}{\gamma} + k_{\parallel} v_{\parallel} = \frac{n\omega_0}{\gamma} \frac{1}{1 - \beta_{\parallel} \cos(\theta)}$$

is expressly used for measuring the parallel energy electron distribution [70].

Oblique ECE can provide a continuous scan of the distribution function in parallel energy by changing the observation angle (and thus the angle θ). By combining the measurement of an oblique LFS ECE with the measurement of a perpendicularly viewing HFS ECE, a 2D scan of the electron distribution function in the velocity space can be performed in principle.

5.2.4 ECE radiometry on TCV

TCV is equipped with a second harmonic ($2\omega_{ce}$) X-mode ECE radiometer operating in the 74-114 GHz range with 24 channels of 0.75 GHz bandwidth. The radiometer can be connected to either of two perpendicularly viewing antennas located on the HFS of the torus at $Z=0$ and $Z=21$ cm [61].

Measurements of the suprathermal ECE in the second and third harmonic X-mode have been performed during ECH and ECCD operation, showing an enhancement of the emission by up to a factor of six over the thermal emission [62].

The radiometer has also been used in modulation studies aimed at resolving the characteristic times of the dynamical evolution of the suprathermal population [67].

A vertical ECE system is currently being installed on TCV and will become operational in late 2011.

TCV is also equipped with a low-field-side radiometer for bulk temperature measurements. It is worth noting that in high-power ECCD experiments even this diagnostic has been found to be affected by suprathermal electrons, and the bulk temperature measurement is significantly polluted. This is attributed to Doppler-shifted oblique emission from the LFS of the nominal resonance entering the system because of the broad angular acceptance of the antenna.

More recently a new LFS receiving antenna in the oblique ECE configuration has been installed in TCV. This radiometer uses one of the steerable EC launchers in an equatorial port as a launcher/receiver, providing the flexibility to view the plasma along symmetrical co- and counter toroidal directions [71].

6 3rd harmonic ECRH absorption enhancement by 2nd harmonic heating at the same frequency in TCV

6.1. Introduction

On the TCV tokamak a number of fundamental studies of EC wave-plasma coupling have been performed over the years [50,67,72], including the role of electron transport in regulating the driven current, through direct measurements as well as Fokker-Planck modeling [49,53]. The TCV tokamak offers also the unique ability to deposit EC power at different harmonics simultaneously in the same plasma. This opens the possibility for novel investigations into the fundamental physics of wave-plasma interaction, both experimental and theoretical, which are the object of the present chapter. The primary simulation tool employed here is the recently developed Fokker-Planck code LUKE [13] described in section 4.2.

The TCV tokamak is ideally suited for the study of high-power density EC heating and current drive (ECCD) with the possibility to inject X2 and X3 EC waves simultaneously as discussed in section 2.3. The X2 and X3 gyrotron frequencies are designed to place the two EC resonances near the magnetic axis at the nominal magnetic field (1.45 T). X3 heating in particular enables access to high density plasmas (up to $n_e > 1.1 \times 10^{20} \text{ m}^{-3}$), whereas X2 is cut off from the plasma for $n_e > 4.3 \times 10^{19} \text{ m}^{-3}$. Since the plasma is optically thin for the 3rd harmonic, the X3 wave is usually injected vertically from the top of the machine in order to align the ray path with the resonant surface and thus maximize the total first-pass absorption by the plasma. X2 injection is effected by means of two clusters of three beams each, launched from the low-field side (LFS) of the vessel.

Early experiments with simultaneous X2 and X3 injection were performed in TCV with X3 also injected from a LFS launcher [49]. More recently, several experiments have benefited from simultaneous X2 and (top-launched) X3 heating. Simultaneous injection at the nominal X2 and X3 frequencies, however, is not the only way to achieve and study combined 2nd and 3rd harmonic wave absorption in TCV. By decreasing the toroidal magnetic field and using only the 82.7 GHz gyrotrons, we can obtain magnetic configurations in which both the 2nd and 3rd harmonic resonant layers are present in the plasma at the same time for the same EC wave frequency. TCV experiments were expressly devised several years ago in TCV to explore this idea and, in particular, to study the influence of 2nd harmonic heating on 3rd harmonic wave absorption. Power injection was effected exclusively through LFS launchers at 82.7 GHz. The interpretation of the experimental results through comparison with numerical simulations is the object of this chapter.

The specific experimental setup is outlined in section 6.2. An overview of the experimental results follows in section 6.3. Since a magnetic-field sweep is the clearest and most direct way to explore the possible synergy and its experimental signatures, an extensive numerical analysis is presented in section 6.4 of an especially representative discharge featuring such a sweep. The interpretation of the numerical results is reserved

for section 6.5, and the crucial comparison of predicted vs measured bremsstrahlung emission is the subject of section 6.6. Conclusive remarks are offered in section 6.7.

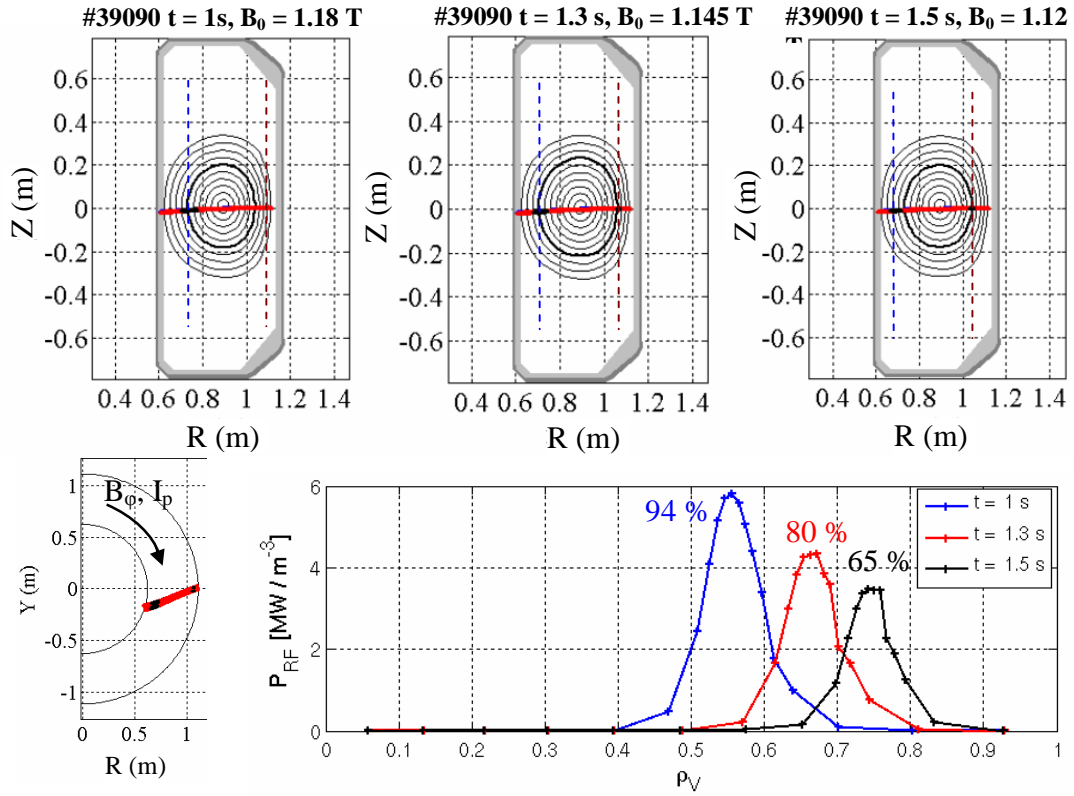


Figure 6.1. Time evolution of the magnetic plasma configuration during a decreasing magnetic sweep in the TCV shot #39090. Two 0.5 MW 82.7 GHz ECRH beams are injected from the LFS with a 16° toroidal angle in counter-current configuration (in the case shown). The 2nd and 3rd harmonic resonant layers move to smaller major radii with time. The dominant 2nd harmonic absorption moves away from the magnetic axis (on the plasma HFS) while 3rd harmonic absorption moves toward the center (on the LFS). The radial total power deposition profiles are generated by the C3PO/LUKE ray-tracing and Fokker-Planck code suite for 3 time slices: $t = 1$ s, $t = 1.3$ s and $t = 1.5$ s. The fraction of absorbed power ($P_{\text{abs}}/P_{\text{inj}}$) for each time slice is indicated near each absorption peak. The radial coordinate here is the square root of the normalized volume (ρ_V) enclosed by a given flux surface.

6.2. Experimental setup

A set of experiments with up to 1 MW EC power from two 82.7 GHz gyrotrons injected from the LFS were performed during this work. Preliminary experiments had been performed several years ago on TCV; these were continued and complemented in the context of this thesis work.

By varying the toroidal magnetic field B_0 while keeping the beam injection geometry constant, it is possible to move the deposited power location along the major radius, shifting it to the LFS or HFS of the magnetic axis. In TCV, there exists a range of B_0 values for which both the 2nd and 3rd harmonic resonant surfaces are present in the

plasma simultaneously for that same frequency. Moreover, for a particular value of B_0 both the 2nd and the 3rd harmonic resonances can be made to lie on the same flux surface. In particular, by gradually decreasing the toroidal magnetic field during the discharge, one can ensure that this combined 2nd and 3rd harmonic heating on the same flux surface will occur at some time t_x during the discharge. This procedure is visualized in Fig. 6.1 where $t_x \approx 1.3$ s.

Ideally, as in all studies of synergistic effects, one would wish to compare cases with and without synergy, under the same experimental conditions. However, the experimental setup clearly precludes this possibility. A magnetic-field sweep therefore appears to be the simplest and clearest means to seek a synergy signature. One must be mindful, however, that conditions change drastically during such a sweep, most notably the absorption rate of the wave. A sensitivity study will therefore be an essential component of this analysis.

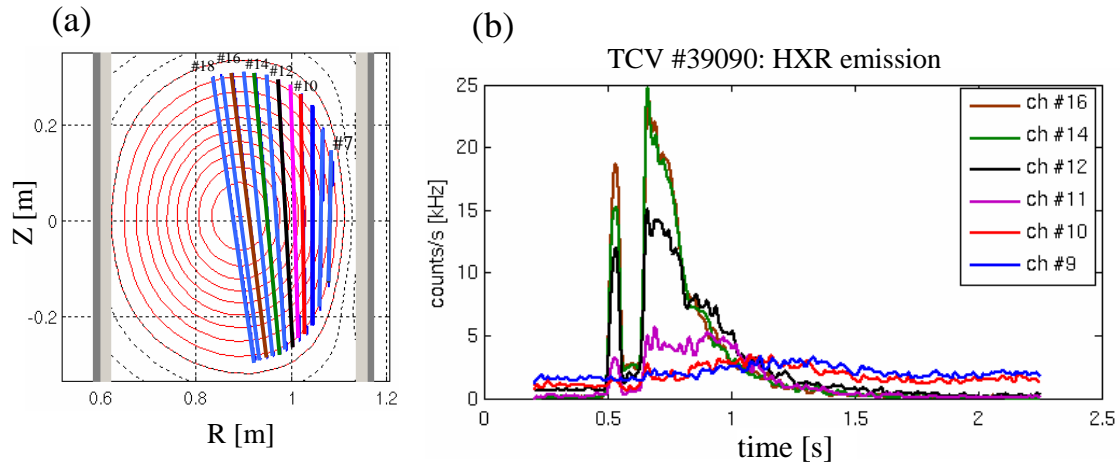


Figure 6.2. (a) Vertically viewing HXR camera geometry on TCV shot 39090. Only chords #7 – #18, shown in the picture, view the plasma (#7 is the rightmost and #18 the leftmost). (b) Non thermal bremsstrahlung emission as a function of time in the 16-40 keV energy range for selected chords.

The goal of the study is to determine the effect, if any, of 2nd harmonic heating on 3rd harmonic absorption. In the remainder of this chapter we shall refer to this effect as "synergy" or "synergistic absorption"; the synergy will be positive if 3rd harmonic absorption increases relative to the level with no 2nd harmonic heating, negative in the opposite case. The expectation, guided also by previous results [49], is that a positive synergy would be mediated by a suprathermal electron population generated by 2nd harmonic wave-plasma interaction. A significant suprathermal population is invariably observed whenever 2nd harmonic waves are injected in ECCD mode, i.e., with a finite parallel wave number [55, 61]. For this reason, the EC beams in the experiment under discussion were injected with a 16° toroidal angle.

Because of the far off-axis location of the power deposition and the intrinsically poor 3rd harmonic absorption efficiency, any enhancement in the latter is not directly measurable (the 3rd harmonic deposited power fraction being of order 1%). However, an indirect indication of a possible synergistic effect on the 3rd harmonic absorption could be

provided by variations in the hard X-ray (HXR) emission, which, for the experiments discussed here, was measured by the vertically viewing, 14-chord HXR camera [68], described in section 5.1.4. Since the camera was not expressly designed for TCV, only 14 detectors (#5 through #18) had a complete or partial view of the plasma, and of these #5 and #6 were generally excluded from the analysis because of parasitical thick target emission from the outer wall. Detectors #7 to #18 (#7 being at the periphery and #18 at the center) provided a complete radial coverage of the LFS half of the plasma poloidal cross section, plus a small fraction of the HFS (Fig. 6.2a). Shielding against uncollimated radiation was provided by a 2 cm lead casing sandwiched between 0.5 cm of stainless steel.

6.3. Experimental results

An initial set of experiments were performed on TCV to explore the synergy effect, prior to the availability of a suitable Fokker-Planck simulation tool. An example (shot 25474) is shown in Fig. 6.3. The measured HXR signal showed a maximum in coincidence with the crossing time ($t_x = 0.9$ s), suggestive of a synergy signature. This time however also coincides with a minimum in density (Fig. 6.3). Subsequent Fokker-Planck analysis showed that the HXR peak is due to the density dip rather than to a synergy effect. These dependences will be discussed in detail in the next section. It is also found that a significant fraction of the HXR signal appears in the uppermost range of the measured energy spectrum ($E > 64$ keV); this component indeed becomes dominant for $t > 1.3$ s in the case shown in Fig. 6.3. These highly energetic transients are visible also in signals from HXR detectors without a direct view of the plasma, as well as from a heavily shielded scintillator-photomultiplier system that measures the flux of hard X-rays escaping the TCV walls. This phenomenology is clearly related to significant runaway electron activity, resulting in thick-target bremsstrahlung emission up to the MeV range.

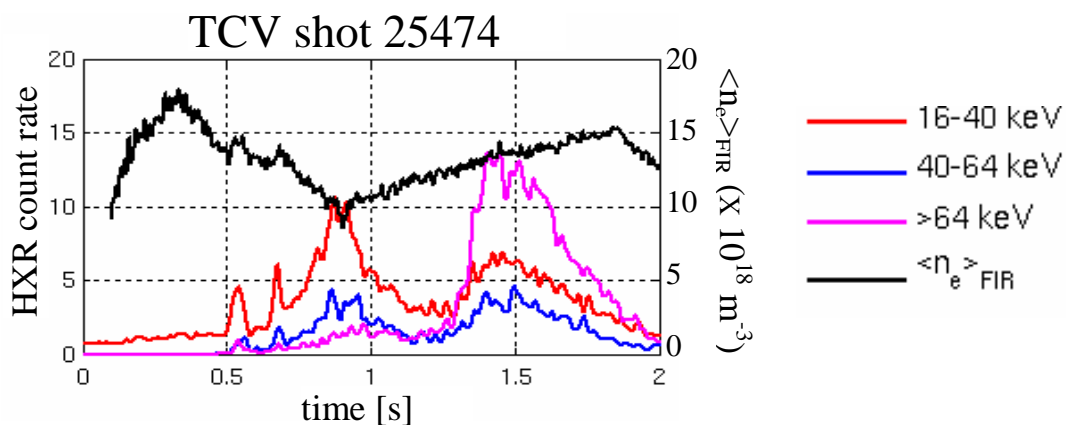


Figure 6.3 TCV discharge 25474: non-thermal bremsstrahlung emission as a function of time in the (red) 16-40 keV, (blue) 40-64 keV and (magenta) > 64 keV energy ranges on chord #12 (mid-radius) of the vertically viewing HXR camera. The line-averaged electron density is shown in black.

Based on these initial results and on the subsequent numerical analysis, a new series of plasma discharges were performed more recently with the goal of achieving better density control and of suppressing the runaway electron generation. The TCV shot 39090 is a particularly representative shot for the present study and will therefore be discussed at some length. All the salient features of the basic physical mechanisms at play are found in this particular discharge. A limited plasma (elongation $k = 1.3$, triangularity $\delta = 0.12$) is centered near the equatorial plane of the machine ($Z_p \approx 8$ cm). The toroidal magnetic field is decreased during the discharge from $B_1 = 1.23$ T at $t = 0.5$ s to $B_2 = 1.07$ T at $t = 1.9$ s. The magnetic configuration for three consecutive time slices ($t = 1.0, 1.3, 1.5$ s, respectively) is plotted in Fig. 6.1. The total plasma current is adjusted during the magnetic field ramp in order to keep the safety factor (q) constant. The plasma is shaped to maximize the radial localization of the power deposition by imposing nearly vertically straight flux surfaces in the equatorial plane where the EC power absorption occurs for both harmonics. Two EC beams (450 kW each) are injected equatorially from the LFS so that their poloidal projections cross the magnetic flux surfaces perpendicularly. The toroidal injection angle is $\phi = 16^\circ$. The EC power is injected from 0.5 to 2.0 s with two modulation phases for $0.55 \text{ s} \leq t \leq 0.65 \text{ s}$ and $1.85 \text{ s} \leq t \leq 1.95 \text{ s}$. The current is sustained primarily by the transformer ($V_{\text{loop}} \neq 0$) with only a minor contribution ($< 5\%$) from ECCD.

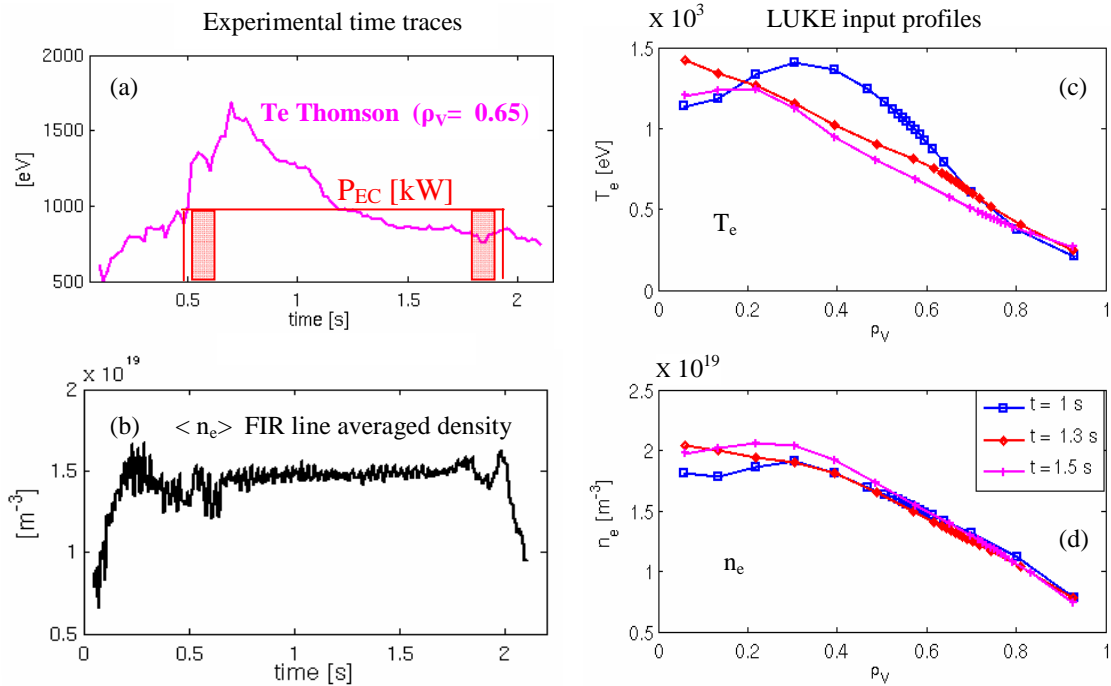


Figure 6.4. Time traces of the electron (a) temperature at the flux surface where the 2nd and 3rd harmonic resonances cross, and (b) line-averaged density in shot #39090, from the Thomson scattering and FIR diagnostics, respectively; fitted LUKE input profiles of (c) temperature and (d) density for three different times. The injected EC power is also shown in (a).

In Fig. 6.4a we show the injected EC power along with the electron temperature T_e measured by a Thomson scattering diagnostic at the location where absorption occurs when the 2nd and 3rd harmonic resonances lie on the same flux surface. The temperature decreases in time as the dominant 2nd harmonic absorption moves off-axis. The absorbed power is 100% at the beginning ($t = 0.7$ s) of the EC injection phase and decreases to 60% at $t = 1.5$ s. The line averaged density measured by a far infrared (FIR) interferometer is $1.5 \times 10^{19} \text{ m}^{-3}$ during the whole EC phase, with fluctuations of less than 10% in the 0.7 s - 1.8 s time interval (Fig. 6.4b). The temperature and density profiles from Thomson scattering are shown for three times in Figs. 6.4c and 6.4d. The density profiles vary little with time ($< 5\%$) in the radial region of interest for the EC wave absorption ($0.4 \leq \rho_v \leq 0.9$).

In the course of the magnetic-field sweep, the HXR emission is seen to decrease with time as the dominant X2 absorption moves to the periphery; however, a minor local peak is seen in the time traces on several peripheral chords (Fig. 6.2b), at $t = 0.9$ s on channels 11 and 12, at 1.1 s on channel 10 and at 1.3 s on channel 9. On the more central chords (13 to 16), on the other hand, no local peak breaks the monotonic decrease with time. In section 6.6, these observations on the non-thermal bremsstrahlung emission will be the object of extensive analysis and comparisons with simulations.

6.4. Numerical modeling of the experiment

Two definitions of synergy are used in the numerical simulations:

- (i) a relative figure of merit $R_3 = \chi_3^{[1,2,3]} / \chi_3^{[3]}$ where $\chi_3^{[1,2,3]} = P_3^{[1,2,3]} / P_0$ and $\chi_3^{[3]} = P_3^{[3]} / P_0$ and $P_3^{[1,2,3]}$ is the power absorbed at the 3rd harmonic calculated when all harmonics (fundamental, 2nd and 3rd harmonic) are taken into account in the Fokker-Planck simulation, while $P_3^{[3]}$ is the absorbed power when only the 3rd harmonic is considered, and P_0 is the total injected power. The quantities $P_3^{[1,2,3]}$ and $P_3^{[3]}$ are provided in output by each LUKE run.
- (ii) the absolute figure of merit $S_3 = \chi_3^{[1,2,3]} - \chi_3^{[3]}$.

In the course of the magnetic-field ramp in shot 39090 the following sequence occurs. Initially the nominal (cold) 2nd harmonic resonance occurs well in the plasma core, whereas the cold 3rd harmonic resonance is outside the plasma. The only electrons that can be resonant at the 3rd harmonic under these conditions are very high-energy ones near the outer edge with strongly relativistically down-shifted cyclotron frequency. As time progresses, the 2nd harmonic resonance moves towards the HFS edge whereas lower and lower energy electrons become resonant at the 3rd harmonic, until the cold resonance enters the plasma. The two nominal resonances coincide at $\rho \sim 0.7$ at $t = 1.3$ s. At later times, the 3rd harmonic resonance is at a smaller minor radius than the 2nd harmonic one.

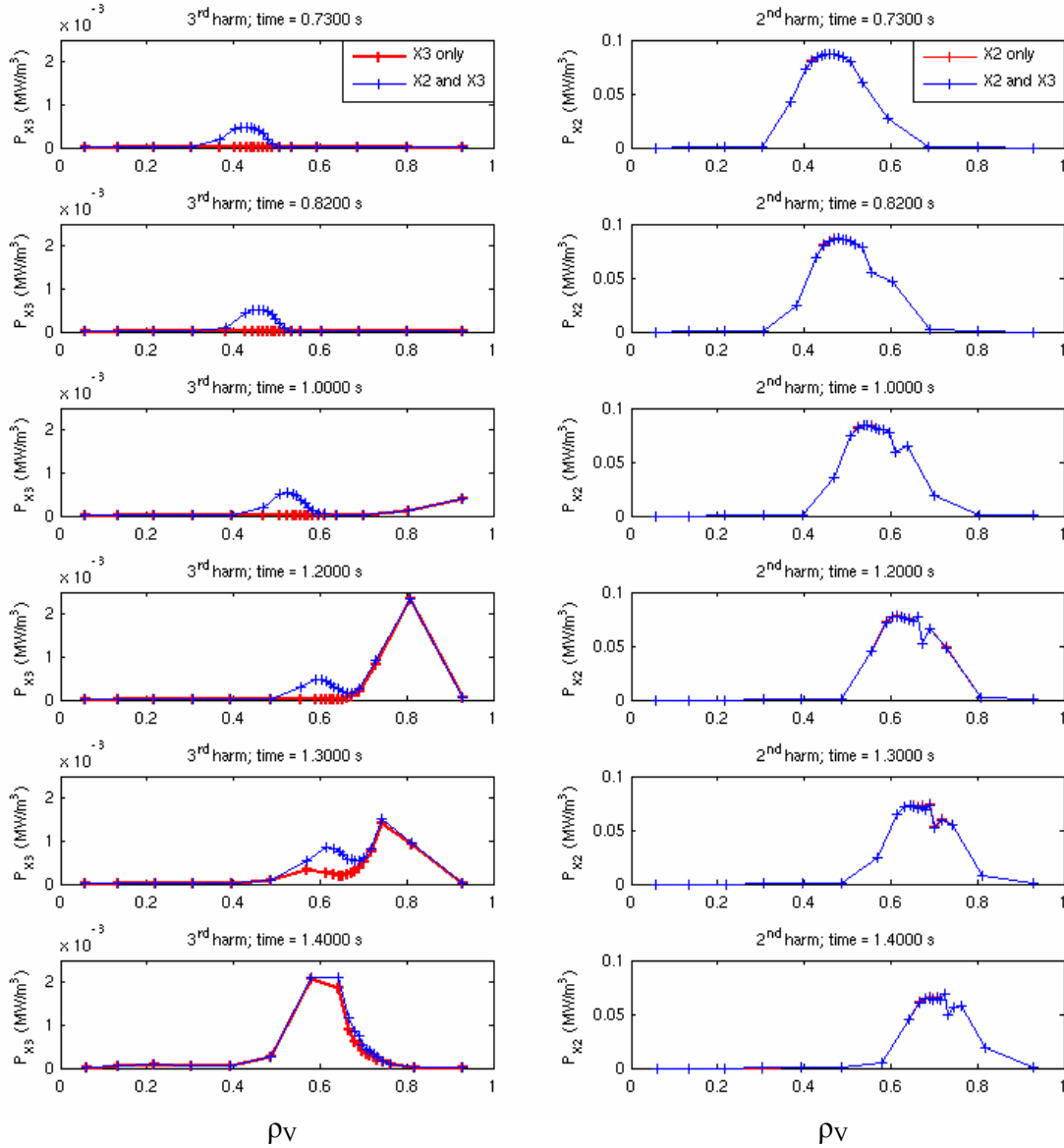


Figure 6.5. TCV shot 39090: the radial power deposition profiles produced by the LUKE FP code for different time slices in the 0.7 – 1.5 s interval. The left column depicts the power absorbed at the 3rd harmonic both when the other harmonics are neglected and when they are taken into account; the equivalent plots for the 2nd harmonic are on the right. Here radial fast electron diffusion is assumed to be absent. The radial width of the deposited power ($\sim 0.2 \rho_v$) is dominated by Doppler shift broadening due to the finite angle of injection ($n_{\parallel} \approx 0.4$).

A series of simulations have been performed to cover the EC phase between 0.7 and 1.5 s with a 0.05 s time sampling or less where necessary. The experimental profiles (n_e , T_e , Z_{eff} , HXR emission) and the magnetic equilibria given in input to the code are averaged on 40 ms time intervals. The constancy of the electron density is a key point in the present analysis, as this is a plasma parameter to which both the synergy and the HXR emission are extremely sensitive. A 10% fluctuation in the electron density corresponds

to a 30% variation in the expected HXR emission (from LUKE/R5-X2 simulations). For each time slice, simulations with all harmonics (fundamental, 2nd and 3rd), with the 2nd harmonic alone and with the 3rd harmonic alone were performed; crucially, in each case the individual contribution of each harmonic to the total absorbed power is generated by the code. It should be noted that the contribution of the fundamental mode has proven to be negligible ($P_{abs}^{1st\ harm} / P_{abs}^{tot} \sim 10^{-6}$) in all the cases analyzed and will accordingly be neglected in the remainder of this work. The simulations were performed first with no fast electron radial diffusion ($D_{ES} = 0$) and were then repeated with $D_{ES} = 0.5\ m^2/s$.

The radial profiles of the EC power deposition generated by LUKE are shown in Fig. 6.5 for the case without diffusion. The outward drift of the 2nd harmonic absorption region is clearly seen in the right-hand column. It is also clear that the (very faint) 3rd harmonic absorption has a negligible influence on the 2nd harmonic absorption. In the left-hand column the bulk 3rd harmonic absorption is seen to enter the plasma at approximately 1 s. In addition, however, there is evidence for synergistic 3rd harmonic absorption well before this time, which translates into very high values of R_3 as shown in Fig. 6.6a. This "anomalous" absorption is radially aligned with the peak of the 2nd harmonic absorption. The absolute synergy ratio is shown in Fig. 6.6b and is seen to decrease very slightly over the 0.73 – 1.2 s time window, followed by a peak at $t = 1.3$ s, the 2nd/3rd harmonic crossing time (t_x).

The main effect of the fast electron radial diffusion observed in our simulations is to broaden the 3rd harmonic radial deposition profile (Fig. 6.7). This effect is more pronounced when the 3rd harmonic absorption occurs at inner radii (and at higher energy for $t < 1$ s).

6.5. Interpretation of the numerical results: phase space analysis

In this experiment the 2nd harmonic absorption occurs on the HFS of the plasma, in a region where the presence of trapped particles is minimum, while the 3rd harmonic absorption occurs in the region of minimum B field where the trapped population is maximum. This configuration is in principle unfavorable for the synergy. Nevertheless, the numerical analysis indicates that the rate of pitch-angle scattering is sufficiently high to result in very efficient redistribution of fast particles across passing and trapped regions, favoring synergy. We shall discuss first the case without spatial transport: synergy can then only occur for a flux surface and class of electrons for which the two resonances coincide.

The early 3rd harmonic peak ($t < 1$ s in simulations with 2nd and 3rd harmonics; Fig. 6.5, left column) can only be explained by 3rd harmonic absorption on the high energy tail of the electron distribution function generated as a consequence of the 2nd harmonic heating. The nominal (cold) 3rd harmonic resonant layer indeed is not even inside the plasma at these times. The presence of a significant suprathermal electron tail generated by the 2nd harmonic absorption is an essential ingredient for this synergy.

In Fig. 6.8, the momentum space dynamics are analyzed for the case $t = 0.82$ s; the 2nd and 3rd harmonic interaction is maximized at large values of the total momentum ($p/p_{Te} \sim 8$) in the core ($\rho < 0.7$) where a large distortion in the electron distribution

function $f(p)$ is seen. Moving to larger radii (right column in Fig. 6.8), the 3rd harmonic interaction moves to regions of lower momentum, whereas the 2nd harmonic interaction occurs mainly on a highly energetic ($p/p_{Te} \sim 10$) but poorly populated part of the electron distribution function, reducing the opportunities for synergy.

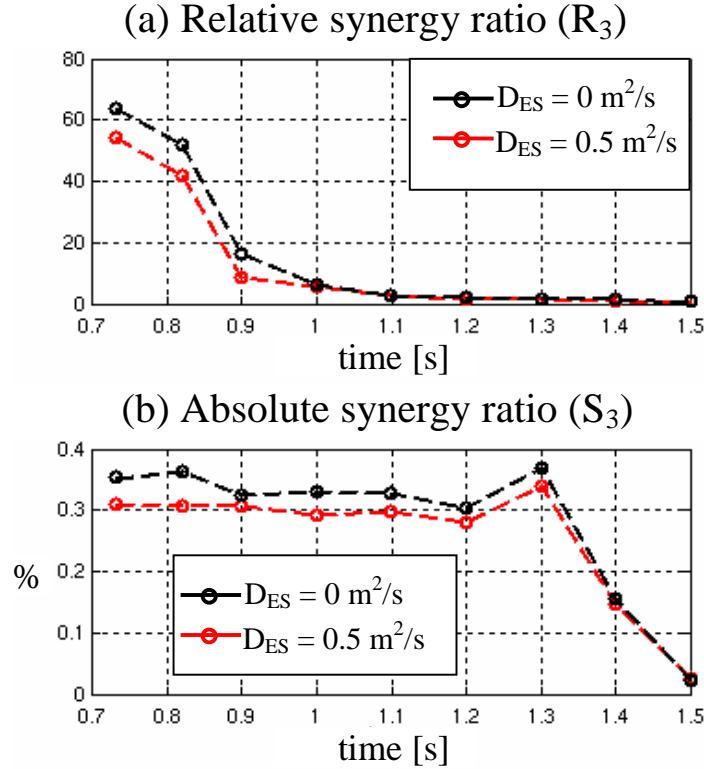


Figure 6.6. (a) Relative R_3 and (b) absolute S_3 figures of merit for the synergy (TCV shot 39090)

The nominal 3rd harmonic resonant layer enters the plasma, from the LFS, at $t \sim 1$ s (as shown in Fig. 6.5) and moves to inner radial positions afterwards (down to $\rho_v \sim 0.58$ at $t = 1.5$ s). Synergistic 2nd/3rd harmonic interaction is found to occur at radial locations where electrons resonating at the 2nd and 3rd harmonic have similar energies in a sufficiently populated part of the distribution function. In addition, a significant synergy requires that the interaction takes place on the LFS of the nominal 2nd harmonic resonance, which is the most efficient means of generating a suprathermal tail as the resonant electrons are less collisional. Also the high rate of pitch-angle scattering makes these electrons available for resonant X3 interaction preferentially on the HFS of the nominal 3rd harmonic resonance. This complex interplay creates relatively favourable conditions for the synergy throughout the first part of the scan up to the point of radial alignment between the nominal resonances at $t = 1.3$ s. The maximum of the absolute synergy S_3 occurs indeed at $t = 1.3$ s where a fair overlap of the two absorption regions in velocity space is observed at $\rho_v \sim 0.7$ (slightly inside the cold resonance location), as seen in Fig. 6.9. At later times the condition that the resonant electrons be on the HFS of

the 3rd harmonic and on the LFS of the 2nd implies an increasing Doppler up-shift for the latter, i.e., a large parallel velocity and therefore a rapidly vanishing population. The synergy accordingly drops rapidly for $t > 1.3$ s.

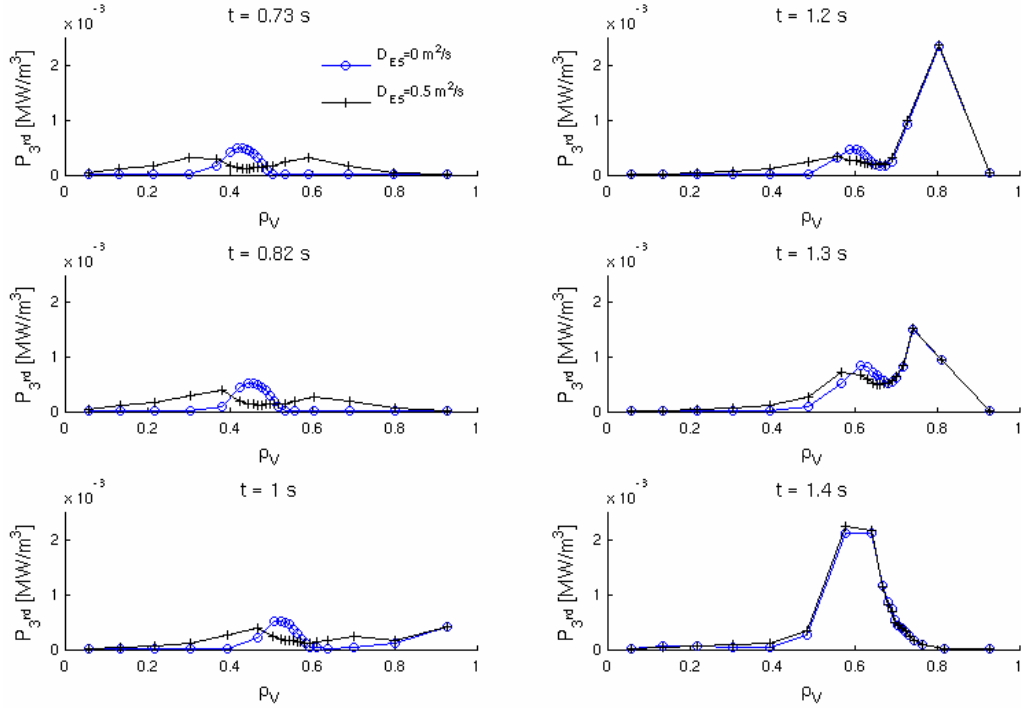


Figure 6.7. Effect of fast electron radial transport on the radial power deposition profiles for the 3rd harmonic (with all harmonics included in the calculation), TCV shot 39090.

When transport is considered (Fig. 6.7), the radial propagation of electrons increases the opportunities for the interaction between the two resonances. The result is, however, a stronger flattening of the distribution function and, somewhat paradoxically, a decrease in absolute synergy (Fig. 6.6, red curves). In the present study, fast electron radial transport is modeled with an electrostatic (ES) model, whereby a uniform and energy independent radial diffusion coefficient (D_{ES}) is applied to fast electrons with $v_e \geq 3.5v_{Te}$. It could be asked whether the experimental value of the plasma current provides a constraint on the value of the diffusivity. However, since the current is primarily carried by the Ohmic component, fast electron diffusion exerts only a weak effect on it (Fig. 6.10). The total current calculated by LUKE is determined primarily by the plasma resistivity and thus depends strongly on Z_{eff} (Fig. 6.10), which in turn is known experimentally only with modest precision. The value of Z_{eff} necessary to reproduce the experimental current is compatible, within the error bars, with the experimental value of Z_{eff} provided by a soft X-ray diagnostic, which averages at 3 (with $\sim 20\%$ fluctuations) during the discharge. The diffusivity has been estimated, rather, by requiring a satisfactory match between the calculated and experimental HXR profiles. At the crossing time, 1.3 s, this suggests the value $D_{ES} = 0.5 \text{ m}^2/\text{s}$, although the optimal value varies during the discharge as discussed

in the next section, where the dependence of the synergy on the diffusivity will be examined in more detail through its effect on the HXR emission.

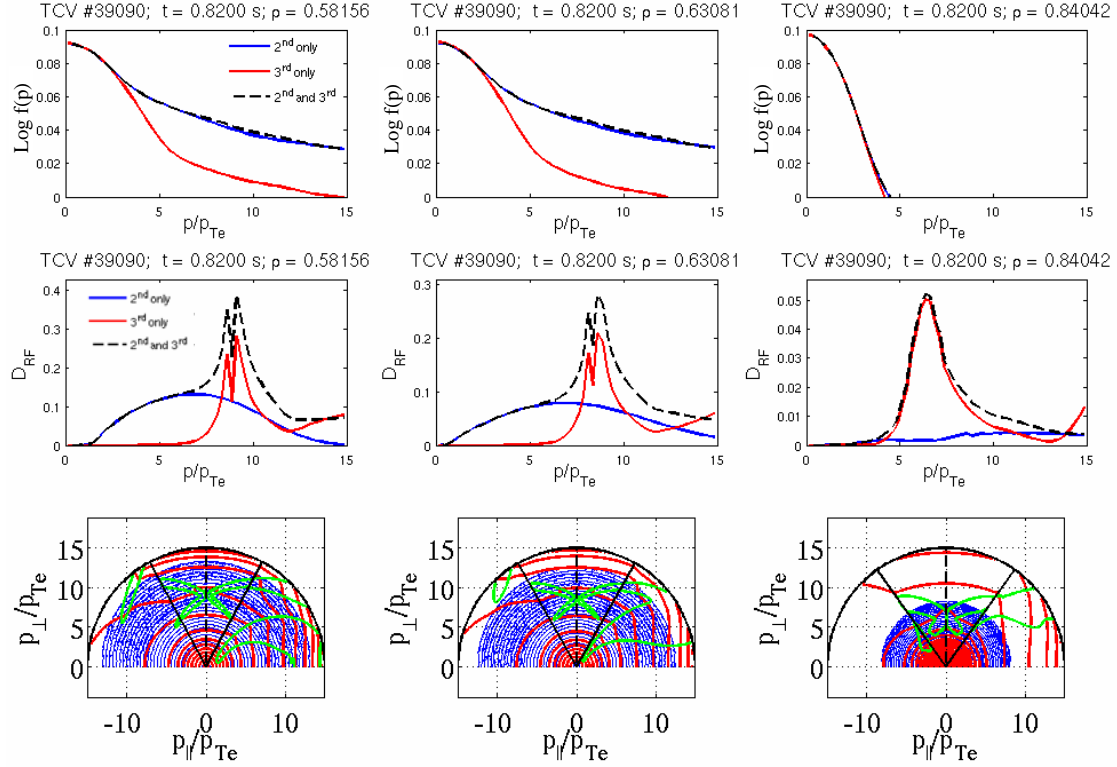


Figure 6.8. Electron distribution function $f(p)$ for TCV shot 39090 at $t = 0.82$ s as a function of the total momentum, at three different radial positions, first row; RF diffusion tensor (D_{RF}) as a function of the total momentum for the same radial positions, middle row; and in 2D momentum space, third row. The wave-particle interaction occurs in velocity space where $D_{RF} \neq 0$ (green region in the contour plots). The total momentum is normalized to the thermal momentum, defined as $p_{Te} = m_e v_{Te}$.

6.6. Modeling vs experiment: non-thermal bremsstrahlung analysis

We now examine the crucial question of whether an experimental signature of the synergy has been detected or can be detected. To this end we compare the HXR experimental signal from the vertically viewing camera with the simulated line integrated signal generated by the LUKE/R5-X2 bremsstrahlung calculator. The measured HXR emission is concentrated in the 16 – 40 keV energy range whereas photon statistics become poor at higher energy. We ignore the energies below 16 keV because signal here can still be dominated by thermal bulk emission and is also more sensitive to distortions due to Compton scattering [15].

The experimental HXR signal in the TCV shot 39090 decreases with time as the 2nd harmonic absorption moves off-axis as a consequence of the decreasing B field. This behaviour is well reproduced by simulations (Fig. 6.11) and is due to the decrease in power absorption as the resonance moves off-axis. The quantitative agreement is also

fair, to within 30% on all chords. However, a systematic mismatch is found in the profile shape: in the early EC phase ($t < 0.9$ s), the experimental profile peaks in the center (chords 16 – 17) whereas the simulated profile peaks off-axis (chord 11).

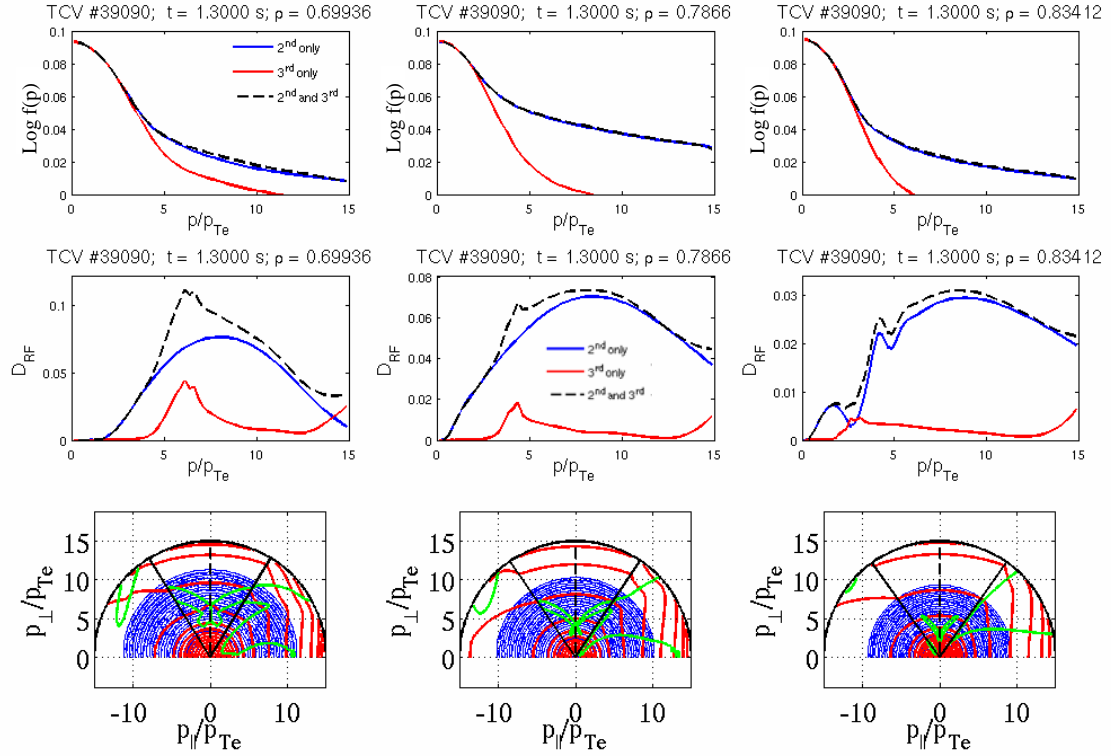


Figure 6.9. Electron distribution function $f(p)$ for TCv shot 39090 at $t = 1.3$ s as a function of the total momentum, at three different radial positions, first row; RF diffusion tensor (D_{RF}) for the same radial positions, middle row; and in 2D momentum space, third row. The wave-particle interaction occurs in velocity space where $D_{RF} \neq 0$ (green region in the contour plots). The total momentum is normalized to the thermal momentum, defined as $p_{Te} = m_e v_{Te}$

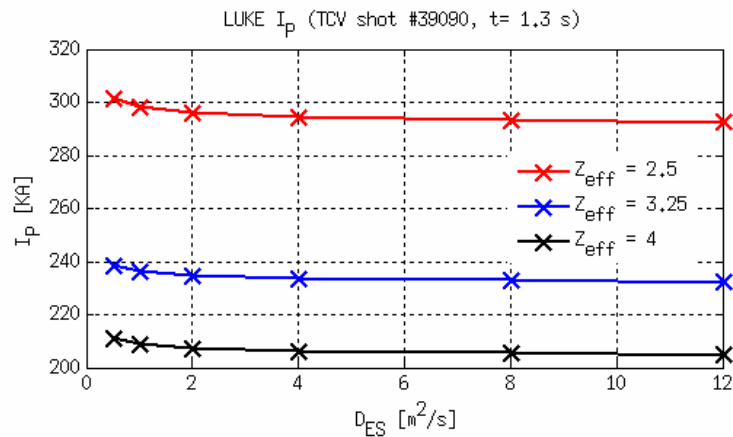


Figure 6.10. Influence of the effective charge (Z_{eff}) and fast electron diffusivity (D_{ES}) on the total driven current (I_p) in the TCV plasma 39090. The equilibrium parameters are taken at $t = 1.3$ s when $Z_{\text{eff}} = 3.25$; the experimental $I_p = 230$ kA at this time is well recovered in the simulation.

While a $\sim 30\%$ agreement can be considered acceptable, we may ask the question of whether transport tuning could improve the match further. In particular, we expect that a higher level of fast electron radial transport would help: it is even possible for radial diffusion to result in a centrally peaked HXR emission profile in the presence of off-axis heating, depending on the details of the phase-space dynamics [73]. Indeed, a better agreement at mid-radius is obtained with $D_{\text{ES}} = 2$ m²/s at $t = 0.8$ and $D_{\text{ES}} = 1$ m²/s at $t = 0.9$ (the optimum level of radial transport increasing with the coupled EC power); however, the central HXR level is not recovered, nor is a central peak observed, even when imposing an unrealistic $D_{\text{ES}} \sim 10$ m²/s. An excellent agreement between experiment and simulation is obtained instead by including a convective term (F_ψ) with a strong radial pinch $V_{r0} = -60$ m/s (Fig. 6.12). It is worth noting, once again, that even such a strong convection does not influence significantly the value of the total current predicted by the FP code. For $0.9 < t < 1$ s, a radial diffusivity of 1 m²/s is sufficient to reproduce the experimental results without the need for a convection term. Finally for $t > 1$ s when the dominant 2nd harmonic power deposition moves further off-axis, an outward convection ($V_{r0} > 0$) of typically 20 m/s along with a modest radial diffusion of $D_{\text{ES}} = 0.5$ m²/s would be needed for an optimal match with the experimental HXR radial profile.

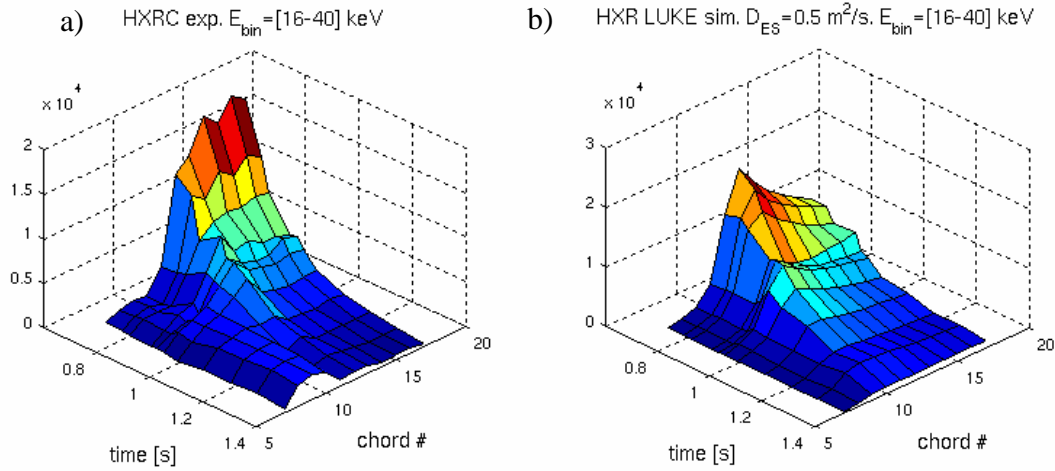


Figure 6.11. Shot 39090: (a) experimental data from HXR camera, (b) simulation results from LUKE/R5-X2 ($D_{\text{ES}} = 0.5$ m²/s).

We have also examined the possibility of matching the experimental HXR profiles by simply tuning the value of Z_{eff} and/or its radial profile within the experimental uncertainty, without assuming a finite level of fast electron radial transport. This possibility is however found to be precluded by the strong constraint exerted on Z_{eff} by the total plasma current value. For instance, to reproduce the central peaked HXR profile at $t = 0.8$ s a Gaussian radial profile peaking at $Z_{\text{eff}} = 12$ in the plasma center and rapidly decreasing to 1.5 at $\rho_V = 0.5$ would be required, giving rise to a total calculated current of 442 kA, incompatible with the experimental value of 240 kA. When the same exercise is

repeated at $t = 1.3$ s with a flat $Z_{\text{eff}} = 2.5$ radial profile, the result is a value of $I_p = 300$ kA that is $\sim 25\%$ more than the experimental value.

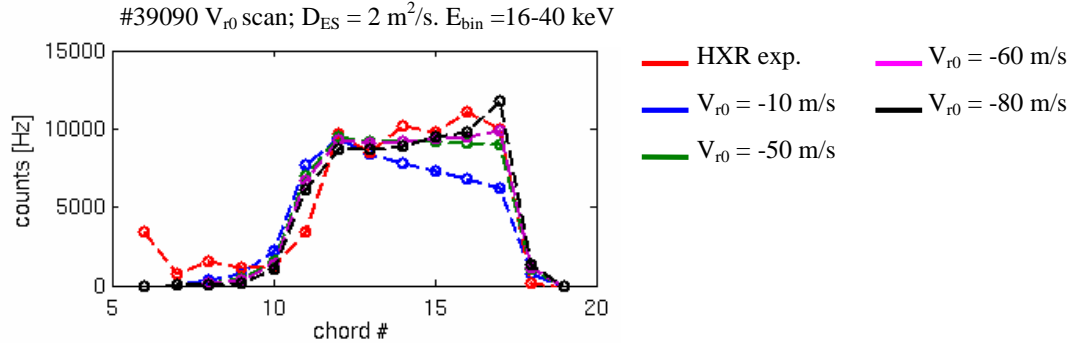


Figure 6.12. TCV plasma #39090, $t = 0.8$ s. Influence of inward convection ($V_{r0} < 0$) on the predicted LUKE/R5-X2 HXR level. The experimental HXR level (curve in red) on chords viewing the plasma core (14 – 17) is better reproduced by adopting $V_{r0} = -60$ m/s (curve in magenta). In these simulation $D_{\text{ES}} = 2$ m^2/s .

The minor peaks observed in the experimental HXR emission as a function of time on the more peripheral chords (section 6.3) must also be investigated individually to determine whether they may be related to the synergistic effect we are studying. The simulated HXR signal (Fig. 6.13b) indeed also shows a secondary peak at $t \sim 0.95$ s on chords #11 and #12. However, this peak is unrelated to synergy because it is still present even in simulations with the 2nd harmonic absorption considered alone. Further analysis reveals that this peak coincides in fact with a maximum in the experimental Z_{eff} (which of course is one of the inputs to the FP solver). By imposing a constant $Z_{\text{eff}} = 3$ in the simulations, this peak disappears (Fig. 6.13c). At $t \sim 1.3$ s (the time at which the nominal 2nd and 3rd harmonic absorption layers coincide), a peak in the HXR simulated profile is present for chords #9 to #13. This peak is also still present in simulations with only 2nd harmonic absorption, thus it, too, cannot be related to synergistic effects.

An alternative way of addressing the problem is to freeze the magnetic equilibrium and the input profiles at a given time (here at $t = t_X = 1.3$ s; $Z_{\text{eff}} = 3.25$; $D_{\text{ES}} = 0.5$ m^2/s) and scan the power deposition location radially by artificially varying the EC beam frequency. In this way the influence of variations in Z_{eff} , density and temperature is eliminated. By covering the 79 – 84 GHz frequency range we can emulate shot #39090, with the dominant 2nd harmonic deposition radius spanning the range from $\rho_V = 0.5$ to $\rho_V = 0.74$. As shown in Fig. 6.14, the simulated HXR signal behaves similarly, peaking at the same frequencies on the different chords, whether the 3rd harmonic absorption is taken into account or not: no visible synergy signature is detected.

Having determined that the local increases in HXR emission during the magnetic- field ramp are not caused by an increase in synergy, we turn to the question of whether any other experimental signature of synergy can be sought in the HXR data. For this, we use a methodology that mirrors the analysis of the synergy in the absorption rate in section 6: we seek to determine the increase in emission due to synergy, if any, and whether it is experimentally measurable. The question of measurability is examined by splitting the problem in two parts. First, to exclude effects directly due to variations in plasma parameters, we keep the plasma equilibrium and experimental profiles fixed, using experimental data at $t = t_X = 1.3$ s. In other words, only the vacuum magnetic field and

plasma current are varied in time. In a second stage, we shall study the dependence on plasma parameters separately. Where not otherwise indicated, the level of fast electron diffusivity used is $D_{ES} = 0.5 \text{ m}^2/\text{s}$.

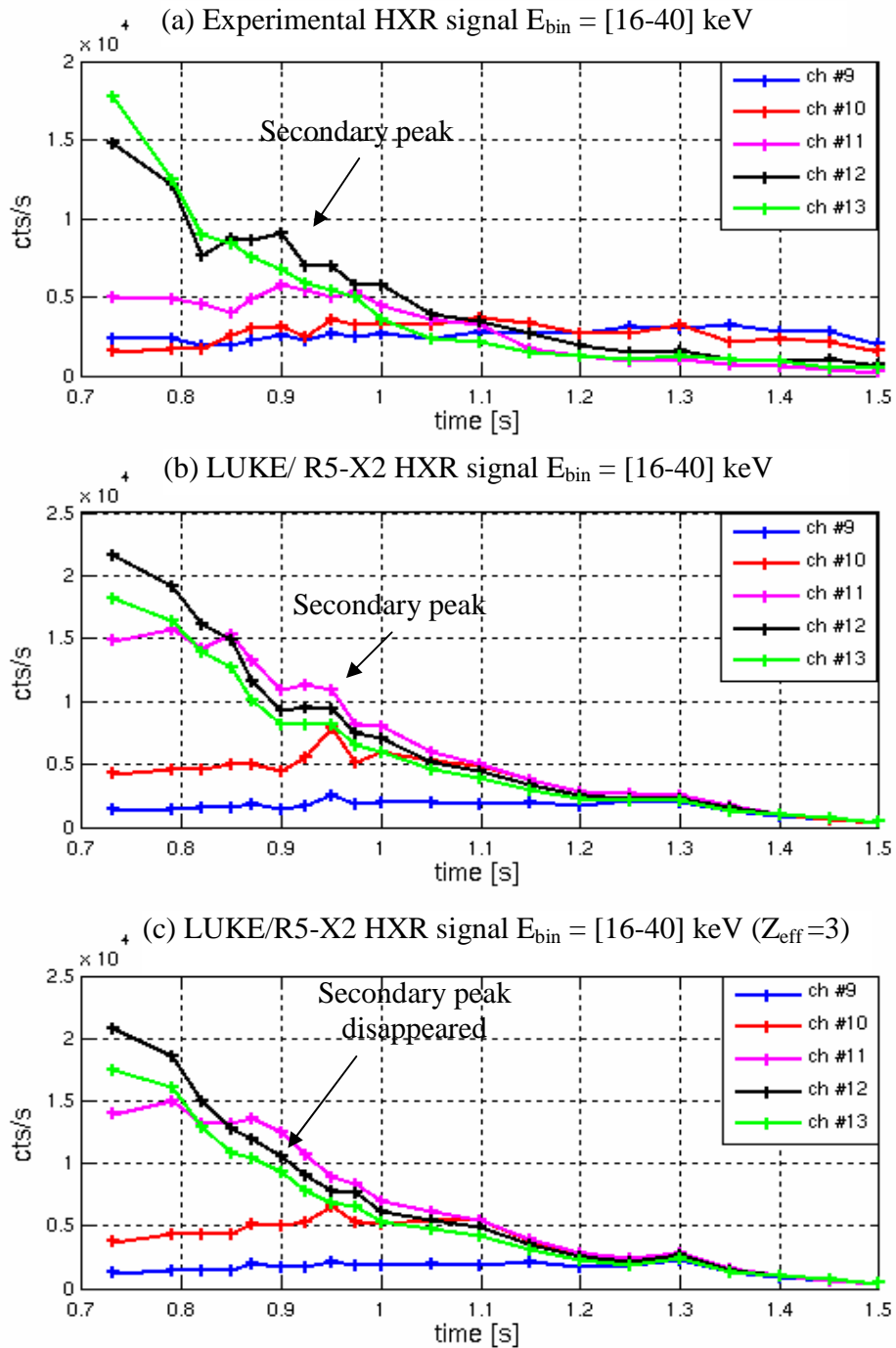


Figure 6.13. (a) Experimental vs. (b) simulated HXR profiles for TCV shot 39090. In (c) the simulation has been repeated with a constant $Z_{\text{eff}} = 3$. The LUKE simulations are performed with a fast electron radial diffusivity $D_{ES} = 0.5 \text{ m}^2/\text{s}$.

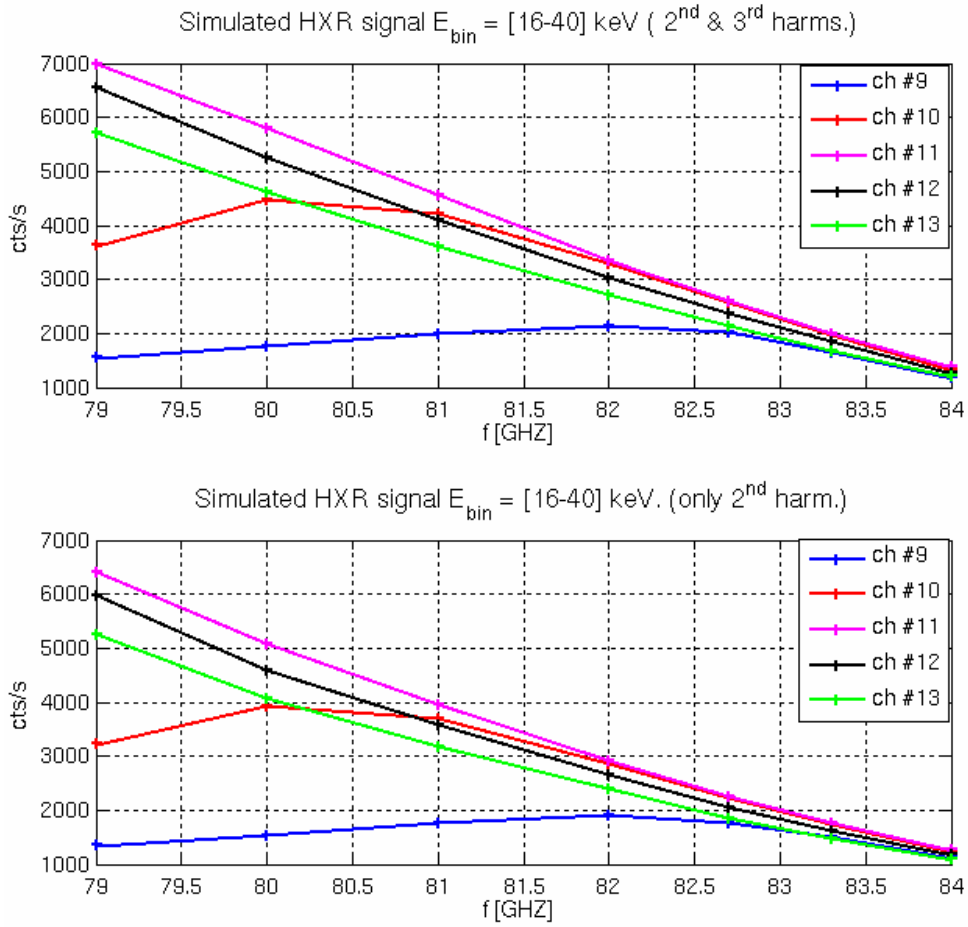


Figure 6.14. LUKE/R5-X2 simulations with EC frequency scan (79 – 84 GHz). Equilibrium profiles taken from TCV shot 39090 at $t = 1.3 \text{ s}$ ($Z_{\text{eff}} = 3$, $D_{\text{ES}} = 0.5 \text{ m}^2/\text{s}$).

According to LUKE/R5-X2 modeling, the synergy results in an increased HXR level on all peripheral chords (until $t = 1.35 \text{ s}$) and does not lead to a local maximum as a function of time. To quantify the variation of the HXR signal due to the synergy we define the following ratio:

$$\Delta\text{HXR}_{\text{syn}} = \frac{\text{HXR}_{[2\text{nd},3\text{rd}]} - (\text{HXR}_{[2\text{nd}]} + \text{HXR}_{[3\text{rd}]})}{\text{HXR}_{[2\text{nd}]} + \text{HXR}_{[3\text{rd}]}}$$

In Fig. 6.15 the value of $\Delta\text{HXR}_{\text{syn}}$ is shown for a few chords. The signal increase is $\sim 15\%$ for chords (#10–#12) viewing the plasma tangentially around mid-radius (where the EC wave is absorbed), whereas it is lower and even becomes negative for more central chords. The HXR emission in the plasma core is dominated by emission due to 3rd harmonic resonant electrons. A broad peak around $t_x = 1.3 \text{ s}$ is present on all chords. The

value of ΔHXR abruptly decreases afterwards, becoming everywhere negative at 1.5 s when the 2nd harmonic is very weakly absorbed in the plasma edge ($\rho \sim 0.75$) and does not contribute significantly any longer to the suprathermal population needed for the synergy.

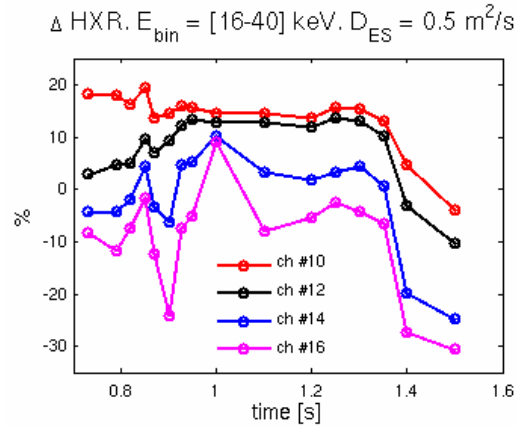


Figure 6.15. TCV shot 39090: calculated synergistic HXR variation on chords 10, 12, 14 and 16. $D_{\text{ES}} = 0.5 \text{ m}^2/\text{s}$.

Next we examine the parametric dependence of the HXR synergistic increase on experimental parameters such as the plasma density, the total injected power and the level of fast electron radial transport, with the aim of gaining insight into the sensitivity of the experimental signatures of synergy to variations in these parameters.

The electron density in particular is found to be a very sensitive parameter influencing the synergy. Keeping the normalized density profile fixed at the experimental shape at time $t = t_x = 1.3 \text{ s}$, and varying the overall density level about the experimental value, we find that $\Delta\text{HXR}_{\text{syn}}$ for all peripheral chords (#7–13) is actually maximum at the experimental value (Fig. 6.16(c,d)). Its maximum value is on chord 10 and is equal to 15%. The experimental conditions ($\langle n_e \rangle = 1.5 \times 10^{19} \text{ m}^{-3}$), therefore, are particularly favourable. We find, however, that a 10% density variation results in a 30% variation in the absolute HXR emission (Fig. 6.16). A 10% density variation is of the same order of magnitude as the experimental error on the local density measured by Thomson scattering and can consequently easily mask the experimental evidence for a 2nd/3rd harmonic synergy in the HXR emission, which does not exceed 20% (Fig. 6.15). We must conclude that the synergy effect is not measurable in our experimental conditions.

We address now the effect of the power deposition on the synergy, to determine whether higher injected power could enhance the effect to the point of making it clearly measurable. Once again, we fix the magnetic equilibrium and the input profiles to the Fokker-Planck code, taking them from experimental data at $t = t_x = 1.3 \text{ s}$, and we artificially increase the injected EC power. We also repeat this operation for different values of the fast electron radial diffusivity D_{ES} from 0 to $5 \text{ m}^2/\text{s}$. The results of this series of simulations are shown in Fig. 6.17.

The synergistic gain in the HXR emission initially grows with power for all the values of D_{ES} considered. At higher injected power, the quasilinear flattening of the electron distribution function begins to play an important role, reducing the dominant 2nd

harmonic absorbed fraction, which ultimately also reduces the excess fast electron population attributable to the 3rd harmonic. This translates in a degradation of $\Delta\text{HXR}_{\text{syn}}$ with power beyond a given threshold. We remark that by increasing the level of fast electron radial transport (a higher level of transport arguably being reasonable with increased P_{abs}), the decrease of $\Delta\text{HXR}_{\text{syn}}$ begins at higher injected power (Fig.6.17a). Additionally, the absolute value of $\Delta\text{HXR}_{\text{syn}}$ increases with the diffusivity. An inspection of the distribution function dynamics suggests that this is due to the greater spatial overlap between the effective resonant regions for the two harmonics.

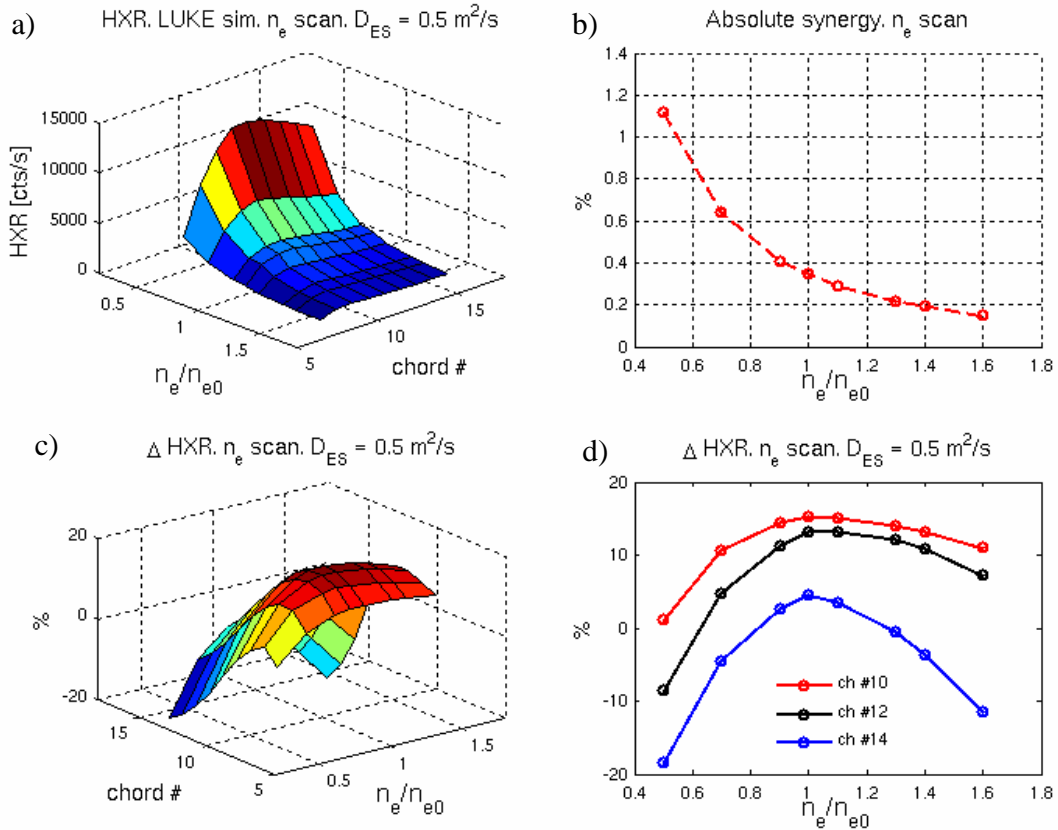


Figure 6.16. TCV shot 39090: calculated synergy dependence on plasma density, with equilibrium profile shape taken at $t = 1.3 \text{ s}$: (a) predicted HXR emission ($E_{\text{bin}} = 16\text{-}40 \text{ keV}$) to be measured by the vertically viewing camera as a function of normalized density n_e/n_{e0} ; (b) absolute synergy S_3 ; (c-d) synergistic variation $\Delta\text{HXR}_{\text{syn}}$.

However, the significant flattening of the distribution function at high power actually results in a decrease of the absolute level of power absorption synergy S_3 with diffusivity, as shown in Fig. 6.17b, even as the fast electron population is enhanced. Also, S_3 increases linearly with the injected power, confirming and extending the result shown in Fig. 6.6.

The combination of a sufficiently high level of diffusivity and injected power results in a $\Delta\text{HXR}_{\text{syn}}$ that can exceed 30%, making it possible in principle to measure experimentally. This is not currently possible in our configuration on TCV, since the required equatorial

injection limits the maximum injected power to 1 MW. More fundamentally, the predicted HXR emission level depends strongly on the transport level and even on the details of the transport model, which can be studied experimentally only in limited and semi-quantitative fashion. An unequivocal confirmation of a synergy effect would then, once again, require a hypothetical direct comparison of scenarios with and without synergy, with otherwise identical plasma parameters.

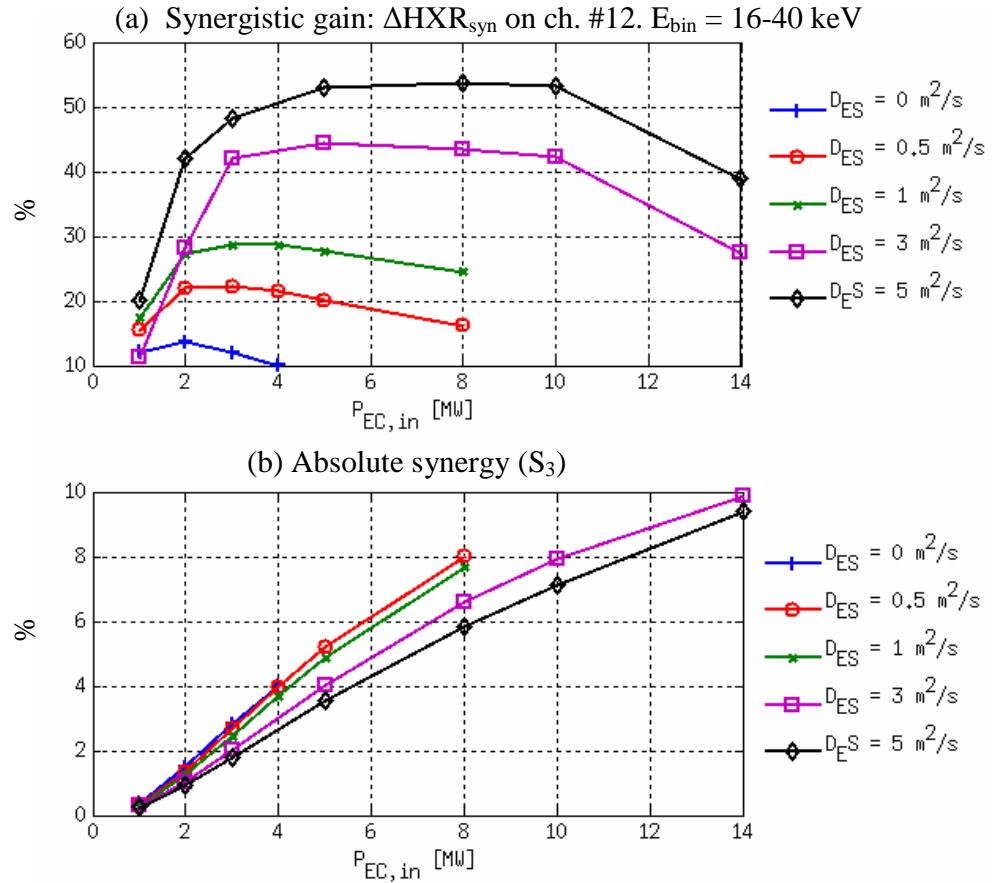


Figure 6.17. TCV shot 39090, equilibrium profiles taken at $t = 1.3$ s: (a) calculated synergistic HXR variation for chord #12 and (b) absolute level of synergy (S_3) as functions of the injected EC power for different levels of fast electron radial diffusivity.

6.7. Conclusions

A study of the interplay between 2nd and 3rd harmonic EC wave absorption at the same frequency, both experimentally in the TCV tokamak and through numerical modeling, has been discussed in this chapter. The TCV experimental configuration enables the simultaneous absorption of the injected EC wave at two different harmonics in the plasma; the 2nd harmonic on the HFS and the 3rd harmonic on the LFS of the magnetic axis. Extensive simulations with the LUKE Fokker-Planck code have evidenced an enhanced 3rd harmonic absorption in the presence of 2nd harmonic heating. This

enhancement is mediated by the presence of a significant suprathermal electron population generated by the 2nd harmonic electron acceleration. Complex conditions of alignment for the wave-particle interactions in both physical space and velocity space must be met for the synergy to occur. The assumed level of cross-field fast electron transport is also found to have a significant influence on the synergy. The process of characterizing these conditions has shed light on the fundamental processes underlying high-power EC wave-particle interactions.

Because of the intrinsically poor 3rd harmonic absorption, no direct measurement of the 3rd harmonic absorption, much less of any synergistic enhancement, is possible. The HXR emission has been investigated as a possible candidate for the indirect manifestation of a possible synergy. The predicted synergistic HXR enhancement in the TCV experimental conditions however is modest, i.e. less than 25%, precluding an unequivocal detection, since such a variation can be easily masked by fluctuations in the electron density and effective charge. More fundamentally, the uncertainties in the model, including - critically - the nature and level of suprathermal electron transport, preclude an unambiguous quantitative comparison even in more extreme conditions (high power and higher diffusivity) in which a stronger HXR enhancement could theoretically occur. The nature of the experimental setup also excludes a direct comparison with and without synergy in the same conditions.

The material presented in this chapter has been recently submitted to Plasma Physics Controlled Fusion [74]

7 Design of a HXR tomographic spectroscopic camera system (HXRS) for TCV

7.1 Introduction

The TCV plasma is routinely heated by means of ECRH; moreover ECCD is extensively used to tailor the current profile. With the injection of EC waves a suprathermal electron population is generated in an energy range from a few tens to a few hundred keV, resulting in hard X-ray (HXR) bremsstrahlung emission. In this chapter we discuss the design and the development of a new set of hard X-ray cameras for the investigation of suprathermal dynamics in TCV with unprecedented spatial and temporal resolution. Our aim is to open the possibility of a full 2D tomographic reconstruction of the HXR emission in the poloidal plasma cross-section (section 7.2), which will be the first such diagnostic for a non circular plasma. For this purpose, a minimum of 3 HXR cameras are needed; the final number of cameras (four) has been determined on the basis of a lengthy quantitative assessment of the effective improvements that can be obtained with each additional camera. Additionally, our goal is to develop a highly flexible system, in particular to access emission both perpendicular and parallel to the magnetic field. We will therefore investigate mechanical arrangements that maximize the flexibility and adjustability of the diagnostic.

Firstly we introduce some basic concepts on tomography in toroidally confined plasma (section 7.2), followed by a description of the detectors available for HXR detection (section 7.3). In section 7.4 we present the results of an extensive series of tests that have led to the choice of detectors for the new diagnostic.

A conceptual design of up to nine cameras was carried out (sections 7.5 to 7.10), based on a novel tungsten collimator design adapted from the Soller collimator concept (section 7.5) [75]. The choice of the vacuum windows and filters is discussed in section 7.6. The problems related to gamma ray emission and neutron flux from the plasma and the resulting shielding requirements are the subject of section 7.7. The detector response, including fluorescence from the collimator, was modelled with Monte Carlo codes as discussed in sections 7.8 and 7.9. Extensive tomographic reconstruction simulations were performed to optimize the geometry and the number of cameras to be built (section 7.10). A trade-off between the poloidal fan coverage and other constraints imposed by the camera design (mainly the limited number of detectors) results in a space resolution of $\sim 2\text{-}3$ cm at the center of the TCV vacuum vessel. The time resolution is to be dictated exclusively by photon statistics and is typically ~ 1 ms. Both space and time resolution are adequate for investigating EC wave power deposition and associated current and energy diffusion in TCV. In particular the time for slowing down of fast electrons is typically in the order of a few ms [52].

7.2 Tomography in plasmas

Tomography is a powerful method that enables a 2D image reconstruction of the local emissivity, making use of line-integrated emission data on multiple chords (or lines of sight). In our case the plasma constitutes the emitting region we want to study.

The fundamentals of tomographic reconstruction were pioneered by Cormac [76, 77] in the context of medical imaging. Plasma physics has already greatly benefited from tomographic techniques: applications to soft X-ray emission [78, 79], magnetic reconstruction and bolometry are widespread in contemporary fusion experiments [80].

In an X-ray tomographic system, measurements of the plasma emissivity $g(r, \theta)$ along collimated chords are carried out by means of detectors mounted in a set of camera arrays. Each detector (i) thus measures the integrated emission along its associated chord:

$$f_i(p, \phi) = \int_{L_i} g(r, \theta) dl \quad (7.1)$$

this quantity, also called “chord brightness”, is an integral evaluated along the total length of the line of sight L_i (Fig. 7.1)

Once the multiple line-integrated measurements are collected, the data need to be inverted in order to recover the local spatial emissivity. Different methods for tomographic inversion have been developed; a review of different methods can be found in [78, 79]. The basic concept is that 2D structures can be discerned better and better as more separate viewpoints are employed, the minimum number of points being two (with the simple intuitive advantage of stereoscopic vision). The third dimension is collapsed by the inherent azimuthal symmetry of the system.

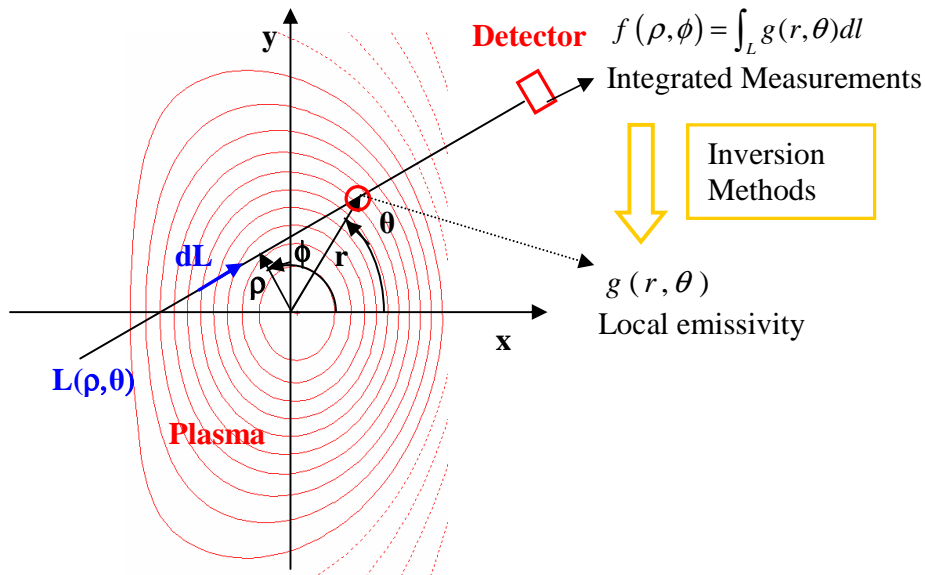


Figure 7.1. The local emission $g(r, \theta)$ can be deduced by inverting the line integrated measurements $f(\rho, \Phi)$.

The aim of a tomography measurement is to identify the spatial structure of the plasma X-ray emission with adequate spatial and temporal resolution; the spatial resolution is determined by the chord spread, whereas the time resolution is primarily determined by the photon statistics, as well as by the characteristics of the detector and of the acquisition system. If spectroscopic information is also required, the resolution in energy is also related to the detector characteristics. A minimum number of cameras observing the plasma from different angular positions (and thus different angular views) is required for spatial structure identification since poloidal periodic structures characterized by the poloidal mode number m can only be resolved by a minimum of $m+1$ cameras.

Figure 7.2 depicts an example of two cameras with their respective lines of sights (on the left). On the right-hand side, three cartoons of a circular plasma give an intuitive image of the poloidal mode number (m) related to a particular structure in the plasma emission: $m=0$ implies axial symmetry, and in this case a single camera is able to reconstruct the emissivity via a simple Abel inversion [65]. An axial asymmetry in emissivity characterizes an $m=1$ mode, while a doublet structure is characteristic of an $m=2$ mode; in order to resolve these two emission patterns a tomographic reconstruction needs two and three cameras respectively. This constraint can be readily generalized to higher poloidal mode numbers ($m>2$).

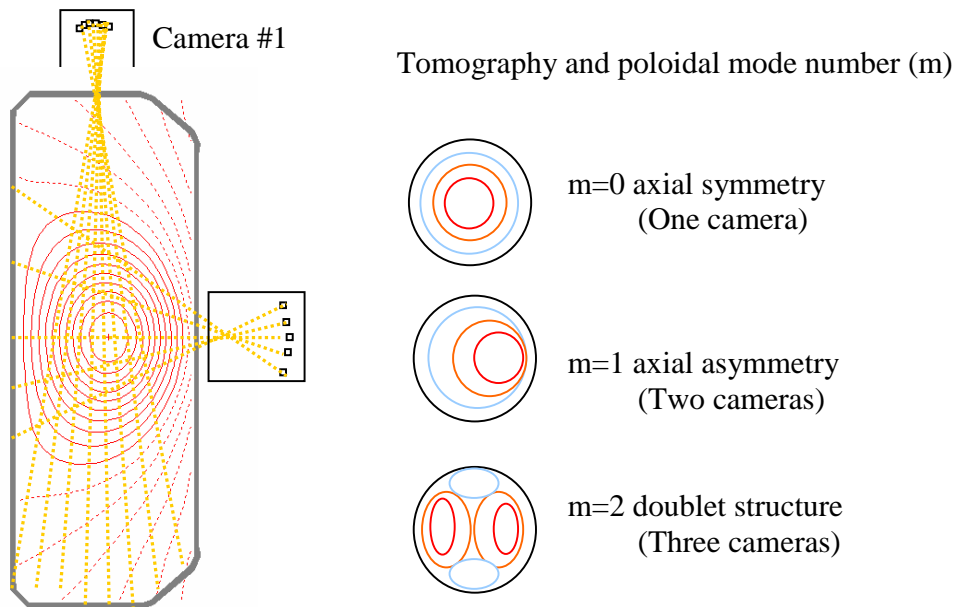


Figure 7.2 Left: example of a tomographic 2-camera setup in TCV. Right: representation of plasma emissivity and related poloidal mode numbers ($0 < m < 2$); the radiation emission intensity isocontours are labelled in red (high intensity emission), orange (medium intensity emission) and blue (low intensity emission).

The interest of a time resolved tomographic reconstruction lies in the possibility to visualize and determine quantitatively the detailed evolution of the 2D shape of the emitting structure in the plasma as a result of diffusion phenomena, instabilities or other perturbations as well as of ECRH and ECCD deposition.

7.2.1 The minimum Fisher tomographic reconstruction algorithm

A tomographic inversion algorithm is used to recover the information about the unknown emission function g making use of the measured chord brightness (eq. 7.1). In the present work we adapted a minimum Fisher regularisation (MFR) algorithm previously developed in TCV for soft X-ray tomography [79] by including the HXR camera geometry under study. The tomographic reconstruction problem is discretized so that the search for the g function is performed on a rectangular pixel grid covering the poloidal plasma cross-section of interest. The number of pixels in the reconstruction grid is given by $n_p = n_R \times n_Z$ (see Fig. 7.3 b). The emission g is assumed to be constant over the pixel area; to satisfy this assumption the pixel size must be sufficiently small, while at the same time the number of pixels must be not too large to ensure a reasonable computing time (usually a few seconds). The tomographic inversion problem (eq 7.1) takes the matricial form

$$\mathbf{f} = \mathbf{T} * \mathbf{g} \quad (7.2)$$

where $\mathbf{f} = (f_1, \dots, f_{n_d})$ is the vector containing the measured chord brightness along each line of sight, the elements in the \mathbf{T}_{ij} ($i=1, \dots, n_d$ and $j=1, \dots, n_p$) matrix are the length of the i -line of sight in each given pixel j while $\mathbf{g} = (g_1, \dots, g_{n_p})$ is a vector containing the value of the local emission in a each given pixel. The tomographic reconstruction process is illustrated in Fig. 7.3.

In magnetically confined plasma devices, because of spatial limitations, it is usual to work in conditions where $n_d < n_p$; the problem of eq. 7.2 is consequently underdetermined and a direct inversion of \mathbf{T} is not possible. To constrain the solution we use a modified least squares inversion method based on the minimization of the Fisher

information $I_F = \int \frac{g'(x)}{g(x)} dx$. The quantity to minimize in this case is

$$\Phi = \frac{\chi^2}{2} + \alpha R \quad (7.3)$$

where $\chi^2 = (\mathbf{T} * \mathbf{g} - \mathbf{f})' (\mathbf{T} * \mathbf{g} - \mathbf{f})$ is the least squares error, αR is the regularization term defining the smoothness of the solution and the t index denotes the matricial transposition. The MFR algorithm minimizes the Fisher information R by iterating over many linear regularization steps (n).

The positive integer α regulates the smoothness of the solution provided by the regularizing functional R which is conveniently defined by $R = \mathbf{g}^t * \mathbf{H} * \mathbf{g}$ where

$$\mathbf{H}^{(n)} = \nabla_R^t * \mathbf{W}^{(n)} * \nabla_R + \nabla_Z^t * \mathbf{W}^{(n)} * \nabla_Z \quad (7.4)$$

and

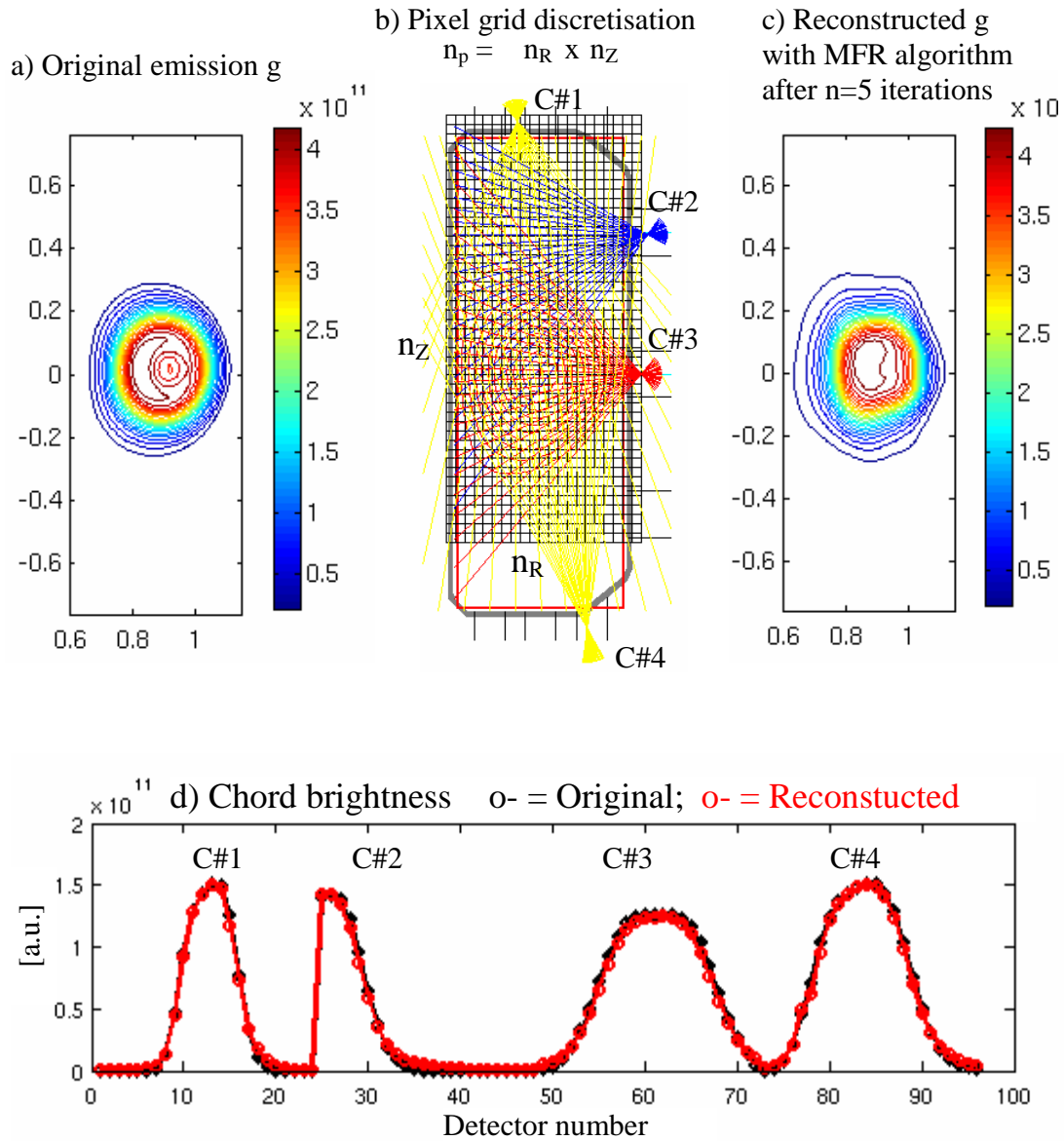


Figure 7.3 An example of tomographic reconstruction using the minimum Fisher regularization algorithm with a four camera arrangement: $n_d = 4 \times 24 = 96$, $n_p = 21 \times 46 = 966$ (3cm square pixels). a) original emission, b) reconstruction pixel grid with lines of sights, c) resulting reconstructed emission, d) comparison between the chord brightness measured on the original emission pattern (red) and the same quantity calculated on the reconstructed emission pattern (black).

$$\begin{cases} W_{ij}^{(n)} = \frac{1}{g^{(n)}} \delta_{ij} \\ \mathbf{W}^{(0)} \equiv \mathbf{1} \end{cases} \quad (7.5)$$

Minimizing the functional Φ is then equivalent to solving the equation through the iteration $(\mathbf{T}^t * \mathbf{T} + \alpha \mathbf{H}^{(n)}) * \mathbf{g}^{(n+1)} = \mathbf{T}^t * \mathbf{f}$ until $\mathbf{g}^{(n+1)} \approx \mathbf{g}^{(n)}$. Usually a few iteration steps are sufficient for the solution to converge, as shown in Fig. 7.3.

The MFR solution for g on a pixel grid has the following interesting features:

- The MFR solution is the smoothest possible one; the smoothing is higher in regions of low emission.
- Better results than other algorithms if the emission is not too pulse-like.
- Good stability with respect to noisy data.
- No assumption on the plasma shape and location in the reconstruction region.

The solution is well suited for tomographic reconstruction of the hard X-ray bremsstrahlung emission which is expected to be more peaked in the plasma core than off axis.

An example of tomographic reconstruction using the MFR algorithm on a 3 cm square pixel grid ($n_p = 966$) is shown in Fig. 7.3; the test uses four cameras equipped with 24 detectors each ($n_d = 96$).

7.3 Semiconductor detectors for hard X-ray detection

7.3.1 HXR detection principles and detector materials

Only semiconductor detectors were considerable for the TCV HXRS diagnostic, The main alternative, scintillators coupled with photomultipliers, was ruled out by their need for bulky magnetic field shielding, which is incompatible with the space constraints around the TCV ports.

In general, solid-state X- and gamma-ray detectors operate by exploiting the fact that an incident photon will, through some interaction in the detector volume, create a charge pulse that can be detected. This charge pulse consists of electrons and holes, which are then separated under the influence of an applied electric field.

The energy gap E_g , the energy necessary to displace an electron from the valence band to the conduction band, as well as the energy for electron-hole charge pair creation E_{pair} , are characteristic of each semiconductor material.

The interaction between radiation and material can be subdivided into the following events:

- 1) Photoelectric absorption
- 2) Compton scattering
- 3) Pair production

Photoelectric absorption is the ideal process for detector operation. All of the energy of an incident photon is absorbed by one of the orbital electrons of an atom within the detector material, which then breaks free of the atom. The resulting photoelectron will have a kinetic energy equal to that of the incident photon minus the atomic binding energy of the electron. In a semiconductor device the photoelectron will lose its kinetic energy via Coulomb interactions with the semiconductor's lattice, creating many electron-hole pairs. This avalanche occurs over very small temporal and spatial scales (ps, nm) so the charges are essentially generated instantaneously at the location of the photon absorption. The number of electron-hole pairs created will be proportional to the energy of the incident photon.

Compton inelastic scattering involves the deflection of the impinging photon, where some of its energy is lost to the outer atomic electron with which it collided. The photon in this case transfers only a fraction of its total energy, so that the resulting scattered electron will produce a number of electron-hole pairs depending on the particular Compton interaction, but in all cases smaller than the photoelectric production; the scattered photon, depending on its residual energy, may eventually be absorbed photoelectrically, resulting in another lower-energy detection event.

If the energy of the incident photon is above 1.02 MeV, an electron-positron pair may be created. Any energy in excess of this amount can go into the kinetic energies of the electron and positron. The positron created in such an interaction is immediately annihilated with an electron present in the material, resulting in two 511 keV photons that can subsequently undergo one of the former interactions (Compton or photoelectric).

Our goal is to perform spectrometric measurements and we are thus interested mostly in the photoelectric interaction. The photoelectric interaction probability of a photon with a detector material of atomic number Z is proportional to Z^n where $4 < n < 5$; therefore materials with high atomic number will have significantly higher sensitivity to gamma- and X-ray photons than low Z materials. The attenuation coefficients for photoelectric absorption, Compton scattering, and pair production for silicon, germanium, cadmium telluride and mercuric iodide are shown in Fig. 7.4.

Compound high Z semiconductor materials, such as CdTe, CdZnTe (CZT), HgI₂, GaAs, and PbI₂, offer advantages in HXR detection compared to classic Si or Ge detectors (see table 7.1), as their higher energy gap results in a lower noise level due to thermal electron-hole generation. The probability per unit time that an electron-hole pair is thermally generated is given by [81]

$$p(T) = cT^{3/2} \exp\left(-\frac{E_g}{2kT}\right)$$

where T is the absolute temperature, E_g the band gap energy, k the Boltzmann constant and c a proportionality constant characteristic of the material. In any case the energy per electron-hole pair creation E_{pair} remains low compared to the impinging photon energy in the HXR range, so any photoelectric interaction produces many charge carriers with beneficial effects on the attainable energy resolution.

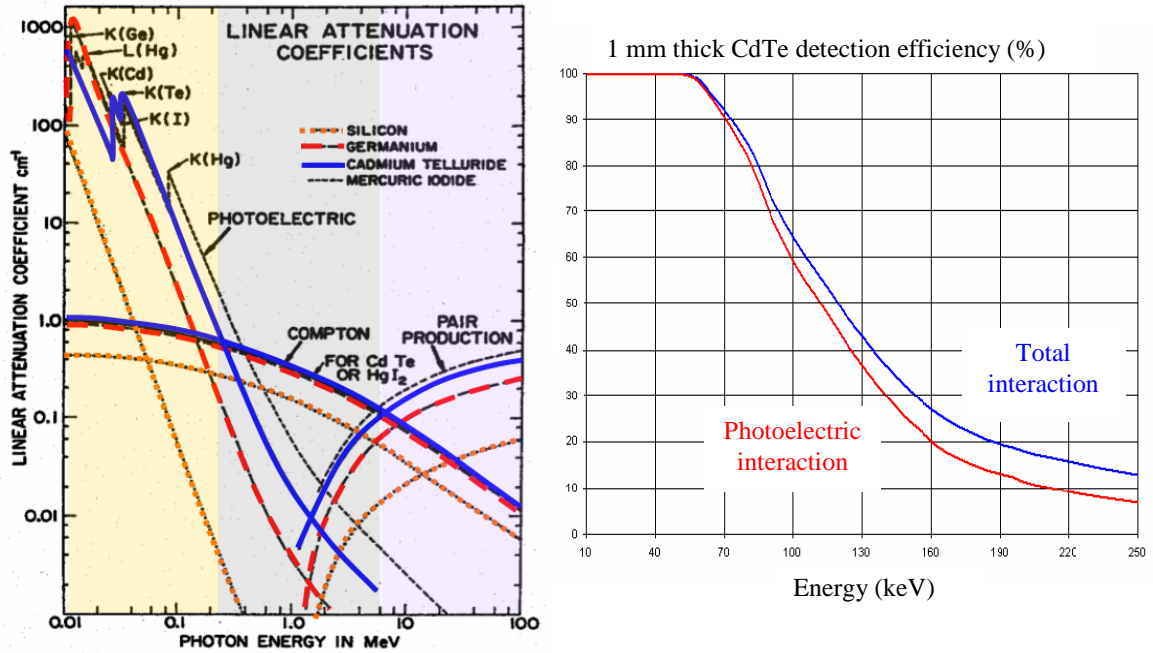


Figure 7.4 Linear attenuation coefficient (μ) for different semiconductor materials as a function of the impinging photon energy (left), showing also the contributions of the individual radiation-matter interaction phenomena. Total interaction efficiency vs photoelectric efficiency of CdTe (right); it is worth noting that $\mu_{ph} \geq \mu_{Compton}$ up to $E_{photon} = 250$ keV.

Material	Si	Ge	CdTe	CZT	GaAs	PbI ₂	HgI ₂
Z	12	32	48/52	48/30/52	31/33	82/53	80/53
ρ (g/cm ³)	2.33	5.33	6.06	~6	5.32	6.2	6.4
E_{gap} (300 K) eV	1.12	0.72	1.52	1.6	1.42	2.55	2.13
E_{pair} (eV)	3.6	2.98	4.43	5	4.3	4.9	4.3
μ_e (cm ² /Vs)	1450	36000	1100	1300	>8000	8	100
μ_h (cm ² /Vs)	450	42000	100	120	400	2	4
τ_e (s)	>10 ⁻⁴	>10 ⁻⁴	10 ⁻⁶	10 ⁻⁶	-	10 ⁻⁶	7x10 ⁻⁶
τ_h (s)	>10 ⁻⁴	>10 ⁻⁴	10 ⁻⁶	2x10 ⁻⁷	-	3x10 ⁻⁷	3x10 ⁻⁶

Table 7.1 Comparison between characteristic parameters of some semiconductor materials used for HXR detection: atomic number (Z), density (ρ), energy gap (E_{gap}), energy for electron-hole pair generation (E_{pair}), electron and hole mobilities ($\mu_{e,h}$) and electron and hole trapping times ($\tau_{e,h}$).

The space limitations and access constraints of the TCV tokamak make room-temperature operation desirable in order to avoid the need for bulky cooling equipment; this suggests the choice of high E_g semiconductor diode detectors [82, 83], such as CdTe, Cd_{1-x}Zn_xTe (CZT) or HgI₂. CdTe and CZT detectors in particular are a well established technology with applications to nuclear medicine[84], astronomy [85] and nuclear fusion [86-87].

7.3.2 Charge collection properties of CdTe, CZT and HgI₂ detectors.

The transport of carriers within the detector volume can be affected by the presence of crystal lattice defects and impurities, which can cause charge trapping and result in a reduction of the height of the electric pulse signal seen at the output. This kind of effect concerns mainly the drift of holes. The purity and uniformity of the detector material clearly play an important role in guaranteeing good carrier transport.

The main parameters characterizing charge trapping are the charge mobility μ and the charge trapping time τ (reported for several detector materials in table 7.1), from which the charge trapping length λ can be derived.

Here we briefly compare the charge carrier transport properties of CdTe, CZT and HgI₂ based detectors. In this section, we consider a cubic 2 mm thick detector. Figure 7.5 shows the geometry we refer to in this section.

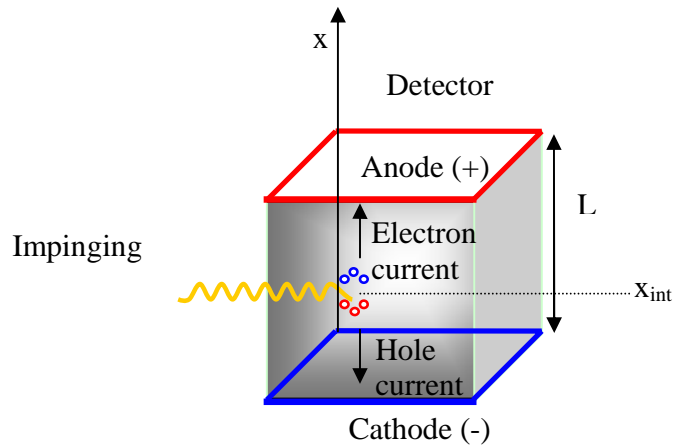


Figure 7.5 Schematic view of the charge generation and collection in a solid state semiconductor detector.

- Charge drift time

The charge drift time (T_D) is the characteristic time scale for complete charge collection at the detector electrodes and is also the duration of the hole and electron current flow. Here we define $T_D = [l/(\mu E)]$, where l is the distance traveled by carriers from the location of the photon interaction (x_{int}) to the relevant electrode and E is the electric field applied over the detector volume. For simplicity we take the electric field as constant and uniform all over the detector volume. Figure 7.5 depicts the geometry considered. The drift times of electrons and holes are linked to the characteristic values of their mobility:

$$T_{De} = [(L - x_{\text{int}})/(\mu_e E)], \quad T_{Dh} = [x_{\text{int}}/(\mu_h E)].$$

Representative curves as functions of voltage for different materials are given in Fig. 7.6a. In order to avoid pile up, we are interested in collecting the total charge generated, as a result of a single photon interaction into the detector volume, in a time not longer than the reciprocal of the expected photon count rate. If we expect, e.g., a 1 MHz count rate we need the drift time not to exceed 1 μ s. In this case CdTe and CZT should be operated at $V \geq 200$ V while in any case HgI₂ does not guarantee complete hole collection even with higher polarization. Clearly high detector bias helps to reduce the carrier collection time.

- Charge trapping length

The charge trapping length has the same meaning as a mean free path for the electric carriers before they hit a trapping location.

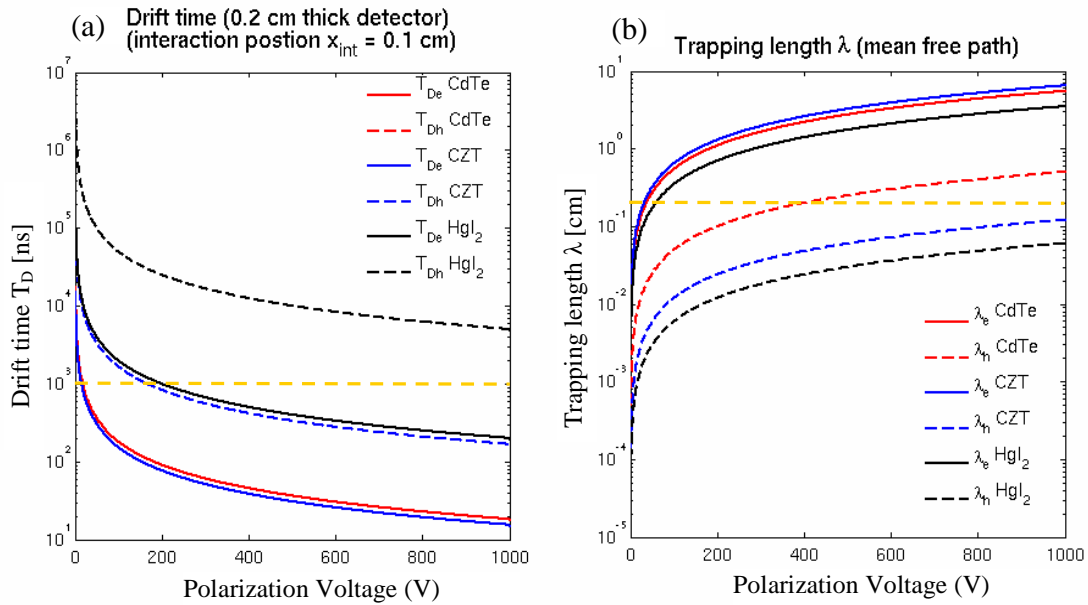


Figure 7.6 (a) drift time as a function of the bias voltage (V) for electrons (T_{De}) and holes (T_{Dh}) in three different detector materials: CdTe, CZT and HgI₂ (b) trapping length as a function of the bias voltage (V) for electrons (λ_e) and holes (λ_h) for the same detector materials. A 2mm thick detector is considered in each case, with photon interaction occurring in the center of the crystal. Dashed curves refer to holes while solid curves refer to the electrons. The hole drift time of CdTe coincides exactly with the black curve of the electron drift time of HgI₂; only the latter is visible in the diagram. The yellow dashed line in (a) indicates $T_D = 1 \mu$ s, the maximum drift time accepted if 1 MHz photon events have to be detected without pile up in the collected signal. Voltage bias exceeding 200 V must be applied to keep the drift time lower than 1 μ s in CdTe and CZT; HgI₂ exhibits a drift time exceeding $T_D = 1 \mu$ s in the entire voltage bias range considered (unless measures are taken to suppress hole collection altogether). In (b), the yellow dashed line depicts $\lambda = L = 2$ mm, which corresponds to the detector thickness. We remark that CdTe is the only detector material that matches the condition $\lambda \geq L = 2$ mm simultaneously for both electrons and holes when the bias exceeds 400 V; this is a necessary condition in order to avoid carrier trapping in the detector volume.

The electron trapping length $\lambda_e = \mu_e \tau_e E$ and the hole trapping length $\lambda_h = \mu_h \tau_h E$ are shown in Fig. 7.6b for the three detector materials. If we want to operate our detector

with maximum efficiency we should keep the trapping length longer than the typical detector size (L). For a 2 mm thick detector this means that again a bias voltage $V \geq 200$ V has to be applied in CdTe, while CZT and HgI_2 suffer from a short trapping length. If the detector size increases the drift distance also became longer and carrier trapping more severe. On the other hand the detector must be thick enough to guarantee sufficient detection efficiency in the energy range of interest. In this work we consider a 2 mm thick CdTe detector to be a good tradeoff, providing detection efficiency always over 20% up to 250 keV and showing a good charge collection behavior.

The charge collection efficiency (η) of a given solid-state semiconductor detector can be quantified by the ratio η between the total charge appearing at the detector electrodes (Q) and the charge generated by the given photon-detector interaction event (Q_0). For a uniform internal electric field this can be expressed by the Hecht relation [88]:

$$\eta(x) = \left(\frac{\lambda_e}{L}\right) \left[1 - \exp\left(-\frac{(L-x)}{\lambda_e}\right)\right] + \left(\frac{\lambda_h}{L}\right) \left[1 - \exp\left(-\frac{x}{\lambda_h}\right)\right]$$

where $x = L - x_{\text{int}}$ is the distance of the photon interaction from the cathode (see Fig. 7.7).

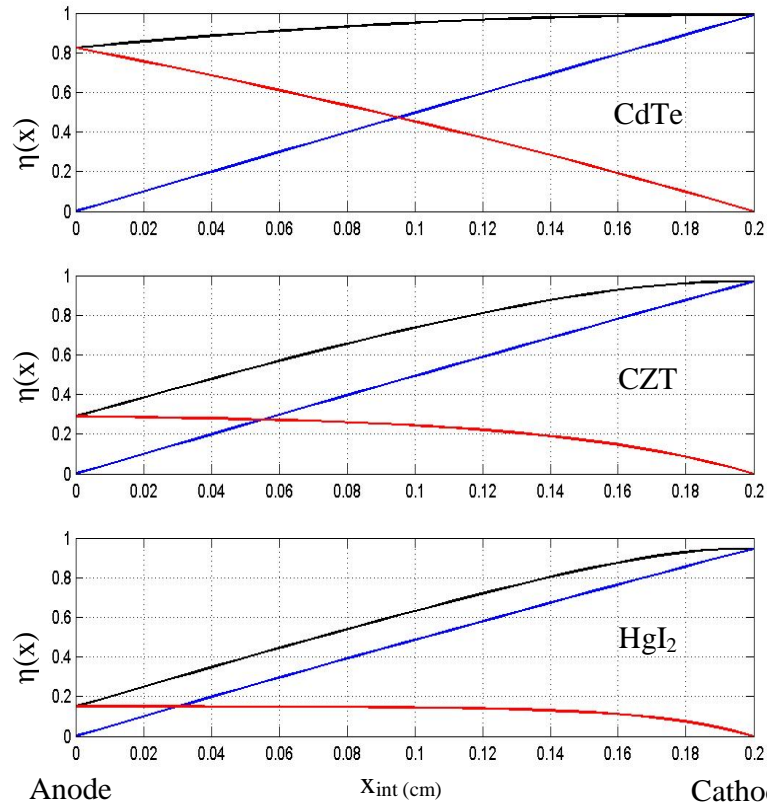


Figure 7.7 Charge collection efficiency η as a function of the distance of the photon interaction position from the anode (x_{int}) in a 2 mm thick detector with an applied voltage bias $V = 500$ V. Three detector materials, CdTe (top), CZT (center) and HgI_2 (bottom), are compared. The total collected signal at the detector electrodes (black curve) is the sum of the electron (blue curve) and hole (red curve) contributions. The CdTe detector shows the lowest sensitivity to trapping.

Figure 7.7 shows the expected charge collection efficiency as a function of the interaction position (x_{int}) for a 2 mm thick detector and an applied voltage bias of 500 V. This confirms the superior charge collection efficiency of CdTe compared to CZT and HgI₂. The efficiency in CdTe attains 100% near the cathode and remains above ~80% at the anode, whereas in the case of CZT and HgI₂ the efficiency near the anode drops to below 30%. It is important to note that higher values of the bias help to reach higher detection efficiency.

Trapping events have important consequences in spectroscopy, the major one being the so called “hole tailing”. The incomplete charge collection, due to trapping of holes, results in a tail-like distortion of the photon energy spectrum towards energies lower than the photo-peak. The extent of the tail decreases with increasing the characteristic trapping length (which depends on the detector material) and increases with the detector size. This behavior is well described in Fig. 7.8 for the case of a collimated, monochromatic photon beam (⁵⁷Co) illuminating two different detector materials, CZT (on the left) and CdTe (on the right)

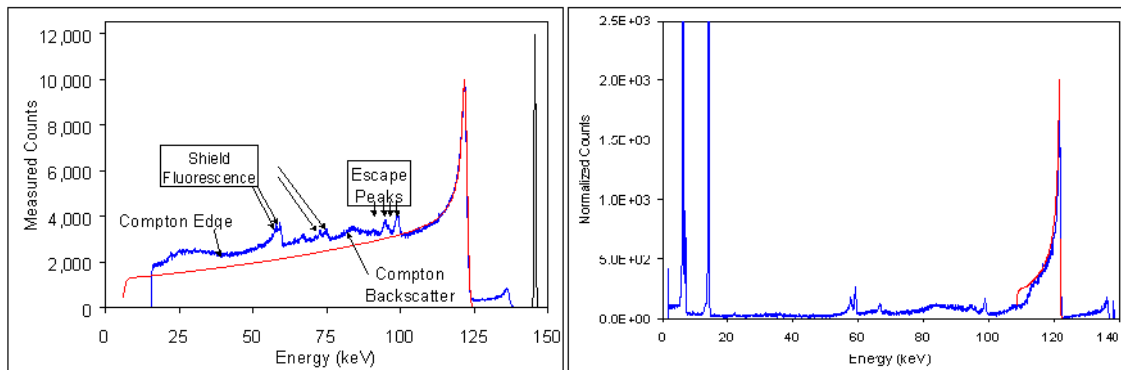


Figure 7.8 Computed (red curve) and measured (blue curve) spectra obtained from ⁵⁷Co with a 1mm thick AmpTek XR-100T CZT detector (left) and a 1 mm thick CdTe detector (right). Source: AmpTek <http://www.amptek.com/anczt2.html>.

The tailing effect is clearly recognizable in the computed spectra (red curve). The tail evidences a cut-off behavior at its low energy end; this corresponds to photon interaction events that occurred in the region of minimum charge collection efficiency that is near the anode. The superior properties of CdTe are clearly visible.

- Detector orientation

The direction of illumination of the detector is an important consideration for maximizing the detector efficiency [89]. For detectors suffering from low charge collection (holes are much less efficiently collected than electrons), as is the case for CZT and HgI₂, a substantial improvement in the spectroscopic performance can be achieved by adopting an opportune electrode geometry that maximizes interaction near the cathode [90, 91].

When relatively low energy photons impinge on the detector, photon illumination from the cathode side is therefore the most favorable configuration; indeed, more than 90% of photons with energies up to 60 keV interact within the first millimeter of the detector

depth and are thus absorbed prevalently near the cathode. As the photon energy increases, more and more photons interact far from the cathode, resulting in an inevitable loss of collection efficiency and thus resolution at high energy (Fig. 7.9 illustrates this concept).

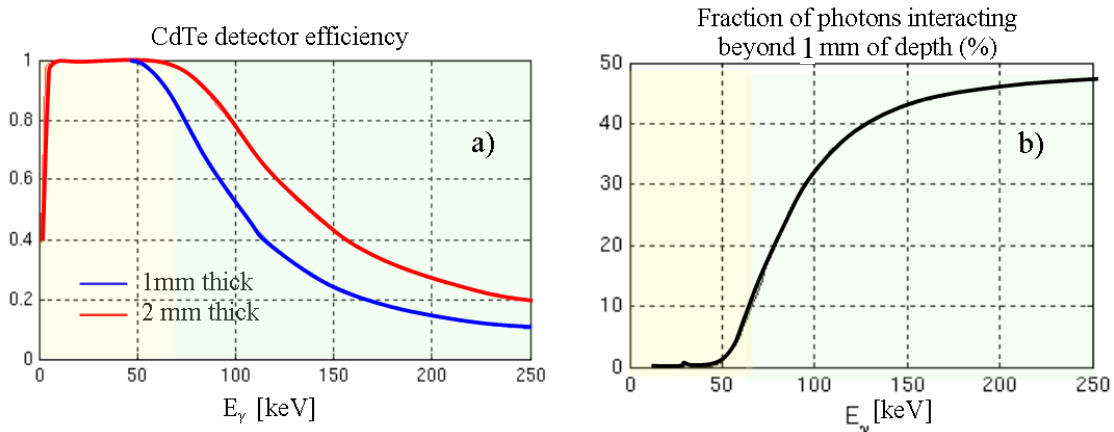


Figure 7.9 (a) Ideal (without trapping) CdTe detection efficiency in a 1 mm (blue curve) and a 2 mm (red curve) thick detector in the 0-250 keV photon energy range. The diagram in (b) shows the fraction (%) of photons interacting deeper than 1 mm into the detector volume (c). The yellow area in each diagram denotes the energy region in which over 90% of the photon-detector interactions occur within the first millimeter of depth into the detector volume.

Bremsstrahlung spectra almost universally decrease rapidly with energy. The cathode illumination scheme (Fig. 7.10), optimizing the detection quality in the low-energy part of the spectrum, is thus the preferable solution.

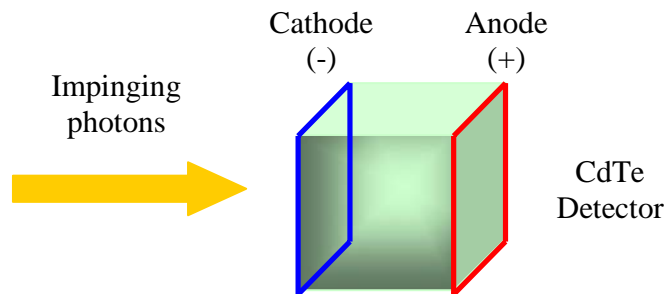


Figure 7.10 Detector photon illumination from the cathode side optimizes the charge collection performance of a solid-state semiconductor detector.

7.3.3 Choice of detector material

Cadmium-telluride (CdTe) detectors appear to meet our requirements. CdTe has a high atomic number of 48 and 52, a volume density 6.06 g/cm^3 , a band gap energy 1.52 eV (higher than silicon or germanium), and photoelectric absorption remains the dominant

interaction mechanism for photon energies up to 250 keV. Figure 7.11 shows the spectroscopic response of CdTe to monochromatic sources, without cooling; the results give an energy resolution of ~ 3 keV at 60 keV (^{241}Am) and ~ 5 keV at 122 keV (^{57}Co). The hard X-ray camera on loan from Tore Supra has demonstrated the validity and reliability of CdTe detectors with high time and space resolution [86].

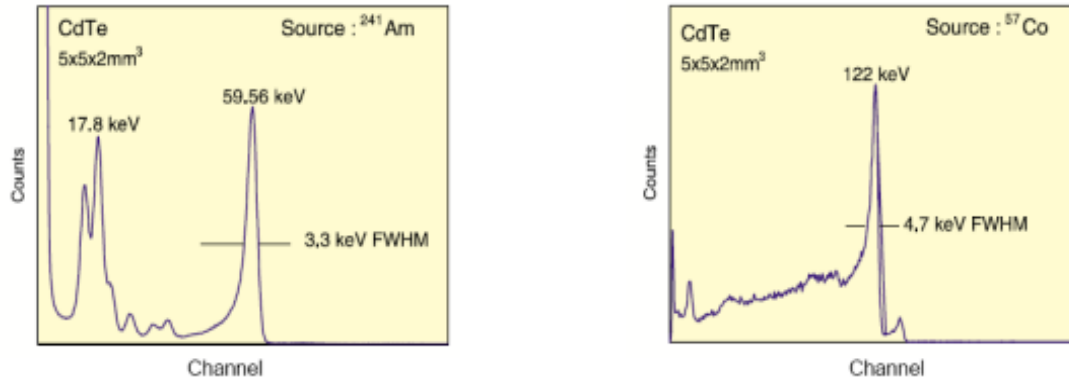


Figure 7.11 Spectroscopic performances of a high resolution CdTe detector element (data source: Eurorad).

The very high stability of CdTe detectors over time is also one of their most valuable characteristics. It allows for very low maintenance, an advantageous feature for operation without easy access. Moreover, no noticeable deviation of the energy calibration has been measured in the course of the period during which the Tore Supra instrument was installed on the TCV tokamak.

CdZnTe has to be considered as an alternative to CdTe [92]. CZT has a higher energy band-gap and consequently lower leakage current, thus better energy resolution than CdTe; however it exhibits poorer charge collection characteristics ($\mu_h^{CdTe} \sim \mu_h^{CZT}$ but $\tau_h^{CZT} < \tau_h^{CdTe}$) resulting in slower operation. Because of the predominantly continuum nature of the radiation measured, energy resolution is not the most critical parameter, whereas we are interested in achieving a high count rate and thus CdTe is considered a better choice for our purposes. According to the discussion in the previous section we can expect that this choice will permit operation up to fluxes of ~ 1 MHz. Other suitable materials such as HgI_2 , GaAs, PbI_2 are at present at the research stage and insufficiently tested.

7.3.4 Detector contact composition

From the point of view of the detector contact composition, two electrode configurations are available on the market of CdTe detectors (Fig. 7.12):

a) Ohmic type: Standard detector

In this type of configuration, platinum electrodes are used on both sides of the detector. This detector type has been produced commercially for a long time, the main

manufacturers (for CdTe) being Eurorad in France and Acrorad in Japan. Its primary merit is stable operation over long periods of time. Furthermore, this configuration enables the sensitive region to extend over up to several millimeters, enough to guarantee adequate detection efficiency up to 250 keV (~20% efficiency for a 2mm thick detector). The FWHM of ohmic-type detectors is typically 4.5keV (7.5%) at 59.5 keV (Am^{241}).

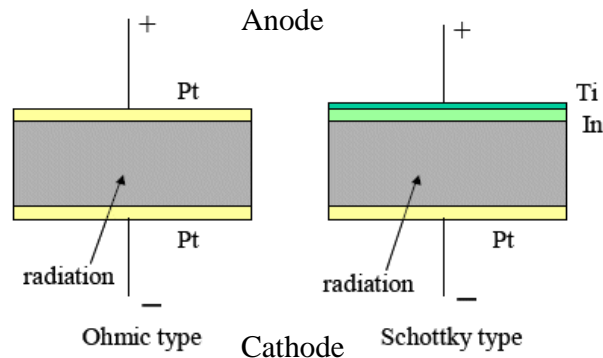


Figure 7.12 The structures of Ohmic and Schottky-type detectors [93].

b) Schottky type: High resolution detector

An indium-titanium electrode is used at the anode of a Schottky-type detector, whereas the cathode electrode is still made of Pt. Owing to the rectifying In-Ti Schottky contact, the collection of holes is suppressed, improving the energy resolution and the charge collection speed; additionally, the dark current can be about two orders or magnitude lower than in ohmic-type detectors. As a result, higher bias voltage can be employed than with the Ohmic type, further increasing the resolution (the typical FWHM is 2keV (3%) at 59.5 keV (Am^{241})) and the maximum count rate. The Acrorad company in Japan specializes in this type of CdTe [93]. However two main drawbacks affect this configuration:

- First, the difficulty of achieving a large depleted region (the limit is typically ~0.5 mm of sensitive thickness). Thus the device exhibits good detection efficiency for low-energy photons, but, as the photon energy increases, the probability that photons penetrate beyond the sensitive layer without interaction increases too, and the collection efficiency drops.
- Second, polarization effects arise a certain time (~ a few hours) after the detector bias has been switched on [94]. When polarization occurs, the photo-electrons and holes generated by the interaction of the photons with the CdTe lattice are not entirely collected by the electrodes; the cause is thought to be the appearance of a space charge field that opposes the externally applied one [94]. If a monochromatic gamma source is used, the main consequences are a photo peak position drift to lower energy channels accompanied by a FWHM increase; this

translates into a loss of spectroscopic performance. High bias voltage and detector cooling help to reduce these polarization effects [94, 95].

These kinds of diodes are currently the subject of further research; e.g., recent developments of low resistance p-type CdTe Schottky detectors have been reported by I. A. Kosyachenko [97]. Furthermore the performance of Schottky contacts on CdTe surfaces have shown to be improved by applying a specific plasma treatment [98].

7.3.5 Summary

The detector elements we have planned to employ are semiconductor CdTe diodes. This compound material shows a variety of favorable features for HXR detection in tokamaks:

- Low energy electron-hole pair generation enables a high electric signal output
- High energy gap implies low thermal noise and room temperature operation
- High Z and high density enable high photoelectric photon slowing power even with moderate element thickness
- Good charge collection efficiency compared to other candidate detector materials (CZT and HgI₂).

We are interested in investigating the HXR bremsstrahlung continuum radiation generated by suprathermal electrons lying in the high energy tail of the distribution function. The energy range of interest is 10-250 keV.

For energy lower than 10 keV, in the spectral region of bulk plasma electrons, measurements are already performed by the tomographic soft X-ray (SXR) system as well as a multiwire proportional soft X-ray counter (MPX).

At the opposite end of the spectrum, 250 keV (Fig. 7.4), is the energy limit for which the probability of the photoelectric interaction in CdTe becomes lower than the Compton scattering interaction.

7.4 Detector tests and choice

7.4.1 Introduction

In order to identify the best candidate HXR detector for the HXRS camera system, we have tested CdTe detectors from two suppliers, Acrorad (Japan) and Eurorad (France), and a CZT detector from Ritec (Latvia), see table 7.2. The main issues examined were the spectroscopic quality (energy resolution, noise level, photofraction) and the long term stability.

Firm	Detector id.	Size (mm)	V _{bias} (V)
Eurorad 1	1100-30i Ohmic CdTe	1x1x1	100
Eurorad 2	1347-24 CD Ohmic CdTe	1x1x2	150
Acrorad 1	Schottky CdTe	4x4x1	700
Acrorad 2	Schottky CdTe	2x2x2	700
Acrorad 3	Ohmic CdTe	4x4x1	60
Ritec	CZT	2x2x2	250

Table 7.2 Summary of detectors tested

7.4.2 Description of the electronic chain setup

These tests involve different kinds of CdTe and CZT detectors equipped with ohmic or Schottky electrode contacts. The radioactive source used in these tests was an Am-241 source emitting photons mainly at the 59.5 keV energy (see table 7.3). The electronic chain used for the spectrum acquisitions is shown in Fig.7.13.

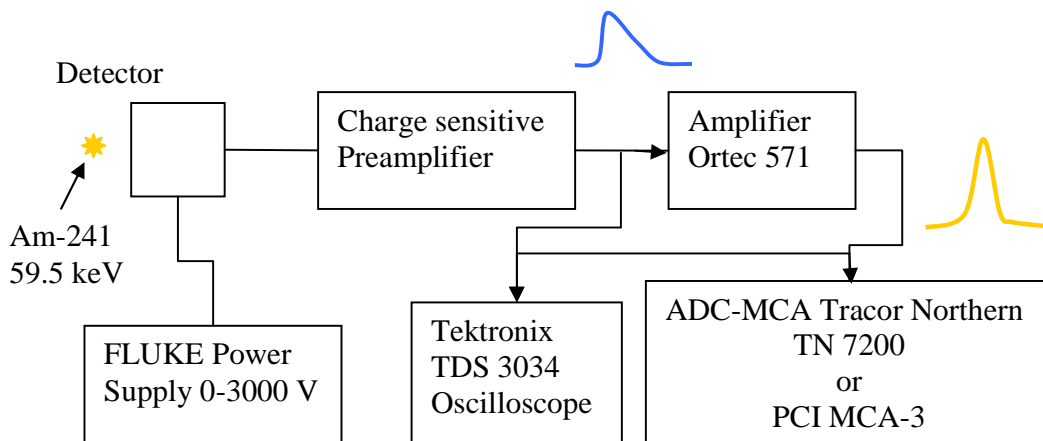


Figure 7.13. Electronic chain used during the test experiments.

The typical configuration setting is as follows. The Am-241 source is placed in front of the detector, which is biased at the voltage specified by the manufacturer. The charges generated in the detector are then collected by a prototype charge preamplifier circuit developed by the CRPP electronic team. The typical signal at the output of the preamplifier is shown in Fig. 7.14 (blue trace) and has a typical amplitude of 50 mV and a decay time $\sim 15 \mu\text{s}$. The rise time is determined by the detector characteristic and is of the order of 200 ns. In the next step the signal is amplified and shaped by an Ortec 571 shaper/amplifier with shaping time 1 μs , generating a positive (unipolar) Gaussian shape trace of amplitude $\sim 2.3 \text{ V}$ (yellow trace in Fig.7.14). The shaped signal is then fed to a multichannel analyzer (MCA). Initial tests were performed with a Tracor Northern TN 7200 module with 2048 voltage division levels. In a second stage we used instead a Fast ComTec MCA-3 PCI card with 512k memory.

isotope	Photon energy (keV)	I (%)
Am-241	13.9	13.5
	17.8	18.4
	20.8	4.9
	26.3	2.5
	59.5	36.0

Table 7.3 Photonic emission from a ^{241}Am source. The photon energy and relative intensity are given for each emitted line.

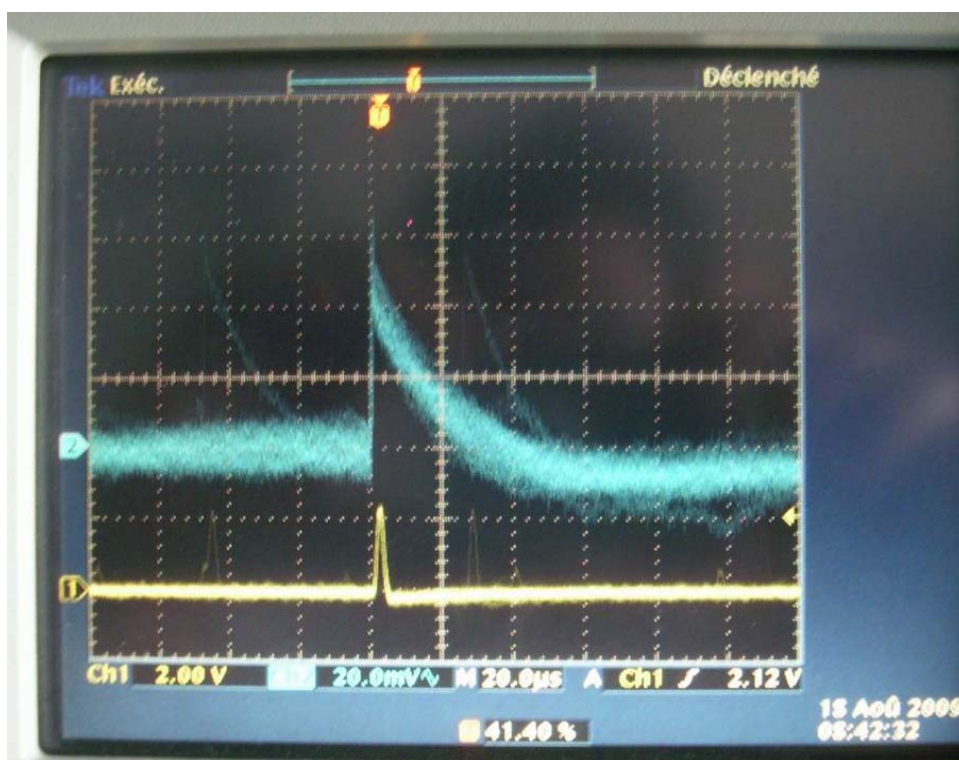


Figure 7.14 Output signal from a CRPP-made charge sensitive preamplifier (blue trace) and Gaussian shaped signal from the Ortec 571 amplifier-shaper module (yellow trace) from a 59.5 keV photon pulse.

To perform a comparative characterization of the detector we recorded the following figures of merit (Fig. 7.15):

- The full width at half maximum (FWHM).
- The photofraction, defined as the ratio of the integral over the region of interest centered on the photopeak (ROI P) to the total number of events. This is less than 100% because of Compton continuum, trapping tail, escape events (partial photon absorption), X-ray (K-edge) fluorescence, and noise.
- The low level of noise (LLN), defined as the point at the low energy end of the spectrum where the noise reaches one half of the photopeak amplitude.

Data were tagged with the time elapsed from the bias voltage turn-on (expressed in minutes), in order to monitor the long-term stability of the detectors.

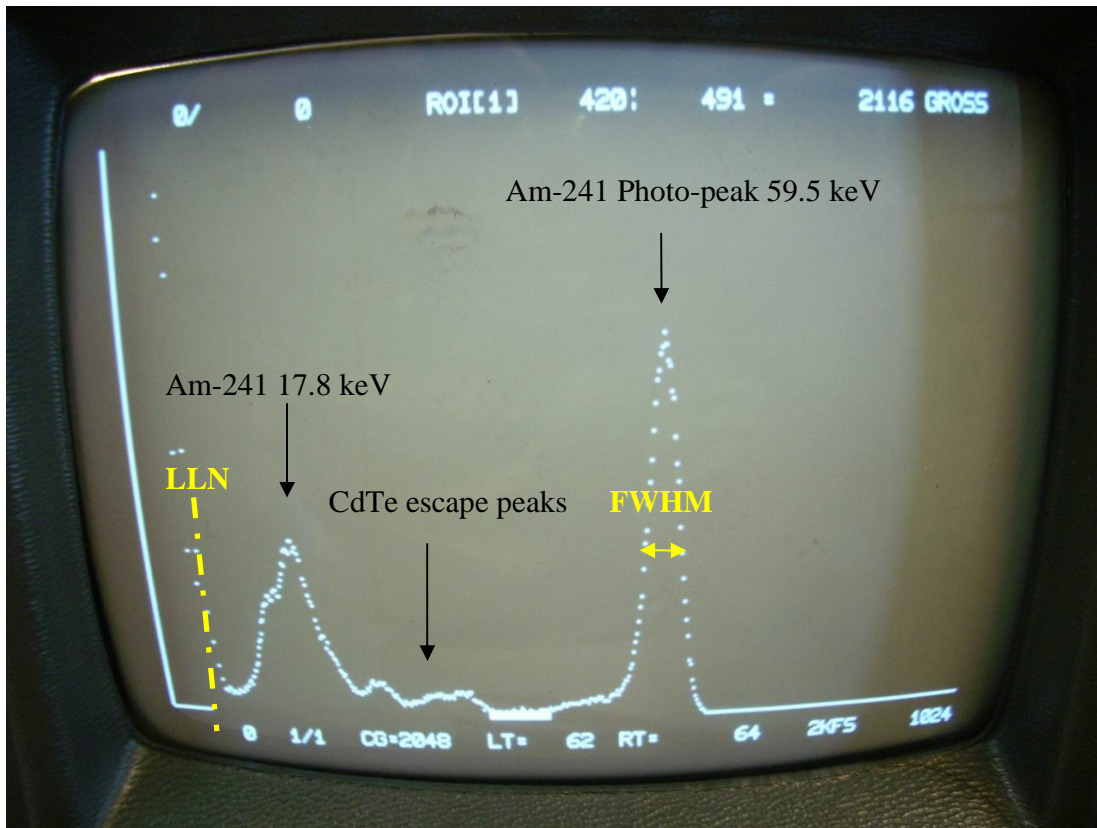


Figure 7.15 Basic detector figures of merit. The picture is taken from the screen of the Tracor Northern TN 7200 multichannel analyzer.

7.4.3 Test of detector performance

7.4.3.1 Spectroscopic performance

The figures of merit of the detectors tested are summarized in table 7.4. The Schottky detectors display the highest photofractions, over 40% compared to less than 30% for the other detectors. The FWHM and LLN are comparable for the detectors tested (~3.5 and ~6.5 keV respectively), except for the Ohmic type Acrorad CdTe specimen, which is considerably noisier (11 keV) and exhibits the worst FWHM (~6 keV) of the group. Because of trapping sites existing in the detector lattice, charge collection can be incomplete, resulting in a tail on the low energy side of the photopeak (as discussed in section 7.4). No appreciable tailing is present in the measured spectrum of a Schottky type detector, whereas it is clearly visible in the spectra of the ohmic-contact detectors, and is especially prominent in the case of the CZT detector, as seen in Fig. 7.16.

detector	FWHM (keV)	photo fraction (%)	LLN (keV)	Polarization (onset time)	tailing
Eurorad 1	3.33	26.9	6.2	NO	YES
Eurorad 2	3.19	27.7	6.2	NO	YES
Acrorad 1 (Schottky)	3.32	43	6.5	YES (2h)	NO
Acrorad 2 (Schottky)	4.05	45	6.5	YES (15')	NO
Acrorad 3 (Ohmic)	5.9	41.6	11	NO	NO
Ritec CZT	3.69	29.7	6.5	NO	YES

Table 7.4 Summary of spectroscopic figures of merit for the detectors tested

7.4.3.2 Long term stability

A crucial issue is the long term stability of the detector. All ohmic-contact detectors displayed stable operation over several hours of biasing. The Schottky-type detectors instead suffer from the so called “polarization” effect, as discussed in section 7.3.4. The main visible signs of the onset of polarization are a displacement of the photopeak toward lower energies, a degradation of the energy resolution (an increase in FWHM) at the photopeak, and an increase in low energy noise (see Fig. 7.17).

Our tests demonstrated a clear dependence, summarized in table 7.5, of the time for polarization onset on the applied bias voltage (V_b) and on the detector thickness, increasing with the former and decreasing with the latter.

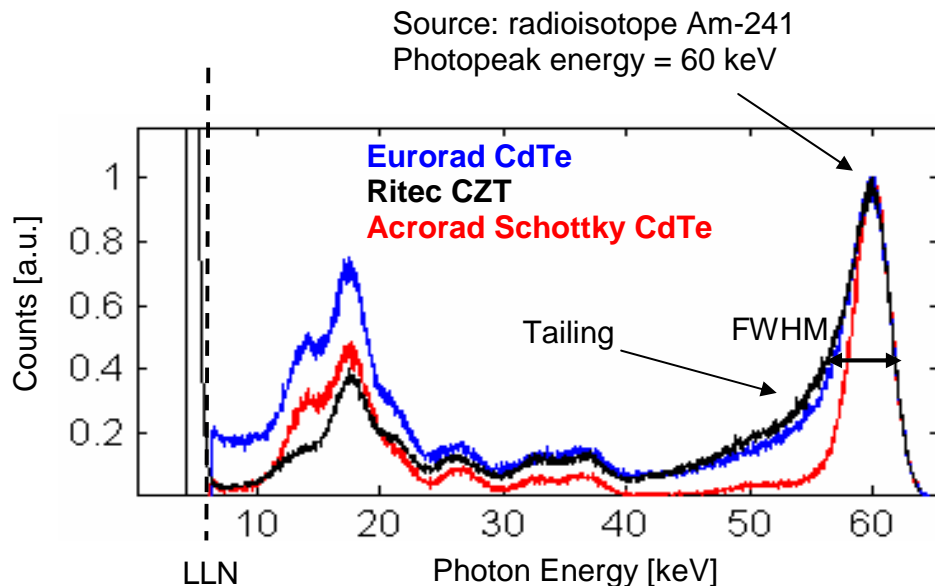


Fig. 7.16 Energy spectrum from an Am-241 source for three different HXR detectors: Eurorad Ohmic-contact CdTe (blue curve), Ritec CZT (black curve) and Acrorad Schottky-contact CdTe (red curve). Photopeak energy resolution and tailing are compared in figure.

Detector	Size (mm)	Vb (V)	FWHM (keV)	LLN (keV)	polarization
Schottky CdTe	2x2x2	500	3	5.2	after 10'
Schottky CdTe	2x2x2	700	3	5.2	after 20'
Schottky CdTe	2x2x2	1000	3	5.6	after 30'
Schottky CdTe	4x4x1	700	3.6	8.1	after 2h
Schottky CdTe	5x5x0.5	300	3.4	6	after 2h
Schottky CdTe	5x5x0.5	500	3.4	6	after 3 h
Schottky CdTe	5x5x0.5	700	3.6	7.5	after 3.5 h

Table 7.5 Polarization onset time for varying detector size and applied bias (Vb).

The 2 mm thick Schottky-contact detector is particularly unstable even at high bias voltage. Although the highest voltages do permit longer operation times, they also cause a higher level of leakage current resulting in anomalous low energy noise which increases with time. Not only is the polarization onset time short but the detector even needs to be turned off for a certain time (~ 1 minute) in order to be properly reset. Most disturbingly, the polarization onset time itself became rather erratic after a certain amount of testing, and optimum performance was lost for days in some cases even after a full reset. It became apparent that these 2-mm thick detectors could not be relied upon even if one were to bias them only for the short duration (a few s) of a TCV shot. Indeed, the literature reports successful use of Schottky type CdTe detectors only up to 1 mm thickness.

When, as in our case, for reasons of detection efficiency at high photon energy a thicker detector is required (space and medicine applications) the solution adopted is to use a stacked structure instead of a single detector [99]. This would however be costly and impractical for our application.

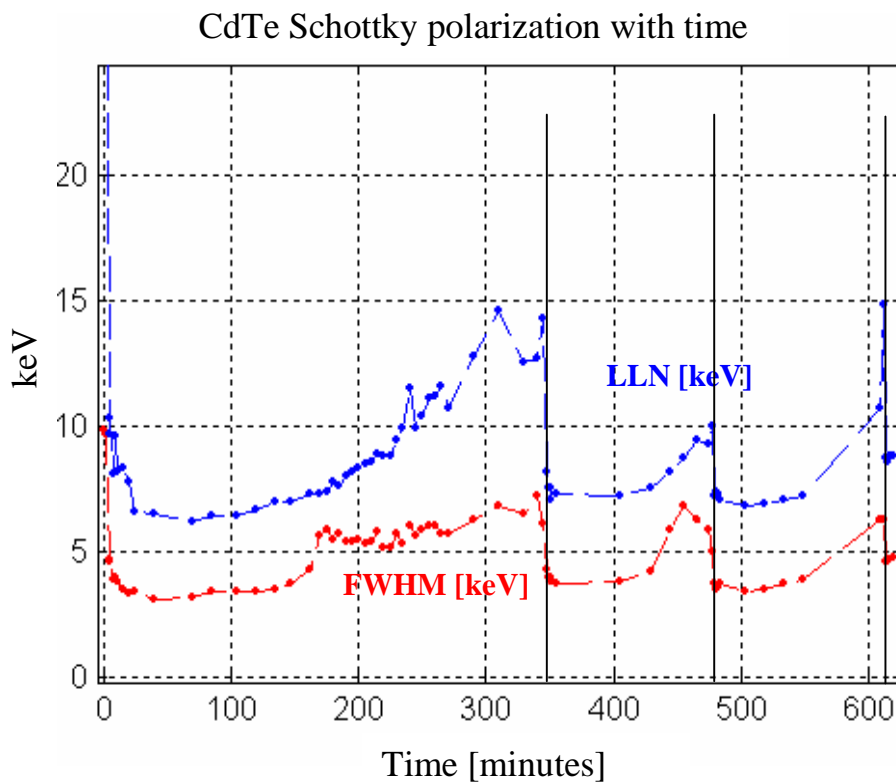
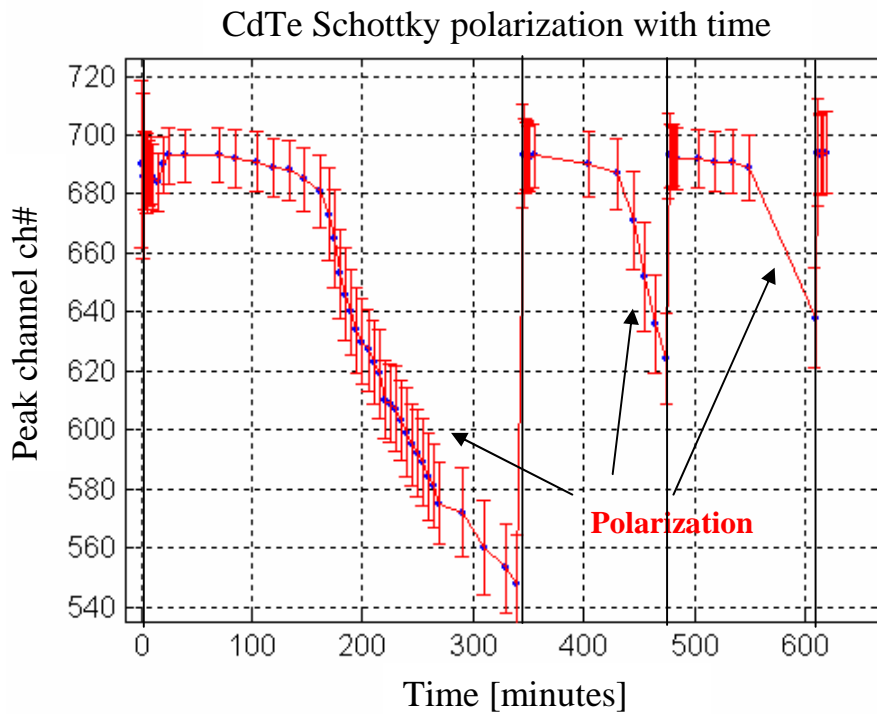


Fig. 7.17 Polarization effect appearing in the Acrorad detector #2 (Schottky CdTe, $V_b = 700$ V). The detector remains stable over approximately 2 hours, after which a spectroscopic degradation appears. Solid vertical lines indicate the moments of switch off/on times.

7.4.3.3 Spectrum vs irradiation direction

Following the discussion in section 7.3.2, we tested the behavior of the detector for different illumination directions. The result is shown in Fig. 7.18.

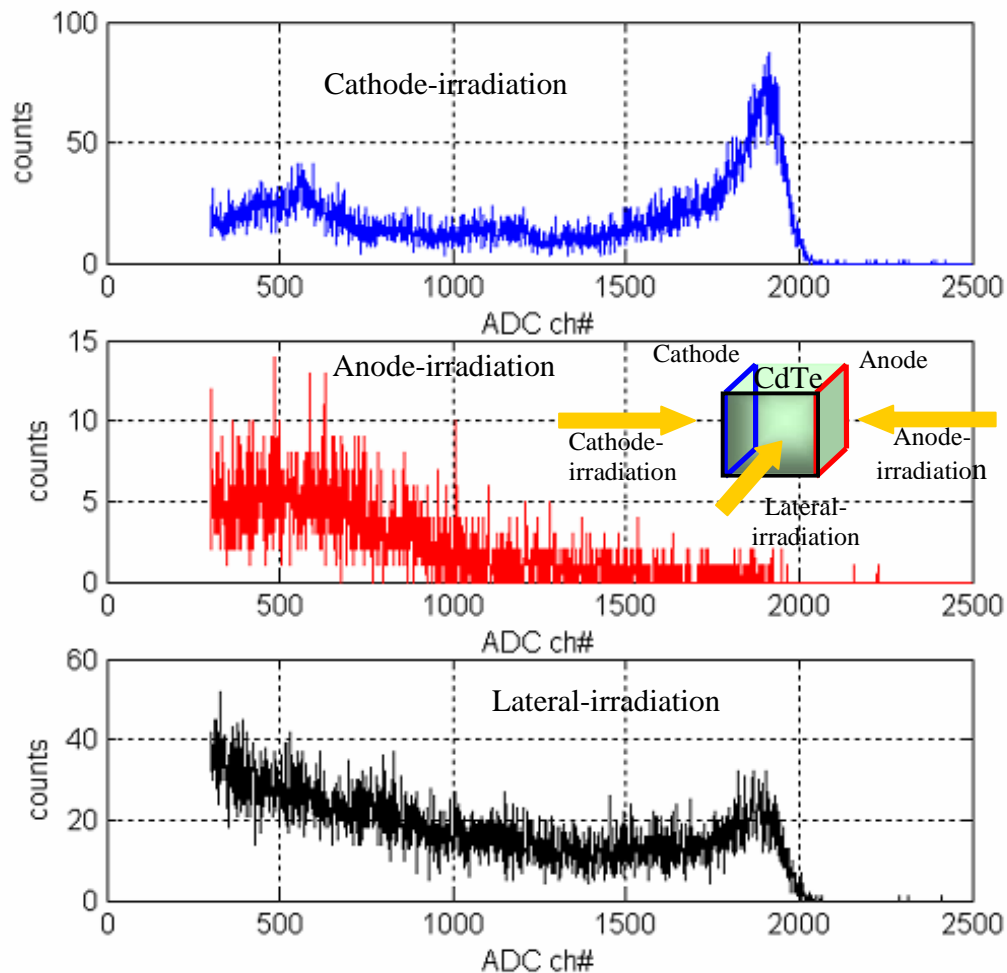


Figure 7.18 Am-241 spectra from the Eurorad CdTe detector #1, biased at 100V and irradiated from three different directions.

It is clear that the direction of irradiation has a strong influence on the quality of the measured spectrum. In particular, irradiation from a direction other than the cathode side results in a broader and down-shifted energy spectrum.

7.4.3.4 Detection efficiency as a function of the detector thickness

We tested the detector stopping efficiency at high energy as a function of the detector thickness (0.5, 1 and 2 mm). In addition to the ^{241}Am source emitting at 60 keV, we employed here a ^{57}Co source with the main photopeak at 120 keV. The photopeak fractions for the detectors used are similar, permitting a quantitative comparison based on

the integrated signal around each photopeak. Firstly we present a comparison with ^{241}Am (Fig. 7.19a.). Here we employ 2 Acrorad Schottky-contact detectors (2 mm and 0.5 mm thick) and one Acrorad Ohmic-contact detector (1 mm thick): the expected efficiencies at this energy are 99%, 95% and 76% for 2, 1, and 0.5 mm thickness respectively. The measured photopeak ratios are 1, 0.96, 0.72 respectively, in reasonable agreement with the expected values.

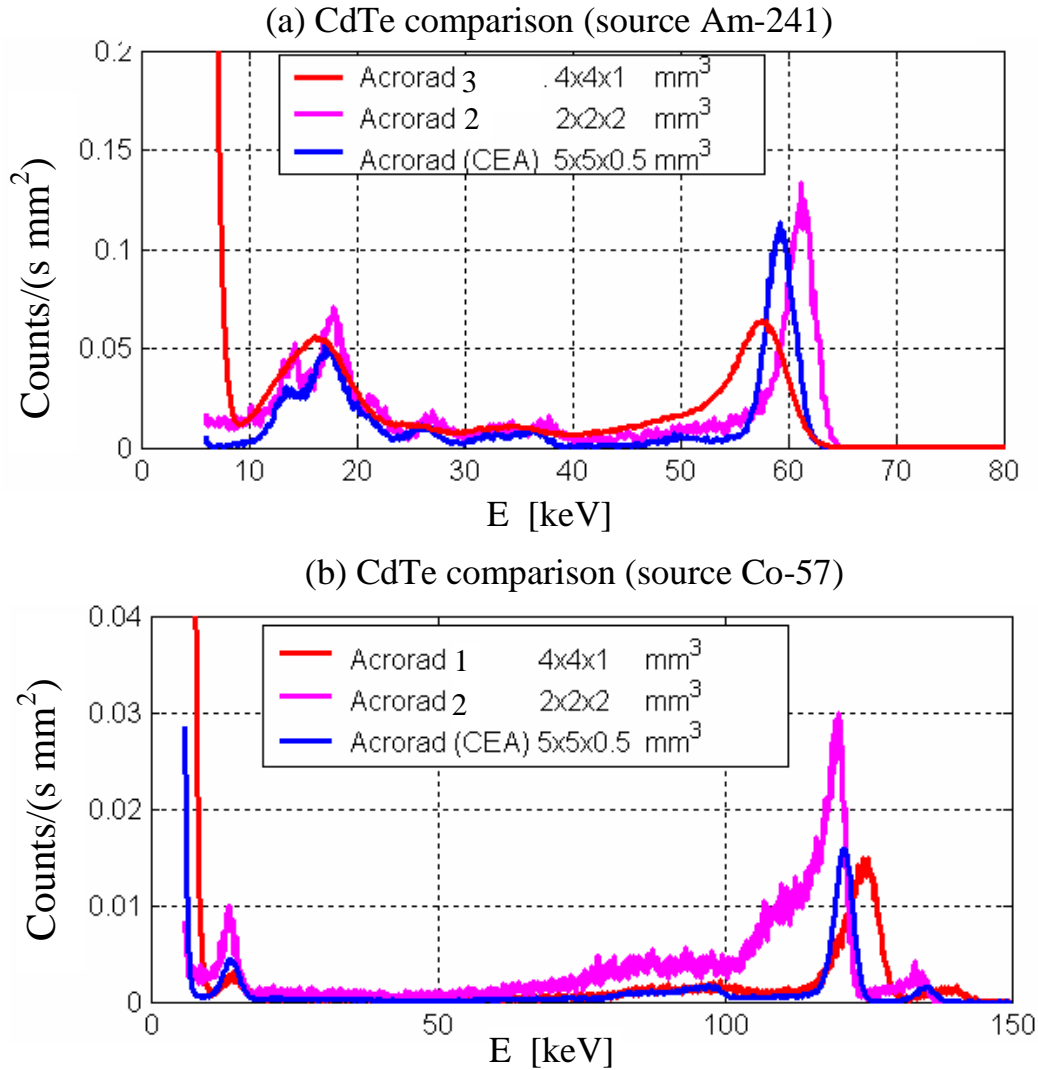


Fig. 7.19 Detection efficiency vs detector thickness (0.5, 1 and 2 mm). The radioactive sources used are: ^{241}Am (60 keV) (a) and ^{57}Co (120 keV) (b).

The efficiency at 120 keV (^{57}Co ; Fig. 7.19b) was measured with 3 Acrorad Schottky-contact detectors 0.5, 1 and 2 mm thick with expected efficiencies 22%, 37% and 60%, respectively. The measured detector efficiencies for 0.5 and 1 mm, normalized to that of the 2-mm thick detector, are 0.3 and 0.45, respectively. Again, the scaling is in fair agreement with the expected ratios. The 0.5 mm thick Schottky-contact detector used in this comparison was provided by CEA-Cadarache as a temporary loan for testing.

7.4.4 Summary

In spite of their superior spectroscopic characteristics when operating at peak performance, 2-mm thick Schottky-contact CdTe detectors have proven too unstable and unreliable to be used in our application. Of the Ohmic-contact detectors, the Eurorad "ultimate grade" line of CdTe detectors displayed the best overall performance. Although the Ritec CZT detector was a strong contender, the poor mobility and trapping properties of the material render it ultimately unsuitable.

7.5 Collimator design

7.5.1 Introduction

The collimator system is a crucial element and has accordingly required a substantial design effort. The two major goals that this element has to achieve are:

- To provide an appropriate collimation of the incoming radiation and define the individual lines of sight
- To provide the necessary shielding against radiation coming from undesired directions.

In order to meet the requirements of compactness, spatial resolution and angular fan view flexibility, three different configurations were considered, which will be compared and discussed in this section. The choice of the most appropriate collimator material is also discussed in turn.

7.5.2 Geometric design criteria

The design implementation has to take into account some essential geometric criteria: the *étendue*, the *line spatial sampling* and the *chord spread* (spatial resolution).

- *Spatial sampling*

We define the *chord spacing* (Δr) as the distance (in units of a flux coordinate, typically on TCv the square root of the normalized volume) between the flux surfaces to which two adjacent lines of sight are tangent, i.e., the smallest minor radii they intersect (see Fig. 7.20). This distance must be sufficiently short to provide a good coverage of the plasma region and a good spatial sampling for tomographic reconstruction. A reasonable number of detectors are then needed in order to obtain the required chord spacing (Δr): $N_{\text{det}} = \Delta r_{\text{fan}} / \Delta r$ where Δr_{fan} is the total fan width for a given camera. While

a larger number of detectors clearly will provide better spatial sampling, the optimum number will result from a trade-off between incremental benefits from improved sampling and the related incremental cost.

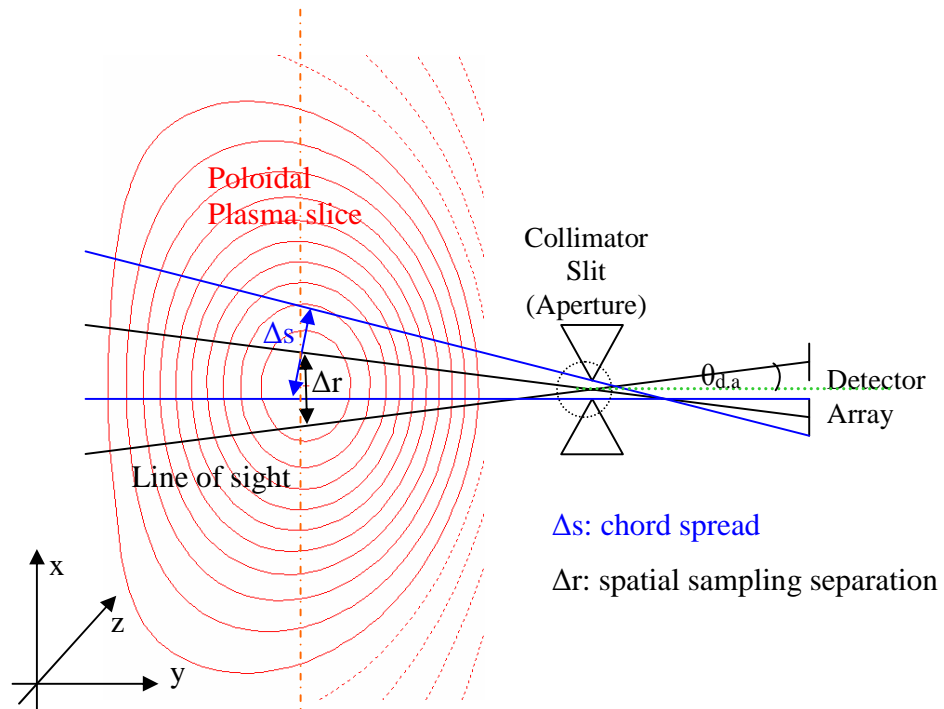


Figure 7.20 Spatial sampling separation (Δr) and chord spread (Δs) for a simple detector collimator scheme.

- *Chord spread (spatial resolution)*

In a real physical system, lines of sight are not true geometric lines, rather they cover a finite solid angle (see Fig. 7.21). Each line of sight is characterized by its *chord spread* (Δs), which gives a measure of the width of the plasma region that contributes to the radiation collected by a detector along its line of sight. i.e., the spatial resolution of the measurement. The chord spread comprises a poloidal and a toroidal component. The former is again defined conventionally in terms of a flux coordinate spread at the point of tangency.

Figure 7.21 illustrates the concept for the case of a chord lying in the poloidal plane, where Δs_x is along the direction lying on the poloidal slice and Δs_t along the toroidal direction (z). A large toroidal spread helps to increase the signal level at the detector, thus increasing the signal-to-noise ratio. The z -direction is a direction of symmetry if the toroidal width of the plasma slice viewed by the detectors is thin enough that we can assume the toroidal variation in the plasma emission to be insignificant.

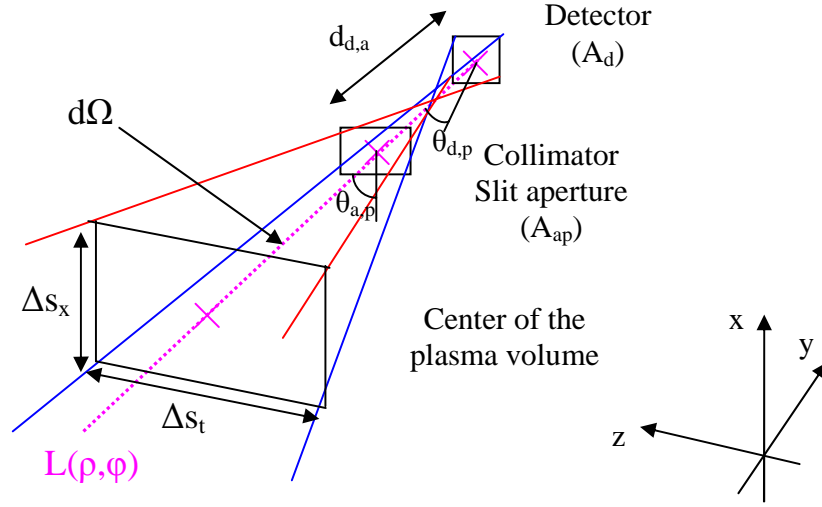


Figure 7.21 Geometric scheme used in the definition of chord spread and étendue

A set of simulations have been performed in order to estimate the influence of the toroidal chord spread on the measured detector signal. This led to the conclusion that a ± 7 degree spread in the toroidal wave number (k_{\parallel}) can be accepted.

- *Etendue*

In a simple picture the *étendue* is given by the detector's sensitive surface (A_d) times the solid angle subtended by the source as seen from the detector. In the approximation of small collimator aperture, the *étendue* can be expressed as follows:

$$G = A_d \Omega = \frac{A_d A_{ap} \cos(\theta_{a,p}) \cos(\theta_{d,p})}{d_{d,a}^2} \quad (7.6)$$

where A_{ap} is the area of the collimator aperture, $d_{d,a}$ is the detector-aperture distance, $\theta_{d,p}$ and $\theta_{a,p}$ are the angles between the direction of the propagating photons and the normals to the detector and collimator aperture planes, respectively (as depicted in Fig. 7.21).

In a more accurate calculation we have to consider that statistically some photons will traverse the collimator metal foil defining the aperture. In this case the actual aperture area A_{ap} is a function of the incoming photon energy $E_{ph} = h\nu$

$$G = \int_{A_d} \int_{E_{ph}} \frac{dA_d (dA_{ap}/dE_{ph}) \cos(\theta_{a,p}) \cos(\theta_{d,p})}{d_{d,a}^2} dE_{ph}. \quad (7.7)$$

The situation is exemplified in the plot below (Fig. 7.22):

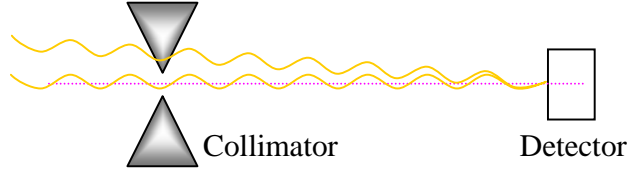


Figure 7.22. The statistical possibility for a photon to traverse a certain thickness of collimator must be taken into account for an accurate calculation of the aperture.

The number of photons recorded by the detector in an energy range $[E_0 - \Delta E/2, E_0 + \Delta E/2]$ and in a given interval of time $[t_i, t_f]$ is given by the integral

$$N_{d,E_0}^{ph} = \int_{t_i}^{t_f} \int_{E_0 - \Delta E/2}^{E_0 + \Delta E/2} \frac{dN_d(t, E)}{dt dE} dE dt \quad (7.8)$$

where $dN_d(t, E)/dt dE$ is the measured photon energy spectrum. This quantity is related to the effective photon energy spectrum $dN_i(t, k)/dt dk$ emitted by the plasma in the direction of the detector by the expression:

$$\frac{dN_d(t, E)}{dt dE} = \int_0^\infty (1 - \eta_A(k)) \eta_d(k) H(k, E) \frac{dN_i(t, k)}{dt dk} dk \quad (7.9)$$

where k is a variable describing the emitted photon energy, $H(k, E)$ is the normalized instrumental function ($\int_0^\infty H(k, E) dk = 1$) which describes the conversion of the impinging photon to a detected signal, $\eta_A(k)$ is the fraction of photons that are absorbed before being detected because of the presence of various objects (others than the collimator) along the line of sight between the plasma and the detector (vacuum window, filters) and $\eta_d(k)$ is the detector efficiency or the fraction of photons that are effectively stopped inside the active detector volume. Here we have used the subscripts d and i in order to distinguish between quantities measured by the detector (d) and quantities related to the impinging photons themselves (i). In the thin chord approximation and confining our attention to detectors having the entrance area in a plane parallel to the collimator aperture, and using Eq. 7.7, we can write

$$\frac{dN_i(t,k)}{dtdk} = \frac{A_{ap}A_d}{d_{d,ap}^2} \int_{l_{\min}}^{l_{\max}} j(l,t,k) dl \quad (7.10)$$

where $L_c = l_{\max} - l_{\min}$ is the chord length in the plasma and $j(l,t,k)$ is the number of photons emitted per unit energy, unit volume, unit solid angle and unit time. Clearly the number of photons reaching the detector from the plasma is regulated by the étendue. The étendue must be sufficiently large to engender a good signal to noise ratio and sufficiently small to avoid pile-up saturation of the collected signal in most cases of interest. Data from the previous HXR camera, having an étendue of $2.5 \times 10^{-9} m^2 sr$, indicate that the photon flux above ~ 10 keV can reach 1MHz for detectors viewing the central plasma region during strong heating and current drive. However, in most situations the flux is far lower. Also, variable absorbers can be used to cut the low-energy flux in cases in which pile-up would otherwise occur. Since, as discussed in section 7.3, the detectors we have chosen can tolerate a photon flux up to approximately 1 MHz, we chose a value of $4.4 \times 10^{-9} m^2 sr$ for our system, 75% larger than in the previous HXR camera.

7.5.3 Collimator system: comparative study of different concepts

7.5.3.1 Single slit collimator with radial detector array (pinhole camera)

The first configuration we have considered is a *single slit* (or pinhole) collimator with a radial detector array, that is, the same kind of configuration we had in the previous camera from Tore Supra [68]; a similar system is employed also, among others, in the Alcator C-Mod tokamak [100] (Fig. 7.23). A single thick slit is placed between the plasma and the detectors in order to collimate the incoming light and provide the necessary shielding. In such a configuration detectors are typically installed on a circular-arc shaped support in order to enable each of them to be orthogonal to the radiation coming from their respective line of sight. Moreover, orthogonal detector illumination in a divergent circularly shaped array configuration minimizes spurious signals induced by photons scattered by adjacent detectors or traversing them without absorption.

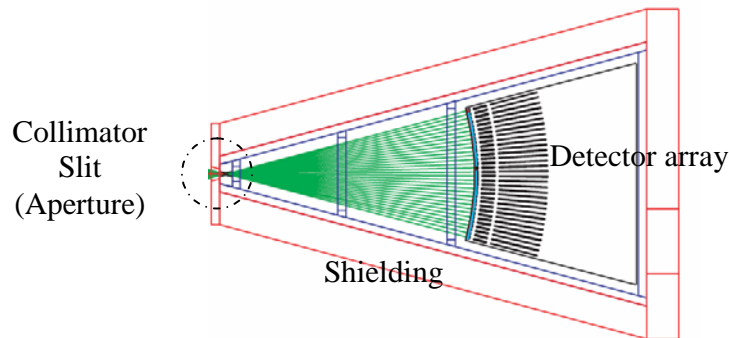


Figure 7.23 A typical pinhole camera design implemented with a radial detector array

In practice, for effective collimation the slit must have a finite longitudinal extent (as shown in Fig. 7.24(b)). For definiteness we shall assume here a 5 mm deep tungsten collimator, which is sufficient to stop 99% of the photon flux up to 250 keV. We also assume 1 mm² area detectors with a maximum geometric étendue of $\sim 1 \times 10^{-9} \text{ m}^2 \text{ sr}$.

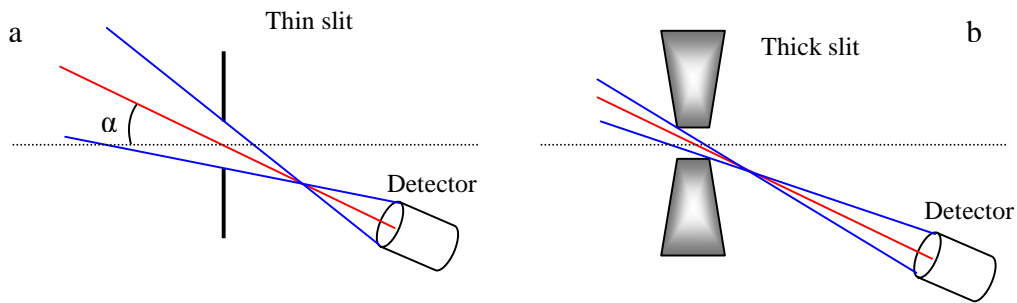


Figure 7.24 The single slit (pinhole) collimator: (a) idealized thin collimator and (b) thick collimator configurations.

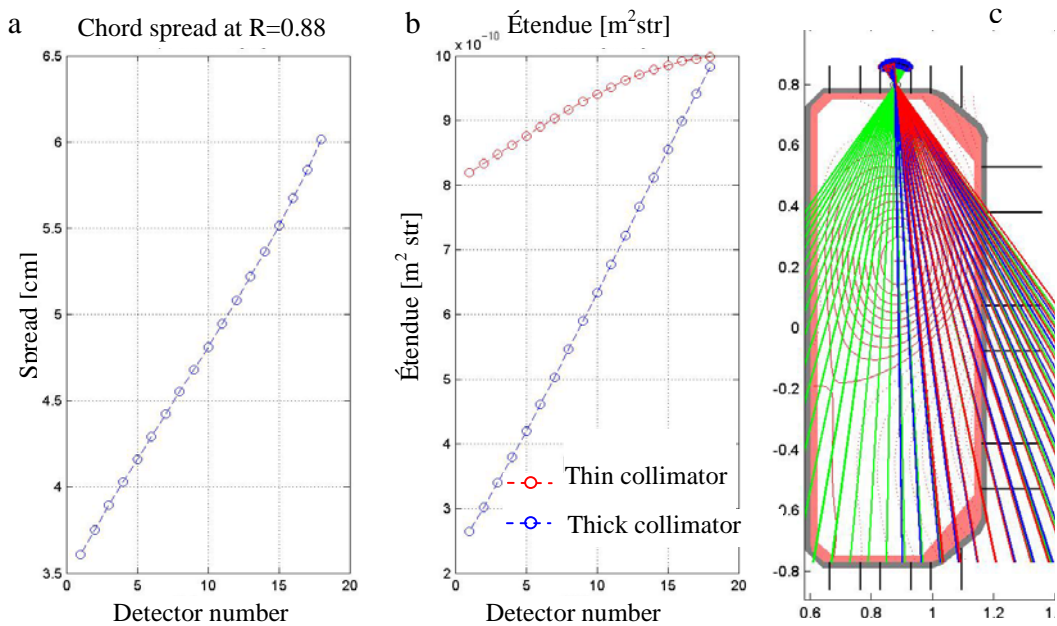


Figure 7.25 (a) Horizontally projected spread at $z = 23$ cm and (b) étendue (for both thin and thick collimator) for left-half detectors (1 to 18) of the vertically viewing camera arrangement shown in (c). Detector 18 has a direct frontal view of the slit aperture: right-half detectors are symmetrically placed. The chord spacing is $\Delta r = 2$ cm at $Z = 0.23$ cm. In this simulation the single slit aperture is centered at $R=0.88$ m, $Z=0.8$ m, and the thick slit is shaped similarly as in the Alcator C-Mod and Tore Supra setups, i.e., as a longitudinally extended channel equivalent to two diaphragms. The aperture size is: 5mm in R, 5mm in Z and 1mm in the toroidal direction; the detector area is $1 \times 1 \text{ mm}^2$; the slit-detector distance is 7 cm.

The single pinhole geometry is not well suited when we want to impose a similar étendue and chord spread for each detector element, since the étendue and chord spread decrease

as the detector position moves away from a frontal view (see Figs. 7.25 and 7.26). The former limitation could be alleviated by using detectors of varying dimensions, but this is highly impractical. If an upper limit in the étendue variation is imposed, for a given plasma size there will then be a minimum acceptable distance between the plasma and the collimator. This distance could be incompatible with the port access constraints. Figures 7.25 and 7.26 show the possible adaptation of the single slit concept for a central upper camera and a central lateral camera on TCV. In particular the variation of the étendue (ΔG) between detectors having a direct frontal view of the slit aperture ($\alpha=0$) and detectors with the maximum oblique view can vary significantly; when a 5 mm thick tungsten collimator is adopted, $\Delta G \approx 70\%$ and $\Delta G \approx 90\%$ are expected respectively for the two cameras ($\sim 20\%$ and $\sim 30\%$ in the thin collimator idealization instead). However this geometrical configuration has the advantage of a relative simplicity of construction.

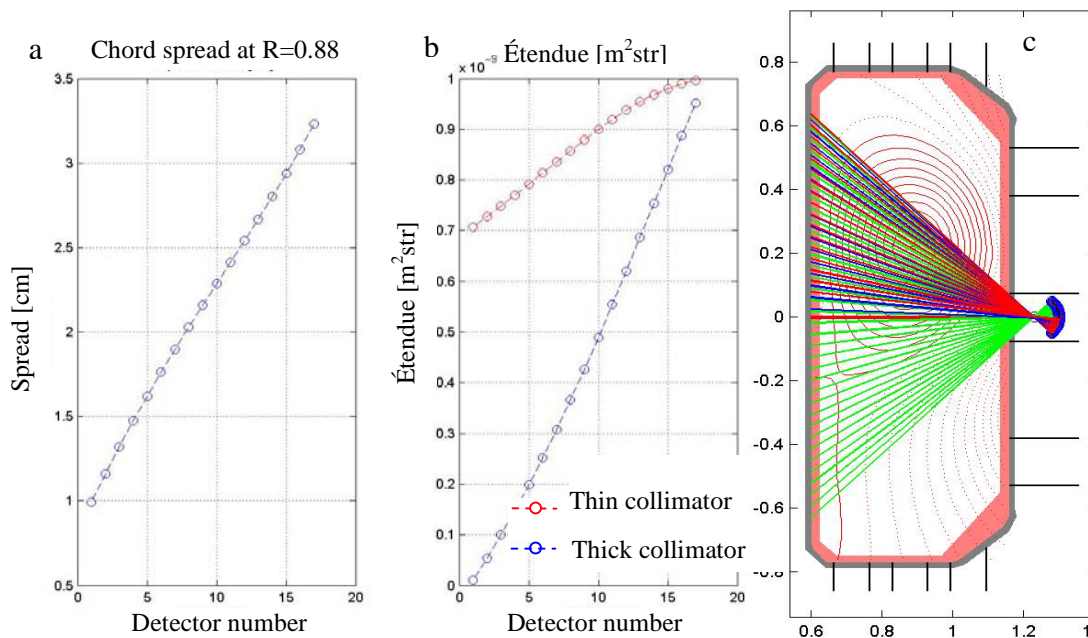


Figure 7.26 (a) Vertically projected spread at $R=88\text{cm}$ and (b) étendue for lower-half detectors (1 to 17) in the horizontally viewing camera arrangement shown in (c). Detector 17 has a direct frontal view of the slit aperture; upper-half detectors are symmetrically placed. The chord spacing sampling is $\Delta z = 2\text{ cm}$ at the plasma center ($R = 88\text{ cm}$). In this simulation the single slit aperture is centered at $R = 1.23\text{ m}$, $Z = 0\text{ m}$, and the collimator and detector dimensions are the same as in Fig. 7.25.

7.5.3.2 The oblique Soller collimator concept

In an attempt to circumvent the limitations of the pinhole configuration, a rather different geometry has been studied as an option for TCV. In this concept the light is collimated by means of Soller-like collimators. Soller collimators [101] are, strictly speaking, parallel plates that select a given, single direction of photon propagation for all detectors while rejecting all oblique trajectories. As such they are not directly suited for spatial surveying. It has been proposed to use a modified version of this concept, in which the

plates are not parallel but form a fan, such as to associate each detector with a different trajectory angle while still preserving the spatial collimation properties.

This collimator scheme enables the adjustment of each collimator aperture dimension in order to define the chord spread of each line of sight and thus the chord overlap in the plasma region. To make maximum use of this extreme flexibility, each metal collimator foil may have to be individually shaped, potentially complicating the mechanical construction. In particular, this concept can guarantee the uniformity of the chord spread, if so desired, as well as enable individual control of the étendue for each detector to maximize the signal to noise ratio. Moreover this result can be obtained while placing the detectors close to the plasma as with a traditional pinhole collimator, thus making optimal use of the limited port space available. Two detector array configurations making use of the oblique Soller collimator concept are examined here.

7.5.3.2.1. Convergent radial Soller collimator

This kind of configuration uses an oblique Soller collimator design, consisting of a set of metal foil elements that collimate photons along convergent chords, each toward its respective detector, providing at the same time the necessary shielding (Fig.7.27(a)).

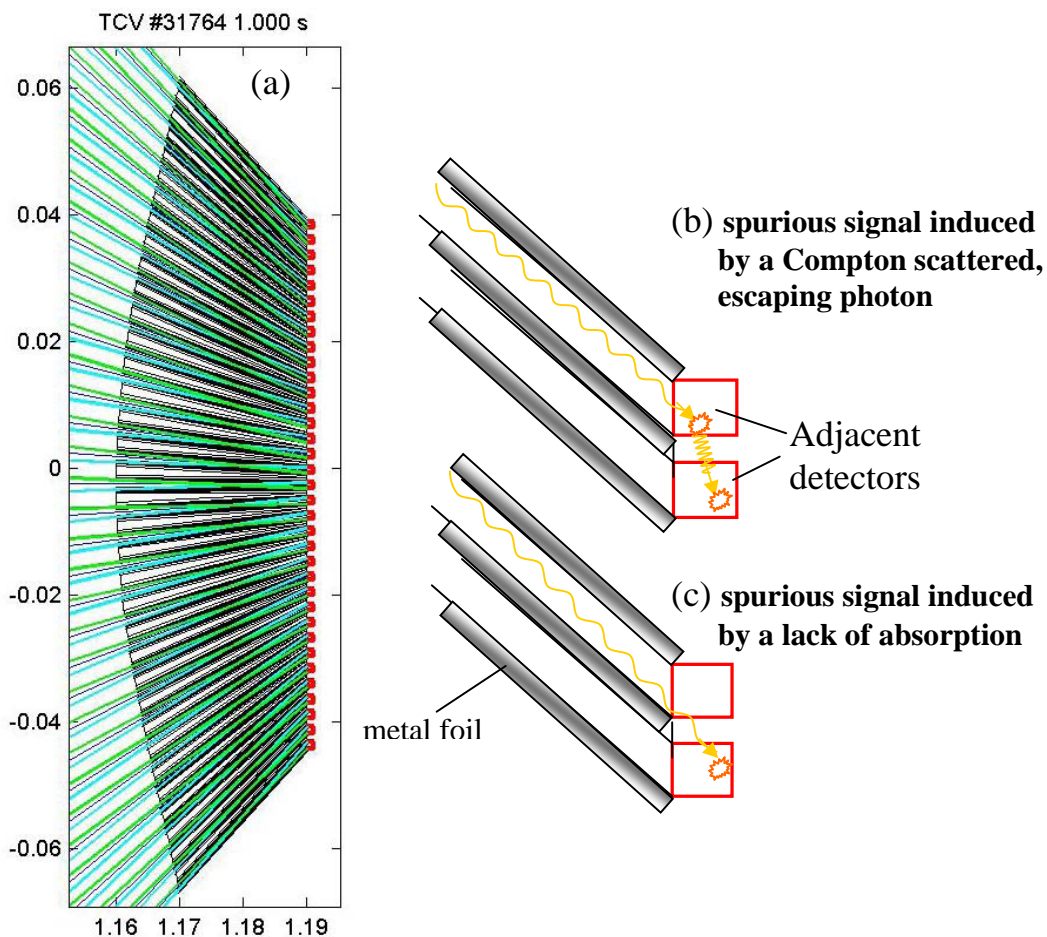


Figure 7.27 (a) Convergent Soller collimator configuration with a planar detector array. Different sources of spurious signal (cross-talk) arising from: (b) a scattered, escaping photon from a neighboring detector and (c) a photon traversing a neighboring detector.

The planar detector array shown in Fig. 7.27 (a) is not the best choice because of the possibility of spurious signals due to cross-talk between detectors. The spatial and energy resolution of a detector are degraded when multiple counts can be induced in adjacent detectors as a result of escaping Compton photons (Fig 7.27 (b)) or photons that cross the crystal without interaction (Fig. 7.27 (c)).

Additionally, even if detectors are sufficiently spaced or shielded against cross-talk, the effective detector thickness viewed by incoming photons is reduced by oblique illumination, causing a non-negligible loss of absorption especially for high energy photons.

These problems are alleviated if detectors are placed along a circular arc instead (radial array), with no loss of detector area or étendue.

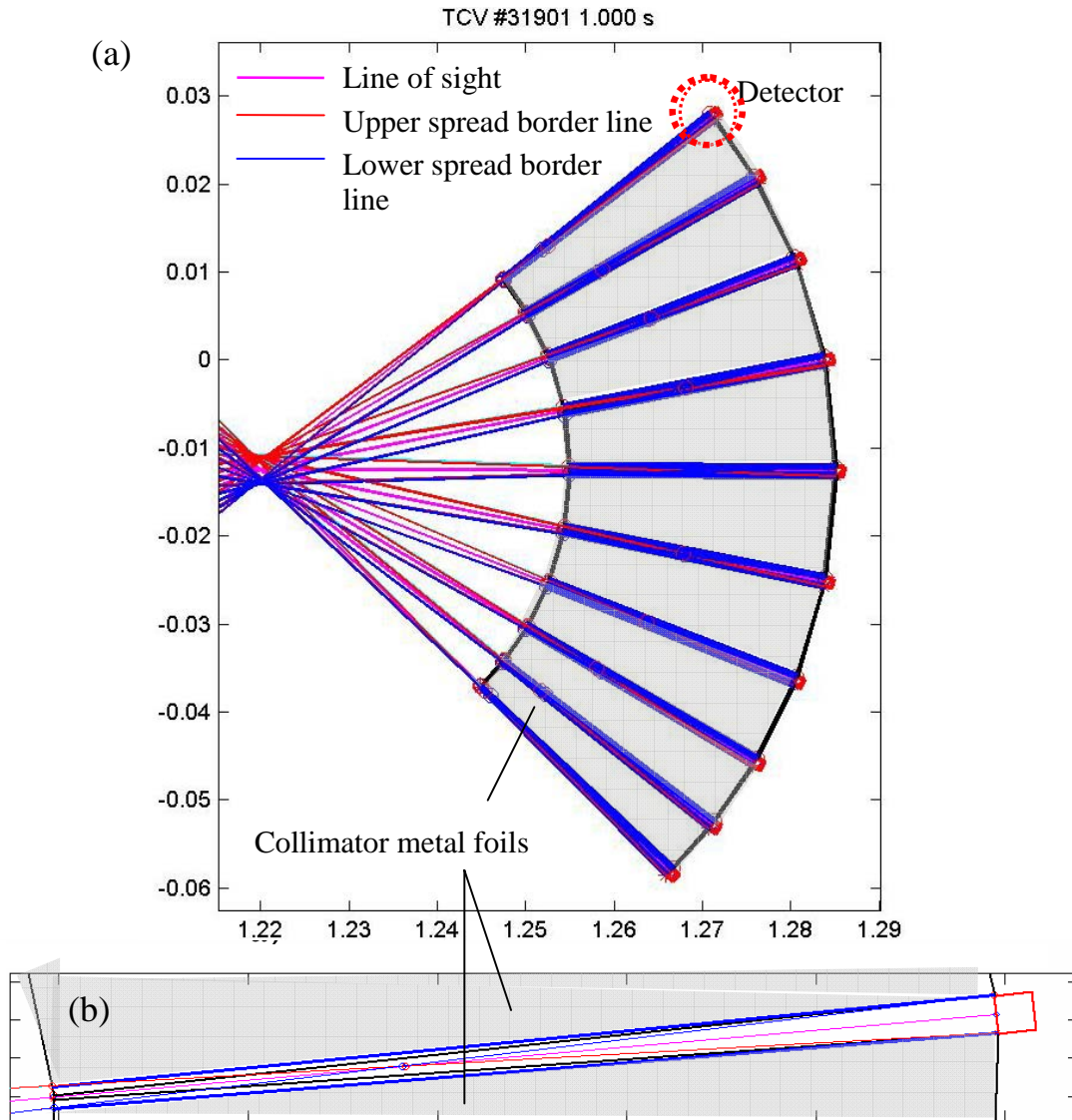


Figure 7.28 a) Divergent radial Soller collimator with radial detector array (for a clear layout only 10 detectors are shown here). b) Detailed view of one single channel.

7.5.3.2.2. Divergent radial Soller collimator

We examine now a second possible scheme utilizing a radial detector array. In this scheme the chords go through a common point (also called “fulcrum”) and intercept detectors in their divergent portion. This scheme retains all the positive features seen for the convergent geometry with radial array. In the convergent case, since the detectors are

placed between the emitting medium and the virtual fulcrum, the detectors can potentially be somewhat closer to the medium than in the divergent case. This could be an advantage when access constraints are particularly severe. However, the existence of a real fulcrum in the divergent scenario offers the highly beneficial option of placing the vacuum interface near the fulcrum, thus keeping its transverse size to a minimum.

This solution fits well our requirements of compactness and flexibility that make the camera design optimal for the TCV environment [75]. It must be noted however that the need for care and precision in the mechanical implementation is more severe than in the pinhole arrangement because of the possibly unique shape of each metal collimator foil.

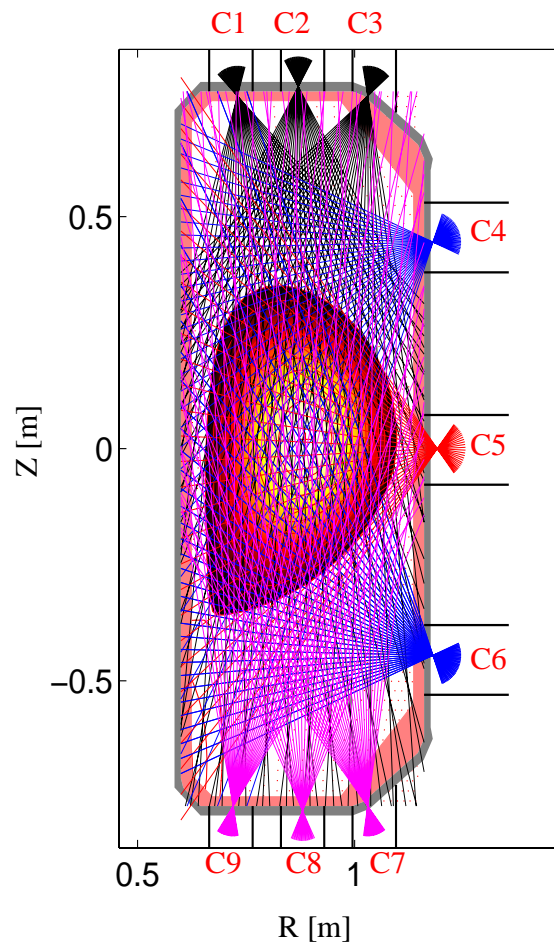


Figure 7.29 View of the TCV cross section with the lines of sight for one of many possible HXR camera designs. In this case the nine cameras are labeled with the progressive notation: C1,...,C9. A flux-surface contour plot of one of the many possible plasma configurations is also displayed.

An example of this geometrical design is shown in Fig.7.28 where for the sake of clarity we have used only ten detectors. A general study was carried out for up to nine cameras located in a typical toroidal sector of TCV, as will be discussed in detail in later sections, and the layout is shown in Fig. 7.29.

Two limiting concepts can be envisioned: one (Fig. 7.30a) characterized by uniform angular detector spacing and thus approximately uniform chord separation in terms of flux surface coordinate; the other (Fig. 7.30b) characterized by uniform chord separation on any plane perpendicular to the camera axis.

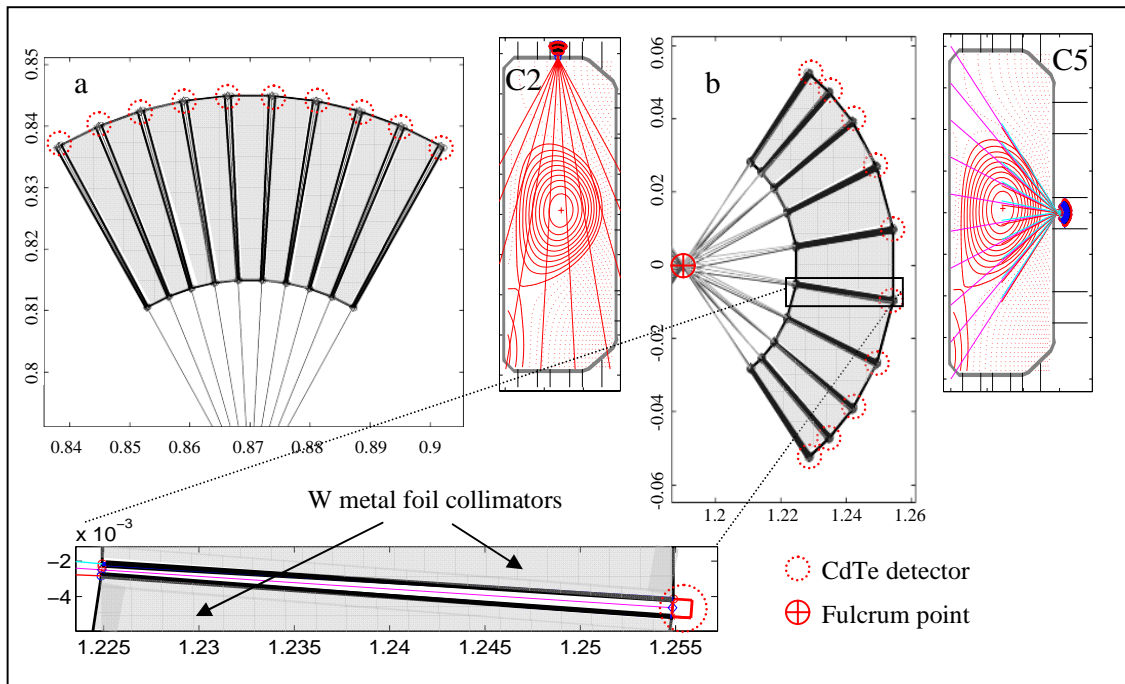


Figure 7.30 HXR camera arrangement based on a modified Soller collimator design. Version *a* is the chosen solution employing equally angularly spaced lines of sight. The alternative version *b* with equal spacing in the plane perpendicular to the camera axis is shown for comparison. The horizontal (R) and vertical (Z) axis dimensions are expressed in m. Here a reduced ten-detector setup is shown for the sake of clarity.

The optimization analysis for tomographic reconstruction (see section 7.10) indicates that the former concept is more suitable for most cameras, as can be expected intuitively, although in the case of C5 both layouts give similar results. The uniform angular spacing being also considerably simpler to design, it was retained as the preferred solution for all cameras.

7.5.4 Tangential detection of fast electron emission

In the context of ECRH and ECCD physics, HXR cameras with poloidal lines of sight are an appropriate diagnostic setup for suprathermal electron studies. This is also the necessary setup for tomographic inversion. However, as was mentioned earlier, no information exists on the pitch-angle distribution of suprathermal electrons accelerated by ECCD, and theoretical predictions indicate that perpendicular and parallel emissions are comparable in this case. Thus, combining a perpendicular and a parallel measurement

would provide novel and unique insight into the physics of EC wave-particle interaction. A parallel measurement offers the additional benefit that it increases the intrinsic spatial resolution by having the direction of integration close to the toroidal direction of symmetry. This aspect makes it also especially valuable for detecting events that are spatially localized. For instance, suprathermal electrons can be generated by large electric fields produced by magnetic reconnection events at low m,n magnetic surfaces, associated with sawtooth crashes and disruptive instabilities [57]. The plasma structure could be investigated during these events in combination with existing diagnostics (soft X-ray tomography and high-resolution multiwire proportional chamber camera, ECE, and a non-spectroscopic HXR tangential camera recently installed in collaboration with the Kurchatov Institute).

Finally, at low density (often required by X2 ECRH operation in TCV), runaway electrons are frequently produced [58]. The bremsstrahlung emission from these suprathermal distributions is in a narrow forward cone along the electron lines of flight and is thus primarily parallel to the magnetic field. This provides additional motivation for a measurement of tangentially emitted X-ray radiation.

Our HXR camera design was therefore expanded to allow measurements of tangentially emitted X-ray radiation and thus to considerably extend its physics potential. This is achieved for cameras C4, C5 and C6 by rotating each entire camera arrangement by 90° (Fig. 7.31).

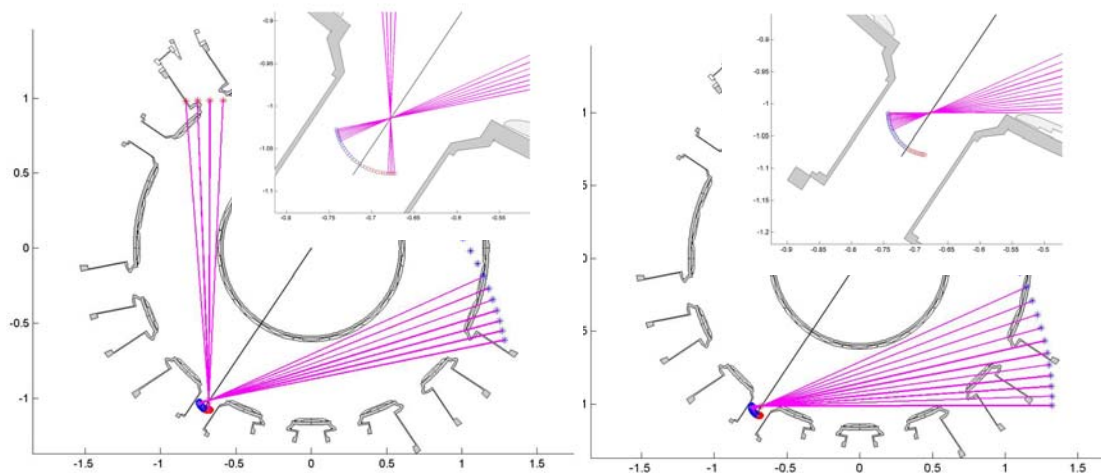


Figure 7.31 Tangential views in the TCV tokamak are achievable by rotating the lateral cameras (C5 in Fig. 7.29) by 90° . On the right, a slight rotation of 11.5° about the horizontal axis leads to truly tangential views matching the pitch angle of the magnetic field. Here only the lines of sight with a significant tangential angle, not intercepting the central column, are shown for simplicity (magenta lines). In the top boxes a detailed plot of the detector position is shown for each configuration.

In this configuration a slight rotation about the horizontal axis, by an angle that depends on the safety factor profile, allows for a truly tangential view, matching the magnetic field pitch angle at a particular location along the line of sight (Fig. 7.31, right). Rotating the vertically viewing cameras (C1-C3, C7-C9), in all practical configurations the angle

of the chords with the magnetic field would never drop below 80 degrees. These cameras are therefore designed to be fixed with views in the poloidal plane.

Since it is envisioned that the primary vacuum interface will be between the collimator and the plasma, the simple rotation of the camera (collimator + detector array) would only involve components outside the TCV vacuum and therefore does not present substantial mechanical difficulties; owing to the cylindrical symmetry of the system no modification of the entrance window is required. Nonetheless the detector assembly is designed to be placed in a secondary vacuum for additional protection of the tokamak vacuum.

7.5.5 Choice of the collimator material

The detectors must be adequately shielded against radiation coming from regions outside their chosen lines of sight. In the Soller configuration the metal collimators are used to perform this task. In order to absorb the undesired photons coming from directions other than the cone defined by the collimator aperture, such photons have to traverse a sufficiently long path through the absorbing material.

The figure of merit in evaluating the gamma-ray shielding efficiency of a particular material is the linear attenuation coefficient μ , which is the product of the mass attenuation ratio μ/ρ and the material density ρ . The mass attenuation ratio is a function of the photon energy and is higher for materials with high atomic number (see Fig. 7.32). For these reasons lead (^{82}Pb) and tungsten (^{74}W) are commonly used in radiation shielding. Gold and platinum are also excellent choices but are generally excluded because of their prohibitive cost.

The intensity I of photons that penetrate a distance x of material without interacting with it is given by: $I(x) = I_0 e^{-\mu x} = I_0 e^{-(\mu/\rho)\rho x}$.

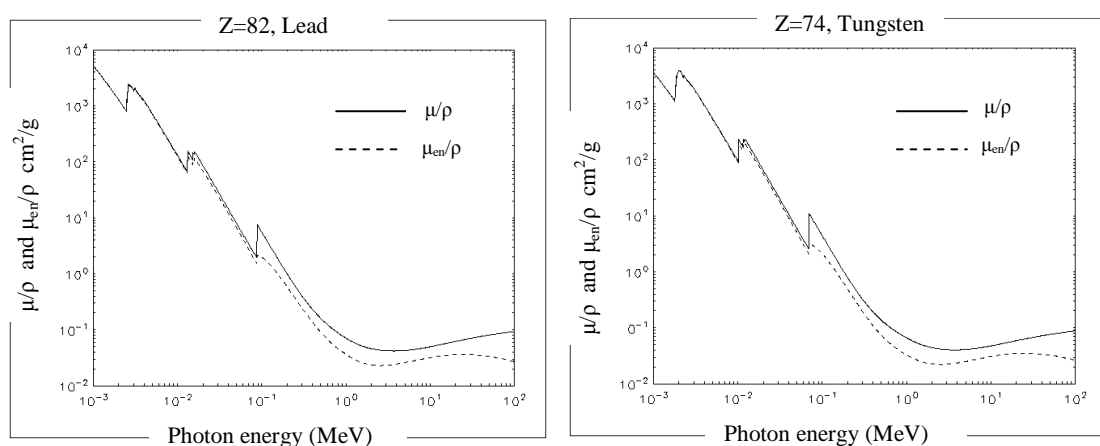


Figure 7.32 The mass attenuation ratios of ^{82}Pb and ^{74}W . The attenuation coefficient is a function of the photon energy. The dashed line represents the mass-energy absorption coefficient μ_{en}/ρ that takes into account the loss of energy due to secondary charged particle bremsstrahlung in the material.

Because of its higher density ($\rho_w = 19.3 \text{ g/cm}^3$, $\rho_{pb} = 11.35 \text{ g/cm}^3$) and in spite of its somewhat lower atomic number, pure tungsten (and, by extension, tungsten alloys) is more effective than lead and is therefore preferable when a high degree of radiation attenuation and compact shielding are required [102]. Accordingly, we made this choice for the TCV system.

In Fig 7.33 we show a comparison between the required thicknesses of lead (dashed curves) and tungsten (continuous curves) for 90% (red) and 95% (blue) absorption in the 0-1 MeV energy range.

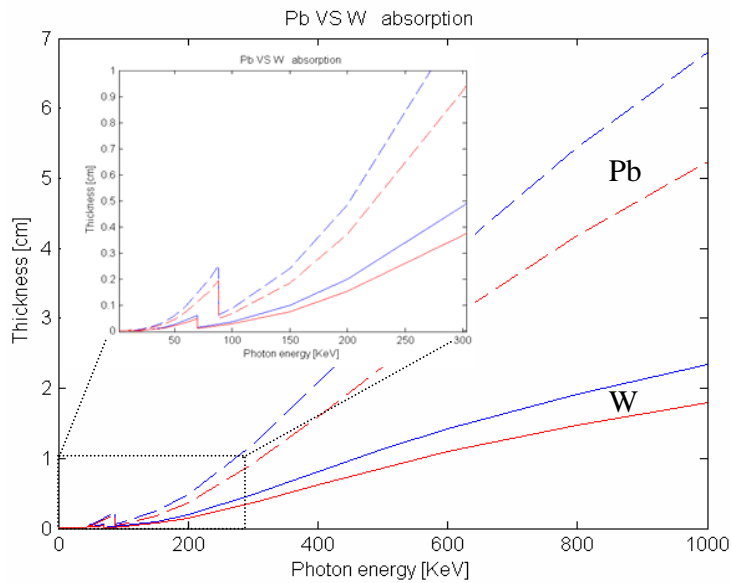


Figure 7.33 Comparison between required thicknesses of lead (dashed curves) and tungsten (continuous curves) for 90% (red) and 95% (blue) absorption in the 0-1 MeV energy range.

7.5.6 Collimator shielding against oblique photon illumination

The ability of the tungsten collimator elements to shield detectors from oblique photon illumination is analyzed in this section. We can note in passing that in the pinhole design (section 7.5.3.1) a single 3 mm thick tungsten collimator would be sufficient to shield the detector array against at least 95% of oblique photon radiation up to 300 keV. For the radial Soller design we have chosen, we consider here the case of the central lateral camera (C5); the quantitative details will differ slightly for the other cameras, since each collimator is separately optimized for the individual geometry and étendue requirements. However the same stopping power specifications can be and have been satisfied in each case. In this analysis we present here the final choice of 2.9 cm long tungsten collimator elements; the width (plasma-side opening) of each collimator element is 1 mm. The detector size is fixed to $2 \times 2 \times 2 \text{ mm}^3$.

Firstly, let us consider the case of photons propagating along an oblique trajectory in the TCV poloidal plane (R,Z). The case of detector #13 chosen here is again representative of the whole detector array.

Figure 7.34 shows the geometry of the system considered; the collimator structure is shown on the right-hand side of the picture, with the detector elements in red at the circular extremity, while the vacuum window is in blue and is centered at the camera fulcrum position ($R=1.21$ m, $Z=0$ m). The detector lines of sight (magenta lines) and the geometric spread limits for each line of sight (yellow: lower spread limit; green: upper spread limit) are also drawn. The incoming oblique photon directions are illustrated with a fan of red lines with its vertex on the center of detector #13. Each oblique photon direction is characterized by the angle θ_γ formed with the detector line of sight; in this case $0 < \theta_\gamma < 9$ degrees. The downward propagating photons (symmetric upper fan) are not considered here because of symmetry considerations.

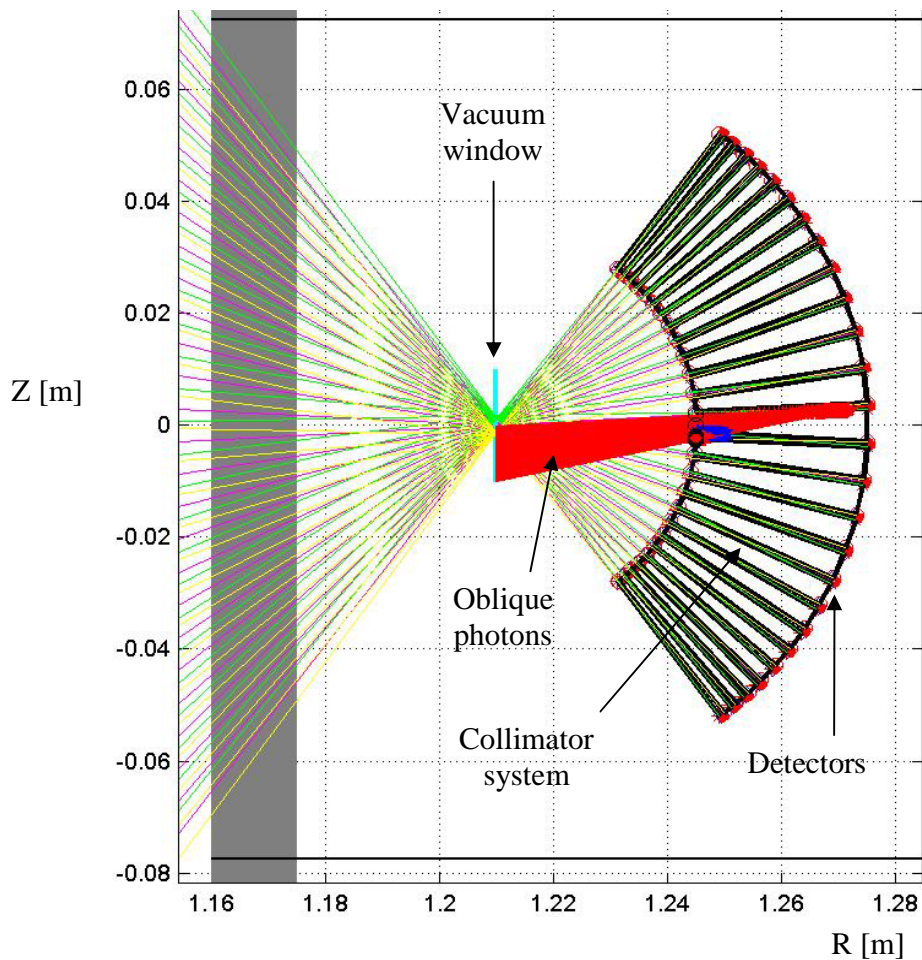
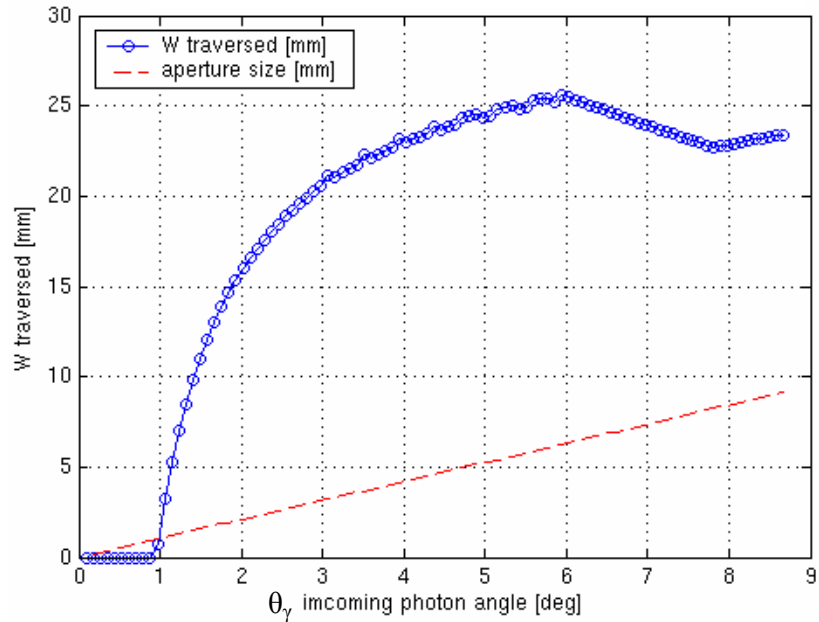


Figure 7.34 Oblique incoming photons (red lines) on a given detector of camera C5.

The total thickness of tungsten traversed by the photons before reaching the detector is shown in Fig. 7.35a. At very small angles, the incoming photons do not intercept the collimator and are in the detector cone of view; at larger angles, from $\sim 1^\circ$ upwards, photons intercept the collimator with a rapid increase of the tungsten thickness traversed. In Fig. 7.35b the oblique photon transmissivity (T_γ) is shown as a function of θ_γ for four different incoming photon energies. As the incoming photons intercept the collimator

($\theta_\gamma \geq 1^\circ$), the associated transmissivity decreases steeply to zero even for relatively high energy photons (~ 300 keV).

a) W thickness traversed by impinging photon detector #13



b) Transmissivity and W thickness traversed vs photon angle, detector #13

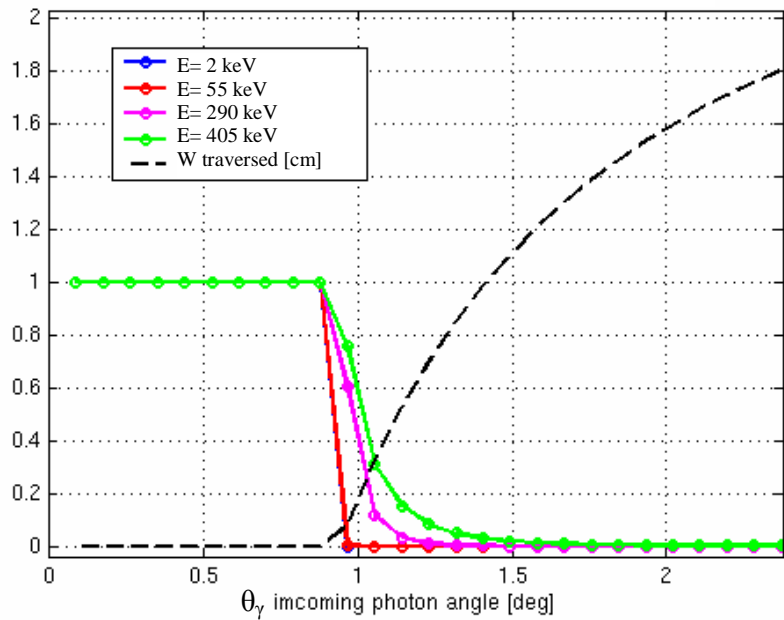


Figure 7.35 (a) thickness of tungsten traversed by impinging photons traveling in the TCV poloidal plane; (b): photon transmissivity for different energies, as functions of the incoming photon angle θ_γ .

It is clear that the proposed collimator is effective in controlling the angular spread of the radiation.

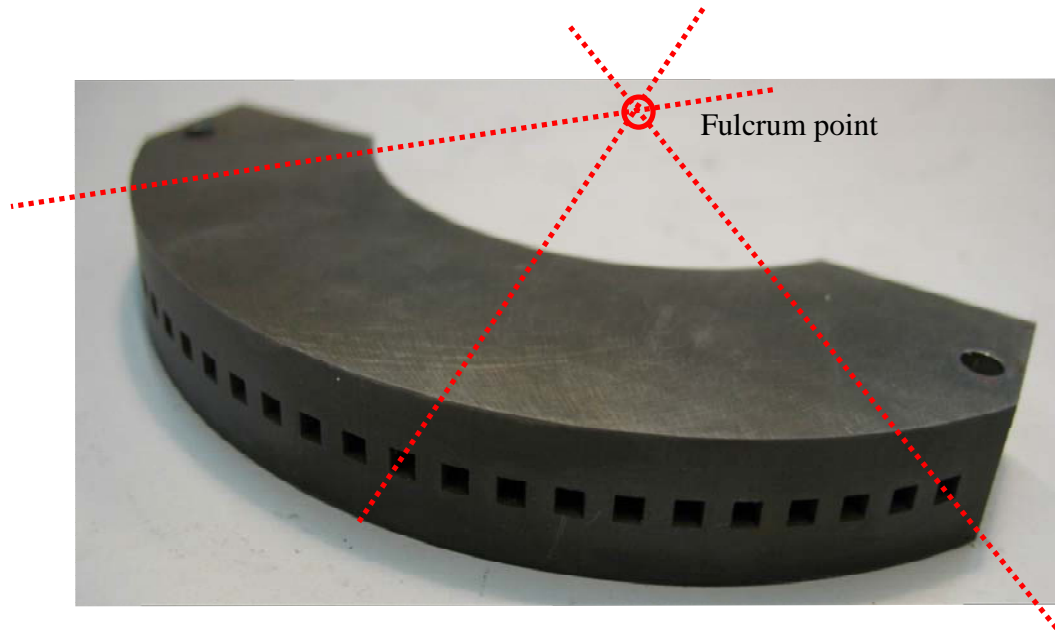


Figure 7.36 Divergent radial Soller tungsten collimator for the equatorial HXRS camera (C5)

The divergent radial Soller tungsten collimator fabricated for the HXRS equatorial camera (C5 in Fig. 7.29) is shown in Fig. 7.36. The precision in the mechanical machining of this component is of capital importance in ensuring the required étendue and has been obtained by Electrical-Discharge Machining (EDM). The square-shaped channel openings on the detector side are visible in the figure.

7.5.7 Conclusions

A technical design for hard X-ray camera collimators has been carried out for three different types of geometry: single pinhole camera, convergent Soller collimator with planar or radial detector array, and divergent Soller collimator with radial detector array. The latter concept meets our requirements of compactness and complete coverage of the plasma poloidal cross section. An optimized conceptual design was produced for several different possible port locations on the TCV tokamak. In addition, we have explored the possibility of rotating the lateral cameras in order to enable emission measurements along a near-tangential direction.

This innovative design for a multi-chord detector array based on radial Soller metal foil collimators would be applicable to other tokamaks in which compactness and flexibility were desired.

7.6 Vacuum windows and filters

7.6.1 Vacuum windows

Beryllium (^4Be) is one of the lowest density and lowest atomic number metals with the highest X-ray transparency of any engineering material. Beryllium has a high melting point and maintains useful mechanical properties up to much higher temperatures than most other metals. These properties have made beryllium the material of choice for X-ray windows used to separate vacuum from the external environment while allowing photons to pass through them. Both planar and hemispherical Be-windows can be manufactured. Beryllium windows with finite thickness also act as a first filter against low energy photons. Figure 7.37 shows the transmissivity of Be windows of varying thickness, multiplied by the efficiency of a 2 mm thick CdTe detector.

Hemispherical Be windows are the ideal configuration in order to guarantee the same photon absorption in each CdTe detector element in a fan arrangement. The concrete advantage of such a configuration, however, has to be carefully evaluated because of the higher cost compared to standard flat windows. Because of the relatively high energy ($>10\text{keV}$) of the investigated radiation, aluminum windows can also be considered. For example a 0.1 mm thick Al absorber is adequate to cut off radiation having energy below 5 keV (Fig. 7.40). Flat, 127 μm thick Be vacuum windows were chosen for the final design. Because of the very low attenuation ($<1\%$ at 10 keV) the hemispherical geometry was deemed unnecessary.

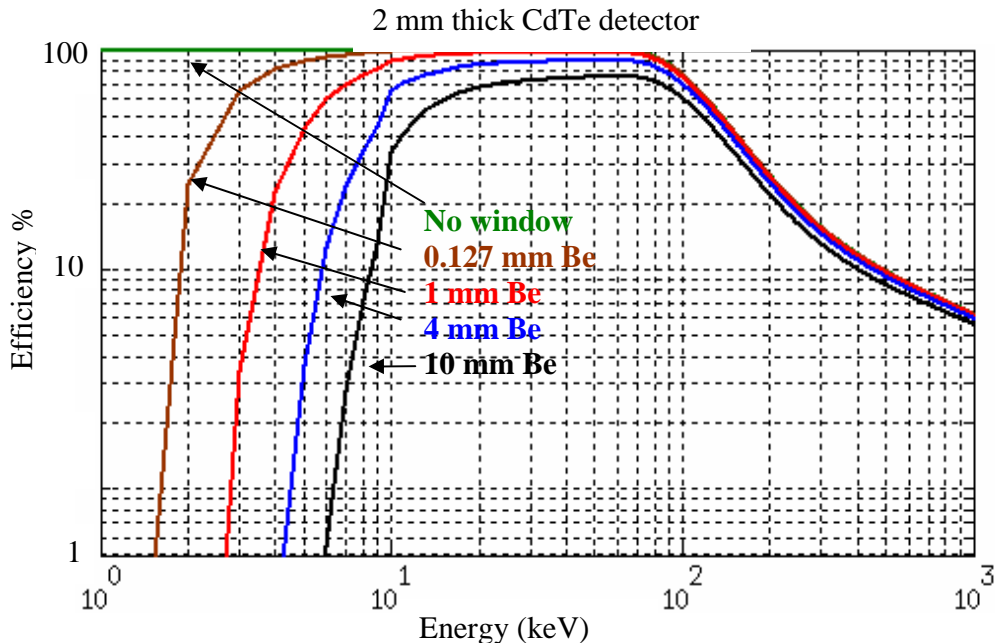


Figure 7.37. Detection efficiency for a 2 mm thick CdTe detector shielded by varying thickness of beryllium between 1 keV and 1 MeV.

7.6.2 Filters

During high power ECRH and ECCD, the HXR flux from the suprathermal population could become high enough to cause pile-up saturation in the signal collected from the detectors. The use of appropriate filters (absorbers) can avoid this undesired effect, enabling only the collection of photons exceeding a certain energy threshold and thus limiting the overall signal (Fig. 7.38). Aluminum and stainless steel are common materials that can be used for this purpose.

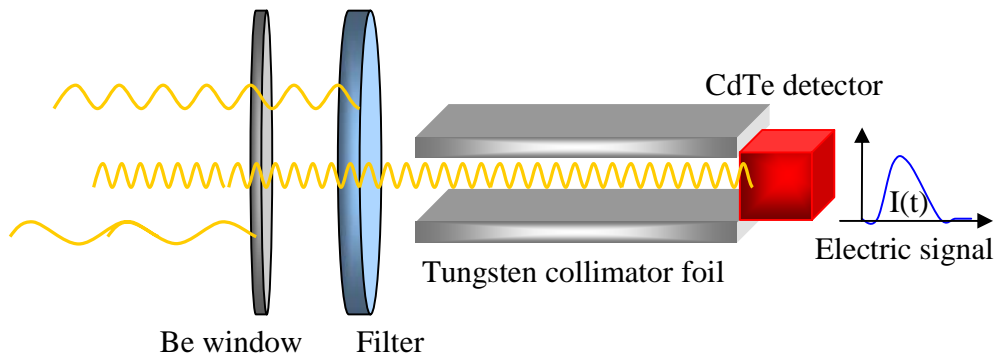


Figure 7.38 Typical window, filter, collimator and detector arrangement employed in our detection system.

Two rotatable filter holders, each holding 5 filters plus one empty hole, are placed in front of the detector array of camera C5, resulting in a total of 36 possible filter combinations. The filters are placed close to the focal point of the detector array (Fig. 7.39).

In its initial configuration, the first camera installed on TCV (C5) includes only one holder with 5 Al filters of thicknesses 0.048, 0.2, 0.95, 1.5, and 2.5 mm. The effect of each filter on the detection efficiency is displayed in Fig. 7.40. A 0.95 mm thick Al filter is enough to cut off 99% of photons with energy less than 10 keV, whereas the thickest filter stops 90% of photons with energy less than 20 keV.

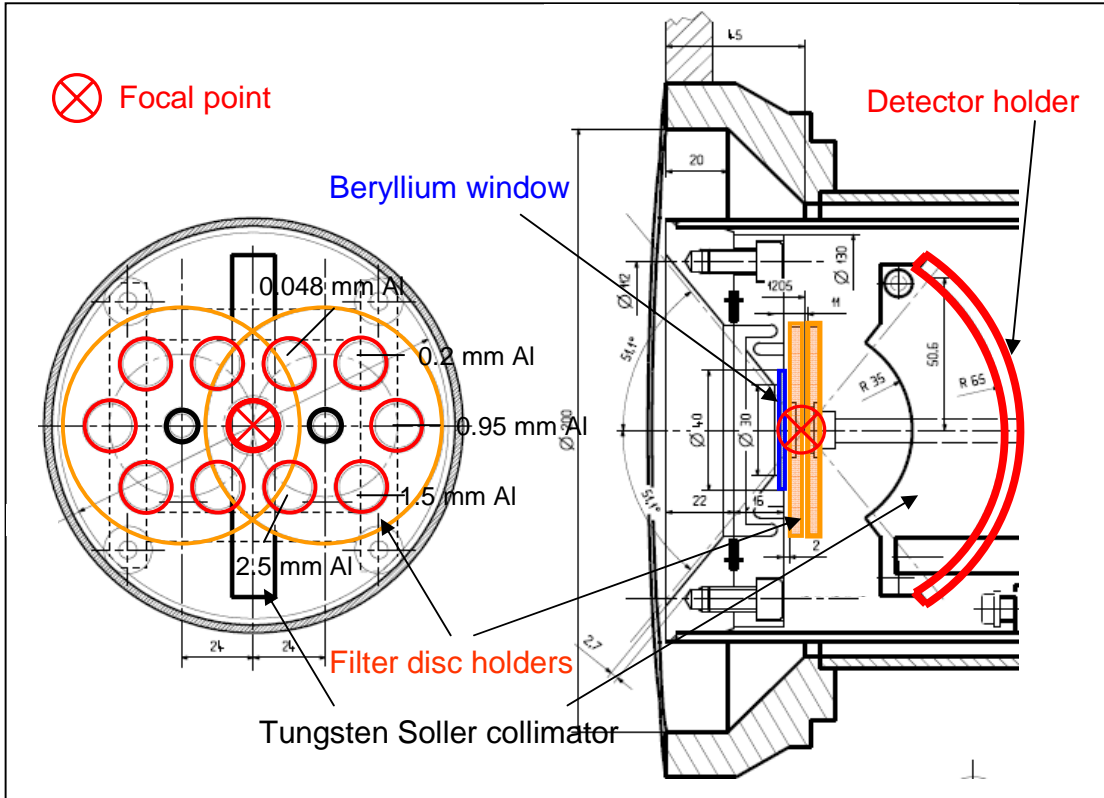


Figure 7.39 Mechanical drawing of the equatorial camera C5: (a) frontal and (b) section from the side views.

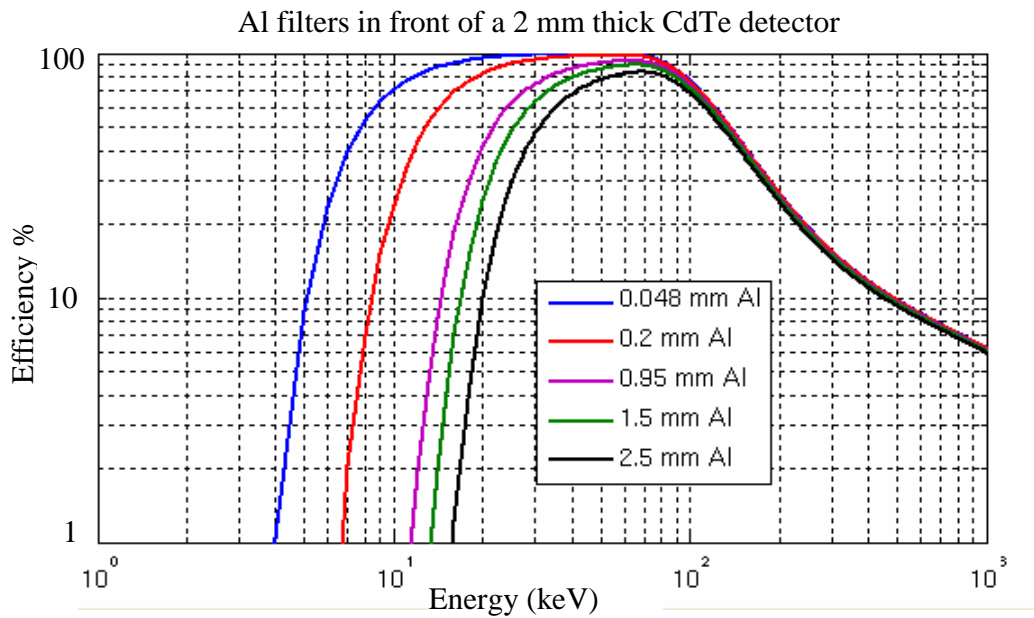


Figure 7.40 Responsivity for a 2 mm thick CdTe detector with the different Al filters currently used in the equatorial camera C5.

7.7 Modeling of detector responsivity in the presence of collimators and shields

7.7.1 Introduction

The detector tests discussed in section 7.4 have been complemented by dedicated simulations to investigate the detector response and possible spurious signals in high-flux conditions.

Experimental tests could also be performed by using a high flux continuum x-ray source. A medical X-ray tube emitting in the 0-120 keV energy range and a linear electron accelerator emitting in the 0-6 MeV energy range are available at the Centre Hospitalier Universitaire (CHUV) in Lausanne, and a contact with the CHUV's staff has been successfully established in view of a possible future collaboration. A further option could be to employ the 90 keV electron beam available from the 2MW, 170 GHz gyrotron for ITER [103], under test at the CRPP as a source of continuum x-ray radiation. However, these tests have not been possible in the course of this thesis, and we have therefore relied entirely on numerical simulations.

7.7.2 Modeling of photon interaction with collimator and detectors

The bremsstrahlung radiation coming from electron-ion interactions in the plasma is not the only radiation that a detector will see: spurious signals can arise from the inelastic (Compton) scattering and typical K-edge fluorescence coming from the material surrounding the detector. The same phenomena can occur in the detector itself and generate possible spurious signals in neighboring detectors (cross-talk). As discussed in section 7.5.3 a radial array arrangement with the oblique Soller collimator configuration results in reduced cross-talk compared to the planar array configuration. Nevertheless, an accurate study of the different phenomena mentioned above was deemed necessary in order to estimate the true detector efficiency and evaluate the expected level of noise induced by fluorescence. In Table 7.6 the characteristic spectroscopic data for the collimator material (tungsten) and the detector compound (cadmium and tellurium) are listed along with the energies of the K, L and M edges and the fluorescence yield of the K and L lines. The L-edge radiation can be neglected because of its relatively low energy and negligible yield compared to K-edge events.

The study we wish to perform requires Monte Carlo simulations and/or experimental measurements of the detector response in a controlled environment. Different Monte Carlo codes have been developed to simulate the interaction of photons with matter, some of the most widely used being: Geant4 (<http://geant4.web.cern.ch/geant4/>), EGS (<http://www2.slac.stanford.edu/vvc/egs/>) and MCNP (<http://mcnp-green.lanl.gov/>). These codes were originally created in view of applications in high energy physics, but have recently evolved to take into account low-energy events as well (fluorescent photons from K, L, M shells, Auger electrons). Such codes are now routinely used to solve

problems related to medical physics and diagnostics and general problems related to detector testing and characterization in different environments and arbitrary geometry.

Element	W	Cd	Te
Z	74	48	52
atomic weight	183.92	112.41	127.6
density (g/cm ³)	19.3	8.65	6.24
k-edge (keV)	69.524	26.711	31.813
L-edges (keV)	12.098;11.542;8.204	4.018;3.727;3.537	4.939; 4.612; 4.341
M-edge (keV)	2.828	0.77	1.006
K-alpha(1); K-beta(1)	59.31; 67.233 keV	23.172; 26.093 keV	27.471; 30.993 keV
L-alpha(1); L-beta(1)	8.396; 9.67 keV	3.133; 3.316 keV	3.769; 4.03; keV
Fluorescence yield			
K	0.958	0.843	0.877
L1	0.147	0.018	0.041
L2	0.27	0.056	0.074
L3	0.255	0.056	0.074

Table 7.6 Characteristic spectroscopic data for tungsten, cadmium and tellurium. The energies of K, L and M edges and the fluorescence yields of the K and L lines are listed. (Source: <http://www.csrii.iit.edu/mucal.html>)

Even without using a Monte Carlo simulator, some basic considerations can give us an idea of the impact of Compton and fluorescence radiation on the performance of our detector-collimator system. Figs. 7.41, 7.43 and 7.44 show the photon cross-sections respectively for tungsten, cadmium and tellurium in the energy range 1-500 keV (data source: Nist XCOM: Photon Cross Section Database <http://physics.nist.gov/PhysRefData/Xcom/Text/XCOM.html>).

In tungsten, the photoelectric effect clearly dominates over Compton scattering in the entire energy region of interest up to 500 keV. The Compton interaction probability is still 10 times less than the photoelectric value at 300 keV.

The situation can be visualized by using the EGS basic simulation tool which will be discussed in detail in section 7.8 [104]. In Figure 7.42, the case of 100 perfectly collimated photons impinging on a 2 mm wide tungsten element is shown for energies 300 keV and 500 keV. The scarcity of Compton events is clearly visible, as is the shortness of photoelectron trajectories, which deliver their energy to the lattice very close to the location of the photoelectric event. These simple considerations lead us to the conclusion that in the energy range 1-300 keV Compton scattering from tungsten collimators can be neglected.

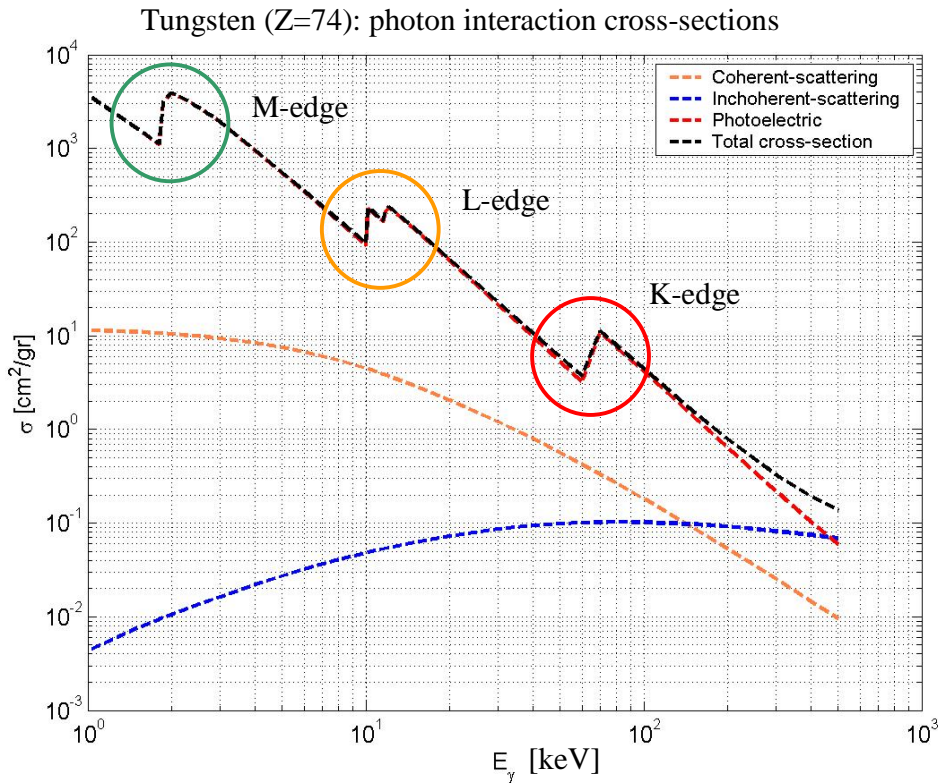


Figure 7.41 Photon cross-section for tungsten. Differential photon interaction cross-sections for coherent, incoherent (Compton) scattering, photoelectric effect; the resulting total cross-section is also plotted. Colored circles indicate the K, L and M edges positions.

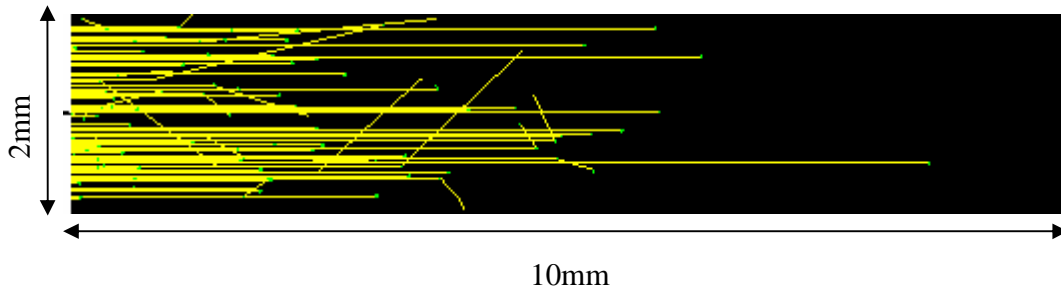
The K-edge fluorescence in shielding and collimating materials has also been evaluated by simplified analytical calculations. Thanks to the strong reabsorption of fluorescence photons in the shielding material, the effect appears completely negligible, accounting for less than 1% of the detected signal in all cases examined. Graded multi-Z shielding was thus deemed to be unnecessary already on the basis of these estimates.

Figures 7.43 and 7.44 show the photon cross-sections for cadmium and tellurium, respectively. For these two elements that constitute the detector material, the photoelectric effect dominates over Compton scattering only up to an energy of ~250 keV, where the two interactions have the same probability. K-edge fluorescence photons are expected to have an impact on the detector efficiency at intermediate energy (Cd K-edge: 26.7 keV; Te K-edge: 31.8 keV).

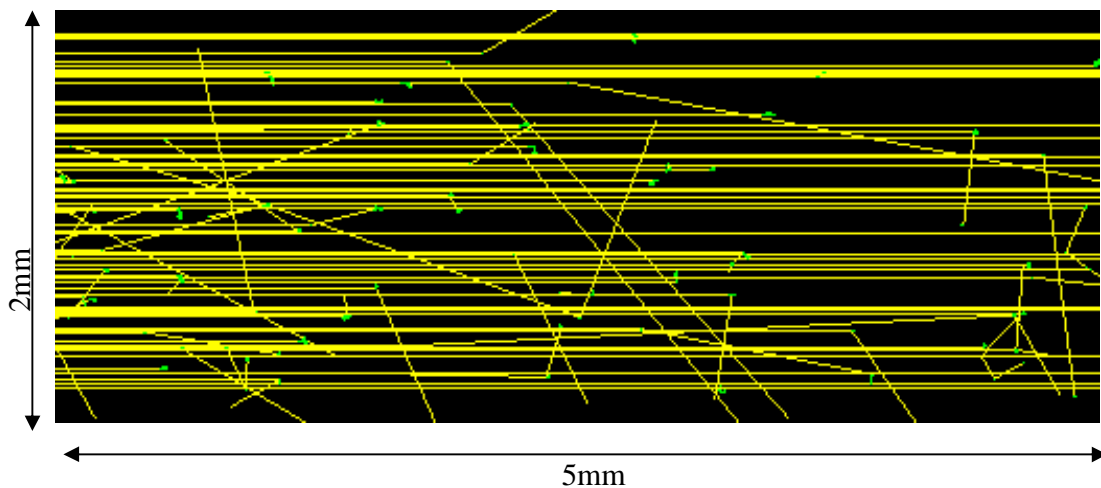
EGS simulation: photoelectric and Compton interactions

Number of incident photons = 100

A) 300 keV photons on a tungsten element



B) 500 keV photons on a tungsten element



- yellow lines = photons
- green lines = trajectories of photoelectrons
- all particles over 10 keV of initial energy are shown
- no cascade events because of relatively low energy photons ($E_\gamma < 511$ keV)

Figure 7.42 Photon-tungsten interaction visualized by using the EGS Monte Carlo code. Case A: 300 keV photon beam (100 photons) on a 2 mm wide, 10 mm long tungsten element; case B: 500 keV photon beam (100 photons) on a 2 mm wide, 5 mm long tungsten element. The Compton events are clearly visible in the yellow lines oriented in directions other than the horizontal.

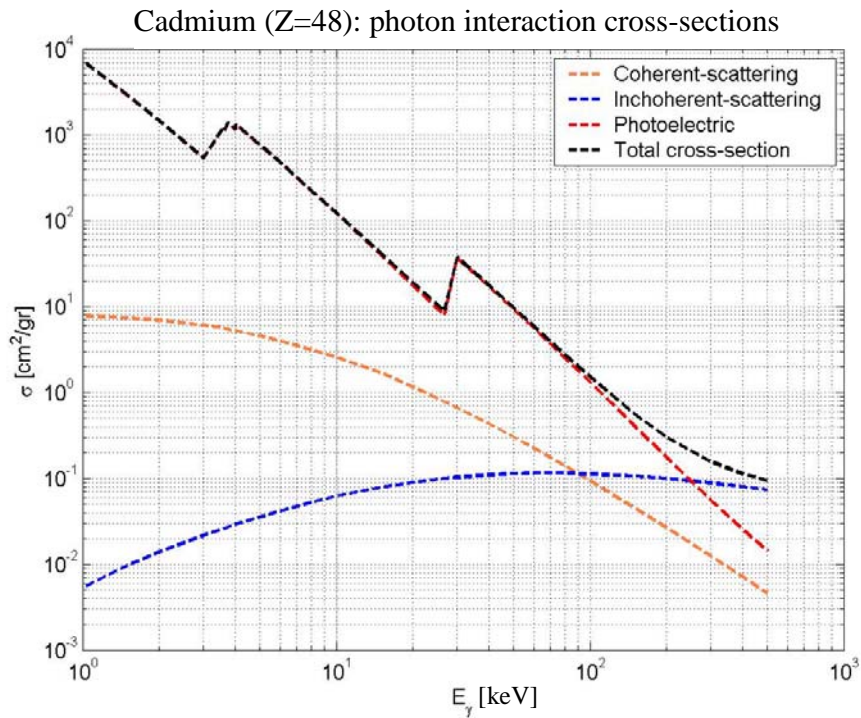


Figure 7.43 Photon cross-section for cadmium: differential cross sections for coherent, incoherent (Compton) scattering, photoelectric effect, and total cross-section.

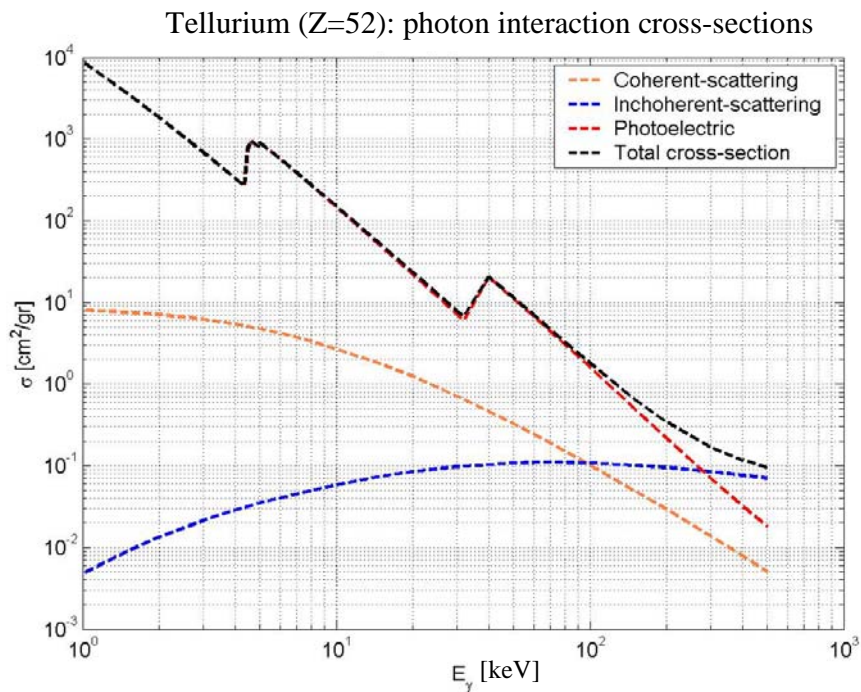


Figure 7.44 Photon cross-section for tellurium: differential cross sections for coherent, incoherent (Compton) scattering, photoelectric effect, and total cross-section.

7.8 System responsivity simulations with the EGSnrc Monte Carlo code

7.8.1 Introduction to EGSnrc

The Electron Gamma Shower (EGS) computer code is a general-purpose package for the Monte Carlo simulation of the coupled transport of electrons and photons in an arbitrary geometry for particles with energies from a few keV up to several TeV. The transport of electrons and photons can be simulated in any element, compound or mixture. EGS was developed at the Stanford Linear Accelerator Center (SLAC) in the late 1970's. The EGSnrc code is just the latest improved release of the EGS family of codes. Bremsstrahlung, photoelectric effect, Compton scattering and pair production are the physical processes that are routinely taken into account by the EGSnrc code. Coherent (Rayleigh) scattering can be included as an option.

The EGSnrc code additionally allows one to treat the relaxation of excited atoms after vacancies are generated by photoelectric or Compton scattering events, and the resulting fluorescence photons (K, L, M shells); furthermore, Auger and Coster-Kronig electrons may be produced and tracked if requested. These features are very important in our simulations which consider relatively low photon energies (1-200 keV). It should be emphasized, however, that the phenomenon of hole trapping in the detector, which gives rise to a low-energy "tailing" of the photopeak (see section 7.4.3), cannot be handled by this code.

The EGSnrc computer code is free software for scientific purposes and can be downloaded from the EGSnrc distribution site (<http://www.irs.inms.nrc.ca/EGSnrc/EGSnrc.html>).

The geometry of the problem to be studied can be freely specified by the user file; a typical geometry used in our simulations is shown in Fig. 7.45. This geometry possesses cylindrical symmetry around the z axis. We defined a "target region", defined by $z \geq 0$ as the region where the incident particles, coming from a particle source, are transported. The $z=0$ plane is called "target plane". All geometric elements in the target region are defined by their radial (r) and vertical (z) positions and depths, and by their material. By combining different geometric elements a detector-collimator configuration can easily be obtained (see Fig. 7.46).

Our simulations involve only a photon source; this source can be set as monochromatic or emitting in a continuum user-defined spectrum. Different types of sources can be defined in the EGS environment: point source emitting in a given solid angle, parallel beam incident with any angle on the target region, and yet other more complicated configurations.

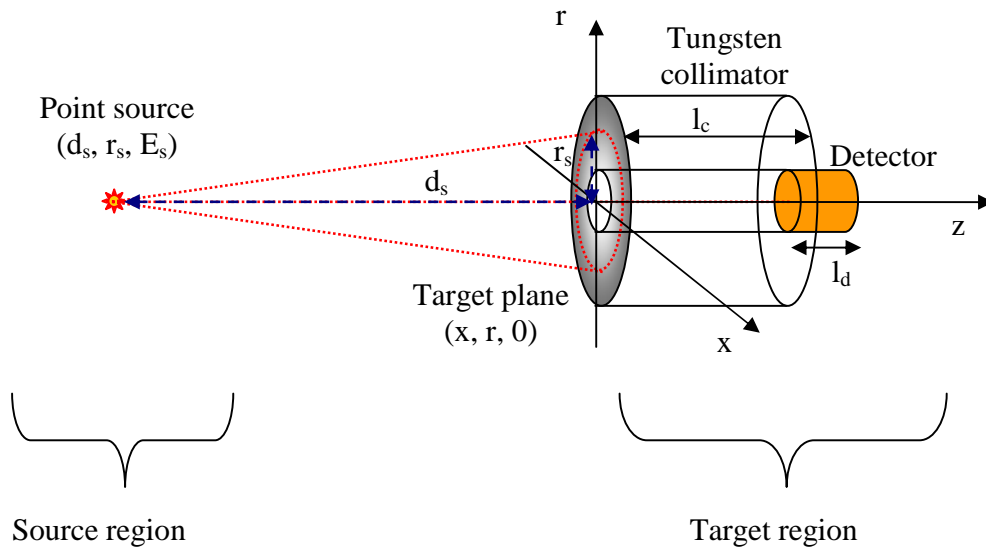


Figure 7.45 The EGS geometric configuration used in our simulations.

7.8.2 Simulations

The purpose of our simulation is to test the responsivity of a CdTe detector, with and without a tungsten collimator, submitted to photon illumination. We have used three different kinds of photon sources:

- S1. A monochromatic (100 keV) point-like photon source set on the detector axis (the z -axis) at a distance d_s from the target plane. The photons are emitted in a cone defined by a height d_s and a base radius r_s as shown in Fig. 7.45.
- S2. A point-like photon source with identical geometry as S1 but emitting in a continuum spectrum.
- S3. A parallel photon beam propagating perpendicularly to the target plane, with continuum spectrum (1-200 keV).

In all simulations we have considered 10^6 photon histories and we have enabled all the transport options of interest for our setup (including spin effects for electron elastic scattering, bound Compton scattering using impulse approximation, Rayleigh scattering and atomic relaxations).

In this section we will employ the following terminology:

- The probability distribution function (PDF) is the photon energy distribution function.
- The pulse height distribution (PHD) is the simulated energy spectrum recorded by the detector.

7.8.2.1 Simulations with a monochromatic photon source

A first set of simulations aimed at assessing the impact of the signal coming from the K-edge fluorescence of the tungsten collimator on the measured signal. For this purpose we have set the energy of the monochromatic photon source (S1 above) at 100 keV, well above the typical tungsten K-edge energy of 67 keV. The geometry of the system is represented by Fig. 7.45 with $d_s=100$ mm, $r_s=2$ mm, $l_c = 30$ mm, $l_d = 2$ mm; $r_d = 1$ mm is the radius of the cylindrical detector base.

In figure 7.46 the results of the simulation are shown for the cases with (blue) and without (red) collimator. The full energy peak (FEP) is well identifiable at the nominal source energy (100 keV), while the Compton tail (from events in the detector) dominates the PHD at low energies. At intermediate energies various peaks appear; in both cases we can observe the escape peaks related to the K-edge energies of Cd ($K_\alpha=23.2$ keV; $K_\beta=26.1$ keV) and Te ($K_\alpha=27.5$ keV; $K_\beta=31$ keV) respectively.

The characteristic tungsten K-edge fluorescence photons are seen only in the simulation with the collimator, as expected.

This first analysis point out the dominance of the CdTe escape peaks over the tungsten fluorescence (the latter being typically two orders of magnitude less than the FEP). However the intensity of the escape peak lines remains ~ 25 times lower than the signal in the FEP. A thicker detector could contribute to mitigating the escape peaks, but the increase in thickness would cause a degradation of the charge collection time.

The analysis was repeated for a detector of larger radius ($r_d = 2.5$ mm). The results are shown in Fig. 7.47. In this case the ratio of the FEP signal to the CdTe escape peaks is increased to 40 due to the increase of the detector radius (r_d), while the ratio of the tungsten K-edge to the CdTe escape peaks increases from 1/21 to 1/8. The increase in detector size clearly improves the efficiency of the detector's re-absorption of its K-edge escaping photons. In our HXR camera system, where the detectors are housed in the tokamak ports, the maximum detector surface is ultimately limited by port size.

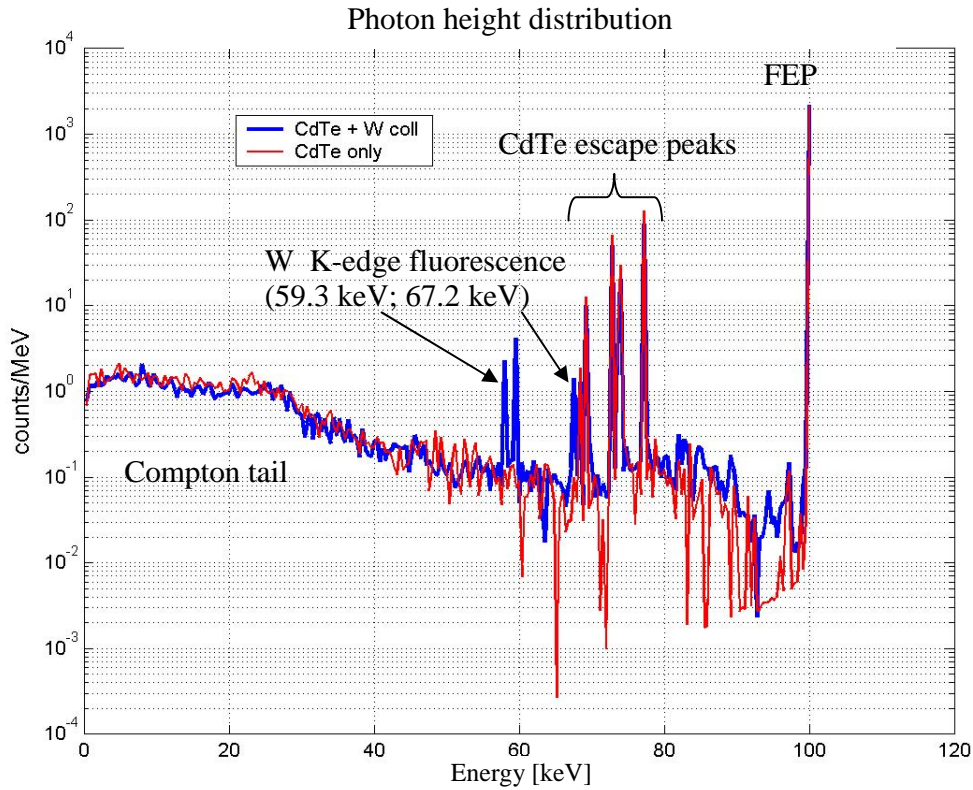


Figure 7.46 Photon height distribution for a CdTe (2mm thick, $r_s = 1$ mm) detector illuminated by a point-like monochromatic photon source ($E_s = 100$ keV). The results of two separate simulations are shown: detector + W collimator (blue curve), and detector only (red curve). The CdTe escape peaks and the fluorescent K-edge events from the tungsten collimator are evidenced in the figure.

In order to confirm the nature of the escape peaks, we have also performed a test using a sample of higher-Z material, i.e. lead (Pb), in place of the CdTe detector. The size of the Pb sample is 2 mm thickness and $r_s = 1$ mm. The results of this simulation are shown in Fig. 7.48. As expected, the characteristic Pb K-edge escape peaks produce intense lines in the low energy part of the PHD, while the characteristic peaks due to the K-edge tungsten fluorescence are unchanged. Furthermore we can distinguish the Pb L-edge escape peaks and an additional series of lines (in the 70-100 keV energy range), which are not well understood, in the Pb + W collimator configuration PHD (blue curve in Fig. 7.48).

We can draw the conclusion that fluorescence effects are expected to be negligible overall. The continuum from Compton events in the detector on the other hand is likely to be significant since it extends over a broad energy range. Its impact will be evaluated in the next subsection.

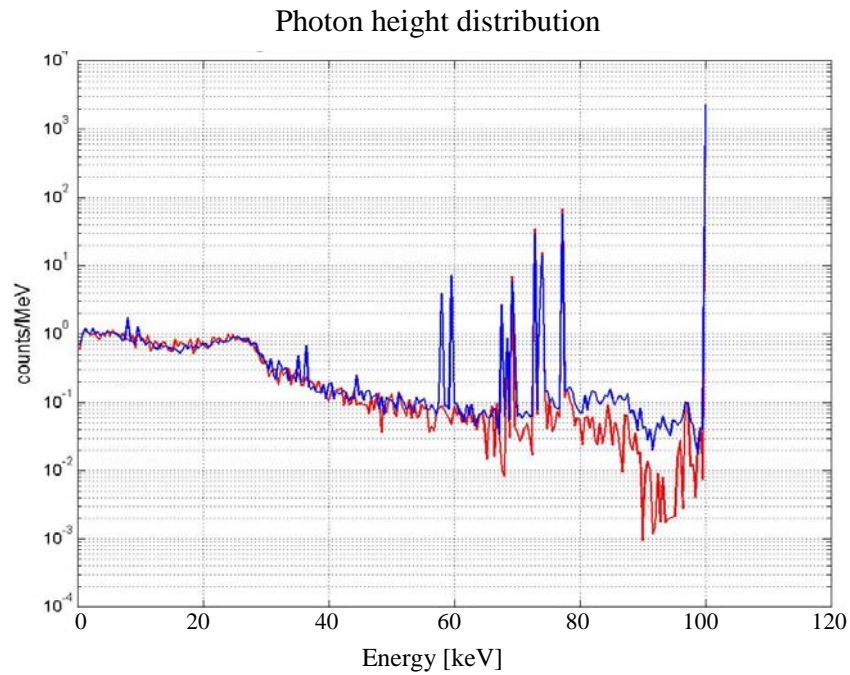


Figure 7.47 Response of a CdTe (2mm thick, $r_s = 2.5$ mm) detector illuminated by a point-like monochromatic photon source ($E_s = 100$ keV). Simulations with detector + W collimator (blue curve), and with detector only (red curve).

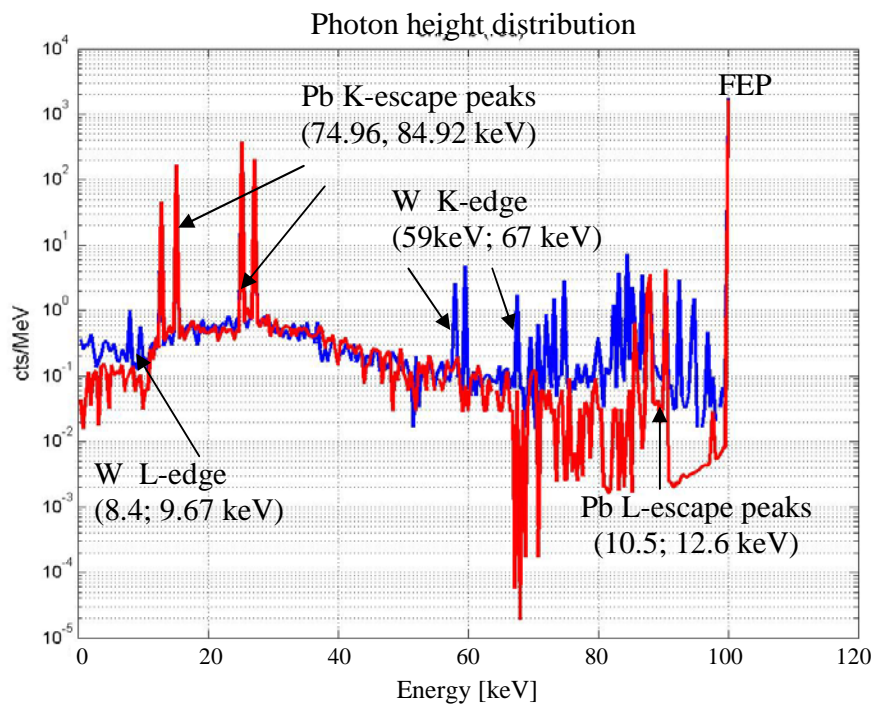


Figure 7.48 High Z (Pb in this simulations) material (2mm thick, $r_s = 1$ mm) illuminated by a point like monochromatic photon source ($E_s = 100$ keV). Simulations with Pb + W collimator (blue curve) and with Pb only (red curve).

7.8.2.2 Simulations with a continuum spectrum photon source

Having established that fluorescence effects do not play a significant role in our geometry, we may ask whether empirical formulas [105] for photon interaction provide an accurate measure of the detected signal. Fig. 7.49 compares such an estimate with the results of an EGS run with an S3-like source, showing a satisfactory agreement.

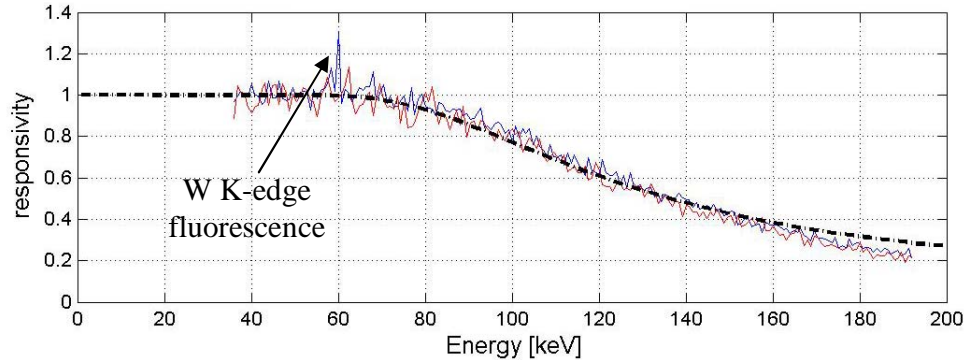


Figure 7.49 Comparison between the responsivity of a $d_l=2\text{mm}$, $r_d=1\text{mm}$ CdTe detector obtained by using data from McMaster et al. [105] (black dash-dotted line) and data output obtained in EGSnrc simulations (using a S3-like photon source): CdTe detector with tungsten collimator (blue line) and without collimator (red line). The two sets of data show good agreement in the energy range considered.

An important point to assess is the capability of our detector system to estimate the temperature of the emitting source (T_s [keV]) when this source emits photons with a Maxwellian energy distribution, thus simulating a thermal plasma source. In this case the source probability distribution function (PDF) exhibits an exponential decay with energy according to the relation: $PDF(E_{ph}) = A_0 \exp(-E_{ph}/T_s)$, where E_{ph} is the photon energy and $A_0 = PDF(E_{ph} = 0)$. The detector size employed in all simulations will henceforth be $l_d = 2\text{mm}$ and $r_d = 1\text{mm}$.

In the first simulations we postulate an S2-like source with $T_s=20\text{keV}$, with the same geometry as in the previous section. We have compared the ability of two different absorbing sample materials, CdTe and Pb, used in different configurations (with and without tungsten collimators), to estimate the source temperature T_s . The results of this test are shown in Fig. 7.50 and Table 7.7. The slope of a log-linear plot of the PHD provides a direct measure of T_s . Here in particular we have used the slope of the whole energy tail of the measured photon spectrum; we referred to this method as “full slope” method to distinguish it from the “second slope” method we introduce later in this section. We remark that all configurations used provide a similar, and accurate, estimate of T_s ; no real advantage is discerned with these parameters in using detector materials heavier than CdTe (e.g. HgI_2).

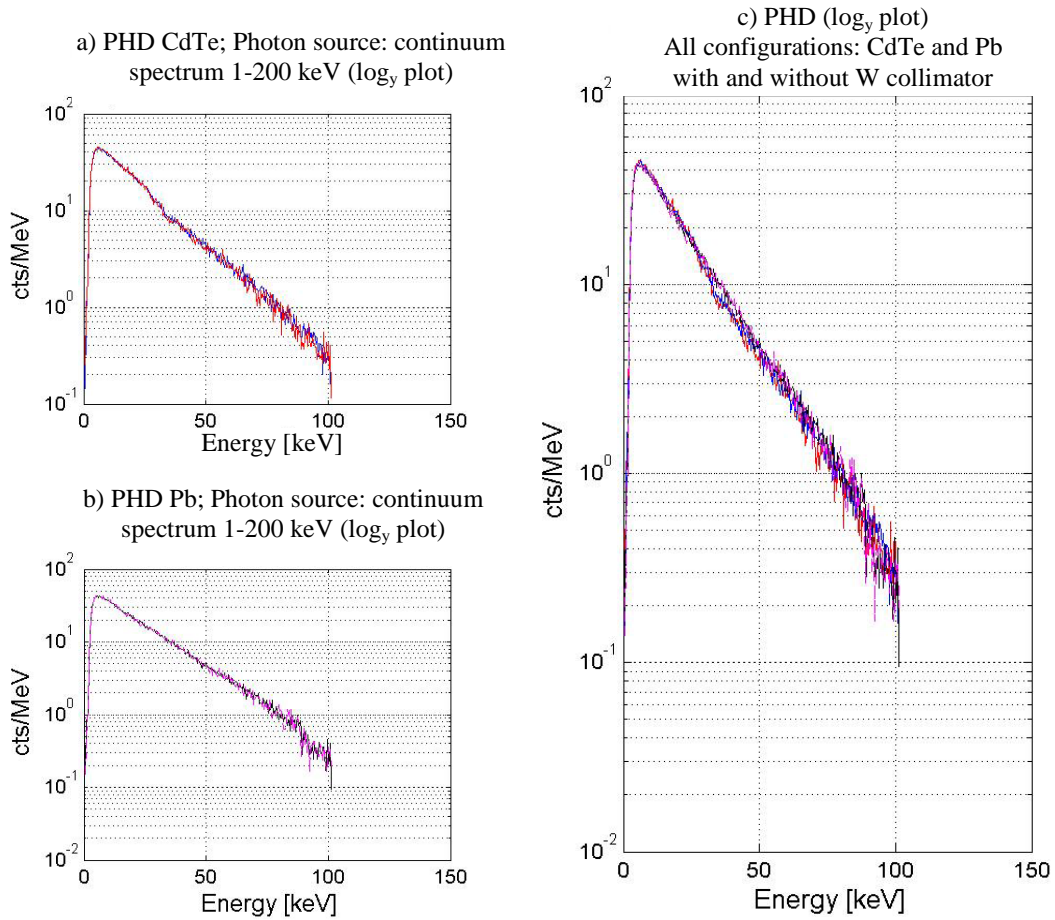


Figure 7.50 Pulse height distributions (PHD) in a semi logarithmic scale. S-2 like photon source emitting in continuum spectrum 1-100 keV with $T_s=20$ keV. a) CdTe detector ($l_d = 2$ mm, $r_d = 1$ mm), with (blue curve) and without (red curve) tungsten collimator; b) Pb “detector” ($l_d = 2$ mm, $r_d = 1$ mm), with (black curve) and without (magenta curve) tungsten collimator. Cases a) and b) are compared in diagram c) evidencing the same behavior for both detector materials and for the different configurations used.

Configuration	p1	p2	Norm of residuals	T_s estimate (keV)
CdTe +W	-0.052	4.110	1.777	19.186
CdTe	-0.053	4.132	2.240	18.765
Pb + W	-0.053	4.181	2.355	18.838
Pb	-0.054	4.199	2.745	18.630

Table 7.7 Linear fit to $\log(\text{PHD})$: $y = p1*x + p2$. $T_s = 20$ keV, estimated $T_s = -1/p1$

Next, we have carried out a temperature scan with the CdTe detector from $T_s = 20$ to 100 keV. The case for $T_s = 80$ keV is shown as an example in Fig 7.51. Table 7.8 summarizes the results of the present analysis for the estimated source temperature. It is clear that an increasingly pronounced discrepancy between the evaluated temperature (T_{ev}) and the source temperature T_s occurs as temperature increases, starting around 30 keV; this effect

is clearly visible in Fig. 7.52 (continuous lines) which suggests a saturation behavior for these energies.

T_s (keV)	Configuration	p1	p2	Norm of residuals	T_{ev} (keV)	T_{ev}^*
20	CdTe +W	-0.052	4.110	1.777	19.186	
20	CdTe	-0.053	4.132	2.240	18.765	
20	Pb + W	-0.053	4.181	2.355	18.838	
20	Pb	-0.054	4.199	2.745	18.630	
30	CdTe + W	-0.036	3.724	1.374	27.566	
30	CdTe	-0.037	3.752	1.703	26.919	
50	CdTe + W	-0.023	3.328	1.171	42.761	47.17
50	CdTe	-0.024	3.337	1.415	42.100	46.9
80	CdTe + W	-0.018	3.045	2.145	54.744	78.3
80	CdTe	-0.019	3.073	2.225	52.952	75.2
100	CdTe + W	-0.019	3.113	2.540	51.822	102.8
100	CdTe	-0.019	3.116	2.468	51.432	98.8

Table 7.8 The data related to the analysis of all cases mentioned in this section are listed here. True photon source temperature (T_s); linear fit parameters (p1, p2 and residuals resulting using the “full slope” method); full slope evaluated temperature (T_{ev}); best evaluated temperature using the (T_{ev}^*) “second slope” method.

We may ask whether a subtler technique than a global linear regression would aid in estimating the real source temperature. To this end, we analyze the PHD (Fig. 7.51). We can clearly distinguish three different regions with three different slopes.

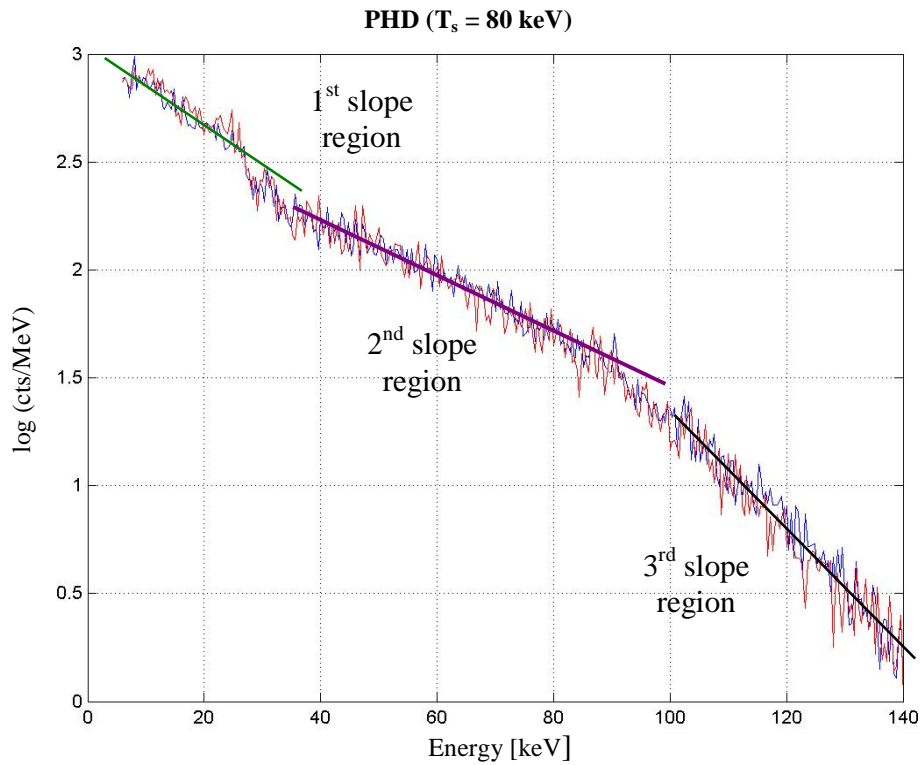


Figure 7.51 Pulse height distributions in a semi logarithmic scale. S-2 like photon source emitting in continuum spectrum 1-150 keV with $T_s=80$ keV. CdTe detector and W collimator as in Fig. 7.45. Three regions with different slopes characterize the measured photon distributions. The three thick lines visualize the three different slopes.

We also recognize that the slope in the second region gives the best temperature estimate while the others ones lead systematically to underestimations. The underestimation in the first region can be attributed to Compton event accumulation shifting signal to lower energies, whereas in the third region it is due to decreasing responsivity.

We have repeated this analysis for all the cases with $T_s > 30$ keV, and the re-evaluated temperatures (T_{ev}^*) are listed in Table 7.8 and are also plotted with dashed curves in Fig. 7.52. In the ideal conditions under analysis (single exponentially decaying source spectrum), this modified method is clearly quite effective.

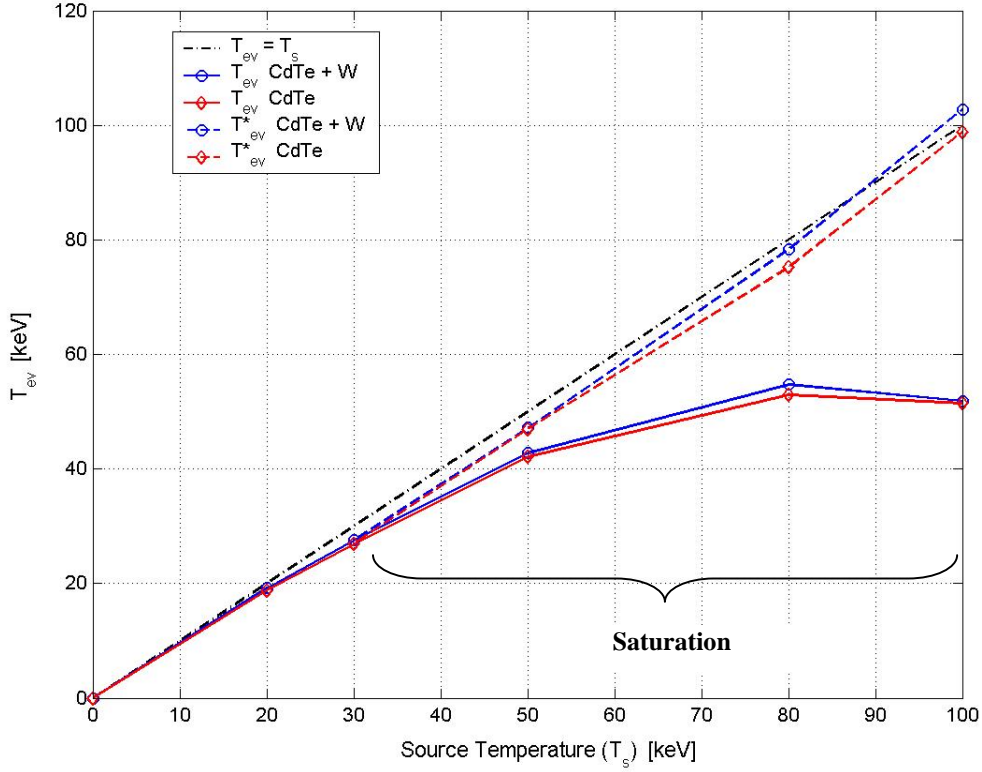


Figure 7.52 Evaluated photon source temperatures (T_{ev}) as functions of the true source temperature (T_s). The “full slope” method (full curves) evidences a saturation behavior for T_s exceeding 30 keV. The “second slope” method (dashed curves) provides an accurate estimate of the true T_s . The black dash-dotted line defines the ideal limit $T_{ev} = T_s$.

7.8.2.3 Simulations with a bi-Maxwellian photon source

Measurements on TCV [50] have shown that a substantial suprathermal electron population is generated when second or third harmonic X-mode heating is applied to the plasma [62]. A simple Maxwellian distribution is no longer an adequate model, and at the next stage of complexity a bi-Maxwellian electron energy distribution has been assumed. With this model, suprathermal temperatures between 10 and 50 keV and densities in the range 1×10^{17} - $6 \times 10^{18} \text{ m}^{-3}$ have been estimated [62].

To simulate the response of a CdTe detector system under these conditions, we have used a S2-like photon source characterized by a bi-Maxwellian spectrum with thermal electron temperature $T_{th}=5\text{keV}$ (typical for a EC heated plasma) and suprathermal electron temperature $T_{st}=30 \text{ keV}$ (compatible with the estimations in [62]), i.e.,

$$A_{th} \exp\left(-\frac{E_{ph}}{T_{th}}\right) + A_{st} \exp\left(-\frac{E_{ph}}{T_{st}}\right) \quad \text{with } A_{th} = \left(2\sqrt{\frac{E_{ph}}{\pi T_{th}^3}}\right), A_{st} = f_{st} \left(2\sqrt{\frac{E_{ph}}{\pi T_{st}^3}}\right),$$

where f_{st} is a weighting factor that controls the contribution of the suprathermal electron population to the total photon signal. We have simulated the representative case

$n_{st} = 0.1n_{th}$ by setting $f_{st}=1/10$ (n_{st} and n_{th} being the densities of suprathermal and thermal electrons respectively).

The result of the EGS simulation is shown in Fig. 7.53 and in Table 7.9. The PHDs measured by the detector in both configurations, with (blue curve) and without (red curve) tungsten collimator, clearly evidence two different slopes.

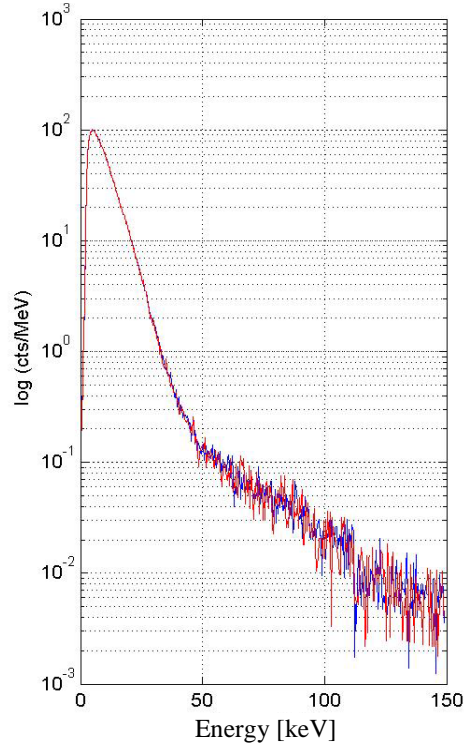


Figure 7.53 Pulse height distribution for a CdTe detector ($l_d = 2$ mm, $r_d = 1$ mm), with (blue curve) and without (red curve) tungsten collimator, for a source bi-Maxwellian spectrum with $T_{is}=5$ keV, $T_{st}=30$ keV and $n_{st}=0.1n_{th}$.

Configuration	p1	p2	norm of residuals	Thermal T_{ev}
CdTe + W	-0.177	5.937	0.448	5.66
CdTe only	-0.1785	5.968	0.535	5.6

				Suprathermal T_{ev}
CdTe + W	-0.0343	-0.368	1.949	29.15
CdTe only	-0.0315	-0.578	2.741	31.75

Table 7.9 Results of the PHD linear fit ($y = p1*x + p2$), $T_{th}=5$ keV, $T_{st}=30$ keV and $n_{st} \approx 0.1n_{th}$. The thermal T_{th} has been evaluated on the 10-25 keV energy range whereas the suprathermal temperature T_{st} has been evaluated on the 50-90 keV range.

In the low energy region, we can remark that Compton accumulation events do not contribute in a significant way to the slope, since the signal is dominated by the thermal bulk electron component, and photoelectric interaction is the dominant process at these

energies. We conclude that the slope of the low energy PHD region is a good measure of the thermal bulk electron temperature. For photon energies exceeding 100 keV the existence of a third slope is still evident; again the phenomenon can be explained by the decrease of the CdTe detector efficiency at these energies. Thus we have retained the 50-90 keV energy region, which permits an accurate suprathreshold electron temperature evaluation.

7.9 Shielding requirements

7.9.1 Thick-target bremsstrahlung emission in the presence of runaway electrons

The electron-ion collision frequency decreases with velocity as v_e^{-3} . In the presence of an electric field E , electrons of sufficiently high velocity will experience an acceleration that dominates the collisional drag on ions. These electrons are accelerated indefinitely and are therefore termed runaway electrons. The plasma becomes predominantly runaway when the electric field exceeds the Dreicer threshold, given by [106]

$$E_D = \frac{q_e \ln \Lambda}{4\pi\epsilon_0 r_D^2} = 0.26 \times 10^{-19} \frac{n \ln \Lambda}{T_e} \quad (7.11)$$

where r_D is the Debye radius, q_e the electron charge, ϵ_0 the vacuum permittivity, $\ln \Lambda$ the Coulomb logarithm, n (m^{-3}) the plasma density, T_e (keV) the electron plasma temperature, and the result is expressed in V/m. At any value of the electric field, however, a finite fraction of electrons will satisfy the runaway condition. The rate of runaway generation (γ_r , [$\text{m}^{-3} \text{s}^{-1}$]) is given by the approximate formula [107]

$$\gamma_r = 0.35 n_e v_c \left(\frac{E}{E_D} \right)^{-3/8} \exp \left\{ - \left(\frac{2E_D}{E} \right)^{1/2} - \frac{E_D}{4E} \right\} \quad (7.12)$$

where v_c is the thermal collision frequency. In a standard low density TCV case, $n_e = 1 \times 10^{19} \text{m}^{-3}$, $T_e = 1$ keV, and $E = 0.2$ V/m, this rate is equal to $3.3 \times 10^{18} \text{m}^{-3} \text{s}^{-1}$.

Part of these runaway electrons can escape the magnetic confinement and strike the TCV wall. The runaway energy in a tokamak can reach several MeV [108, 109], and as a consequence high energy photons are produced, mainly by the Compton and pair generation processes.

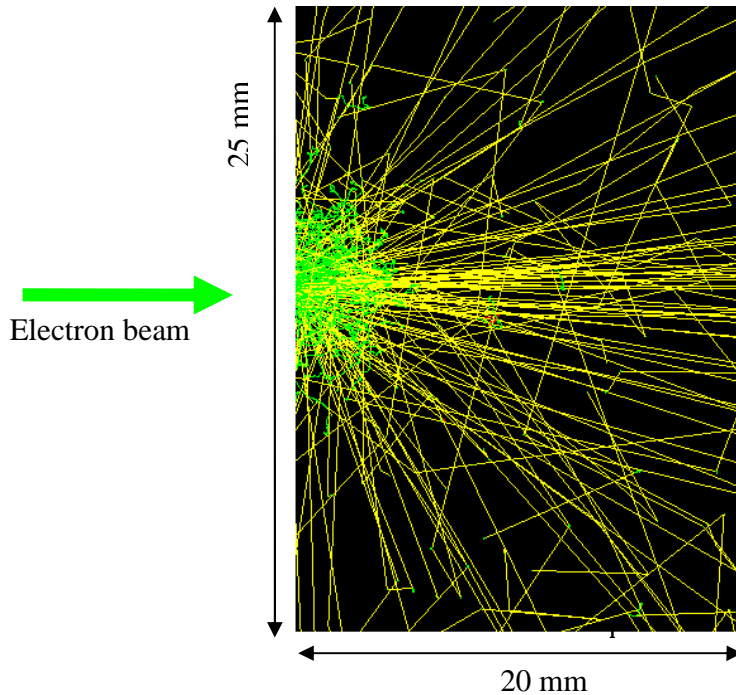


Figure 7.54 EGS simulation: 100 electrons of 10 MeV energy incident on a 2 cm thick iron target; yellow lines = photon trajectories, green lines = electrons; red lines = positrons.

The case of a 10 MeV electron beam (EGS simulation with 100 electrons in the beam) incident on a 2 cm thick iron target is displayed in Fig. 7.54. The resulting high-energy photons can traverse the metallic walls and the collimators, giving rise to spurious signal in the detectors. At these energies, the interaction with the detectors is primarily due to Compton scattering, resulting in a down-shifted energy spectrum (<100 keV), as confirmed by EGS simulations (Fig 7.54).

Preliminary tests with a prototype collimator-detector-amplifier assembly for the HXRS equatorial camera revealed significant signal during low density (line-averaged density $<1.5 \times 10^{19} \text{ m}^{-3}$) TCV discharges, even in the absence of ECRH, which decreased and eventually disappeared as the density increased. Such a signal was detected even in conditions in which the detector lines of sight in the prototype system didn't intercept the plasma. The energy spectrum of this signal was indeed predominantly in the 10-100 keV energy range, with a statistically significant tail extending up to several hundred keV. To discriminate the source of this signal we progressively shielded the prototype system from side illumination with up to 1 cm of lead (the front view is collimated by at least 2 cm of tungsten) obtaining only a partial reduction of the signal. Furthermore, we varied the orientation of the system over a wide range, without significant variation in the recorded signal.

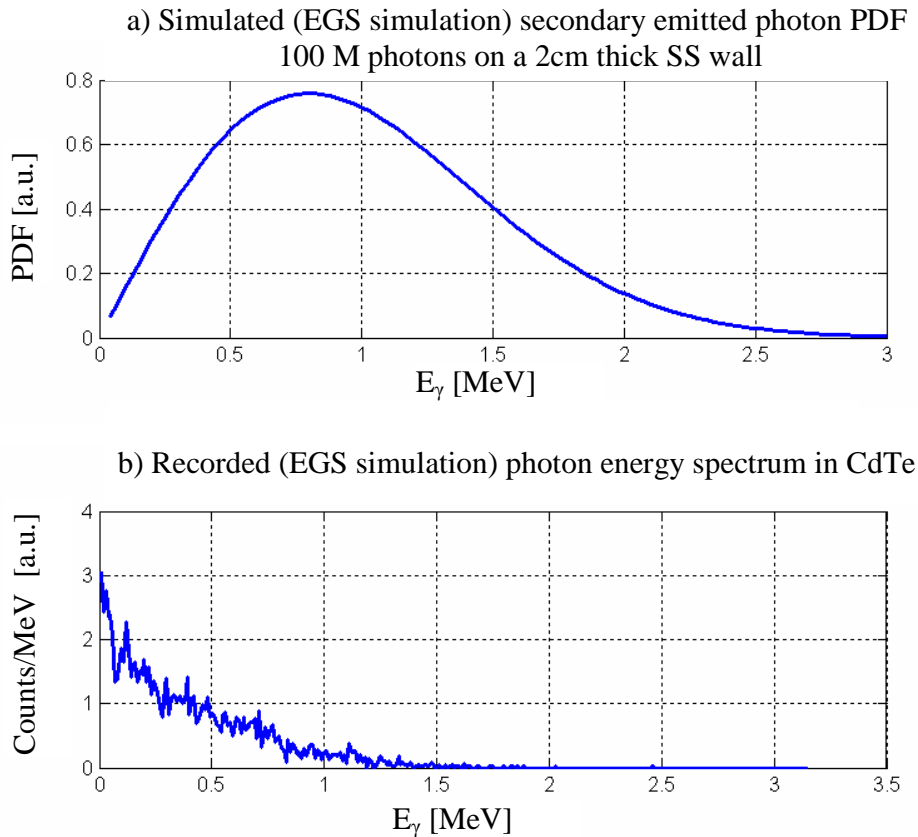


Figure 7.55 Modeled secondary emission from thick target bremsstrahlung due to interaction of electrons with a stainless steel wall. a) A 1 MeV Maxwellian photon distribution is assumed (100M photons in the simulation). b) The resulting simulated spectrum measured by a CdTe detector ($r_d = 1$ mm, $l_d = 2$ mm), placed behind the wall, shows an accumulation of events in the low energy region of the spectrum as observed in experiments.

In many of these low density discharges a heavily shielded scintillator-photomultiplier system that measures the flux of hard X-rays escaping the TCV walls also detected a signal in coincidence with the HXRS test system (observation of runaway activity with the HXRS equatorial camera is discussed in more detail in section 8.2).

These observations motivated the addition of more shielding than was originally planned. For the case of the first completed camera, C5, the shielding is composed of two separate parts: a 2 cm thick tungsten ring surrounding the flange that houses the camera, plus another 2 cm thick tungsten disc filling the space close to the Soller-collimator/detector-holder assembly inside the flange (see Fig. 7.56). In such a way, at least a 2 cm thickness of tungsten exists between the detectors and the vessel in all directions other than the collimator channels. Furthermore, we added an extra CdTe “blind” detector, completely shielded, in each HXRS camera to monitor the runaway activity. Giving the high incidence of runaway emission, at least in common TCV conditions, this detector has become an essential discriminator element in this kind of system.

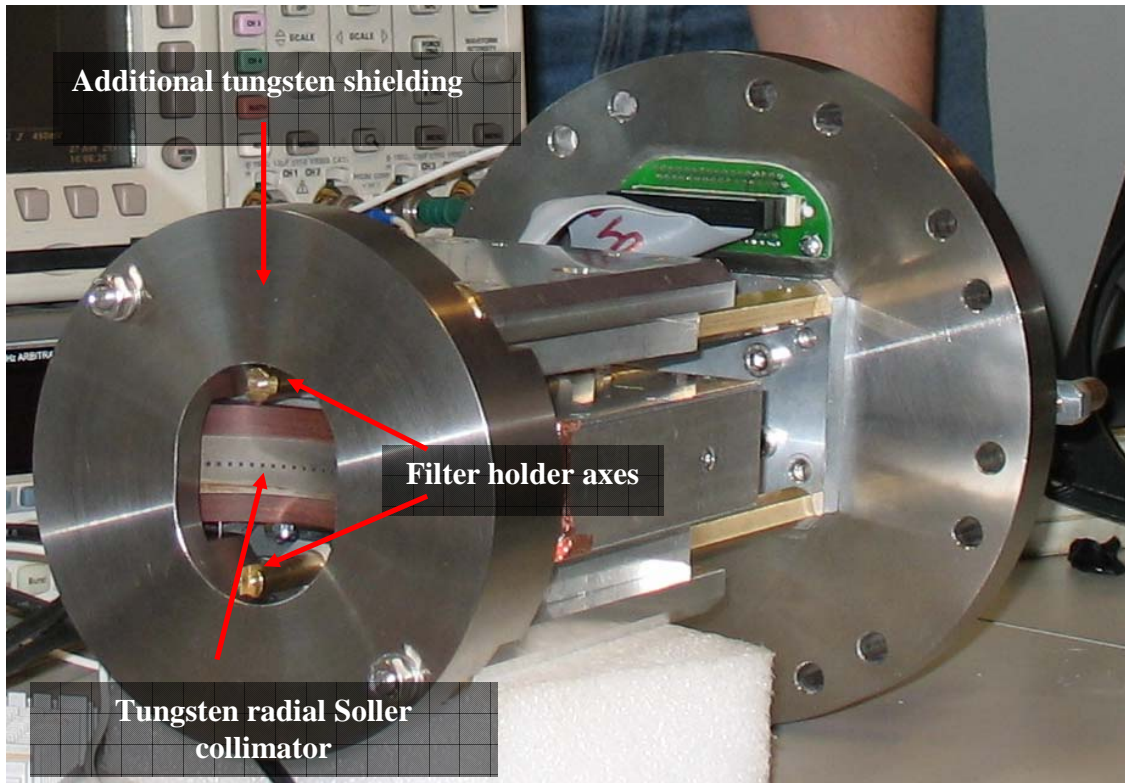


Figure 7.56 The 2-cm thick additional tungsten shielding disc in the equatorial HXRS camera. The radial Soller collimator is visible behind the shield; the rotatable filter holder axes are also indicated.

7.9.2 Neutrons

Direct ion heating is not a goal in the TCV tokamak at present: typical ion temperatures (T_i) are in the range 200–500 eV even though a minority suprathermal ion population has been observed ($T_i^{\text{sup}} \sim 3\text{keV}$, $n_i^{\text{sup}} \sim (0.1-0.3)n_i^T$) [110].

For $T_i \leq 25\text{keV}$ the deuterium-deuterium fusion reaction rate averaged over a Maxwellian distribution is given by the following empirical formula

$$[111]: R_{DD} = \frac{1}{4} n^2 \langle \sigma v \rangle_{DD} \text{ m}^{-3} \text{ s}^{-1}, \quad \text{where}$$

$$\langle \sigma v \rangle_{DD} = 2.33 \times 10^{-20} T^{-2/3} \exp(-18.76 T^{-1/3}) \text{ m}^3 \text{ s}^{-1}.$$

A rough estimate (typical ion density $n = 5 \times 10^{19} \text{ m}^{-3}$, ion temperature $T_i = 0.5\text{keV}$, and simple flat temperature and density profiles, plasma volume $\sim 1 \text{ m}^3$) gives a neutron flux to the vacuum vessel ($a \sim 0.3\text{m}$) of a few hundred counts per cm^2 per second. This results in a few neutrons per second impinging on a single detector. The absorption rate of fast neutrons in the CdTe crystal is also low, of the order of 3%. By contrast, the absorption of thermal neutrons in cadmium is very efficient; however, the emission of thermal neutrons by the plasma is completely negligible. The noise due to neutron interaction in the detector bulk material will thus be negligible and neutron shielding is therefore considered unnecessary in the TCV environment.

A possible TCV upgrade in order to operate plasmas with similar electron and ion temperature $T_i \simeq T_e$ is under discussion. The most probable option in this sense is to install a neutral beam injector (NBI). In this case we can envisage to have a possible scenario where $T_i = 5\text{keV}$, and a study similar to the one presented just above shows that the neutron yield may no longer be negligible, of the order of $1 \times 10^3 \text{ s}^{-1}$ per detector; furthermore, neutrons can interact also with the surrounding collimators and shields, potentially increasing the level of noise. In this scenario the neutron induced noise could become potentially more significant and would have to be re-evaluated.

7.10 Optimization of HXRS diagnostic design by simulations of tomographic reconstruction

7.10.1 Introduction to quantitative assessment criteria

In the conceptual design up to nine HXR cameras were considered, located at different vacuum vessel positions determined by the available ports, as shown in Fig. 7.29. The number and distribution of the cameras is determined by a compromise between the quality of tomographic reconstruction and the cost, within the constraints set by the TCV port geometry. In order to base the choice on a quantitative foundation, we have performed simulations to compare imposed (or “original”) HXR emissivity patterns with the tomographic inversions resulting from the calculated detector signal distributions in different configurations [75]. Different emission patterns have been used in the analysis: poloidally-symmetric emissivity profiles reconstructed from past, non-tomographic HXR measurements during ECRH in TCV, as well as periodic poloidal distributions with a poloidal wave number m , to simulate increasingly complex poloidal asymmetries. More recently, the newly developed fully relativistic 3D bounce-averaged Fokker-Plank solver LUKE, coupled with the C3PO ray tracing code and the R5-X2 bremsstrahlung calculator (see section 4.2), has been used to simulate realistic non-thermal bremsstrahlung emission patterns from past ECCD shots in TCV (Fig. 7.57). These simulations reveal a poloidal asymmetry in the non-thermal photon emission, which is a particularly pertinent test for the validation of our camera setup. The simulation code performs a line integration of the simulated photon emissivity $g(R,z)$ along the i-detector’s line of sight (L_i) in order to obtain the so-called chord brightness

$$f_i = \int_{L_i} g(R, z) dl .$$

This information is then fed to the tomographic algorithm that generates the reconstructed plasma emissivity on a $N_p = n \times k$ pixel grid using the minimum Fisher information method [79] (described in section 7.2.1) in order to condition the solution; here n and k are the numbers of vertical and horizontal pixels, respectively, constituting the reconstruction grid over which the unknown emissivity function is derived.

A quantitative estimation of the quality of the reconstructed emissivity is given by the

reconstruction variance: $RV(R, O) = \frac{\sum_k \sum_n \left(\frac{R_{kn}}{\bar{R}} - \frac{O_{kn}}{\bar{O}} \right)^2}{\sqrt{\sum_k \sum_n (R_{kn} / \bar{R})^2 \sum_k \sum_n (O_{kn} / \bar{O})^2}}$, where

$$\bar{F} \equiv \left(\sum_k \sum_n F_{kn} \right) / N_p ,$$

which compares the original simulated emission (O) with the reconstructed one (R). Here, O and R are positive definite quantities. The reconstruction variance approaches zero when the normalized values of R approach the normalized values of O . We have applied the minimum RV criterion to identify the best set of N

cameras (N=2,3,4,...) to be employed in an envisioned tomographic setup. As expected, the quality of the tomographic reconstruction increases when cameras viewing the plasma from maximally separated directions are added.

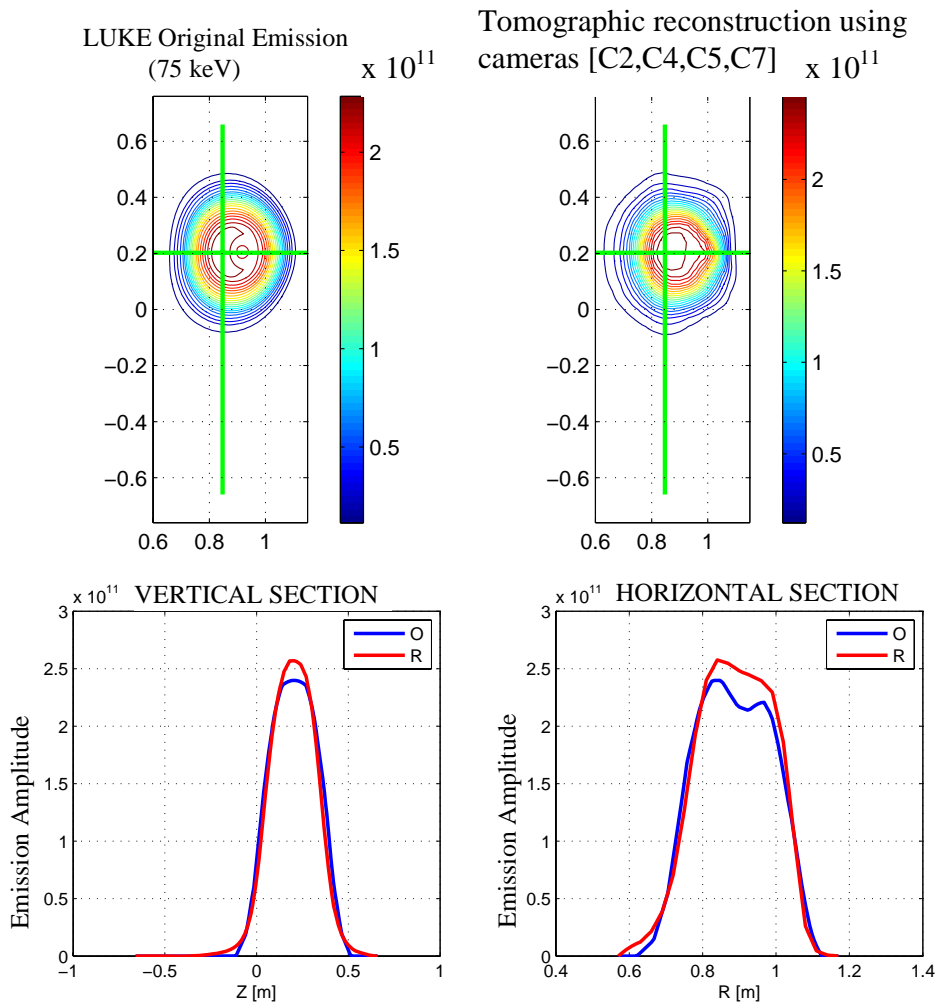


Figure 7.57 Tomographic reconstruction of non-thermal bremsstrahlung emission from a C3PO-LUKE-R5-X2 simulation (TCV shot 21657, $t=1s$, photon energy 75keV) by using the [C2, C4, C5, C7] camera setup. Top: bremsstrahlung emission contour plots for the original (O) and the reconstructed (R) emission. Bottom: comparison between R and O profiles along the vertical and horizontal sections defined by green lines in the contour plots above (the two lines intersect at the point of maximum O emission). The position of maximum emissivity, the relative emission amplitude, and the poloidal emission asymmetry are all satisfactorily recovered (in this case $RV=0.0138$). The emission amplitude is given in $\frac{\text{photons}}{m^3 \cdot s \cdot sr \cdot keV}$.

Figs 7.58 and 7.59 show the tomographic reconstructions for different camera combinations (2 and 3 cameras in Fig. 7.58 and 4 cameras in Fig. 7.59), for two different

emission patterns, each consisting of a superposition of an $m=0$ and a $m=2$ emission pattern. One original emission corresponds to the case of a $z=0$ plasma centered in the middle of the vessel, whereas the other original emission corresponds to a plasma centered at $z=21$ cm.

These $m=0+m=2$ original emissions have been used as the initial basis of the optimization, since the majority of TCV plasmas are centered between $z=0$ and $z=21$ cm. The reconstruction variances for the two positions are averaged to provide a single figure of merit. This is then minimized by repeating the simulation for varying camera combinations and setups. Once the minimization is achieved, it is then performed again for an $m=0+m=1$ original emission as a cross-check.

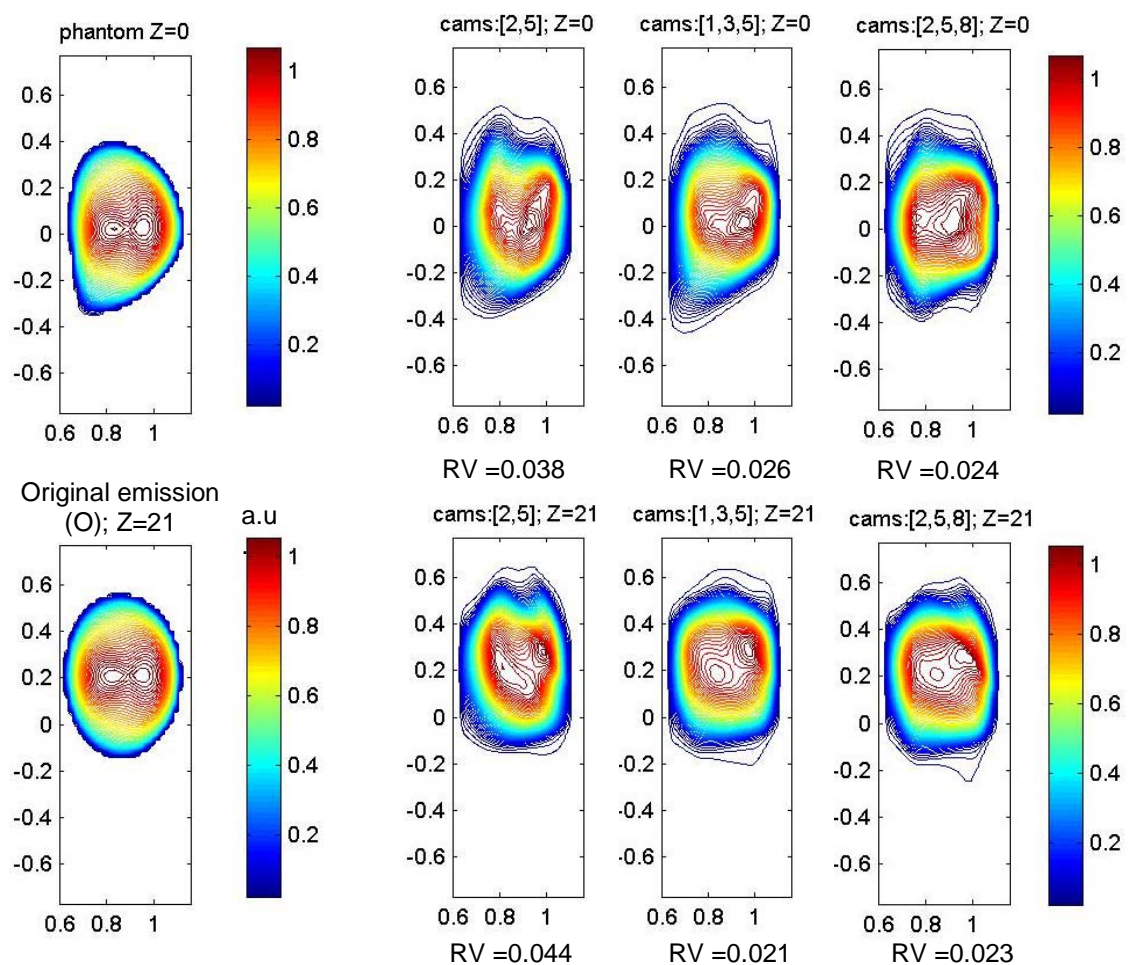


Figure 7.58 Tomographic reconstruction of a ($m=0 + m=2$) original emission pattern centered at $z=0$ (top) and $z=21$ cm (bottom), by using the best set of 2 camera setups [C2,C5] and two different sets of 3 cameras, respectively [C1,C3,C5] and [C2,C5,C8]. For each reconstructed emission the RV value is given below the plot.

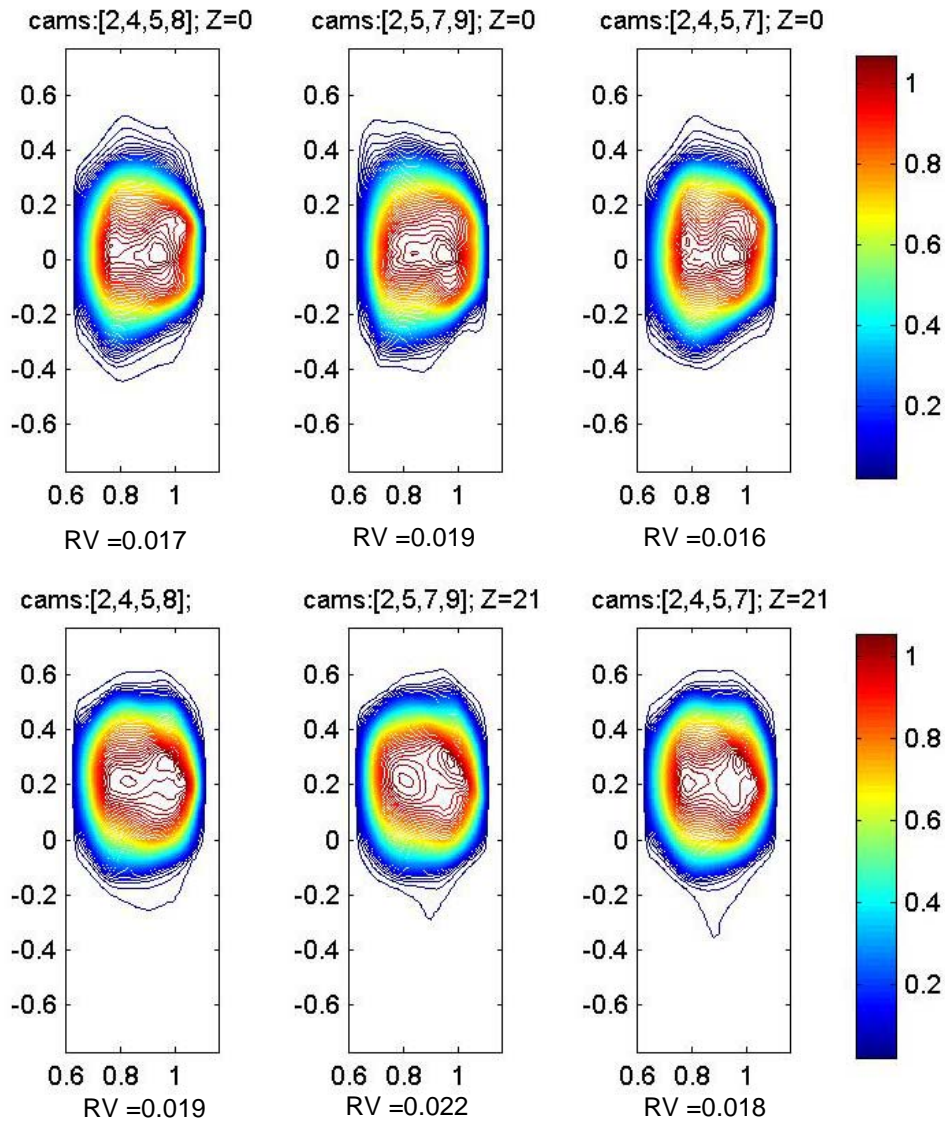


Figure 7.59 Tomographic reconstruction study for three different 4-camera setups. The original emission is the same as in Fig. 7.58. In this case the [C2,C4,C5,C7] camera setup gives the best performance for both the Z=0 and Z=21 cm cases.

7.10.2 Trade-off between tomographic performance and costs

The gain in the quality of the reconstruction obtained by adding an additional camera is not a constant, the benefits being more significant when going from a 2 to a 3 camera setup and from 3 to 4 and becoming modest with each additional one as shown by the graph at the bottom of Fig. 7.60. Here, the optimization procedure described in the previous section was carried out for all combinations of cameras up to a total number of 5. The figure of merit shown is the minimum achieved for each number of cameras.

The result is similar for all the emissivity patterns described above.

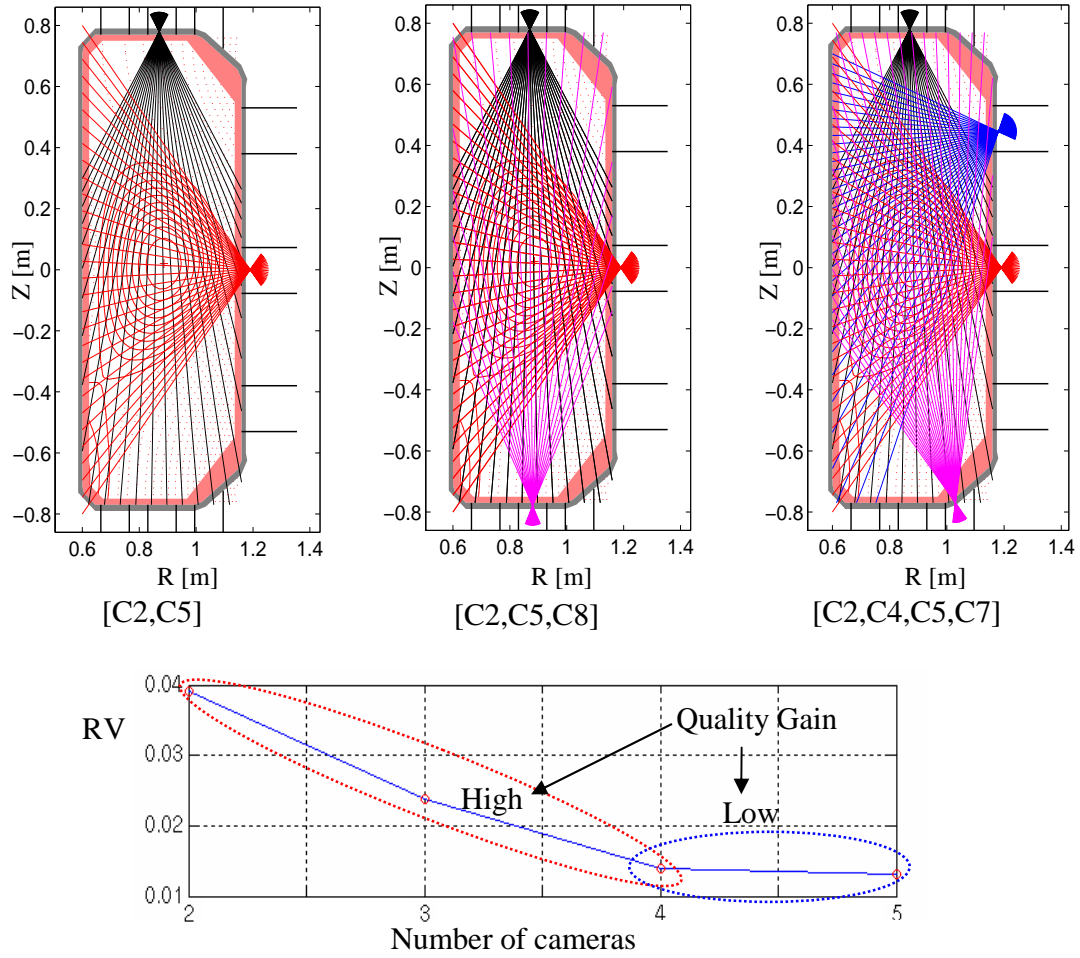


Figure 7.60 Best camera setups for N-camera systems (N=2 to 5). The quality of the tomographic reconstruction is measured using the RV factor. The graph at the bottom, here obtained from a particular emission pattern ($m=0$ and $m=2$), shows the typical RV behavior obtained in our validation process. The quality gain is high when incrementing the number of cameras from 2 to 3 and from 3 to 4 and saturates beyond 4. These simulations employ 28 detectors in each camera.

A four-camera setup can be considered a good compromise between tomographic performance, costs, and vacuum vessel coverage. Furthermore, the main features in the reconstructed emission pattern, such as peak position, relative intensity, and poloidal asymmetries ($m=1,2$) from a broad range of imposed emissivity patterns can be recovered satisfactorily.

7.10.3 Camera position optimization

For a given camera setup, the position of each camera has been varied in order to determine the geometric design offering the highest tomographic reconstruction quality (i.e. the minimum RV value). The parameter used for this study is the coordinate position (R,Z) of the fulcrum point for the camera under consideration. We treat here as a salient example the case of the [C2,C5,C8] camera setup that is a possible choice for a 3-camera setup. At first we imposed fixed positions for cameras C5 and C8 and we allowed C2 to vary within the space available in its port. The results (see Table 7.10) show that the camera (fulcrum) position has a modest influence on the quality of the reconstruction, as the overall variation of RV does not exceed 3 %. Once the optimal C2 fulcrum position was found it was then fixed and the same process was repeated for camera C5 and then for C8. The variation of RV is confirmed to be modest in all cases.

RV for C2		Z 1	Z 2	Z 3
		0.87	0.88	0.89
R 1	0.76	0.0344	0.0345	0.0349
R 2	0.77	0.0346	0.0347	0.0352
R 3	0.78	0.0349	0.035	0.0354
R 4	0.79	0.0353	0.0352	0.0356

Camera	C 5	C 8
N detectors	30	30
R	1.19	0.88
Z	0	-0.78

Table 7.10. Fulcrum position optimization for camera C2 in the [C2,C5,C8] camera setup. Each camera is equipped with 30 detectors. The fulcrum positions for cameras C5 and C8 are fixed. The RV parameter has been evaluated for different (R, Z) positions within the upper central port of the TCV vacuum vessel. The pixel dimension used is 3cmx3cm. The original emission used is an m=1 pattern centered at Z=21 cm as in Fig. 7.59.

Owing to the weak influence of the fulcrum position on the quality of the tomographic reconstruction, the position of each camera within its port was ultimately decided primarily by considerations of mechanical convenience (ease of manufacturing, installation and implantation of the associated electronics).

7.10.4 Optimum number of detectors per camera

Another important point to assess is how many detectors are needed for each camera in order to achieve a good trade-off between tomographic reconstruction quality and cost. Therefore a set of tomographic simulations with varying number of detectors per camera (14 to 35) have been carried out for the two 4-camera setups, [C2,C4,C5,C8] and [C2,C4,C5,C7].

The detector number scan has been repeated for different original emission patterns (plasma emissions with poloidal asymmetry $m=1$ and $m=2$, respectively, superimposed on a $m=0$ original emission) and for different plasma positions (at $z=0$, and $z=21$ cm). An overall figure of merit was obtained here by adding the reconstruction variances for all four cases. The results (summarized in Fig. 7.61 here below) reveal that a number of ~ 25 detectors per camera is appropriate, as the tomographic performance (RV) does not improve significantly beyond that number. The final choice was 24, a convenient choice as acquisition modules are generally manufactured in multiples of 8 channels.

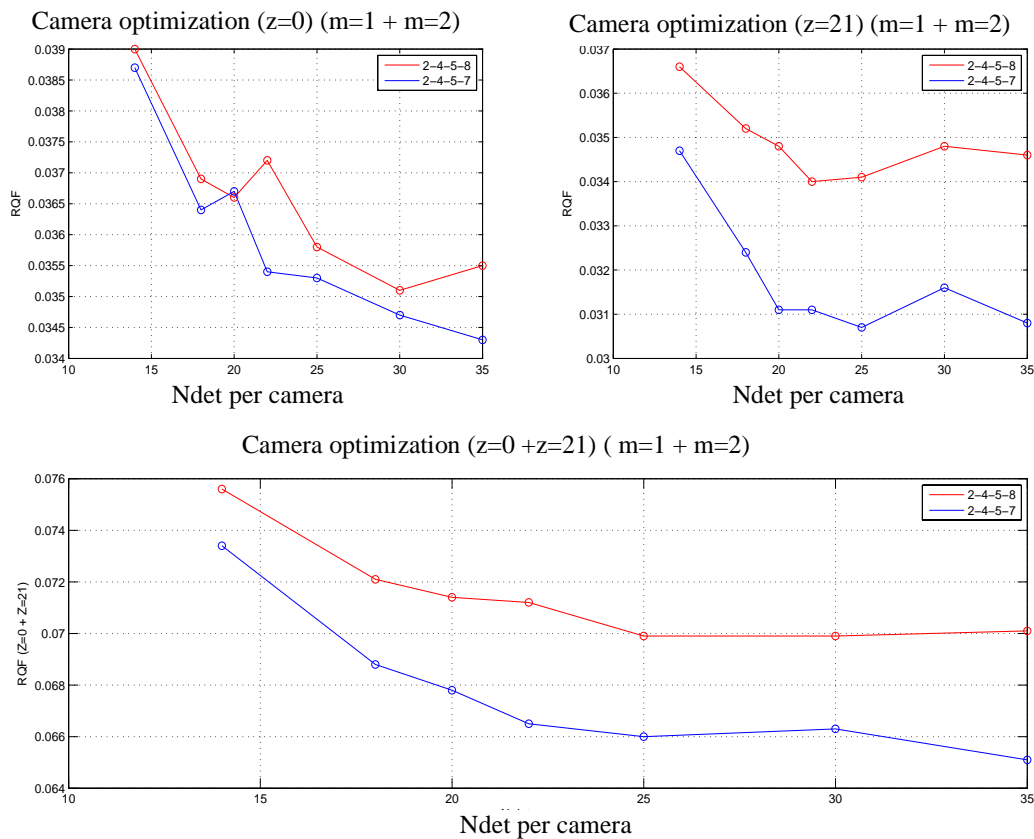


Figure 7.61. Tomographic reconstruction quality of two 4-camera setups, [C2,C4,C5,C8] and [C2,C4,C5,C7], as a function of the number of detectors per camera. The quality of the reconstruction (RV) does not improve significantly when more than 25 detectors are employed in each camera. The [C2,C4,C5,C7] camera setup exhibits superior performance compared to the [C2,C4,C5,C8] camera setup.

7.10.5 Sensitivity to errors in detector positioning

Another issue to address is the sensitivity of the tomographic reconstructions to possible errors in the positioning of the detectors in the radial Soller system. Such an error

translates into a modified direction of the line of sight along which the detector views the plasma.

We start our analysis by considering the standard geometry of 24 detectors per camera. The position of each detector is defined by the angle subtended by the respective line of sight and the main camera axis. A uniform angular distributions is used in all cameras. As usual we use the RV value to quantify the quality of the tomographic reconstruction.

We have considered two sources of error in the detector position:

First: a systematic error is introduced in the radial angle defining the detector position. This error is positive (counter clockwise) for even-numbered detectors (detectors 2,4,6...) and negative (clockwise) for odd-numbered detectors (detectors 1,3,5...). The situation degenerates in the extreme case in which neighboring detectors overlap. In this case (worst case) the number of independent lines of sight per camera is reduced by one half. Note for reference that the angular separation between adjacent channels is 0.05, 0.06, 0.08, and 0.03 radians, respectively, in cameras C2, C4, C5, and C7. A smaller error angle has been used in the case of camera C7 compared to the others because of its smaller angular spread. The results of this analysis are presented in Tables 7.11a and 7.11b.

Z=0 plasma	error (radians)	RV	RV variation %
C2,C4,C5,C7	0	0.014654	-
Case 1	0.01 - 0.005	0.015205	3.8
Case 2	0.02 - 0.007	0.016524	12.8
Case 3	0.03 - 0.01	0.018659	27.3

Table 7.11a

Z=21 plasma	error (radians)	RV	RV variation %
C2,C4,C5,C7	0	0.014198	-
Case 1	0.01 - 0.005	0.013161	-7.3
Case 2	0.02 - 0.007	0.015291	7.7
Case 3	0.03 - 0.01	0.016834	18.6

Table 7.11b

The systematic angle error has been increased from case 1 to case 3. The error angle is given in the second column; the first value corresponds to the error in cameras C2, C4 and C5, the second to C7.

For a small systematic angle error it can even happen that the reconstruction improves (negative RV variation as for the z=21 plasma case 1) but as we can expect the reconstruction worsens as the systematic angle error increases (increasing positive RV variations).

Second: we have introduced a random error in the radial angle defining the detector position. In this case a given detector has equal probability of moving in the clockwise or counterclockwise direction by an angle within 0 and the maximum random angle error allowed. In our simulations the maximum random error allowed corresponds to the worst

case error angle used in the previous analysis (0.03 radians for C2 C4 C5 and 0.01 radians for C7), the angles necessary to cause an overlap between neighboring detectors.

Z=0 plasma	Max error (radians)	RV	RV variation %
C2,C4,C5,C7	0	0.014654	-
	0.03 - 0.01	0.015102	3.1
	0.03 - 0.01	0.015122	3.2
	0.03 - 0.01	0.016253	10.9
	0.03 - 0.01	0.01393	-4.9
	0.03 - 0.01	0.01433	-2.2
	0.03 - 0.01	0.01421	-3.0
	0.03 - 0.01	0.012656	-9.1
	0.03 - 0.01	0.015354	4.8
	0.03 - 0.01	0.017347	18.4
	0.03 - 0.01	0.014919	1.8

Table 7.12a

RV values for 10 tomographic reconstructions with a random error in the angle defining each detector line of sight. Original plasma emission centered at Z=0 cm.

Z=21 plasma	Max error (radians)	RV	RV variation %
C2,C4,C5,C7	0	0.014198	-
	0.03/0.01	0.01484	4.5
		0.014867	4.7
		0.01499	5.6
		0.014756	3.9
		0.014875	4.8
		0.013366	-5.9
		0.01285	-9.5
		0.015138	6.6
		0.015585	9.8
		0.014206	0.1

Table 7.12b

RV values for 10 tomographic reconstructions with a random error in the angle defining each detector line of sight. Original plasma emission centered at Z=21 cm.

We have considered 10 different random arrangement for the detectors in the [C2, C4, C5, C7] camera system. The results shown in Tables 7.12a and 7.12b give an average degradation in the RV value of ~2.5% compared to the standard case: thus the random error appears to be less severe than the systematic error.

In 10 independent random arrangements we never obtained a RV degradation exceeding 10% at z=21 cm, and we had only two exceeding 10% at z=0. Again we found several randomly modified arrangements that actually improved the reconstruction. The random

error is the kind of positioning error we expect with the highest probability; the degradation of the reconstruction variance expected is much lower than 10% on average, and this value is considered acceptable in our final design. This implies that the tolerance on the detector positioning is greater than or equal to the distance between the detectors divided by 1.414, i.e., of the order of 1.5-2 mm. This is a very generous tolerance and is easily attained in detector mounting. A key factor in this analysis of course is the assumption that the positions of the detectors, even if not optimal, are *known* to a high degree of precision. By using the correct positions, the tomographic analysis remains substantially accurate even if the spacing is not even. This is seen as a reasonable assumption, as the positions of the detectors after mounting can be measured to a precision of 0.1 mm or less.

In this analysis we have ignored the presence of the collimator. In practice, the choice of the radial Soller collimator arrangement, which essentially consists of individual collimators for each chord, limits the acceptable tolerance in the detector positioning. The collimator channel opening on the plasma side is the key factor controlling the étendue and chord spread, whereas the opening on the detector side is much less critical. For this reason the opening has been set at $2.5 \times 2.5 \text{ mm}^2$, i.e., 0.5 mm wider than the detectors, for all cameras. In practice, the achievable precision in the positioning of the detectors is always better than the 0.5 mm tolerance.

7.10.6 Pixel size optimization

The various optimizations discussed in this section have informed our choices for the implementation of the diagnostic. We discuss here a further optimization process that concerns only the computational data processing, but uses the same methodology. This is the determination of the best tomographic reconstruction pixel size. This has been performed by a scan over the squared pixel size dimension, for a wide range of simulated original emission patterns and using different camera setups; the results indicate that the optimal pixel size is between 3 and 4 cm. Larger pixel sizes cause a loss of spatial resolution in the reconstructed emission and thus a degradation of the quality of the reconstruction itself. For smaller pixel sizes the quadratic increase of the number of pixels with size and the attendant increase in calculation time outweigh any improvement in the reconstruction quality. In addition, below 2 cm an abrupt degradation of the reconstruction quality can arise when high-emissivity pixels are not intersected by any line of sight, since the reconstruction uses a thin-chord approximation.

7.10.7 Conclusion

This extensive series of tomographic simulations indicates that 4 cameras of ~ 25 detectors each constitutes an optimum trade-off between cost and tomographic reconstruction quality; in particular the group of four cameras [C2,C4,C5,C7] has been identified as the best candidate for a 4-camera tomographic setup.

7.11 Signal acquisition and processing

7.11.1 Introduction

The electric pulse generated by the photo-interaction in the detector bulk is collected and shaped by means of a charge sensitive preamplifier. The performance of a spectroscopic system depends strongly on the method employed for charge collection and amplification. Additionally, it is essential to accurately determine the absolute time and amplitude of each pulse.

The amplifier card for the HXRS diagnostic has been developed in-house by the CRPP electronics department and is presented in the remainder of this section. It was decided to store the full pulse time trace digitally, and effect the pulse height analysis by software after the shot. Two (still preliminary) numeric pulse height analysis methods are also presented in this section.

7.11.2 Pulse formation: the CRPP-HXRS amplifier

The electron-hole charge generated as a consequence of a photoelectric conversion, in a biased detector, is collected at the detector electrodes (holes at the cathode and electrons at the anode). The typical charge collection time in a 2 mm thick CdTe detector is in the order of hundreds of ns, therefore this is the order of magnitude we require for the charge integration time.

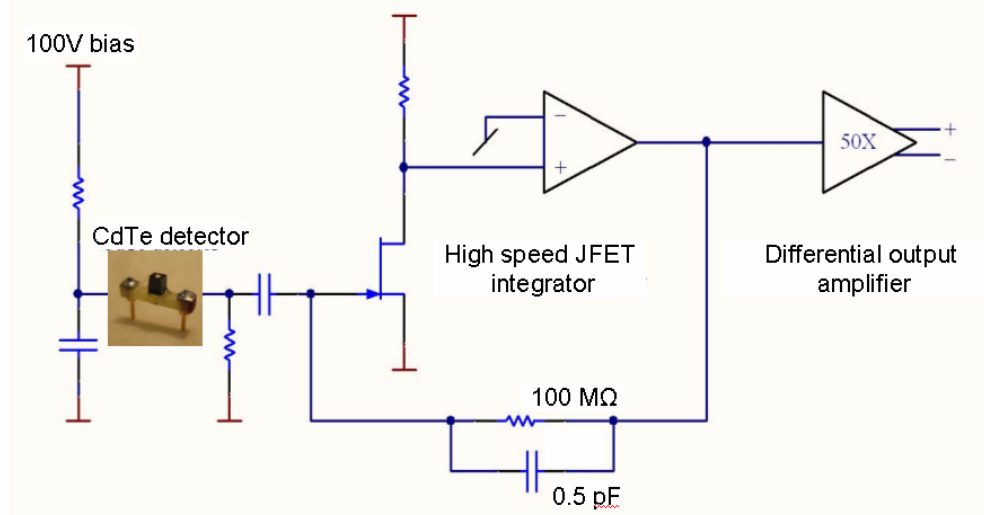


Figure 7.62 Schematic diagram of the CRPP-HXRS amplifier circuit.

The amplifier card for the HXRS system was developed at the CRPP. While commercial solutions do exist, they are costly. Additionally, the additional requirement of integration

into the tight space of the compact HXRS cameras made an internal development a more attractive solution on all fronts.

The CRPP amplifier is composed by two main stages (Fig. 7.62): a fast integrator (60 MHz bandwidth, 5 ns response time) followed by a twin amplification stage with a total gain of ~ 50 , acting also as a current driver. The integrator decay time τ_d must be long enough to ensure complete charge collection but sufficiently short to permit a high count rate (up to 1 MHz) without pile-up. A compromise is found for $\tau_d = 5 \mu\text{s}$. Each amplifier card includes 2 identical channels for two detectors; the electronic card layout is shown in Fig. 7.63.

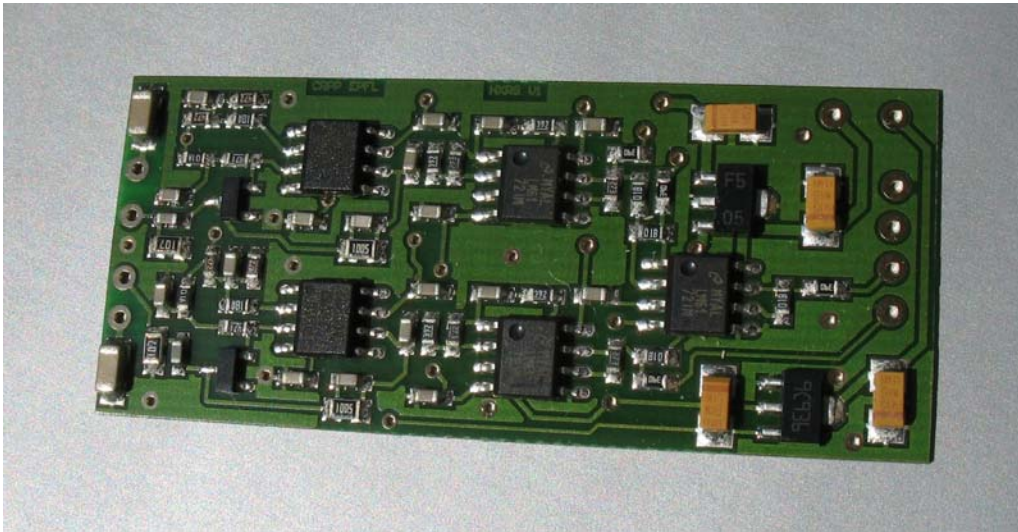


Figure 7.63 The 53x23 mm CRPP-HXRS amplifier card. Each card contains 2 channels with differential outputs. Active elements are supplied by $\pm 12 \text{ V}$ generated onboard.

Each HXRS camera, with 24 +1 (blind) CdTe detectors, is equipped with 13 amplifier cards (see Fig. 7.64); the blind detector in the first camera (the only one currently installed on TCV) is located between the two central channels 12 and 13 (see Fig. 7.64). The 26th electronic channel is not connected with any detector and is used to monitor the background electronic noise. The output signals from the amplifier card, as well as the amplifier power supply voltages and the 100 V detector bias voltage, are carried by a short SCSI cable between the amplifier box and the main diagnostic flange, and by a second 3-m SCSI cable from the flange to the acquisition and power supply modules. The vacuum feedthrough is composed of dual SCSI connectors embedded in a vacuum-resistant epoxy, which is adequate for the moderate preliminary vacuum of the port assembly. A conversion from SCSI to differential LEMO cables is effected near the acquisition modules.

To avoid overheating (since all electronics are in vacuum and are therefore not convectively cooled), the power supplies are only turned on by a timer a few seconds before the shot and are turned off again a few seconds after the end of the shot. The electronics have been measured to come to full stabilization in less than 100 ms.

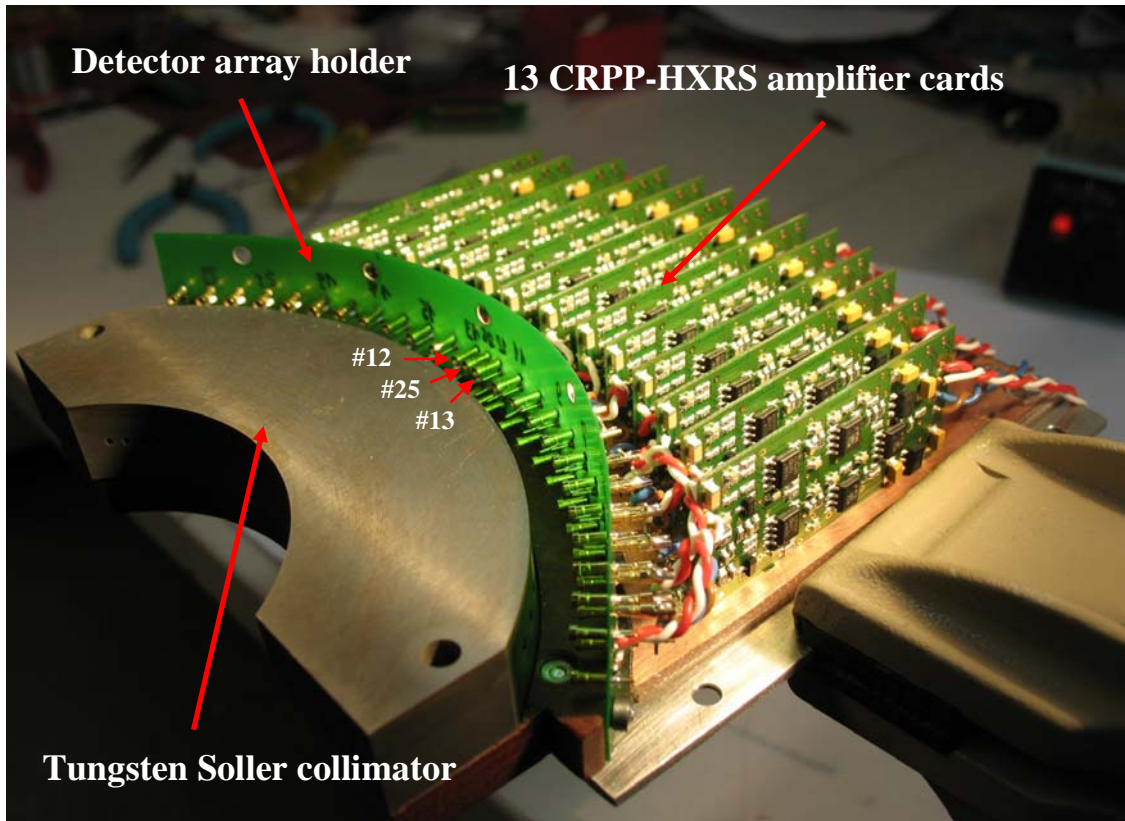


Figure 7.64 HXRS camera assembly before detector installation. The 13 CRPP-HXRS amplifier cards are aligned behind the detector array holder and connected to the detector sockets by twisted cable pairs. The detector sockets are mounted on a flexible circuit board behind the tungsten Soller collimator.

7.11.3 Digitization

The digital conversion is performed by two 16-channel, 12 Msamples/s DTACQ ACQ216PCI modules fitted with 5 MHz anti-aliasing filters. The sampling rate is high enough to follow the individual photo-signal ramp phase (see Fig. 7.65). The typical digital acquisition time length is 2 s per shot generating a total of 1.2 GB per shot for the current 25 channels. The storage of and backup of the data are effected currently on a dedicated PC with a multi-TB HDD.

In the initial phase of exploitation of the HXRS system, the algorithms for peak identification and spectroscopic analysis are in a development phase, which motivates the storage of the full time traces. This initial experience is expected to lead to the implementation of an automatic post-shot analysis algorithm. The final goal would eventually be to store only the time sequences of the detected pulses with their respective energies, reducing the storage requirements by orders of magnitude.

7.11.4 Noise and system performance

While the port assembly, the collimators, and the tungsten shields are at torus ground, the electronic cards and their housing were initially floating, all signals being differential. After first tests revealed excessive ambient noise during TCV discharges, it was decided to ground the electronics to torus ground as well through a connection on the main diagnostic flange. This solution brought the rms noise level, in equivalent energy units, down to ~ 8 -10 keV, comparable to the system resolution. Furthermore, most of the noise comes from tokamak power supply switching frequencies, peaking at 1.3 kHz. A high pass filter at 2 kHz (easily applied in post-processing) reduces the rms noise further to < 1 keV.

7.11.5 Signal post-processing

The first HXRS camera was installed towards the end of this thesis work and only preliminary data could be obtained thus far. Two numerical techniques of pulse height analysis were developed and tested on these initial data.

7.11.5.1 Pulse-Shape Discriminator (PSD) algorithm

In conditions of sufficiently high signal to noise (S/N) ratio, the shape of each single photo-generated pulse at the output of the amplifier (blue curve in Fig. 7.65) has an amplitude proportional to the energy deposited by the photon into the detector. As discussed earlier, the rise time (τ_r) and decay time (τ_d) are characteristic of the amplifier circuit. Digital conversion with a sufficiently high sampling rate (12 Ms/s in our case) preserves the output signal shape (black dots in Fig. 7.65).

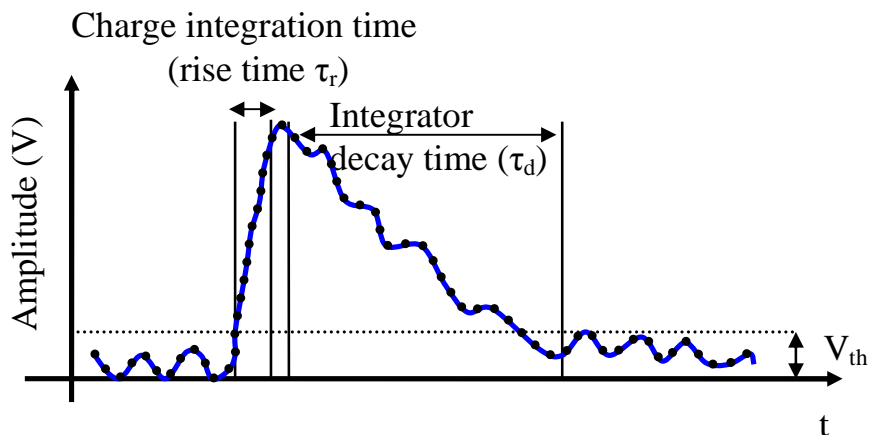


Figure 7.65. Photo-pulse shape in output from the CRPP-HXRS amplifier card (blue solid curve). Discrete digitized time trace (black dots).

The presence of noise can manifest itself in the form of baseline oscillations with rise time potentially close to the characteristic pulse rise time. Under such conditions, the knowledge of the characteristic pulse shape is of great help in discriminating signal from the noise.

A Pulse-Shape peak Discrimination (PSD) algorithm has been implemented in the Matlab language. A search is performed, in the digitized time trace, for events having a rise time (τ_r) compatible with the characteristic one ($\sim 1 \mu\text{s}$) depicted in Fig. 7.65. Additionally, thresholds in both the signal time derivative and the absolute step side are applied: the latter is set at a level that ensures full discrimination against background noise, i.e. typically $V_{th} = 10 \text{ keV}$. For each pulse satisfying these conditions, a few (3 in our tests) points in the time trace following the peak are checked to verify that the decay time is close to the characteristic τ_d . If this last condition is verified as well, the event is considered valid and stored.

The method was validated by laboratory tests with an Am-241 radioactive source and unoptimized assembly with modest signal-to-noise ratio. In Figure 7.66, the energy spectrum constructed by a Fast/MCA-3 PCI ADC combined with an Ortec-571 Gaussian shape amplifier is compared with the result of the PSD algorithm applied to the D-TACQ digitized time trace. The photopeak emission at 60 keV is identified well by both systems, but the Am-241 secondary emission at 18 keV is not revealed by the Ortec 571/MCA-3 system. Rejection of the spurious noise in the low energy part of the spectrum is key to the numerical technique's ability to discern this peak..

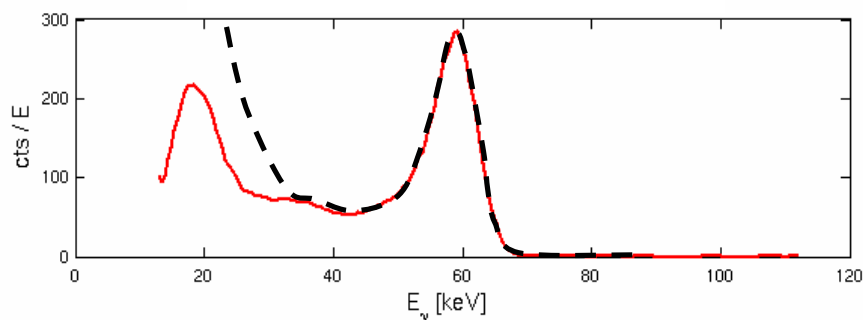


Figure 7.66 Comparison between Am-241 pulse-height analysis spectra produced by an MCA (dashed black curve) and by a numerical post-processing algorithm (solid red curve).

The PSD method outlined above suffers from two primary limitations:

1. Photon interaction, especially for highly penetrating radiation (energetic photons, $E > 100 \text{ keV}$), can occur deep in the detector volume generating the electron-hole cloud far from the cathode. Because of the poorer hole mobility compared to electrons, for the same drift length, holes take a longer time to be collected than electrons (as discussed in section 7.3). When the resulting extended charge collection time (Fig. 7.67) exceeds τ_r (typically $1 \mu\text{s}$) the search algorithm fails.

2. Severe pile-up makes it impossible to detect the decay slope of each pulse, as the signal keeps rising from multiple events. In initial measurements it appears that the algorithm works properly for count rates below 100 kHz.

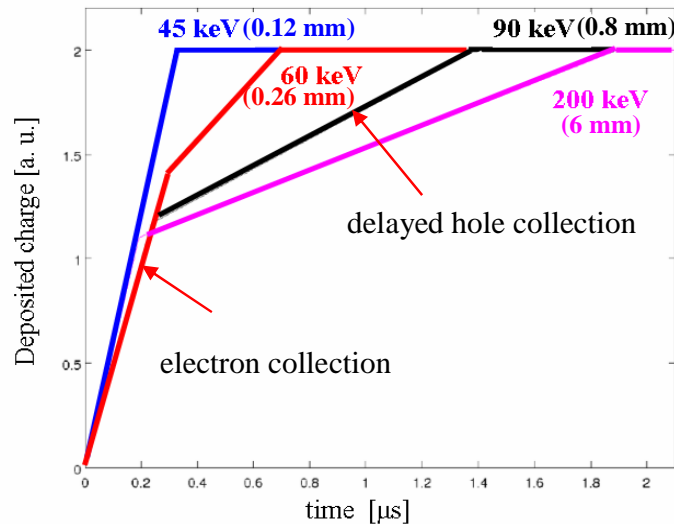


Figure 7.67. Charge pulse formation as a function of time for photoelectric conversion in a 2 mm thick CdTe detector. The average photo-interaction location moves away from the cathode for increasing photon energy resulting in a delayed hole collection. The characteristic penetration depth is indicated next to each energy value.

7.11.5.2 The differential Change In Sign (CIS) algorithm

A second peak discriminator algorithm was developed in an attempt to remedy some of the limitations of the PSD method. This algorithm is based on the Change In Sign (CIS) of the differentiated signal time trace (S_t).

The photo-peak discrimination process is composed of the following steps:

- (i) The acquired (digitized) raw signal time trace S_{t0} (Fig. 7.68a) is first smoothed by a multi-point moving average filter. Typically the smoothing is performed on 8 points in order to remove fast oscillations while preserving the charge collection rise phase (see Fig. 7.68b).
- (ii) The smoothed time trace S_{t1} is then differentiated and changes in the sign of this derivative are sought: negative to positive identifies a candidate pulse start, whereas positive to negative identifies a candidate pulse peak (see Fig. 7.68b)
- (iii) The difference $V_p = S_{top} - S_{base}$ along the time trace is evaluated and only events satisfying the condition $V_p > V_{th}$ are accepted for spectroscopic analysis, the others being discarded.

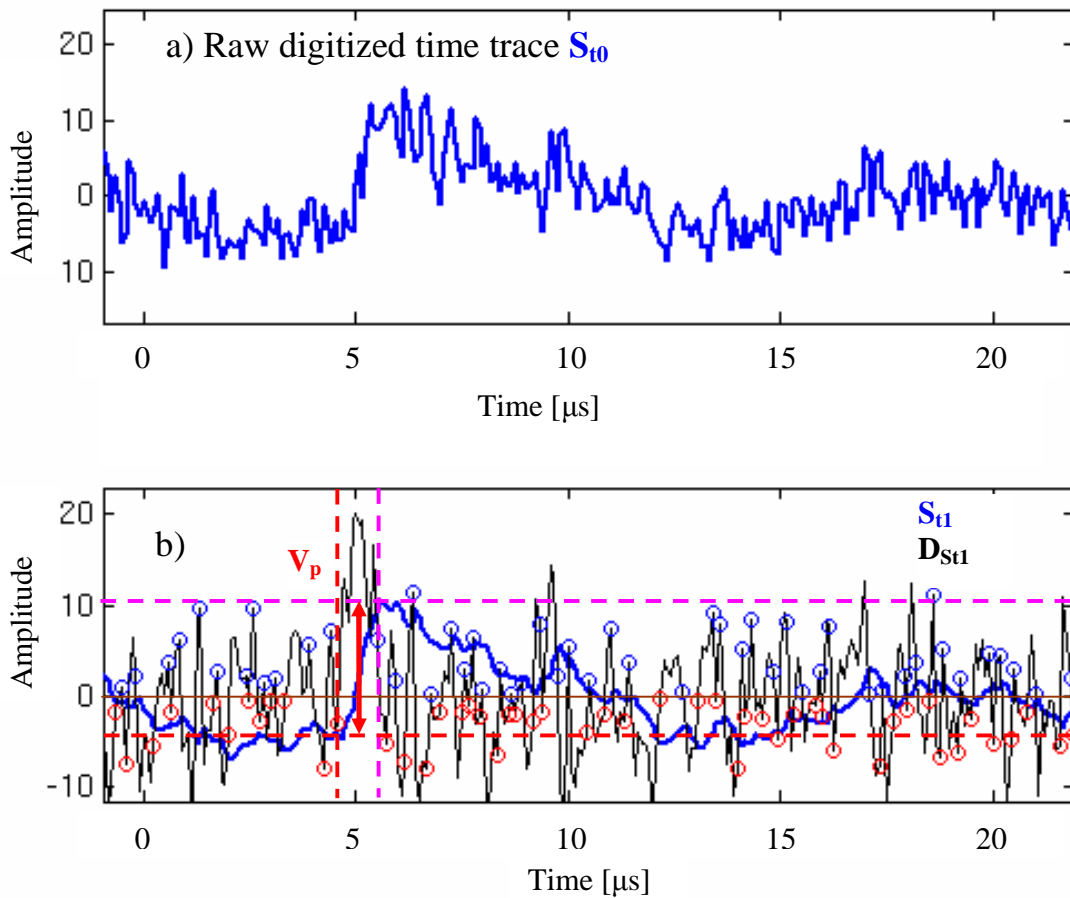


Figure 7.68. Example of pulse analysis with the CIS method on a HXRS time trace: (a) raw digitized signal S_0 ; (b) 8-point moving average filtered signal S_{t1} (thick blue trace) and derivative (finite difference) $D_{S_{t1}}$ (thin black trace). The red and blue circles denote points when the derivative switches from negative to positive and from positive to negative, respectively. The dashed red and magenta lines denote the time and signal level of the start and end points of the peak respectively. In the case analyzed, a 15 keV photoevent is identified.

The CIS method is simple to implement, it tolerates a higher count rate than the PSD and is characterized by a reasonable execution time ($\sim 5'$ (similar to PSD) for the analysis of 25 channels \times 2 s long time traces) compatible with the requirement of inter-shot analysis. For these reasons it is currently the favored algorithm.

7.11.6 The pile-up problem

Figure 7.69a show a typical HXRS time trace acquired during ECCD experiments in TCV. Because of the statistical character of the bremsstrahlung emission and photon absorption in the detector, pile-up events may occur, in which one or more additional photons are absorbed by the crystal during the pulse rise caused by a previous photon. These events become more and more frequent as the count rate increases. A true pile-up makes individual photon detection impossible. The goal for a well-designed detection

algorithm is to successfully detect photons that are as close in time as possible without technically piling up.

An example is given in Fig. 7.69b with photon interactions occurring $2 \mu\text{s}$ apart, so that the second pulse starts during the decay tail of the first one. In such conditions of relatively low average count rate (100 kHz), two such events are easily disentangled by the CIS algorithm.

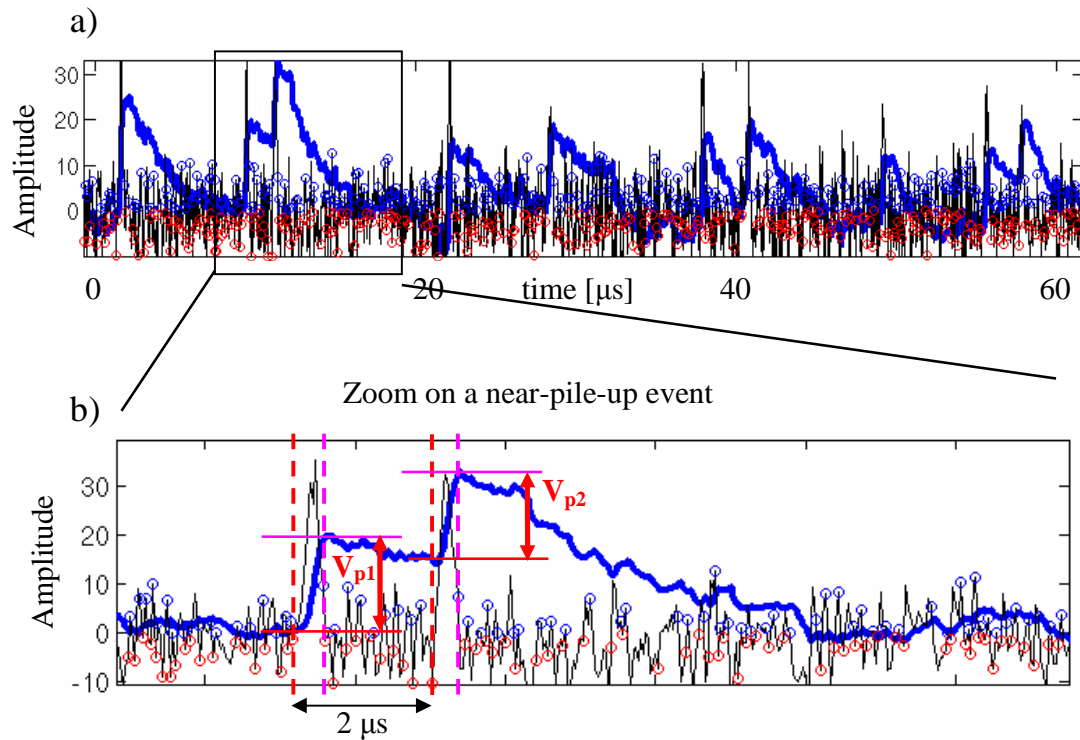


Figure 7.69 (a) a sample of the digitized signal time trace (S_{t1} obtained with an 8 point moving average filter) analyzed with the CIS method, (b) zoom on a near-pile-up event: in the case considered, two photo-peaks are separated by a $2 \mu\text{s}$ time delay, but both are correctly recognized by the algorithm.

When the photon count rate exceeds a few hundred kHz so that multiple near-pile-up events occurs, a distortion of the acquired time trace may result, with deleterious effects on the spectroscopic performance of the system. In Figure 7.70, four photo-peaks (from a real TCV HXRS time trace) are artificially arranged in time to simulate different count rates in a controlled way. It is shown that at 150 kHz the CIS algorithm works properly; at 300 kHz it detects the individual events but underestimates their amplitude, and at 600 kHz it becomes altogether unable to separate the events.

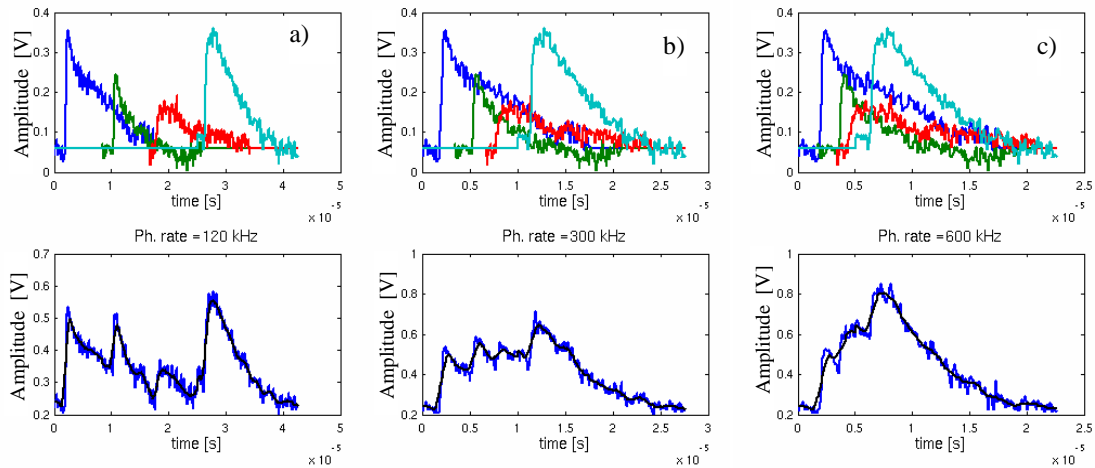


Figure 7.70. Pile-up study in an artificially time-shifted combination of four photo-events. Three count rates are simulated: a) 120 kHz, b) 300 kHz and c) 600 kHz. Severe pile-up influences the ability to correctly recover the true count rate and energy spectrum.

This analysis clearly highlights the importance of adopting appropriate filtering to control the photon statistics during the experiments. It should be noted that having access to the full signal time histories offers a great advantage in this type of analysis compared to a traditional analog comparator system, in which most of the information contained in the detailed pulse shape is irretrievably lost after acquisition.

7.12 Implementation of the equatorial HXRS camera

The equatorial HXRS camera is the first element of the 4-camera HXRS tomographic system to be installed in TCV. The steps for its conceptual design have been discussed in the preceding sections of this chapter. The final mechanical design for the equatorial HXRS camera is presented in this section. The first experimental results obtained in the commissioning phase are presented and discussed in the next and conclusive chapter of this thesis.

Figures 7.71 and 7.72 show 3D mechanical drawings of the camera made with the CATIA CAD software; a photograph is shown in Fig. 7.73. The housing of the CdTe detectors and amplifier cards is visible in the middle of the assembly. In Fig. 7.71 (front-lateral view) one can see the two rotatable filter holders, discussed in section 7.6.2 (in orange, for more visibility) and the additional tungsten shielding discussed in section 7.9.2.

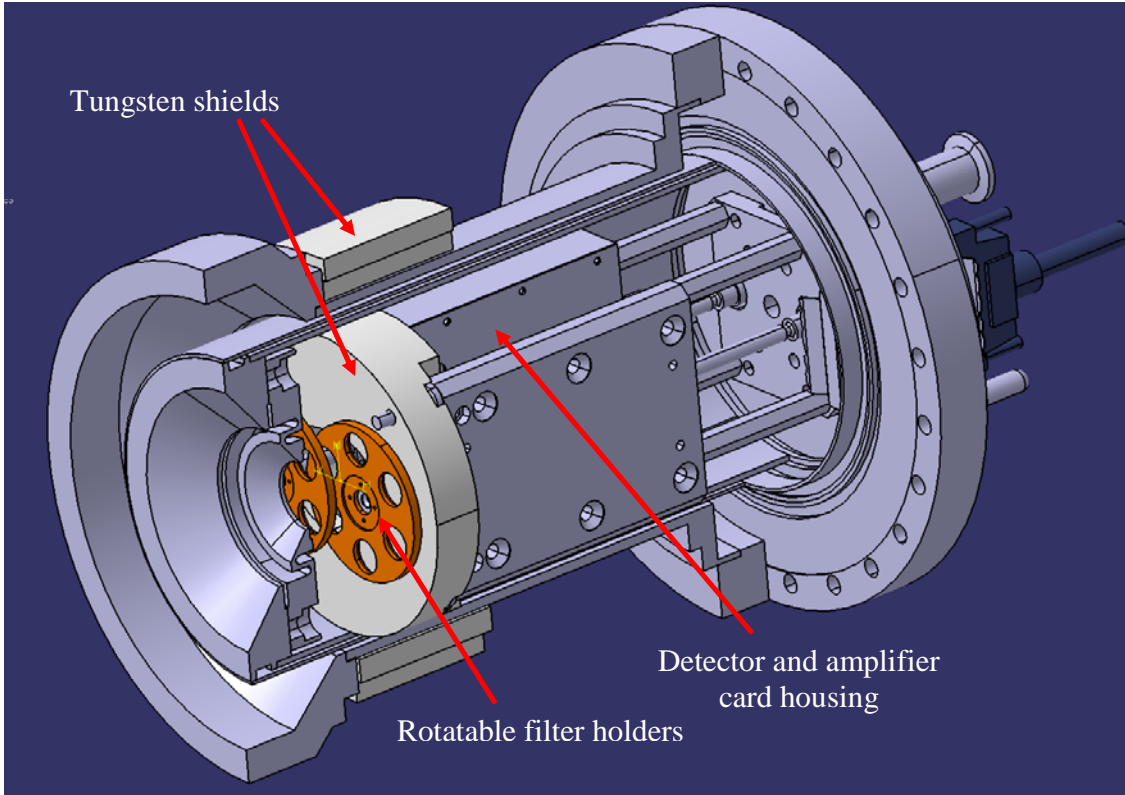


Figure 7.71 Front-lateral view of the equatorial HXRS camera in a CATIA © mechanical drawing.

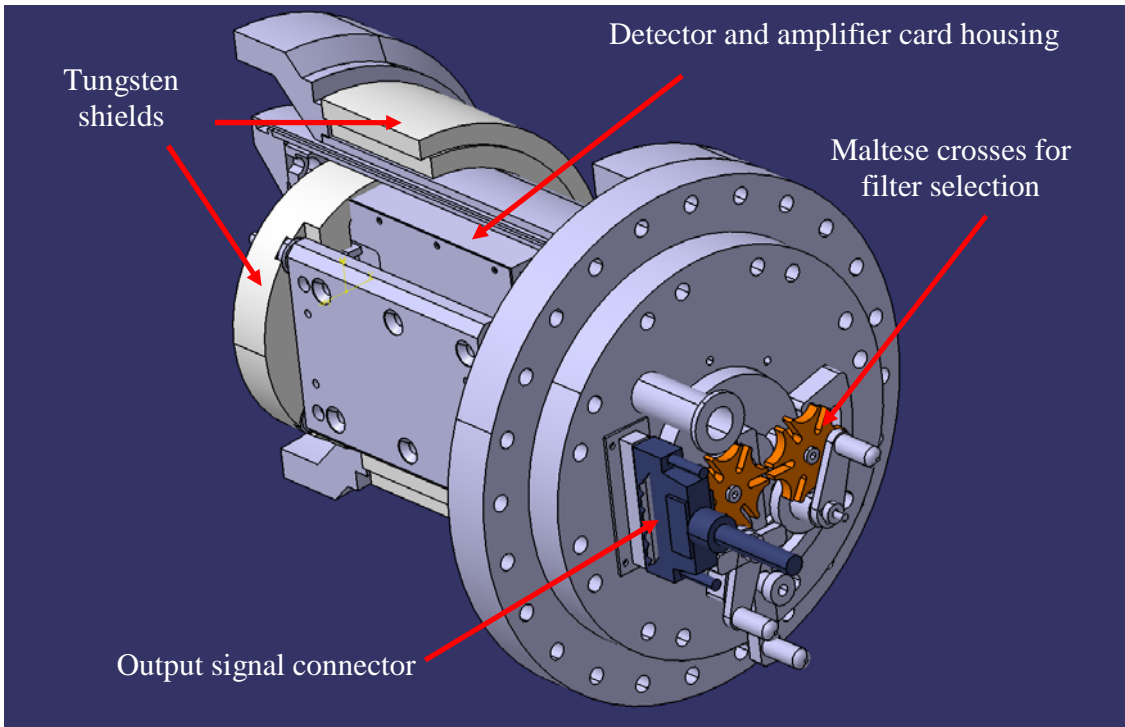


Figure 7.72 Rear-lateral view of the equatorial HXRS camera in a CATIA © mechanical drawing.

The positions of the two filter holders, at present, are set manually between shots by acting on two handles connected through Maltese crosses (also known as Geneva drives) to the filter axes (visible in Fig. 7.72). In the future, these holders will be driven by remotely controlled pneumatic actuators.

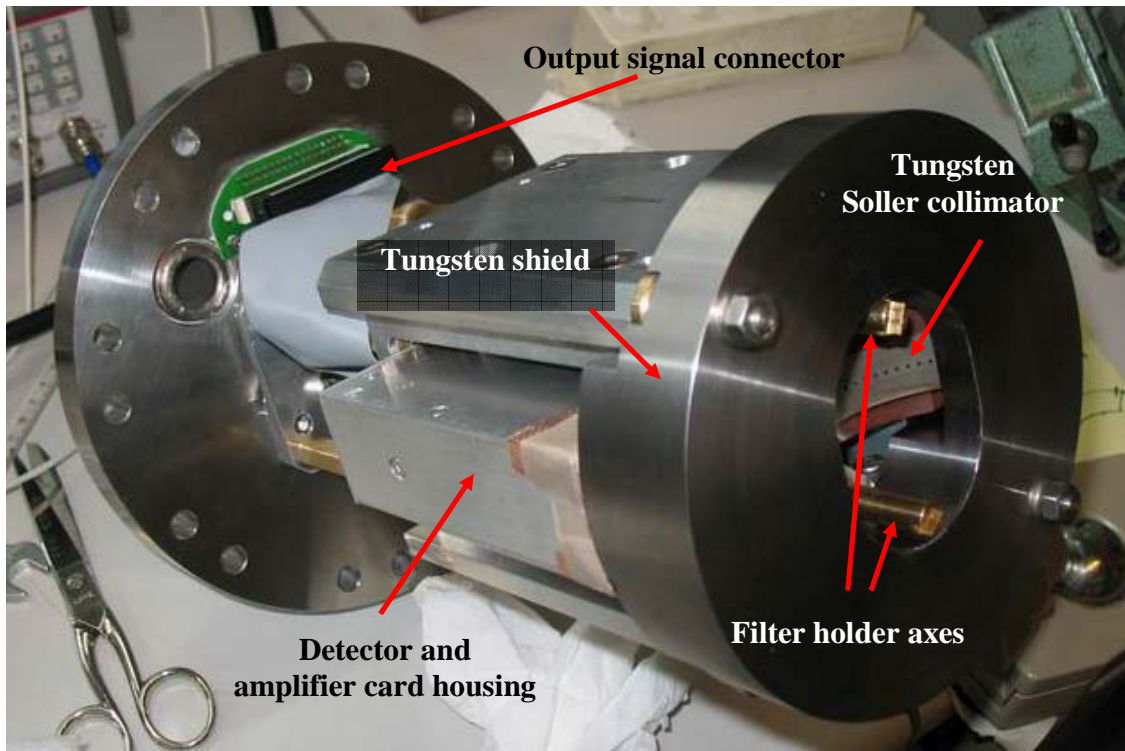


Figure 7.73 The equatorial HXRS camera during the final testing in the electronics laboratory preceding the installation on the TCV tokamak.

The 90 degree rotation of the whole camera system is achieved by manually acting on a handle located on the main flange as shown in Fig. 7.74.

The inner assembly is cooled by water circulating in a thin cylindrical jacket. This is primarily to keep the system cooled during baking (to 250 C). The cooling hoses, as well as the tube for the vacuum pumping, can also be seen in Fig. 7.74. Figure 7.75 shows a global view of the TCV sector in which the HXRS camera is installed.

7.13 Conclusion

The HXRS system is a completely new diagnostic conceived to study the suprathreshold electron dynamics in TCV in the hard-X ray region of energy. Spatial information by tomographic reconstruction and spectroscopic detail of the electron bremsstrahlung emission can be obtained with a temporal resolution of a few ms, depending on the photon statistics. In this chapter, the conceptual design of the diagnostic has been extensively discussed. Tomographic aided design has played a crucial role in defining the

optimal system parameters, such as the number of cameras, the number of detectors per camera, the camera orientation and positioning under spatial constraints typical of the TCV machine. Extensive detector testing identified the better overall performance of the Eurorad CdTe detectors compared to other candidates such as Acrorad CdTe and Ritec CZT. A modified tungsten Soller collimator has been expressly designed and manufactured to define the detector cones of views and to guarantee uniformity of étendue in each line of sight. The sensitivity of the diagnostic to k-edge fluorescence from the tungsten collimator has been probed by EGS Monte Carlo simulations. Fast signal acquisition is performed by the CRPP-HXRS amplifier card.

Preliminary measurements with a prototype camera revealed the presence of significant stray radiation in low density plasma discharges. An additional tungsten shielding has been integrated to minimize this spurious component related to runaways-generated thick target bremsstrahlung from the TCV vessel. Furthermore, we decided to add one blind detector in each HXRS camera to monitor the runaway activity. The full-pulse digital acquisition is analyzed by dedicated Matlab routines which identify the occurrence of each photon interaction and provide spectroscopic analysis. The pile up discrimination remains a challenging task for recovering the correct count rate and spectroscopic information.

A first HXR camera has been recently installed and commissioned in TCV. The discussion of the preliminary experimental results is the subject of the next chapter.

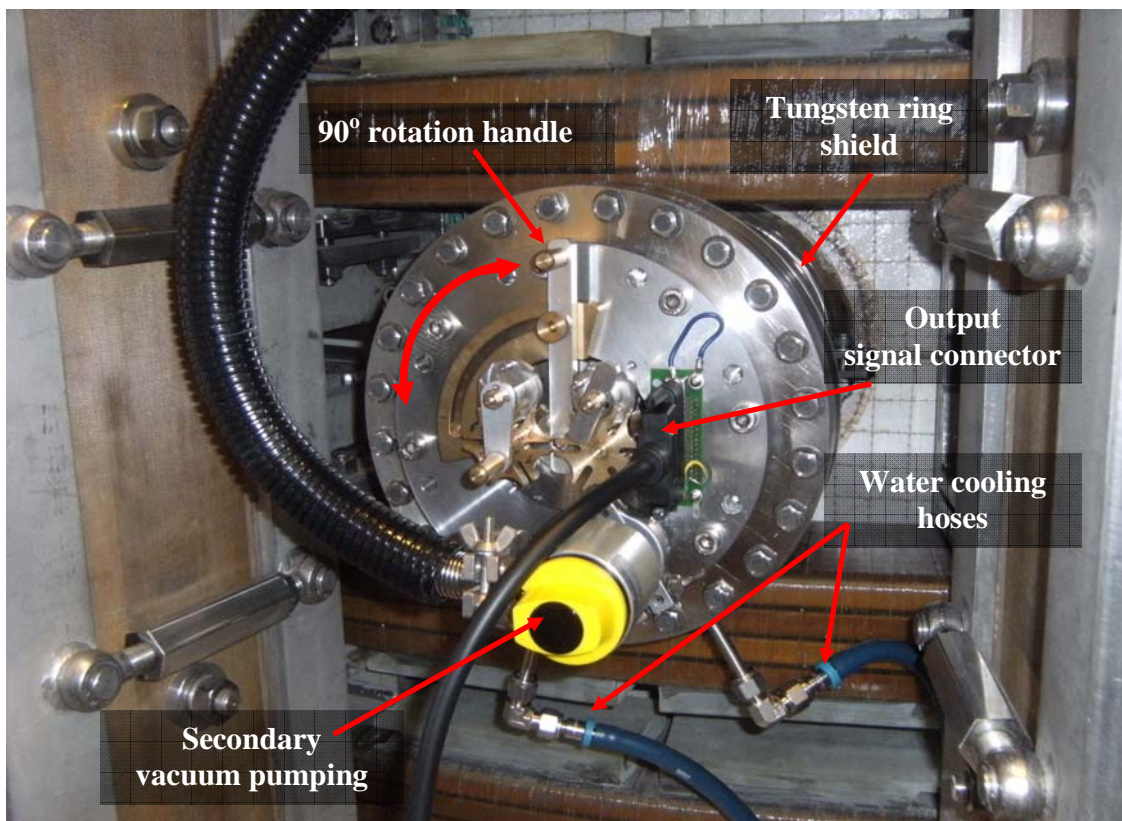
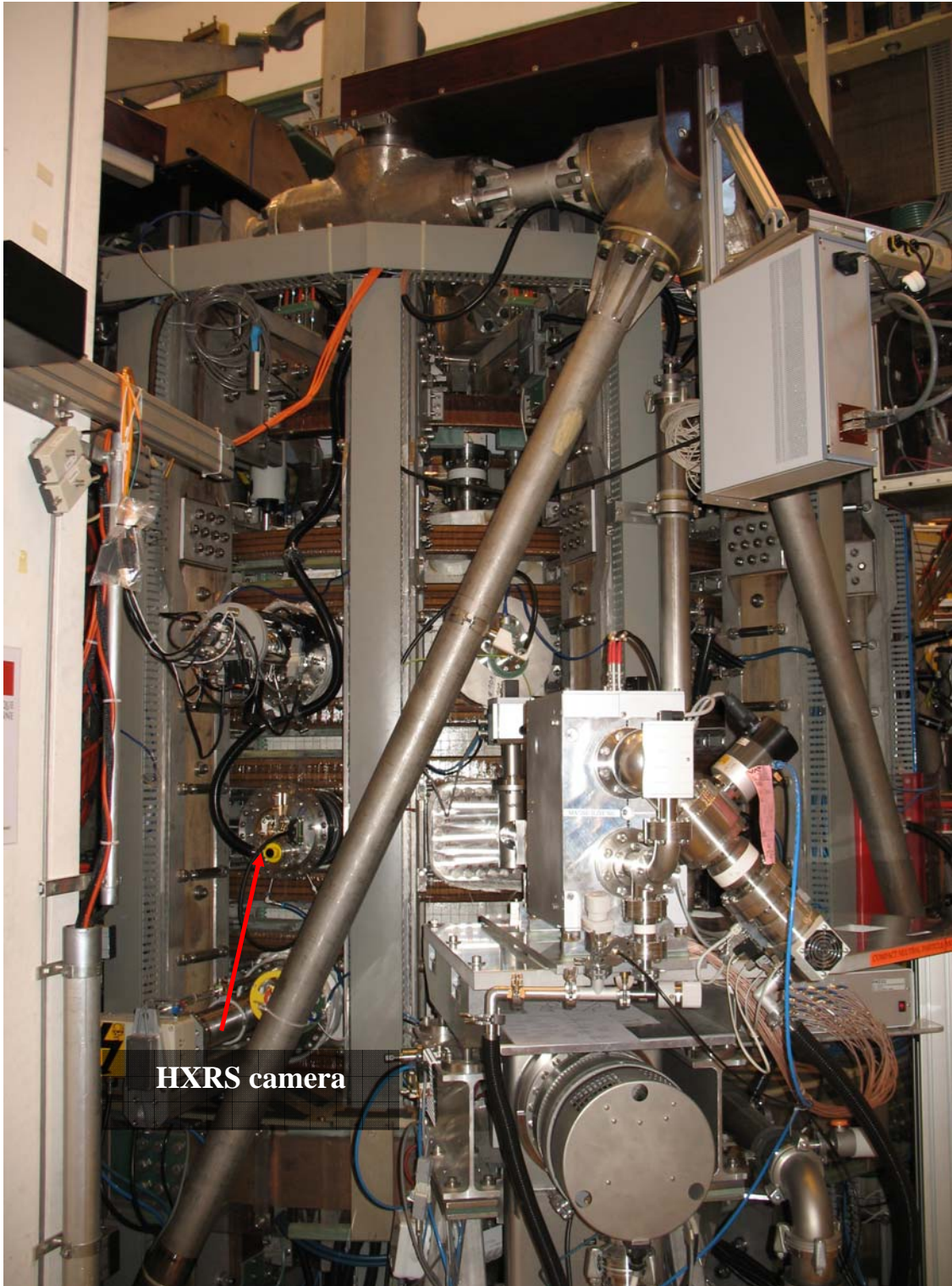


Figure 7.74 External view of the equatorial HXRS camera installed in sector #9 of the TCV tokamak.



HXRS camera

Figure 7.75 Global view of the equatorial HXRS camera installed in sector #9 of the TCV tokamak

8. HXRS camera commissioning and first experimental results

8.1 Introduction

The equatorial HXRS camera has been installed in TCV at the end of April 2011. The first few weeks of operation have been devoted to commissioning the system. At first the camera worked parasitically during TCV operations, the primary goal being to check its proper operation and to study and improve the signal to noise ratio. This initial operation revealed a high level of noise that severely limited the detectable signal. The problem was identified in a non optimal grounding of the detector/amplifier housing and a dramatic improvement was obtained after the grounding scheme was modified, as described in section 7.11.4.

This chapter presents a set of initial observations and preliminary studies that were made on TCV in the short time since the camera installation.

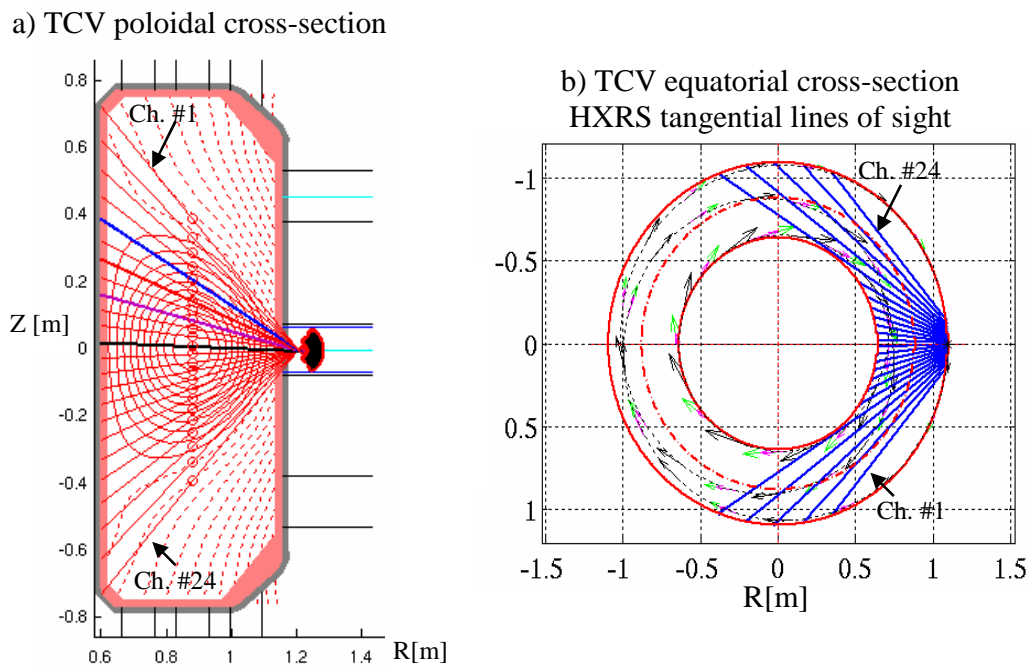


Figure 8.1 a) TCV poloidal view, plasma equilibrium from shot 43211 with HXRS camera lines of sight; b) TCV top view with superimposed tangential HRXS lines of sight.

Data on very high energy photons, particularly in low density plasmas and/or in the presence of stabilized, long-period sawteeth, are presented in section 8.2. In sections 8.3 to 8.5, results from experiments devoted to the suprathreshold bremsstrahlung emission in the presence of strong EC current drive are discussed. Section 8.3 reviews some basic parameter scans, whereas section 8.4 describes the co-counter parallel emission

asymmetry with comparison to modeling. Section 8.5 focuses on the dynamic response to ECCD modulation.

Shown in Fig. 8.1, for convenience, are views of the TCV poloidal and equatorial cross sections with the HXRS lines of sight for both the vertical and the horizontal configuration of the camera system. Channel numbering is #1-24 from top to bottom in the vertical arrangement, or left to right (viewed from the detectors) in the horizontal one. Channel #25 is the blind detector used for gamma ray discrimination.

8.2 Observation of runaways during low density plasma discharges and with stabilized sawteeth

The first observations with the new HXRS system were carried out in plasma discharges with long sawteeth (ST) stabilized by off-axis ECH. Such experiments in TCV are typically performed in conditions of relatively low density. In this section we present experimental results from two representative TCV shots, #42981 and #43082. These plasmas evidence the presence of a significant runaway component, confirmed by a shielded scintillator/photomultiplier X-ray detector located far from the TCV machine, which only detects highly energetic photons escaping the TCV vessel.

8.2.1 Runaway dominated phases

TCV shot #42981 is a plasma with magnetic axis centered on the equatorial plane of the machine ($Z_p \sim 0$), entirely covered by the equatorial HXRS camera lines of sight.

The primary plasma parameters are: $I_p = 300$ kA, $B_0 = 1.2$ T, $V_{loop} = 1.3$ V, $T_{e0} = 1.4$ keV and $n_{e0} = 1.5 \times 10^{19} \text{ m}^{-3}$, where T_{e0} and n_{e0} are the central plasma temperature and density provided by Thomson scattering.

The sawtooth period is stabilized to 20 ms by EC power deposition close to the $q=1$ surface by using active real time (RT) control of the EC power deposition [112].

The time traces of the density measured by a far infrared interferometer (FIR), the soft X-ray signal from a multiwire proportional chamber (DMPX), and the PMTX signal are shown in Fig. 8.2a. In Fig. 8.2b the raw digitized time trace from the HXRS central channel #12 viewing the plasma core is shown. The spectroscopic analysis is performed with the CIS algorithm (section 7.11). In Fig. 8.2c the total count rate is displayed for channels 6-12 and 25. Clearly all the channels in the HXRS camera record a very similar count rate.

During the “runaway burst” visible in the PMTX in the 0.25-0.45 s time interval, the signal in all the HXRS channels is for the most part saturated, resulting in an effective detection paralysis (Fig. 8.3, left column), precluding any spectroscopic study. Transient saturations are recorded during ST crashes when a substantial runaway population is generated (PMTX peaks synchronous with the crashes in the DMPX traces) as shown in Fig. 8.3, right column.

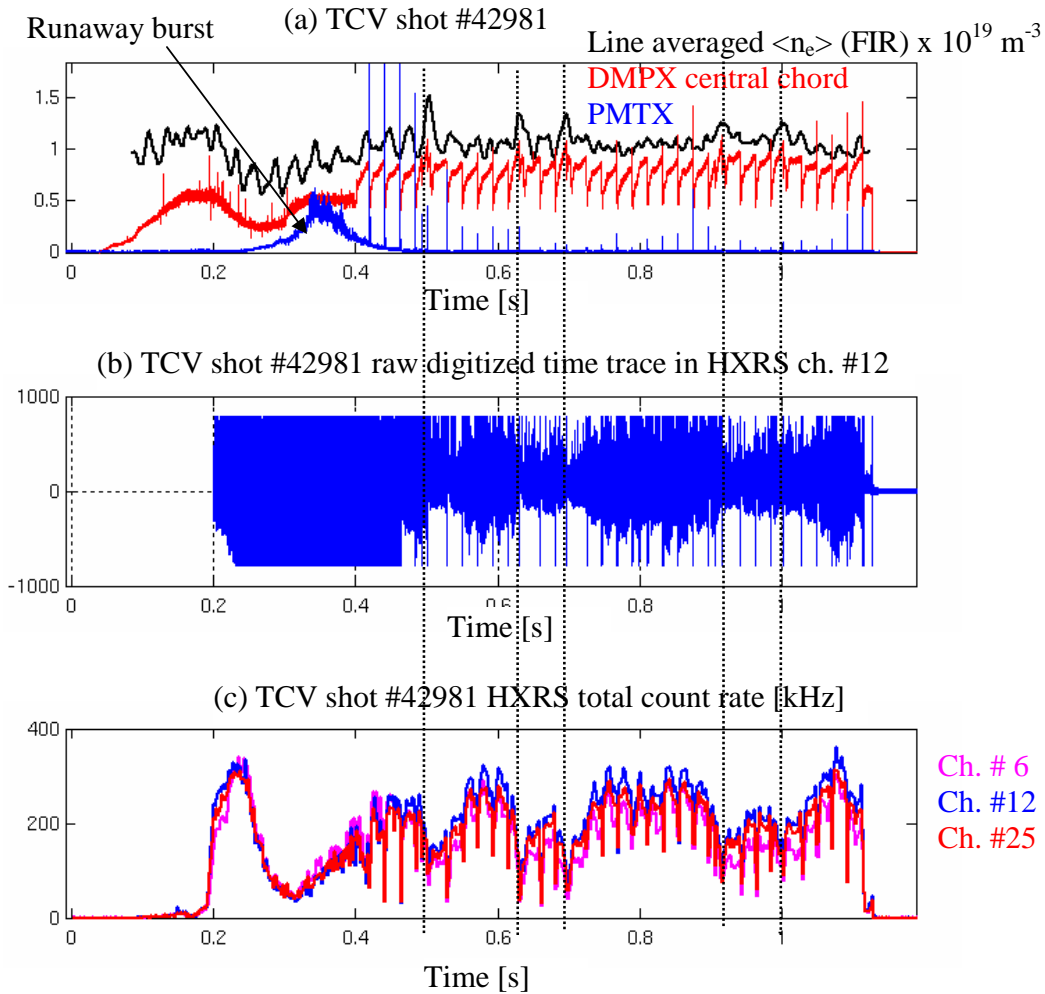


Fig. 8.2 TCV shot 42981. (a) Line-averaged plasma density, DMPX and PMTX time traces. (b) Raw digitized signal from HXRS channel #12. (c) Total count rate in chs. #6, 12 and in the blind detector, ch. #25. The count rate drop during the saturated phase is an artifact due to paralysis of the peak detection algorithm.

From Fig. 8.2 we can also see that the runaway activity drops drastically as density increases. The five local density maxima (thin dotted vertical lines) are accompanied by decreased count rates.

8.2.2 Spectral analysis of partially runaway phases

TCV shot 43082 is a plasma discharge similar to #42981, with $I_p=280 \text{ kA}$, $B_0 = 1.2 \text{ T}$, $V_{loop} = 1.3\text{V}$, $T_{e0} = 1.2 \text{ keV}$ and $n_{e0} = 2.3 \times 10^{19} \text{ m}^{-3}$. In this case the EC power is deposited near the $q=1$ surface without any active RT control (continuous power injection). Two ST phases are present during the discharge, the first one ($\sim 30 \text{ ms}$ ST period) for $0.4 \leq t \leq 0.8 \text{ s}$ and the second one ($\sim 40 \text{ ms}$ ST period) for $1 \leq t \leq 1.2 \text{ s}$ as visible in the DMPX and PMTX time traces in Fig. 8.4a. The higher density, compared to shot #42981,

limits the runaway signal to a lower level; as shown in Fig. 8.4c, the signal in the blind detector # 25 is smaller than in channels viewing the plasma but still non zero.

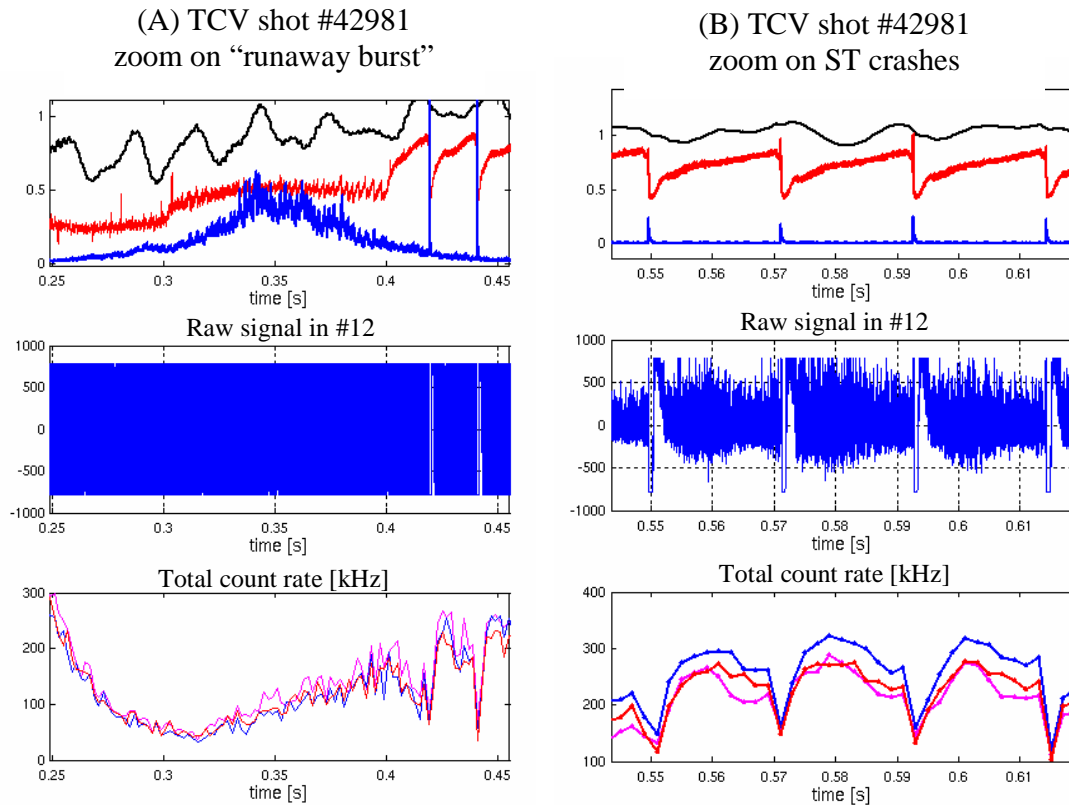


Figure 8.3 TCV shot 42981, zoom on two time intervals from Fig. 8.2: (A) PMTX “runaway burst” and (B) sawtooth crashes.

The spectrogram of the detected signal in channel #12 is given in Fig. 8.4d. Because of the modest plasma temperature, the non-thermal bremsstrahlung signal is mostly in the lower energy region below 20 keV. We can recognize the two ST phases in which a significant fraction of the signal (even at the lower photon energies) is due to the presence of runaway generated thick target bremsstrahlung. These two phases can be compared with the “runaway quiescent” phase in the $t = [0.85-0.95]$ s time interval, when the suppressed ST activity coincides with an increase in the plasma density. In the spectrogram, an extended energy tail is observed in coincidence with each ST crash, with high photon statistics up to 120 keV. Two examples, one for each ST phase, are displayed in Fig. 8.5.

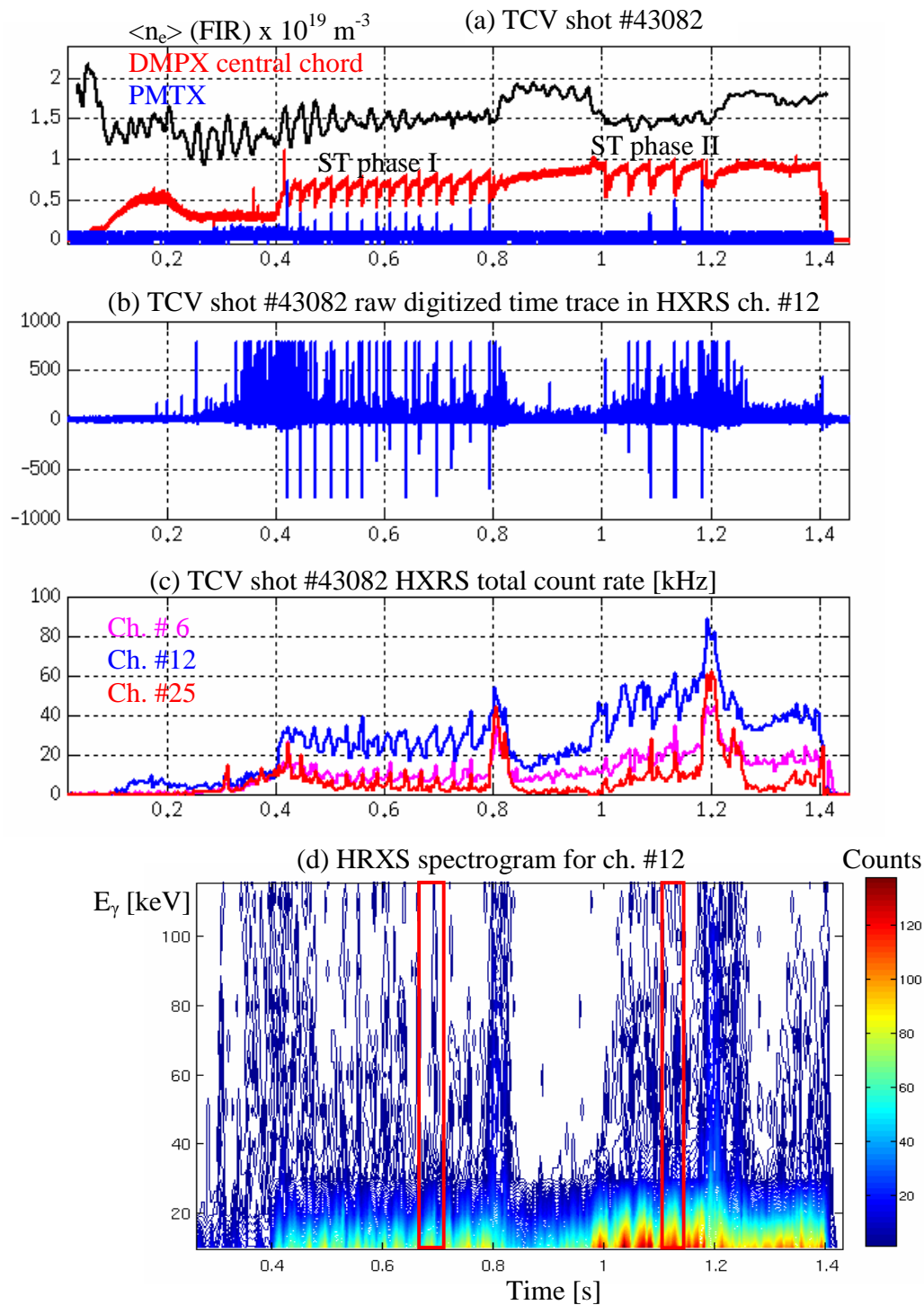


Figure 8.4 TCV shot 43082. (a) Line averaged plasma density, DMPX and PMTX time traces. (b) Raw digitized signal from HXRS channel #12. (c) Total count rate in chs. #6, 12 and in the blind detector, ch. #25. (d) Energy spectrogram for the central HXRS chord #12. The red enclosures in (d) identify the ST crashes analyzed in Fig. 8.5.

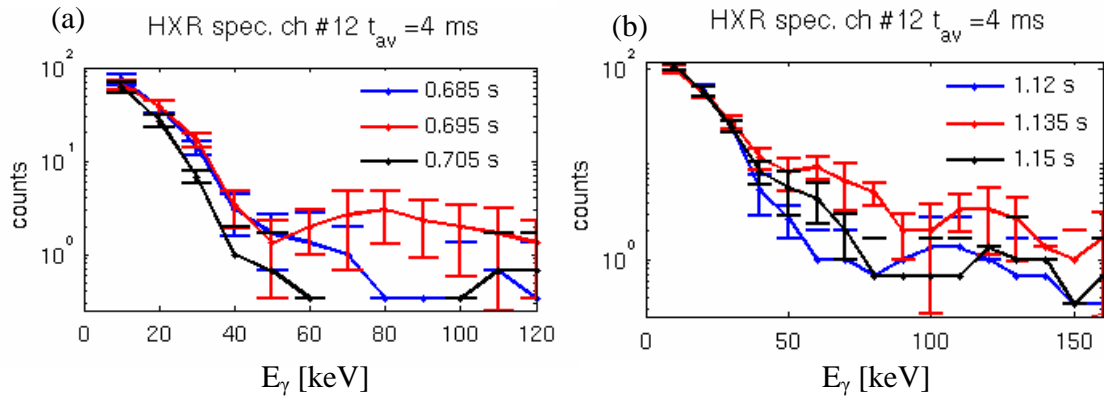


Figure 8.5. Energy spectra for (a) ST crash in phase I and (b) ST crash in phase II (from Fig. 8.4) just before the crash (blue), at the crash (red), and just after the crash (black). The distortion of the spectrum toward high energy is visible in coincidence with the crash (red curve in both diagrams).

The density and loop voltage time traces for TCV shots 42981 and 43082 are compared in Fig. 8.6. The loop voltage is very similar in the two discharges while the density in 43082 is $\sim 40\%$ higher than in 42981. This density difference is therefore sufficient to make the transition from runaway dominated bremsstrahlung to only a moderate runaway component. The “runaway burst” in the PMTX signal in shot 42981 at around 0.25 s is correlated with a dip in density and a slightly higher value of the loop voltage compared to later in the discharge. In both cases the electric field $E \sim 0.2$ V/m is well below the Dreicer field ($E_D \sim 3.0$ V/m, from eq. 7.11, with $T_e = 1.5$ keV, $n_e = 1 \times 10^{19} \text{ m}^{-3}$ and $V_{\text{loop}} = 1$ V), thus the plasma is not grossly runaway; however, as discussed in section 7.9, a significant runaway component can still exist.

The (limited) experience accumulated so far leads us to a practical rule of thumb for keeping the runaway signal manageable: the line averaged density must be kept above $2 \times 10^{19} \text{ m}^{-3}$ in typical conditions of $V_{\text{loop}} \sim 1\text{-}1.5\text{V}$.

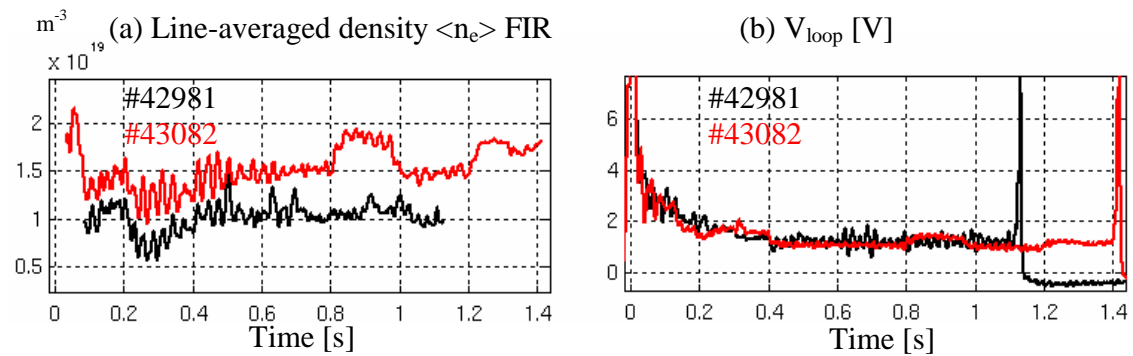


Figure 8.6 Comparison of plasma density and loop voltage in TCV shots 43291 and 43082.

8.2.3 Concluding remarks

The study of HXR emission in low density discharges with finite loop voltage has highlighted the need to limit runaway activity and, in any case, to monitor it correctly in order to avoid misinterpreting the results. This is made possible in the new HXRS system by the acquisition of the full pulse waveforms and, crucially, by the presence of a heavily shielded “blind detector”. This is not the arrangement commonly used in the past. The impact of runaway emission on past measurements, including those performed on TCV with a HXR camera on loan from CEA-Cadarache, remains to be cross-checked. Such experiments were often carried out at densities below the critical runaway level and non zero loop voltage.

In the remainder of this chapter, we shall discuss experimental results from plasma discharges in which the plasma density was deliberately kept above $2 \times 10^{19} \text{ m}^{-3}$ to prevent pollution from runaway emission.

8.3 Suprathermal emission in ECCD plasmas

The generation of suprathermal electrons by ECCD in TCV is well documented [50], and is one of the key motivations for the development of the HXRS diagnostic. Accordingly, initial experiments with the first camera focused on simple studies of the dependence of the suprathermal bremsstrahlung emission on plasma and ECRH parameters.

8.3.1 Suprathermal bremsstrahlung emission vs density

As discussed in section 6, the plasma density has a strong influence on HXR emission during ECCD. On this theme, we present here a basic analysis of the HXR emission in TCV shot 43204. This is a limited plasma, $I_p = 255 \text{ kA}$, $V_{\text{loop}} = 1 \text{ V}$, $B_0 = 1.4 \text{ T}$, $T_{e0} \sim 1.5 \text{ keV}$; the peak density is in the neighborhood of $2.5 \times 10^{19} \text{ m}^{-3}$ but the line-averaged density varies by about 15% during the shot, decreasing first and then increasing again after 0.6 s. ECCD is applied with $P_{\text{in}} \sim 450 \text{ kW}$ and a toroidal angle of 20° (CO-ECCD injection in the plasma core). The 15% density variation causes an opposite 40% variation in HXR emission as shown in Fig. 8.7.

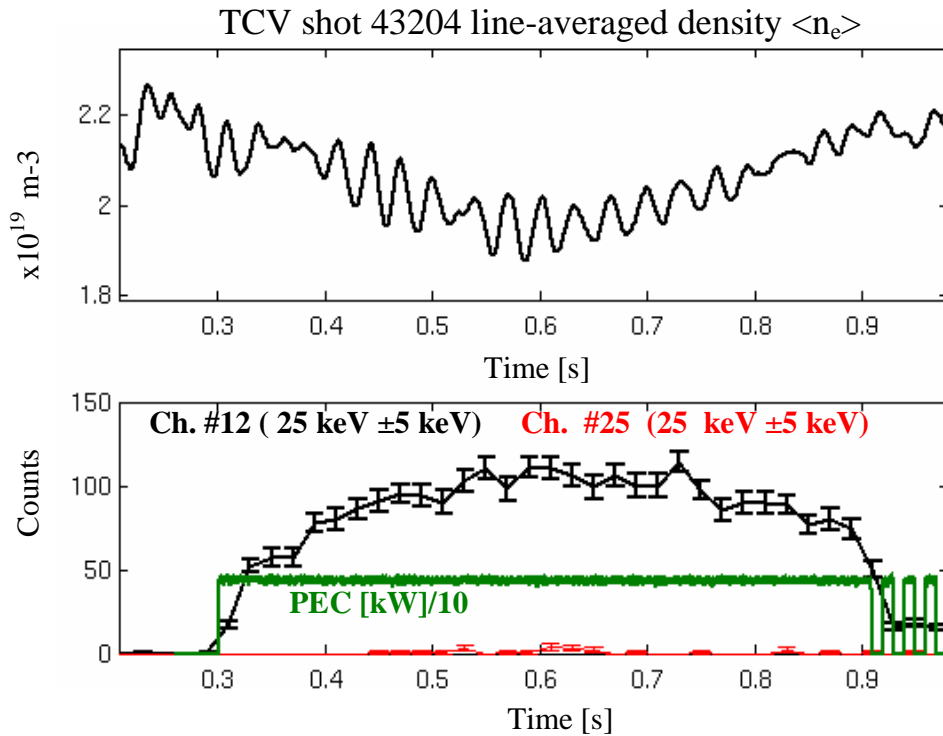


Figure 8. 7 HXR emission dependence on density. The signal in the central chord #12 displays the highest photon statistics. The blind channel 25 is also shown for comparison.

This simple analysis confirms the Fokker-Planck simulations of section 6 and confirms the need for any comparative studies of suprathermal HXR emission to be carried out in conditions of similar density.

8.3.2 Suprathermal bremsstrahlung emission vs toroidal injection angle

In this section we discuss a series of four TCV shots in which the toroidal angle of ECCD injection and thus the parallel wave number (k_{\parallel}) was varied between shots. The limited target plasma, as well as the power injection time trace, were identical for the four shots. An initial constant power phase is followed by two power modulation phases with 20 and 60 ms periods (100% depth and 50 % duty-cycle), respectively. Four gyrotrons provide the requested EC power ($P_{in} \sim 1.8$ MW), through two equatorial and two upper lateral LFS launchers. Complete wave absorption, in each case, is predicted by Toray and LUKE/C3PO calculations.

The magnetic equilibrium and the EC injection geometry are shown in Fig. 8.8 for the case of $\sim 20^\circ$ CO-ECCD injection (shot 43619). To avoid saturation or pile-up, filter #3 (0.2 mm Al) was used here (low-energy cut off-at 7 keV). The first shot (#43618) was in pure ECH with injection in the poloidal plane ($\phi=0$, $k_{\parallel} \sim 0$); in the other shots (#43779,

#43619 and #43783) the toroidal angle of injection was progressively varied to $\phi_{inj} = [\sim 10^\circ, \sim 20^\circ, \sim 30^\circ]$. The latter value is close to the limit beyond which the beams are strongly refracted out of the plasma in these conditions.

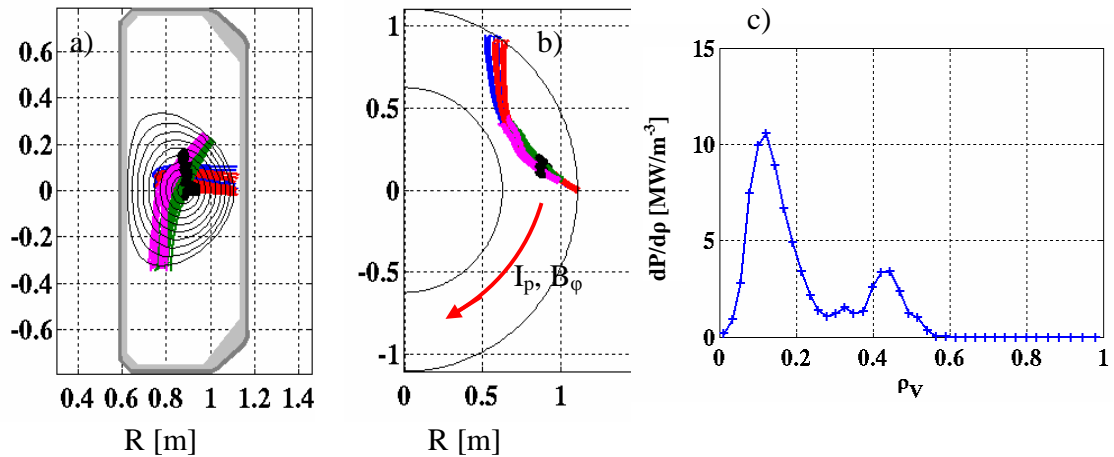


Figure 8.8 TCV shot 43619; 20° CO-ECCD injection. Magnetic equilibrium (a) and LUKE/C3PO EC beam geometry (a-b). c) Radial profile of the absorbed EC power (LUKE).

As previously discussed, HXR emissions levels have to be compared in conditions of very similar density. Since the density control was non-optimal during these shots, we analyzed the data in different time intervals in the different shots: $t = 0.5$ s. in the ECH, 20° and 30° shots and $t = 0.68$ s in the 10° shot (Fig. 8.9). No sign of parasitic signal was seen from the blind detector #25 during the flat top, constant EC power injection phase.

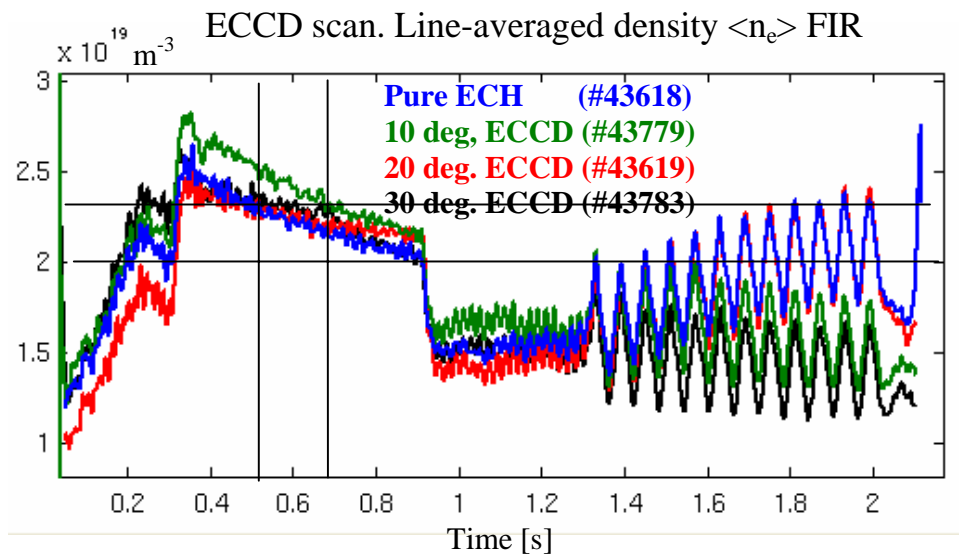


Figure 8.9. Density time traces for shots analyzed in the CO-ECCD scan.

The results of the analysis are summarized in Fig. 8.10, where the energy spectra of the four cases are compared in the 20 -100 keV energy range in which the HXR statistics are sufficiently high.

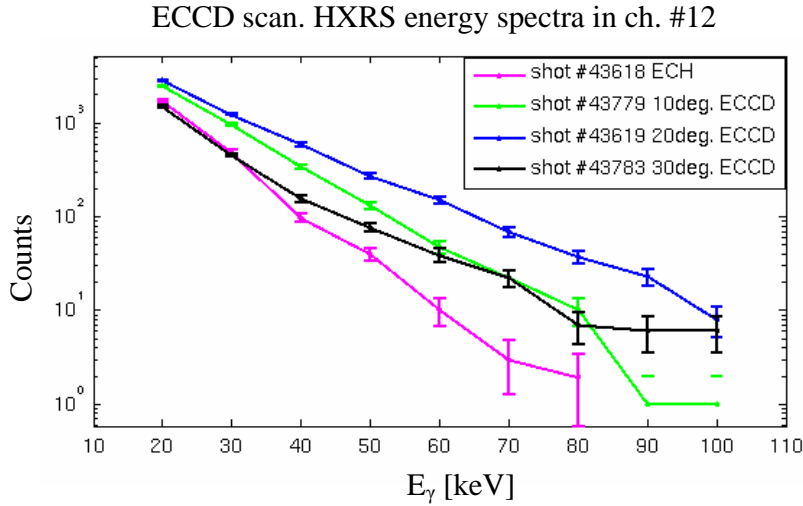


Figure 8.10 Co-ECCD toroidal injection angle scan. HXR spectra are obtained from a 40 ms integration around $t = 0.5$ s for the ECH, 20° and 30° CO-ECCD cases and around $t = 0.68$ s for the case of 10° CO-ECCD.

The non-thermal bremsstrahlung emission is clearly maximum in the case of 20° CO-ECCD injection. As a complement to this analysis, we have also estimated the apparent photon temperature (T_{ph}) by using the slope method described in section 5.1.2. We have performed the fit in the 40-60 keV energy range to guarantee good statistics while minimizing pollution from both the thermal bulk and low energy Compton accumulation (as discussed in section 7.8.2). The results are summarized in table 8.1

shot type	T_{ph}
43618 pure ECH	8.8 ± 2 keV
43779 10° CO-ECCD	10.7 ± 2 keV
43619 20° CO-ECCD	14.7 ± 3 keV
43783 30° CO-ECCD	14.5 ± 3 keV

Table 8.1

8.4 Parallel asymmetry of non-thermal bremsstrahlung emission

The ability to rotate the equatorial HXRS camera by 90 degrees to view the plasma tangentially opens the possibility of studying non-thermal bremsstrahlung emission parallel to the magnetic field.

Relativistic forward emission is expected to dominate the high energy part of the HXR spectrum (see section 5.1.3). Electrons accelerated in the toroidal direction by the ohmic electric field are therefore expected to display a parallel asymmetry. Similarly, in the case of ECCD, the preferential heating of electrons with a given sign of the parallel velocity could create a sign imbalance in the emission (although it should be remembered that the heating process increases the *perpendicular* velocity).

The results obtained in section 8.3 suggest that a toroidal injection angle near 20° is optimal for suprathreshold electron generation, especially in the high energy domain, where relativistic effects dominate. For this reason we performed two shots with high power injection ($P_{EC} = 2.3$ MW) and 20° ECCD injection angle, one (#43784) in co-ECCD and one (#43787) in counter-ECCD. The magnetic equilibria and wave injection geometry are shown in Fig. 8.11, and the density, loop voltage, total current and EC injected power time traces in Fig. 8.12. The HXRS lines of sight are depicted in Fig. 8.13a. The total current is primarily sustained by the transformer (220 kA) with a 42 kA contribution from the EC wave (results from LUKE Fokker-Planck simulation).

The plasma parameters, including the density, are well matched in the two shots in the $t = [0.5-0.8]$ s period, permitting a long time averaging to improve statistics. In such time interval the central electron temperature from Thomson scattering is ≈ 2.3 keV.

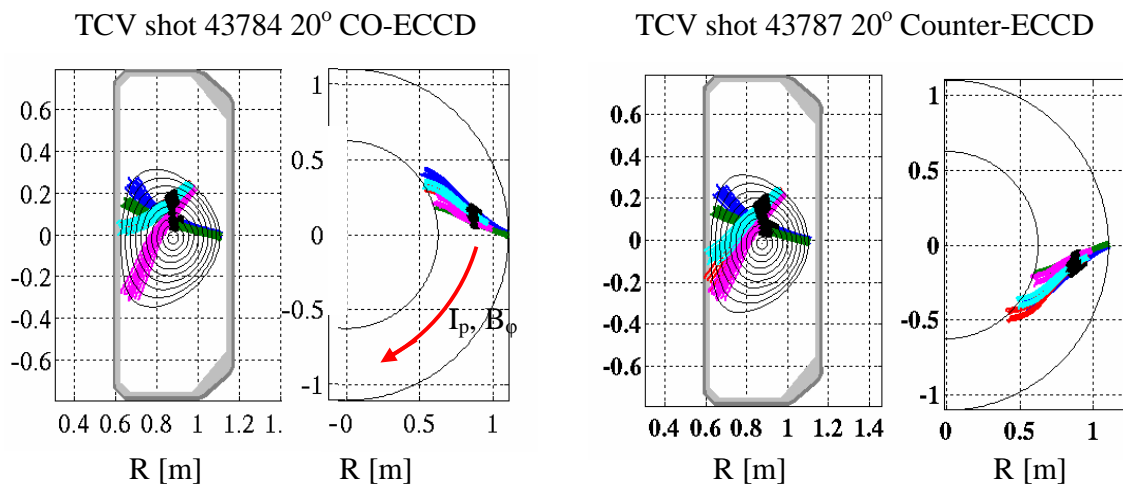


Figure 8.11 LUKE/C3PO ray tracing for TCV shots 43784 (left) and 43787 (right).

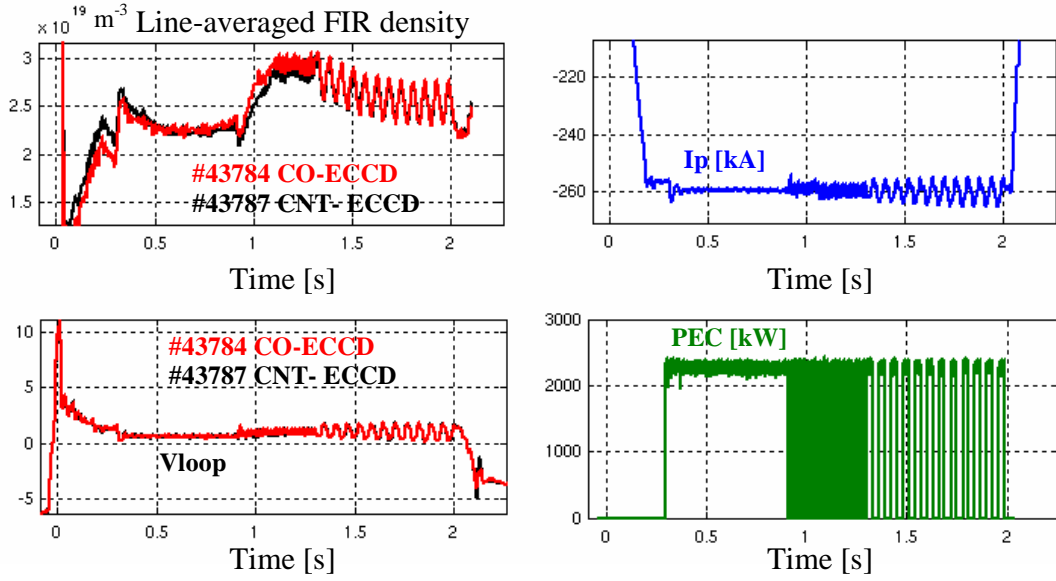


Figure 8.12 Time traces of line-averaged density current, loop voltage, and injected EC power in TCV shots 43784 (CO-ECCD) and 43787 (Counter-ECCD).

In Figure 8.13b we show the recorded HXRS photon count (as a function of the chord number) integrated over a 120 ms time interval centered at $t = 0.64$ s for the 95-105 keV energy range, for both shots. It is clear that at this high photon energy the tangential emission in both the co- and counter- directions is considerably larger than the perpendicular emission. In particular, the signal peaks in chords 3 and 22. It must be remembered, however, that geometric effects play a strong role since the integration length is also much longer for tangential chords.

The most interesting feature is the co-counter asymmetry in the amplitude of the emissivity. Limiting the analysis to chords 3 and 22, the factor of asymmetry

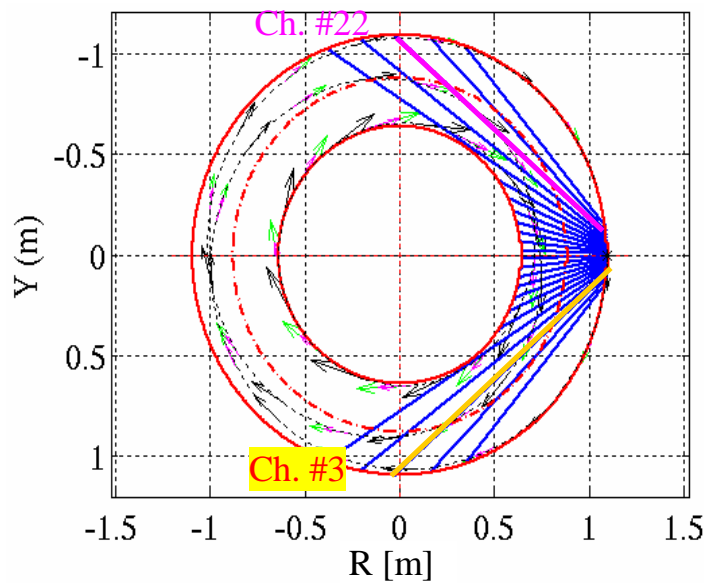
$$\Delta\text{HXR}_{\text{tor,asym}}(E_\gamma) = \frac{N_{c3}(E_\gamma) - N_{c22}(E_\gamma)}{N_{c22}(E_\gamma)}$$

is plotted in Fig. 8.14a as a function of the measured photon energy (E_γ). A positive value of this factor indicates preferential emission in the direction *opposite* to the plasma current, i.e., the direction of the co-ECCD electron velocity imbalance. A large positive value is indeed observed, as intuitively expected, in the co-ECCD case. In the counter-ECCD case the asymmetry factor is reduced but remains positive except at the very highest energies.

We modeled these discharges with LUKE/R5-X2. Using the experimental value of $Z_{\text{eff}}=3$ and an ES suprathermal electron diffusivity of $2 \text{ m}^2/\text{s}$ (see section 4.2.3), the calculated current is 275 kA, close to the experimental value of 260 kA. The calculated HXR emission exceeds the experimental one in the 20-40 keV energy range while it is comparable at higher energy. The modeled factor of asymmetry is plotted in Fig. 8.14b.

In the CO-ECCD case, the code predicts a higher level of asymmetry at all energies considered (20-100 keV energy range), up to a value of 6 for $E_\gamma > 80$ keV. In the counter-ECCD case the asymmetry is inverted but is also much weaker (~ 0.4). The specular inversion between the co- and counter-ECCD cases is opposed by the presence of a significant electric field, which clearly makes a strong contribution to the emission imbalance. This prediction is very clearly confirmed at least qualitatively by the experiment, although for the moment a quantitative match has not been obtained. A refinement of the model, particularly of the fast electron transport, could conceivably improve the agreement, but this is left for future work.

a) HXRS camera in horizontal configuration (toroidal coverage)



b) HXR emission in the tangential direction at $t = 0.64$ s

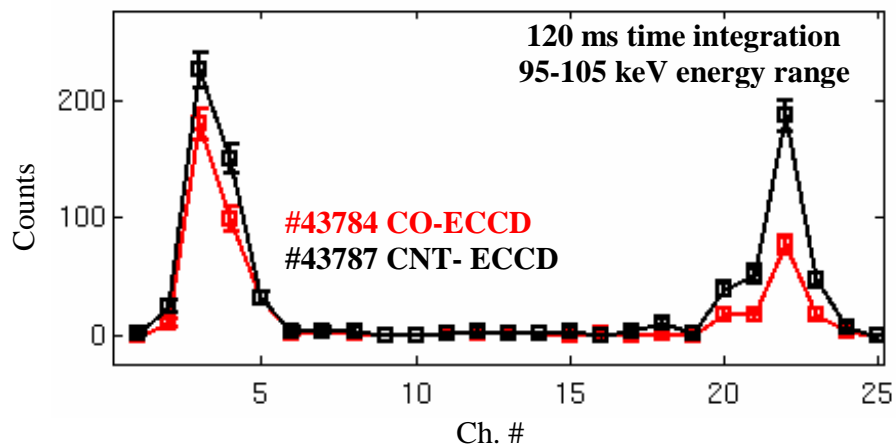


Figure 8.13 a) Toroidal lines of sight in the horizontal HXRS camera configuration (top view); b) HXRS signal as a function of chord number, integrated from $t = 0.58$ to 0.70 s in the 95-105 keV energy range.

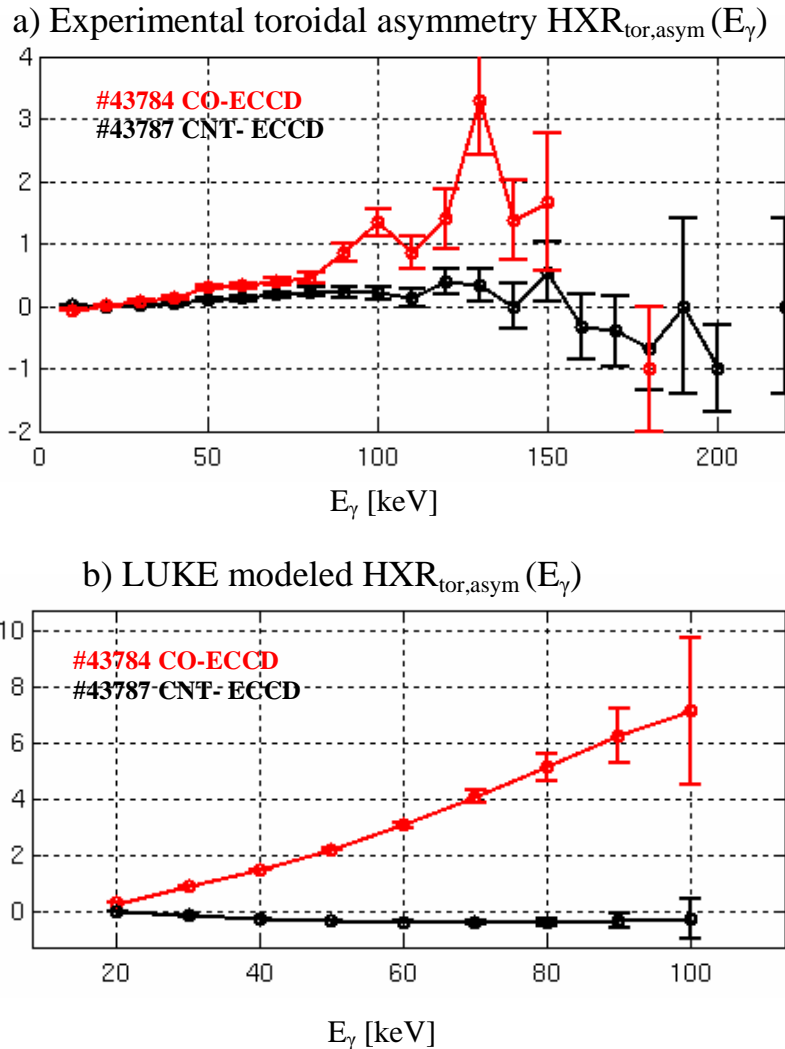


Fig 8.14 a) Experimental and b) LUKE/R5-X2 modeled HXR asymmetry in the toroidal direction as a function of the photon energy (E_γ) for both co-ECCD (red curves) and counter-ECCD (black curves) injection.

8.5 Coherent averaging on modulated ECCD experiments

8.5.1 Introduction

All the ECCD experiments discussed in this chapter include an initial phase of constant power injection followed by two phases with power modulation (50% duty cycle) with characteristic 20 and 60 ms period. Up to now we have focused on the initial constant phase. Now we move to a preliminary analysis of the ECCD modulation phase to explore the dynamical response of the suprathermal electrons.

We have applied a coherent averaging technique, whereby the signal at each time point in the modulation cycle is averaged over several identical periods to improve the photon statistics. The characteristic time scales for the generation of the suprathermal electron population along with the slowing down and radial transport dynamics can in principle be studied in this way. The limited goal of this preliminary study is to investigate the potential of this technique in revealing the underlying time scales.

Two representative TCV discharges were chosen for this analysis. The detector array was oriented vertically in the first shot and horizontally in the second.

8.5.2 Vertical camera orientation

Here we examine TCV shot 43211, with 10° CO-ECCD injection ($P_{EC} = 2.4$ MW), $I_p = 260$ kA, $B_0 = 1.4$ T, $T_{e0} = 3$ keV, $n_{e0} = 2.8 \times 10^{19}$ m⁻³. Because of the high EC power density deposited in the plasma during the modulation phase, the global plasma profiles (T_e , n_e) are also modulated, as can be seen in Fig. 8.15a. The magnetic equilibrium and the geometry of the EC power injection, except for the toroidal angle, are the same as in shots 43784 and 43787 displayed in Fig. 8.11. The HXRS equatorial camera is oriented vertically and the lines of sight collect non-thermal bremsstrahlung emission in the poloidal plasma cross-section. During the 20 ms EC modulation phase the density drops considerably and runaway radiation is seen on ch. 25; for this reason we limit the analysis to the 60 ms EC modulation phase.

Figure 8.16 summarizes the results from the coherent averaging analysis (time-integrated on 2 ms intervals). Figure 8.16a shows the coherent averaged photon statistics in ch. #12 viewing the plasma core for different energies. The analysis indicates that the non-thermal bremsstrahlung signal rises on slightly different time scales depending on energy. The signal in each energy bin is characterized by two distinct slopes, an initial and faster one (s_1) related to the generation and relaxation of the suprathermal electron population and the second (and slower) one (s_2) describing the relaxation likely driven by the time evolution of the global plasma profiles.

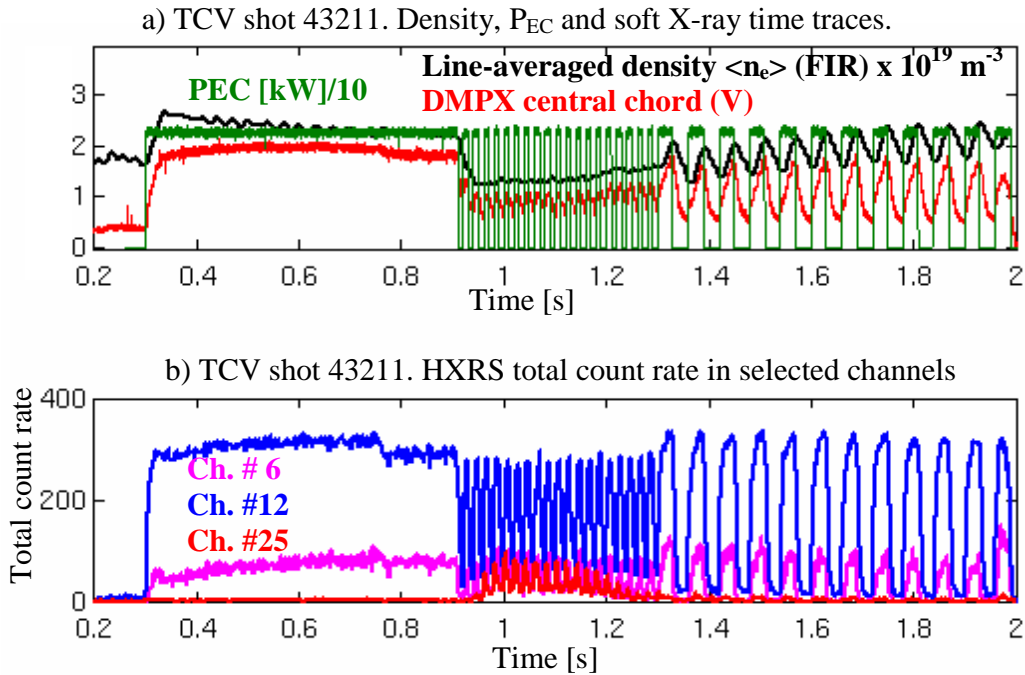


Figure 8.15 TCV shot 43211. a) Line-averaged density (from FIR), EC power, and soft X-ray (DMPX) time traces. b) Total count rates in selected HXRS channels (6, 12, and 25).

Here we define the typical rise time of the HXR signal (τ_{rX}) as the time interval starting at the beginning of the EC injection and ending at the intersection of the two slopes (colored circles in Fig. 8.16a). The time τ_{rX} increases from 8 ± 2 ms at 25–35 keV up to 12 ± 2 ms at 85–95 keV. The decay time after switch-off is of the order of 4–6 ms at all energies. (While the collisional slowing-down time increases with energy, it must be remembered that the bremsstrahlung emission at each energy E is a convolution of radiation emitted by all electrons with energy $> E$).

Spectroscopic information is given in Fig. 8.16b where the fitted photon temperature, T_{ph} , is displayed for selected HXRS chords 5, 7, 9 and 12 (cf. Fig. 8.1). In the particular magnetic configuration of shot 43211, these chords are tangential to the $\rho_v \approx 0.6$, 0.4, 0.2, and 0 flux surfaces, respectively. The photon temperature at the plasma center, $T_{ph} \sim 20$ –30 keV, is systematically higher than in chords viewing the plasma off axis: $T_{ph, \#7} \sim 12$ keV and $T_{ph, \#5} \sim 7$ keV. Note that for the case of central chords 9–12 a photon temperature of ~ 7 keV is measured up to 20 ms after the switch off.

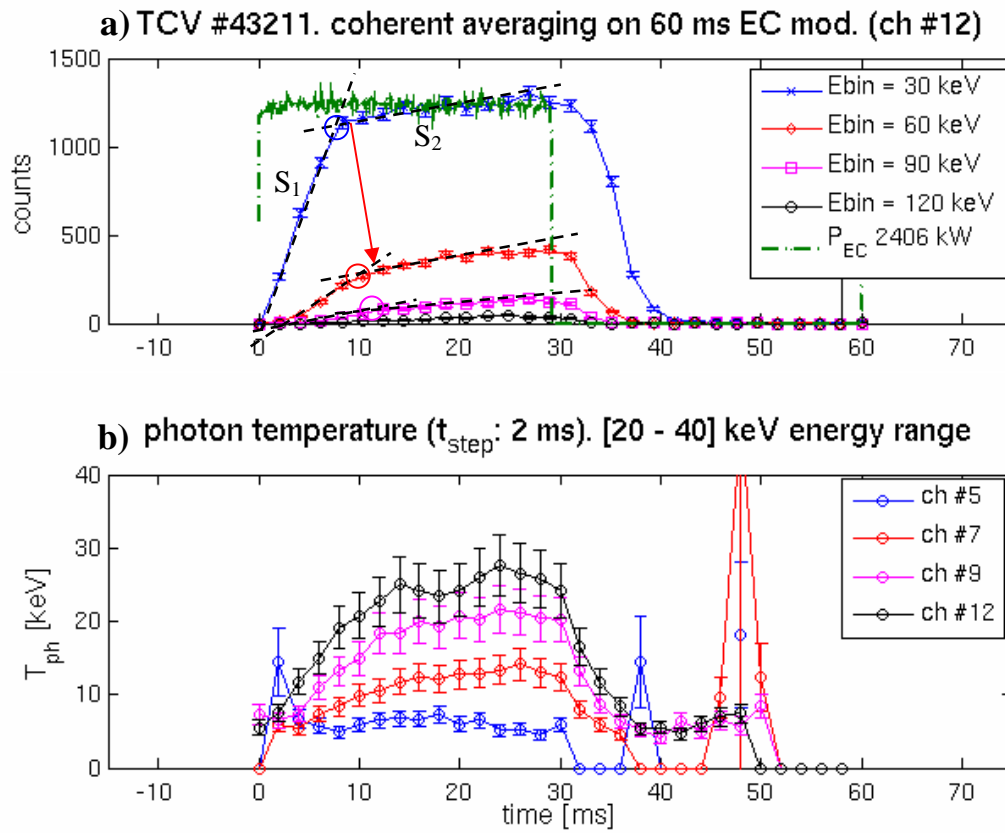


Figure 8.16 TCV shot 43211. a) Coherent averaging analysis of HXRS non-thermal bremsstrahlung emission in the central chord #12. b) Estimated photon temperature for selected chords.

8.5.3 Horizontal camera orientation

The same magnetic equilibrium and power injection scheme of TCV shot 43211 were adopted in TCV shot 43209, but the EC power was reduced to 1.42 MW. The HXRS camera here was in a horizontal configuration (tangential views).

The experimental density profile, soft X-ray emission and EC power time traces are shown in Fig 8.17a, whereas the HXRS signal is given in Fig. 8.17b for selected chords. The gamma-ray signal in ch. #25 is negligible.

TCV shot 43209. Density, P_{EC} and soft X-ray time traces.

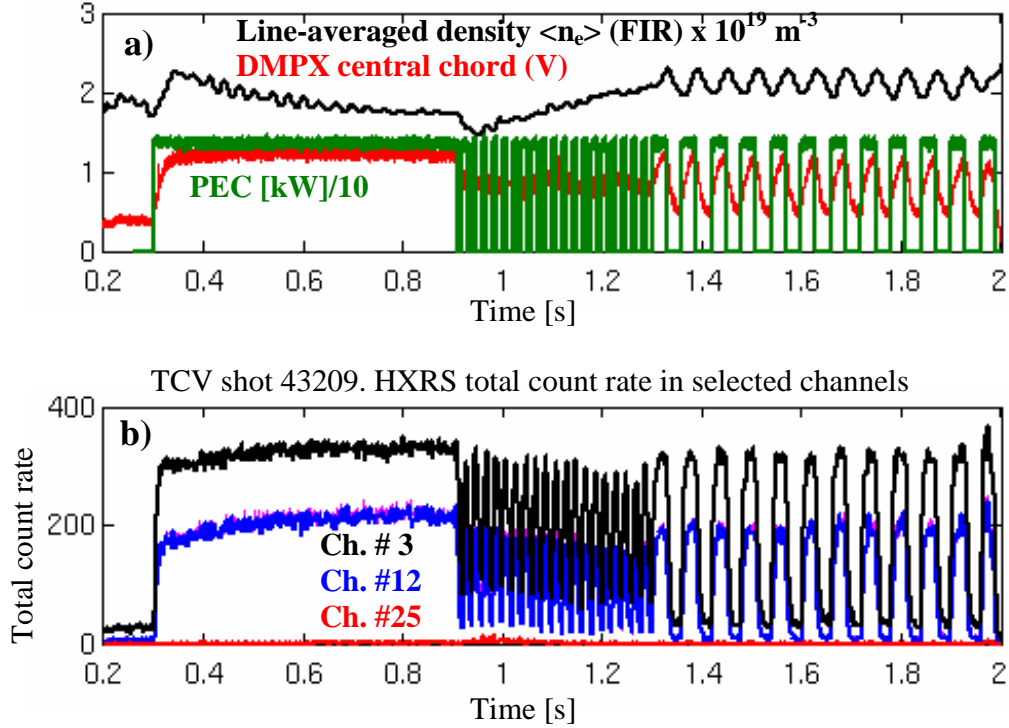


Figure 8.17 TCV shot 43211: $I_p = 260$ kA, $B_0 = 1.4$ T, $V_{loop} = 0.8$ V, $n_{e0} = 2.5 \times 10^{19} \text{ m}^{-3}$, $T_{e0} = 2$ keV. a) Line-averaged density (from FIR), EC power, and soft X-ray (DMPX) time traces. b) Total count rates in selected HXRS channels (3, 12, and 25).

The result of the coherent averaging on the HXRS signal, in the 60 ms modulation phase, is displayed for ch. #3 (viewing the plasma along a co-tangential view) in Fig. 8.18a. As in the case of shot 43211, the time ramp of the HXR signal is faster at low energy, and similar values of τ_{rX} are found. Photon temperatures for selected chords are compared in Fig. 8.18b. The estimated photon temperatures in the tangential chords #3 (co-direction), and #22 (counter-direction) are of the order of 20 keV, twice as large as in channels #7 and #12, close to perpendicular to the magnetic axis. The lower photon temperature in #12 compared to the case of TCV shot 43211 can presumably be attributed to the lower level of injected power. There is no clear evidence for a difference in the estimated photon temperatures between #3 and #22, at least within the experimental uncertainties.

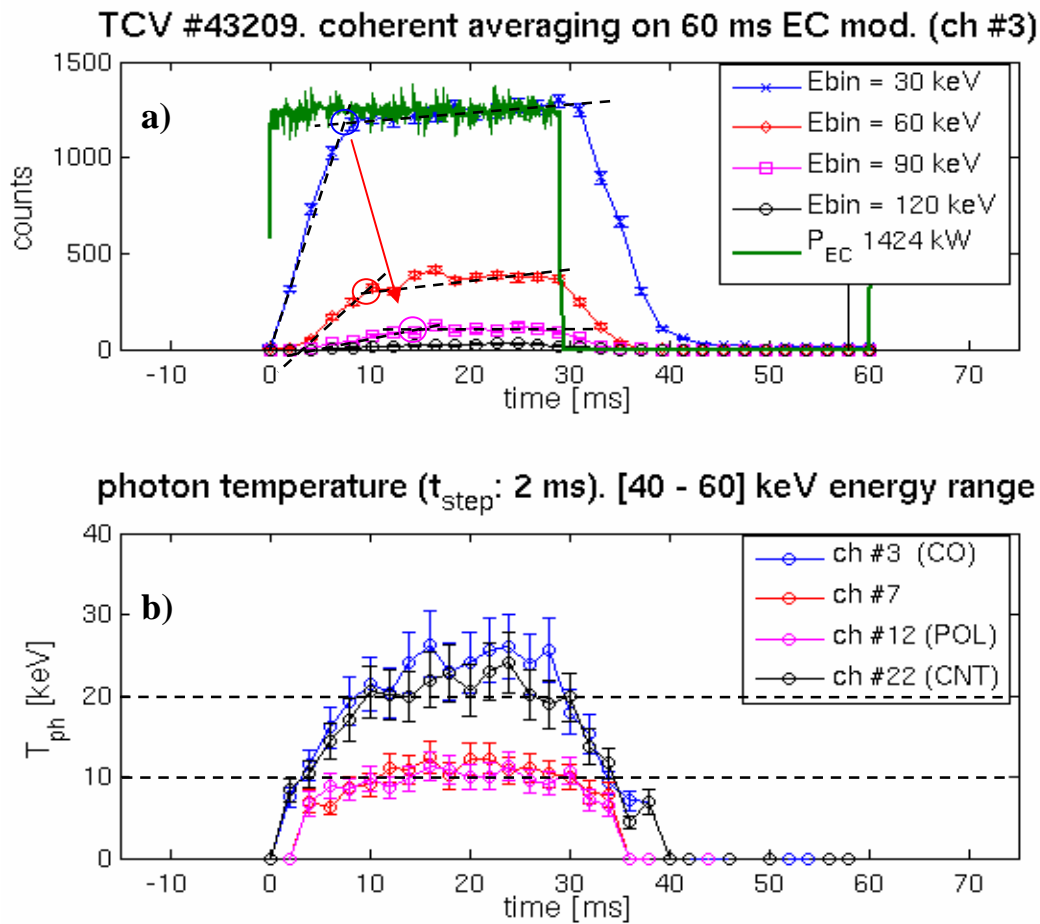


Figure 8.18 TCV shot 432091. a) Coherent averaging analysis of HXRS non-thermal bremsstrahlung emission in the tangential chord #3. b) Estimated photon temperature for selected chords.

8.6 Conclusion

The first HXRS camera has been installed on the LFS equatorial plane of the TCV vessel at the end of April 2011. In its initial period of operation the camera has provided useful observations on low density plasma discharges with stabilized sawteeth, revealing the presence of runaway dominated phases in which transient ADC saturation can occur. A rule of thumb for keeping the runaway signal manageable has been identified consisting of operating at line-averaged plasma density greater than $2 \times 10^{19} \text{ m}^{-3}$. The sensitivity of the HXR emission to plasma density has been probed in experiments with density ramps. The dependence of the non-thermal bremsstrahlung emission on the toroidal injection angle of the EC wave has been studied and a maximum in the emission has been found for 20° co-ECCD injection; the estimated photon temperature also increases with the injection angle.

Preliminary results on the parallel asymmetry of the non-thermal bremsstrahlung emission have been presented. In this case we exploited the ability of the HXRS camera to rotate on its axis to move from poloidal coverage to toroidal co- and counter- views along the toroidal direction. The experimental evidence of the toroidal asymmetry in the HXR emission is qualitatively confirmed by LUKE F-P simulations.

An initial study of the suprathreshold electron population generation and dynamics has been performed by employing coherent averaging techniques during EC power modulation experiments in TCV. In this preliminary study a delayed high energy tail is measured compared to the instantaneous signal seen at lower HXR energy. Furthermore a higher photon temperature is seen in the toroidal direction than on the emission coming from lines of sight close to perpendicular to the magnetic field.

9. Conclusions and outlook

The main motivation for this thesis work was to advance the fundamental understanding of the physics of EC wave-particle interaction and ECCD, both through experimental measurements and through numerical modeling. To this end, the characterization of the suprathermal electron distribution function is a key point.

A novel hard X-ray 4-camera tomographic spectrometer (HXRS) has been designed and the first camera has been installed and commissioned recently in TCV. The camera has confirmed the validity of the conceptual design of the detector-collimator system, and the performance of the in-house manufactured amplifier cards; in particular, a high signal to noise ratio has been obtained.

The HXRS system performs full digitisation of the acquired wave form and is equipped with a monitor detector for stray radiation identification (one per camera). These characteristics make the system very flexible as they allow the diagnostician to easily determine the proper conditions of operation; in particular, runaway dominated phases and pile-up saturations can be easily identified.

In support of simultaneous 2nd and 3rd harmonic coupling experiments in TCV, the LUKE Fokker-Planck code has been integrated in the TCV environment. A collaboration with the code's authors has been started to integrate the code in the TCV environment. The possibility to compare the experimental measurements with synthetic HXR data provides a powerful tool for the understanding of the basic physical phenomenology at play during ECH and ECCD operation, including fast electron radial transport.

As a result, a new and complete diagnostic for the study of the suprathermal electron dynamics is now available in TCV, including both the multi-camera HXRS system and the modelling tools provided by the LUKE Fokker-Planck code.

The basic physical mechanisms governing simultaneous 2nd and 3rd EC harmonic absorption at the same frequency in TCV were explored both through experiments and modelling, as discussed in chapter 6.

In the last chapter of this thesis, the preliminary experimental results obtained with the first HXRS camera installed in TCV have been discussed.

The upgrade of the HXRS system with the remaining three cameras is expected in the near future, providing a first tomographic reconstruction of the non thermal bremsstrahlung emission in a non-circular tokamak. An interesting and straightforward verification will concern the possible existence of a poloidal asymmetry on the HXR emission as predicted by the LUKE Fokker-Planck code, especially in plasmas with off-axis EC power deposition. The HXRS camera geometry is already available for the R5-X2 bremsstrahlung calculator, in view of modelling of future experiments.

Further work remains to be performed to refine the analysis of the experimental data presented in chapter 8, with particular emphasis on asymmetric tangential HXR emission. Fokker-Planck modelling of simultaneous 2nd /3rd harmonic absorption is to be extended to experiments with two harmonic injections at different frequencies, X2 from the LFS and X3 from the TCV top launchers.

The potentiality of the HXRS system for measuring non-thermal photon emission in the tangential direction is still to be fully exploited. Extended studies of the electron acceleration and consequent suprathermal bremsstrahlung generation during magnetic

reconnection (such as long period sawtooth activity) could well be performed in the future.

The runaway activity in TCV also needs to be characterized more fully, in particular to correlate the runaway population with density and loop voltage. The possible influence of EC heating and current drive on a preexisting runaway population should also be investigated.

In conclusion, this thesis work has provided a substantial advancement in the diagnostic techniques for the study of suprathermal electron dynamics through suprathermal bremsstrahlung emission in tokamak devices. The integration of the LUKE Fokker-Planck code in TCV offers the possibility of deepening the physical insight and aiding the interpretation and the design of present and future ECH experiments.

Bibliography

- [1] EIA, International energy outlook 2010 www.eia.gov/oiaf/ieo/
- [2] P.J. Lomas, Plasma Phys. Control. Fusion **42** (2000) B115
- [3] Y. Camenen et al, Nucl. Fusion **47** (2007) 586
- [4] A. Pochelon et al, 22nd IAEA Fusion Energy Conference, 50th Anniversary of Controlled Nuclear Fusion Research, Geneva, Switzerland, 12-18 October 2008, EX/P5-15
- [5] A. Marinoni et al, Plasma Phys. Control. Fusion **51** (2009) 055016
- [6] J. Wesson, "Tokamaks", Oxford university press (2004)
- [7] R.J. Bickerton, J.W. Connor, J.B. Taylor, Nature Phys. Sci. **229** (1971) 110
- [8] J.W. Connor et al, Nucl. Fusion **44** (2004) R1
- [9] B. S. Taylor, Plasma Phys. Control. Fusion **39** (1997) B47
- [10] T. Ohkawa, Nucl. Fusion **10** (1970) 185
- [11] R. J. La Haye, Phys. Plasmas **9** (2002) 2051
- [12] C. Angioni, Nucl. Fusion **43** (2003) 445
- [13] J. Decker and Y. Peysson, report EUR-CEA-FC-1736, Euratom-CEA (2004)
- [14] Y. Peysson and J. Decker, report EUR-CEA-FC-1739, Euratom-CEA (2008)
- [15] Y. Peysson and J. Decker, Phys. Plasmas **15** (2008) 092509
- [16] K. Matsuda, IEEE Trans. Plasma Sci. **17** (1989) 6
- [17] R.H. Cohen, Phys. Fluids **30** (1987) 2442
- [18] R.W. Harvey, M.G. McCoy, Proc. IAEA Technical Committee Meeting on Advances in Simulation and Modeling in Thermonuclear Plasma (Montreal) (Vienna: IAEA), 1992, p 498
- [19] F. Hofmann et al, Plasma Phys. Control. Fusion **36** (1994) B277
- [20] F. Piras et al, Phys. Rev. Lett. **105** (2011) 155003
- [21] T.P. Goodman and the TCV Team, Nucl. Fusion **48** (2008) 054011
- [22] J I Paley et al, Plasma Phys. Control. Fusion **51** (2009) 124041
- [23] O. Sauter et al, Phys. Rev. Lett. **84** (2000) 3322
- [24] M.A. Henderson et al, Phys. Plasmas **10** (2003) 1796
- [25] S.Coda et al, Proc. 22nd IAEA Fusion Energy Conference, Geneva, Switzerland, 2008 (IAEA, Vienna, 2008), EX/2-3
- [26] N. J. Fish, Rev. Mod. Phys. **59** (1987) 175
- [27] C.F.F Karney, N.J. Fisch, Phys. Fluids **22** (1979) 1817
- [28] M.Maraschek et al, Phys. Rev. Lett. **98** (2007) 025005
- [29] N.H. Fisch, A.H. Boozer, Phys. Rev. Lett. **45** (1980) 720
- [30] V.V. Alikaev, V.V. Parail. Plasma Phys. Control. Fusion **33** (1991) 1639
- [31] T. Ohkawa, General Atomics Report GA-A13847 (1976)
- [32] C.C. Petty et al, Nucl. Fusion **42** (2002) 1366
- [33] M. Rome et al., Plasma Phys. Control. Fusion **45** (2003) 783
- [34] J. Decker, 30th EPS Conference on Contr. Fusion and Plasma Phys., St. Petersburg, 7-11 July 2003 ECA Vol. **27A**, P-3.205
- [35] R. Prater, Phys. Plasmas **11** (2004) 2349
- [36] C. Petty et al, 29th EPS Conference on Plasma Phys. and Contr. Fusion, Montreux, 17-21 June 2002 ECA Vol. **26B**, P-4.057 (2002)
- [37] G. Giruzzi et al, Phys. Rev. Lett. **93** (2004) 255002

- [38] A. Polevoi et al Nucl. Fusion **48** (2008) 015002
- [39] T.J.M. Boyd, J.J. Sanderson, "The Physics of Plasmas", Cambridge University Press (2003)
- [40] J. Decker, "Electron Bernstein Wave Current Drive Modeling in Toroidal Plasma Confinement", Phd Thesis, Massachusetts Institute of Technology 2005
- [41] W.E. Drummond, D. Pines, General Atomics Report GA-2386 (1961)
- [42] A.A. Vedenov, E.O. Velikhov, R.Z. Sagdeev, Nucl. Fusion **1** (1961) 82
- [43] I. Lerche, Phys. Fluids **11** (1968) 1198
- [44] C.F. Kennel, F. Engelmann, Phys Fluids **9** (1966) 2377
- [45] C.F.F. Karney, Computer Physics Reports **4** (1986) 183
- [46] T.H. Stix, "Waves in Plasmas", Springer-Verlag New York, Inc. (1992)
- [47] M. Brambilla, "Kinetic Theory of Plasma Waves", Clarendon Press, Oxford (1998)
- [48] M. Rosebluth, W.M. MacDonald, L. Judd, Phys Rev. **107** (1957) 1
- [49] R.W. Harvey et al, Phys. Rev. Lett. **88** (2002) 205001
- [50] S. Coda et al, Nucl. Fusion **43** (2003) 1361
- [51] R.W Harvey, M.G. McCoy, General Atomics Report GA-A20972 (1992)
- [52] S. Alberti et al, Nucl. Fusion **42** (2002) 42
- [53] P. Nikkola et al, Nucl. Fusion **43** (2003) 1343
- [54] F. Hofmann, G. Tonetti, Nucl. Fusion **28** (1988) 1871
- [55] Y. Peysson, Plasma Phys. Control. Fusion **35** (1993) B253
- [56] K. Ushigusa et al, Nucl. Fusion **32** (1992) 1977
- [57] P.V. Savrukhin, Phys. Rev. Lett. **86** (2001) 3036
- [58] P.V. Savrukhin, Plasma Phys. Control. Fusion **48** (2006) B201
- [59] F.C. Schuller, Plasma Phys. Control. Fusion **37** (1995) A135
- [60] I. Klimanov et al, Plasma Phys. Control. Fusion **49** (2007) L1
- [61] I. Klimanov et al, Rev. Sci. Instrum. **76** (2005) 093504
- [62] P. Blanchard et al, Plasma Phys. Control. Fusion **44** (2002) 2231
- [63] R.W. Harvey et al, Phys. Rev. Lett. **62** (1989) 426]
- [64] S.Coda, Rev. Sci. Instrum. **79** (2008) 10F501
- [65] I.H. Hutchinson, "Principles of Plasma Diagnostics", Cambridge University Press (1992)
- [66] S. von Goeler et al, Nucl. Fusion **25** (1985) 1515
- [67] S. Coda et al, Plasma Phys. Control. Fusion **48** (2006) B359
- [68] Y. Peysson and F. Imbeaux, Rev. Sci. Instr. **70** (1999) 3987
- [69] Y. Peysson, S. Coda and F. Imbeaux, Nucl. Instrum. and Methods in Phys. Res. A **458** (2001) 269
- [70] T. C. Luce et al, Rev. Sci. Instrum. **59** (1988) 1593
- [71] T.P. Goodman et al, Fus. Sci. Tech. **53** (2008) 196
- [72] O. Sauter et al, Phys. Rev. Lett. **94** (2005) 105002
- [73] J.M. Rax, D. Moreau, Nucl. Fusion **29** (1989) 1751
- [74] S. Gnesin, et al, 3rd harmonic ECRH absorption enhancement by 2nd harmonic heating at the same frequency in a Tokamak, submitted to Plasma Phys. Control. Fusion.
- [75] S. Gnesin et al, Rev. Sci. Instrum. **79** (2008) 10F504
- [76] A.M. Cormac, Journal of Appl. Phys. **34** (1963) 2722
- [77] A.M. Cormac, Journal of Appl. Phys. **35** (1964) 2908

- [78] R.S. Granetz, P. Smeulders, Nucl. Fusion **28** (1988) 457
- [79] M. Anton et al, Plasma Phys. Control. Fusion **38** (1996) 1849
- [80] L.C. Ingesson et al, Fusion Sci. Tech. **53** (2008) 528
- [81] G.F. Knoll, "Radiation Detection and Measurement", John Wiley & Sons, 2000
- [82] D. S. McGregor, H. Hermon, Nucl. Instrum. and Methods in Phys. Research A **395** (1997) 250
- [83] P.J. Sellin, Nucl. Instrum. and Methods in Phys. Research A **513** (2003) 332
- [84] C. Scheiber, Nucl. Instrum. and Methods in Phys. Research A **448** (2000) 513
- [85] T. Takahashi et al., Nucl. Instrum. and Methods in Phys. Research A **436** (1999) 111
- [86] Y. Peysson, R. Arslanbekov, Nucl. Instrum. and Methods in Phys. Research A **380** (1996) 423
- [87] P.V. Savrukhin, I.V. Klimanov, Rev. Sci. Instrum. **72** (2001) 1668
- [88] K. Hetch, Zeits. Phys. **77** (1932) 235
- [89] E. Perillo et al., Nucl. Instrum. and Methods in Phys. Research A **458** (2001) 233
- [90] P.N. Luke, Nucl. Instrum. and Methods in Phys. Research A **380** (1996) 232
- [91] K. Nakazawa et al., IEEE Trans. Nucl. Sci. **51** (2004) 1881
- [92] T. Takahashi, S. Watanabe, IEEE Trans. Nucl. Sci. **48** (2001) 950
- [93] M. Funaki et al, "Development of CdTe detector in Acrorad", Acrorad Co., Ltd.
http://www.acrorad.co.jp/_skin/pdf/Development_of_CdTe_detectors.pdf
- [94] N. Niraula et al., Nucl. Instrum. and Methods in Phys Res. A **491** (2002) 168
- [95] H. Toyama et al., Jpn. J. Appl. Phys. **45** (2006) 8842
- [96] T. Seino, I. Takahashi, IEEE Trans. Nucl. Sci. **54** (2007)
- [97] I.A. Kosyachenko et al, Semicond. Sci. Technol. **23** (2008) 1
- [98] H. Toyama et al, IEEE Nuclear Science Symposium Conference Record **3** (2005) 1395
- [99] N. Kishi et al., 2008 IEEE nucl. Sci. symposium Conference Record **2** (2008) 969
- [100] J.Liptac, R. Parker, V. Tang, Y. Peysson, J.Decker, Rev. Sci. Instrum. **77** (2006) 103504
- [101] W. Soller, Phys. Rev. **24** (1924) 158
- [102] S. Kobayashi, N. Hosoda, R. Takashima, Nucl. Instrum. and Methods in Phys. Res. A **390** (1997) 426
- [103] J.P. Hogge et al., J. Phys.: Conf. Series **33** (2005) 25
- [104] EGS basic simulation tool,
<http://www2.slac.stanford.edu/VVC/egs/basicstool.html>
- [105] W.H. McMaster et al, Compilation of X-Ray Cross Section, LLNL Report UCRL-50174 (1969). Available on line at: <http://cars9.uchicago.edu/~newville/mcbook/>
- [106] H. Dreicer, Phys. Rev. **115** (1959) 238
- [107] M.D. Kruskal, I.B. Bernstein, Princeton Plasma Physics Lab. Report no. MATT-Q-20 (1962) 172
- [108] B. Esposito et al, Phys. Plasmas **10** (2003) 2350
- [109] Z.Y. Chen et al, Phys. Letters A **351** (2006) 413
- [110] A.N.Karpushov, B.P.Duval, T.P.Goodman, Ch.Schlatter, 33rd EPS Conference on Plasma Physics, Rome, 2006, **30I** (2006) P-1.532
- [111] NRL formulary (p.44)
http://wwwppd.nrl.navy.mil/nrlformulary/NRL_FORMULARY_06a.pdf

[112] T.P. Goodman et al, Phys Rev. Lett. **106** (2011) 245002

Acknowledgement

This thesis work and the results achieved are not due to only to my self, instead, they are the consequence of a rich and continuous interchange with smart people surrounding and supporting me during the time I spent in the centre des recherché en physique de plasmas in Lausanne.

At first, I would like to express my deep and sincere gratitude to my supervisor, Dr. Stefano Coda. His wide experience in experimental physics, rational thinking, excellent intuitions and clear interpretation of physical phenomena, have been fundamental to guide me through this work. Moreover I would like to express him my gratitude for his human skills, for spending efforts in supporting me even in difficult periods.

A special and warm thanks is for Dr. Basil Duval and Dr. Timothy Goodman that follows my steps in experimental plasma physics at the TCV tokamak. They greatly help me on the interpretation of experimental results and transmitted to me the passion for this work. Further more they gave me a great help with punctual remarks to improve my conference presentations and, more fundamental, for the preparation of my PhD thesis defence.

A substantial part of my work was devoted to the integration of the LUKE Fokker-Planck code in the TCV environment. This task would not be possible without the formidable contribution of Dr. Joan Decker. His excellent mastering of all sort of theoretical tricks with permanent and pertinent interpretation of the experimental physical phenomenology make him the veritable "LUKE's GOD". I greatly profited and enjoyed from the continuous mail exchange and many hours of telephone and Skype calls spent in these years of collaborations.

I want to express my sincere gratitude to the CRPP electronics staff for the great job done in support of the HXRS camera system. In particular I warmly thank Mr. Philippe Marmillod that designed the amplifier cards for the system and provided an indispensable support for detector testing. His wide experience and professionalism have been fundamental for the success of the HXRS. I profited a lot of fruitful discussions we had that permitted to improve my understanding on the electronics signal formation and amplification. A special thank for Severino Antonioni who done an essential job to implement the electronics for the HXRS camera.

Concerning the mechanical implementation of the HXRS system I would like to express my gratitude to Guy Pochon and Jean Michel Mayor whos performed the CAD design of the HXRS diagnostics and to René Chavan which helped the development and the design of the tungsten Soller collimator. A special acknowledgement to the CRPP mechanics staff who machined and assembled the components of the HXRS camera system.

The working daily life during this 5 years spent at the CRPP has been really pleasant, and this thanks to the very nice CRPP PhD student community.

I would like to thank “in primis” the colleagues of my office that stand heroically in my presence and in the presence of my “animals”. Among them, Dr. Loic Curchod, Dr. Andreas Pitzschke, Dr. Theodoros Panis, Dr. Gennady Plyushchev, Dr. Yann Camenen and Dr. Sun Hee Kim. We shared a lot of fun, good and hard periods.

I would like to warmly thank two wonderful girls at the CRPP: the PhD students Lucia Federspiel and Annamaria Masetto who greatly support me during this last period of my thesis, and in particular during the writing of the thesis manuscript, they both have excellent “canapés”.

The Italian PhD community represented by: Francesco Piras, Federico Felici, Mattia Albergante, Annamaria Masetto, Costanza Zucca, Alessandro Marinoni, Alessandro Bortolon, Mario Podesta, Francesca Maria Poli, Silvia Puddu, Fabio Avino e Daniele Brunetti, was of great help to make the CRPP a nice place and to give to it an authentic taste of Italy.

I wish to thank Josef Kamleitner the PhD student that inherits my work and with which I have shared this last year of thesis, I am honoured to work with him and there is no doubt he will improve the work I have done up to here. I wish to him a great satisfaction and success in physics as in his life during his PhD time (and beyond of course).

I would like to express my gratitude to the members of the CRPP directive staff, who allowed to me of living this beautiful adventure in plasma physics research. A special and warm thanks is for the secretaries (and in particular Edith Grueter) which help all of us, PhD students, to live in a comfortable and pleasant environment.

At the end I owe my gratitude to all persons which with their friendship and love made the time I spend in these 6 last years so special and helped me to overcome difficult periods, among them: Isabelle Bergeon and her family, Julia Voirol and her family, Giovanni Polito and the friends of the Aumônerie des Etudiants UNIL-ÉPFL, Pierfilippo Sbicego and his family, Simone Carmignato and his family, Stephanie Rotzinger, Alexandra Paillusson and the friends of the Polyssons, Alicia Cart and Romain Charlet, Sara Gobbo, Fabio Gnesin, Diego Dalla Benetta and his wife Sara, Lorenzo Beltrame and his wife Elisa, Leone and Marta, Mr. Andrea Lombardo and his wife Marta.

Silvano Gnesin

Chemin de Montelly 43 B
1007 Lausanne (Switzerland)
Nationality: Italian (Swiss C-permit)
Date of birth: 28-08-1977

Mobile phone : +41 774129776
e-mail : silvano.gnesin@gmail.com



STRONG SKILLS

PHD in physics at EPFL
International academic background
Strong experience in nuclear radiation diagnostic

EDUCATION AND TRAINING

- ◆ From January 2006: **PhD** thesis work on: suprathreshold electrons dynamics in the TCV tokamak. EPFL/CRPP Lausanne, Switzerland. PhD private thesis defence on 1st of September 2011.
- ◆ February 2005/January 2006: **Master** in Plasma Physics and Engineering. Università di Padova - Consorzio RFX (Padova - Italy).
- ◆ October 2004: **Degree in Physics** At “ Università degli Studi di Padova” (Padova – Italy).
- ◆ September 2003/September 2004: **Master thesis (Erasmus program)** on: Development and characterization of a ion beam for electric field measurements in plasma. Marseille (France) at “Equipe Turbulence Plasma“, Université de Provence Aix-Marseille.
- ◆ 1991-1996: General Certificate of Education: School of commerce.

EXPERIENCE IN NUCLEAR PHYSICS

- ◆ Original design and commissioning of the tomographic hard X-ray camera system for the TCV tokamak, under constraint of budget and time.
- ◆ Characterisation of semiconductor detectors for X-ray spectroscopy.
- ◆ Development of tomographic algorithms applied to bremsstrahlung plasma emission reconstruction in tokamaks.
- ◆ Study of the electron cyclotron wave absorption by hard X-ray and electron cyclotron emission diagnostics.
- ◆ Monte Carlo applications to radiation shielding problems by means of EGS code simulations.

- ◆ Good knowledge of standard nuclear instrumentation and related digital data acquisition and analysis.

OTHER RELEVANT EXPERIENCE

- ◆ 1-week BNF stage in molecular biology (theory + experiment, September 2011)
- ◆ Basic knowledge on radiophysics (dosimetry and radioprotection), two week experience (stage) on Boron Neutron Capture Therapy (BNCT). at the “Istituto Nazionale di Fisica Nucleare (INFN) di Legnaro”, (Padova – Italy, spring 2003).
- ◆ Guide for visiting groups at the nuclear site TCV (http://crppwww.epfl.ch/crpp_tcv.html). The visit is given in French, English, and Italian.
- ◆ Participation at « salon de l'énergie renouvelable et des technologies nouvelles: Energissima 2009 (<http://energissima.ch/> Fribourg Suisse) » as representative of the centre pour la recherche en physique des plasmas (CRPP/EPFL).
- ◆ Teaching support at the EPFL

SPOKEN LANGUAGES

■ Italian: mother tongue; ■ French: fluent; ■ English: fluent.

COMPUTER SKILLS

■ Good knowledge of Linux and Windows environments; ■ Matlab programming ■ LabView data acquisition ■ Fundamentals of C++

REFERENCES (ADDITIONAL INFORMATION UPON REQUEST)

Dr. S. Coda, CRPP/EPFL Lausanne, Switzerland, PhD supervisor. Stefano.Coda@epfl.ch
Dr. J. Decker, CEA Cadarache, France. joan.decker@cea.fr
Dr. T.P. Goodman CRPP/EPFL Lausanne, Switzerland timothy.goodman@epfl.ch

INTERESTS AND HOBBIES

■ Theatre: four years as actor with the “Polyssons” (the EPFL theatre team);
■ dance; ■ hiking; ■ playing guitar.

Refereed scientific journals:

- ◆ S. Gnesin, S. Coda, J. Decker and Y. Peysson, Suprathermal electron studies in the TCV tokamak: design of a tomographic hard-X-ray spectrometer, [Rev. Sci. Instrum. 79 \(2008\) 10F504](#)
- ◆ S. Gnesin, J. Decker, S. Coda, T.P. Goodman, Y. Peysson and D. Mazon, 3rd harmonic ECRH absorption enhancement by 2nd harmonic heating at the same frequency in a Tokamak, submitted to Plasma Phys. Control. Fusion.

Conference proceedings, refereed by abstract:

- ◆ S. Gnesin, J. Decker, T.P. Goodman, S. Alberti, S. Coda, and Y. Peysson Synergy of 2nd and 3rd harmonic electron cyclotron absorption mediated by suprathermal electrons in the TCV tokamak, 36th EPS conference ECA 33E, P-2.139, Sofia (2009).
- ◆ S. Gnesin, S. Coda, Design of a tomographic hard X-ray spectrometer for suprathermal electron studies with ECRH, [AIP Conference proceedings 988 \(2008\) 222](#).
- ◆ J. Decker, S. Coda, Y. Peysson, S. Gnesin, S. Alberti and L. Curchod. Modeling of third harmonic ECRH experiment in TCV, 37th EPS conference Dublin (2010)
- ◆ J. Decker, Y. Peysson, S. Coda, L. Curchod, S. Gnesin, et Al., Fast electron physics in tokamak plasmas, 20th ITC conference, Toki, Japan (2010).

Abstracts in conference proceedings:

- ◆ S. Gnesin, T.P. Goodman, J. Decker, S. Coda, and Y. Peysson. Synergetic X2/X3 electron cyclotron power absorption in TCV: experiment and Fokker-Planck modeling, 52nd APS Chicago, IL (2010).
- ◆ S. Coda, S. Gnesin, P. Marmillod, J. M. Mayor, B. Duval and R. Chavan, Suprathermal electron studies in the TCV tokamak: the novel tomographic hard-X-ray spectrometer, 52nd APS Chicago, IL (2010).